Computational Investigations on Excited State Properties of Cyanine Dyes and Carbene-bound Main Group Elements

by

Mohammad Reza Momeni Taheri

A thesis submitted in partial fulfillment of the requirements for the degree of

Doctor of Philosophy

Department of Chemistry
University of Alberta

Abstract

The first section of this thesis is concerned with the computational study of excited state properties of boron-dipyrromethene (BODIPY) organic dyes using ab initio and time-dependent density functional theory (TD-DFT) methods. Through a comprehensive benchmark of TD-DFT methods against experiment for the BODIPY and Aza-BODIPY families, it was found that all TD-DFT methods systematically overestimate excitation energies. However, due to the high linear correlation of TD-DFT results with experiment, most functionals were found to be useful in predicting the excitation energies if corrected empirically. Through extensive examination of common TD-DFT problems (i.e., charge transfer (CT), multi-reference (MR) and double electron excitations), the deviation from experiment for TD-DFT was found to originate from contributions of multi-reference character and double electron excitations for the BODIPY family. We determined that the local coupled cluster method (LCC2) offered the best compromise between accuracy and efficiency for these systems.

An extensive benchmark study on vertical excitation energies of 11 different BODIPY and Aza-BODIPY dimers was performed using 15 different TDA-DFT methods. Adiabatic excitation energies were obtained for all structures using the M06-2X meta hybrid functional. Among the TDA-DFT functionals used, B2GP-PLYP and PBE0-2 double hybrid density functionals were found to yield the least amounts of mean absolute deviations (0.188 and 0.202 eV, respectively) when compared to experiment. The possible applications of BODIPY and Aza-BODIPY dimers in photodynamic therapy were examined by determining their spin-orbit coupling matrix elements, CASSCF occupancies along with the LCC2 vertical excitation energies and [S_0–T_1] and [S_1–T_1] singlet-triplet gaps. A systematic study on possible

azo-linked BODIPY and Aza-BODIPY dimers was accomplished and novel near infrared heavy atom free dyes were introduced.

In the second section of this thesis, the chemistry of carbene bound borane and silane adducts is discussed extensively with a particular focus on the propensity of these adducts for C–N bond cleavage of the carbenic species. A significant difference was observed between N-heterocyclic carbenes (NHCs) and aminoalkyl carbenes (^{Me}CAAC) in terms of the propensity of their element hydride complexes to participate in ring expansion chemistry. The computations showed that formation of a ring expanded product from $ImMe_2$-BH_3 is kinetically unfavourable due to the high energy barrier for the H-atom migration from boron to carbon. In the case of the silane adducts with NHC, the simultaneous presence of at least one hydrogen atom and one phenyl ring is crucial as the ring expansion reaction is not likely to happen for SiH_4 and $SiPh_4$; these computational findings are in agreement with the experimental observations.

Bonding analyses of boron-nitride substituted adducts with N-heterocyclic carbenes and phosphino yilides were carried out using EDA-NOCV, NBO and AIM techniques. Considering the Gibbs free energies, values greater than –50 kcal/mol were found for the complexation energies. From the NBO, AIM and EDA-NOCV approaches, the existence of a polar covalent bond between carbene and the boron atom was confirmed in each adduct studied. A donor-acceptor strategy showed that LB·$(BN)_n W(CO)_5$ (n = 1–3) complexes could be experimentally achievable (LB = Lewis base). Finally, analysis of the EDA-NOCV results in these adducts showed that the carbene–boron bonds are stronger in the presence of $W(CO)_5$ as a Lewis acid mainly because of a dramatic decrease in Pauli repulsion rather than an increase in the electrostatic/orbital attraction.

Preface

Chapters 1 and 2 constitute the introduction and theoretical background, respectively, and represent unpublished works as well as portions taken from the published research chapters.

Chapter 3 has been published as **Momeni, M. R.**; Brown, A. *Why Do TD-DFT Excitation Energies of BODIPY/Aza-BODIPY Families Largely Deviate from Experiment? Answers from Electron Correlated and Multi-reference Methods, J. Chem. Theory Comput.*, **2015**, *11*, 2619-2632.
Mohammad R. Momeni conceived the research project, carried out all computations, and wrote the manuscript. A. Brown contributed editorial and scientific comments on research project and manuscript.

Chapter 4 has been submitted as **Momeni, M. R.**; Brown, A. *A Local CC2 and TDA-DFT Double Hybrid Study on BODIPY/Aza-BODIPY Dimers As Heavy Atom Free Triplet Photosensitizers for Photodynamic Therapy Applications, J. Chem. Theory Comput.* **2015**.
Mohammad R. Momeni conceived the research project, carried out all computations, and wrote the manuscript. A. Brown contributed editorial and scientific comments on research project and manuscript.

Chapters 5 and 6 have been published as **Momeni, M. R.**; Rivard, E.; Brown, A. *Carbene-bound Borane and Silane Adducts: A Comprehensive DFT Study on their Stability and Propensity for Hydride-mediated Ring Expansion, Organometallics*, **2013**, *32*, 6201-6208.
Momeni, M. R.; Shulman, L.; Rivard, E.; Brown, A. *Interplay of Donor-acceptor Interactions in Stabilizing Boron Nitride Compounds: Insights from Theory, Phys. Chem. Chem. Phys.* **2015**, *17*, 16525-16535, *Advanced Article* (**Open Access**).
These chapters form part of a research collaboration with Prof. Eric Rivard led by Prof. Alex Brown at the University of Alberta (UofA). The molecules discussed in these two chapters were brought to our attention by Prof. Rivard at the UofA. Prof. Rivard also contributed to the editing of their corresponding manuscripts. Lisa Shulman conducted some of the geometry optimizations and NBO computations required for chapter 6 of this thesis.

The author has contributed (as the second author) to a number of other research projects that are *not included in this thesis*. The publications are:
Lummis, P. A.; **Momeni, M. R.**; Lui, M. W.; McDonald, R.; Ferguson, M. J.; Brown,

A.; Rivard, E. *Accessing Zinc Monohydride Cations via Coordinative Interactions, Angew. Chem. Int. Ed.* **2014**, *53*, 9347-9351.

Al-Rafia, S. M. I.; **Momeni, M. R.**; Ferguson, M. J.; McDonald, R.; Brown, A.; Rivard, E. *Stable Complexes of Parent Digermene: An Inorganic Analogue of Ethylene, Organometallics*, **2013**, *32*, 6658-6665. (**Invited Manuscript**: Special Issue: Applications of Electrophilic Main Group Organometallic Molecules)

Al-Rafia, S. M. I.; **Momeni, M. R.**; McDonald, R.; Fergsuson, M. J.; Brown, A.; Rivard, E. *Controlled Growth of Dichlorogermanium Oligomers from Lewis Basic Hosts, Angew. Chem. Int. Ed.* **2013**, *52*, 6390-6395 (**VIP article**).

These works were results of a collaboration with Prof. Rivard's group at the University of Alberta. The author was responsible for performing all the computations presented in the original published papers as well as initial composition of the relevant theory parts of the manuscripts and supplementary materials.

"Make books your companions; let your bookshelves be your gardens; bask in their beauty, gather their fruit, pluck their roses, take their spices and myrrh."

Jābir ibn Hayyān

Acknowledgements

We thank the Natural Sciences and Engineering Research Council (NSERC) of Canada for financial support and the Canadian Foundation for Innovation (New Opportunities Fund) for support for computational infrastructure. This research has been (partially) enabled by the use of computing resources provided by WestGrid and Compute/Calcul Canada.

Mohammad is indebted to Dr. Alex Brown for his helps and supports during preparation of this PhD thesis. Members of the theoretical and computational chemistry in UofA are also gratefully acknowledged.

Dr. Eric Rivard from UofA is gratefully acknowledged for his valuable advices and also supports.

Members of the examining committee, Prof. Mariusz Klobukowski, Prof. Yunjie Xu, Prof. Frederick G. West, Prof. Jonathan G. C. Veinot, and the external referee, Prof. Denis Jacquemin, are gratefully acknowledged for reading this thesis.

Mohammad also wishes to thank technical supports from Dr. Grigory Shamov and Dr. Masao Fujinaga, WestGrid Compute Canada site leaders at the University of Manitoba and UofA, respectively.

To the best and biggest incident of my life, "Farnaz".

Abbreviations & Symbols

AIM	Atoms-in-molecules
Aza-BODIPY	Aza-boron-dipyrromethene
B3LYP	Becke's three-parameter hybrid with LYP correlation
BLYP	Becke 88 exchange with LYP correlation (a GGA)
BODIPY	Boron-dipyrromethene
BN	Boron-nitride
CAAC	Cyclic aminoalkyl carbene
CASSCF	Complete active space self-consistent field
CASPT2	Complete active space second order perturbation theory
CCS	Coupled cluster singles
CCSDR(T)	Linear response coupled cluster singles, doubles and non-iterative triples
CCSDR(3)	Linear response coupled cluster singles, doubles and non-iterative triples
CIS	Configuration interaction singles
CIS(D)	Configuration interaction singles and perturbative doubles
CISD	Configuration interaction singles and doubles
DFT	Density functional theory
EOM-CCSD	Equation of motion coupled cluster singles and doubles
EDA-NOCV	Energy decomposition analysis natural orbitals for covalent valence
GGA	Generalized gradient approximation
GS	Ground state
HF	Hartree-Fock
HOMO	Highest occupied molecular orbital
IR	Infrared
ISC	Intersystem crossing

KS	Kohn-Sham
LA	Lewis acid
LB	Lewis base
LCC2	Local coupled cluster singles and approximate doubles
LDA	Local density approximation
LUMO	Lowest unoccupied molecular orbital
LYP	Lee, Yang, and Parr
MAD	Mean absolute deviation
MBPT	Many-body perturbation theory
MCSCF	Multi-configuration self-consistent field
Mean AE	Mean absolute error
MP2	Møller-Plesset second-order
NBO	Natural bond orbital
NHC	N-heterocyclic carbene
occ	Occupied
PBE	Perdew, Burke, and Ernzerhof
PBE0	Hybrid functional based on PBE$\tilde{\text{O}}$s GGA
PDT	Photodynamic therapy
PES	Potential energy surface
PT	Perturbation theory
PS	Photosensitizer
revPBE	Revised PBE
revPBE0	Revised PBE0
RPA	Random phase approximation
SAC-CI	Symmetry adapted cluster configuration interaction
S.E.	Schrödinger equation
SOC	Spin-orbit coupling
TD	Time-dependent
TDA	Tamm-Dancoff approximation
TD-DFT	Time-dependent density functional theory
TD-HF	Time-dependent Hartree-Fock
unocc	Unoccupied

UV	Ultraviolet
virt	Virtual
xc	Exchange-correlation

$\lambda_{max}^{(abs.)}$	Maximum absorption wavelength (in nm)
$\lambda_{max}^{(fl.)}$	Maximum fluorescence wavelength (in nm)
ϵ	Molar absorptivity (in $M^{-1}cm^{-1}$)
ϕ_F	Fluorescence quantum yield
ϕ_{ISC}	Intersystem crossing quantum yield
$\langle \mathrm{i} \vert$	$f_i^*(\mathrm{r})$
$\vert \mathrm{i} \rangle$	$f_i(\mathrm{r})$
$\langle \mathrm{i} \vert \hat{A} \vert \mathrm{j} \rangle$	$\int f_i^*(\mathrm{r}) \hat{A} f_i(\mathrm{r})\ \mathrm{dr}$

Contents

List of Figures

List of Tables

Chapter 1

Introduction

1.1 Highly Fluorescent Dipyrromethene Fluorophores

1.1.1 Syntheses and Applications

Boron-dipyrromethenes (known as BODIPYs), where boron difluoride is attached to conjugated dipyrromethene, are a very important class of organic fluorophores [8] (see Figure 1.1 for the structure of the fully unsubstituted (parent) BODIPY). Despite the small sizes

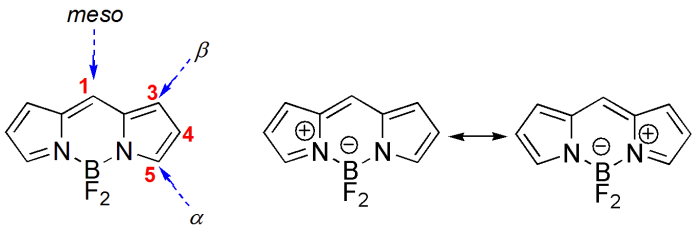

FIGURE 1.1: Structure, different atom numberings and resonance forms of the parent BODIPY molecule.

and relatively simple structures, BODIPYs exhibit excellent photophysical properties such as high extinction coefficients and quantum yields (for the photophysical properties of the parent BODIPY, see Table 1.1) [8, 9]. Due to their excellent photophysical properties, BODIPYs find use in a wide range of applications such as laser dyes [10, 11], labelling and fluorescent indicators and probes [12–14], imaging and sensing agents [15, 16] and sensitizers in dye-sensitized solar cells [17] (see Figure 1.2).

TABLE 1.1: Photophysical properties of the parent BODIPY molecule in CH_2Cl_2 solution [7].

$\lambda_{max}^{(abs.)}$ [nm]	$\lambda_{max}^{(fl.)}$ [nm]	ϕ_F [%]	ϕ_{ISC} [%]	ϵ [$M^{-1}cm^{-1}$]
503	512	90	1.1	5×10^4

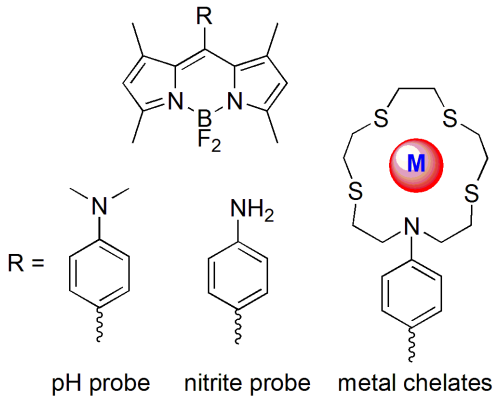

FIGURE 1.2: BODIPYs used as probes and sensors.

The first report of the synthesis of BODIPY goes back to 1968 by Treibs and Kreuzer (Figure 1.3) [18].

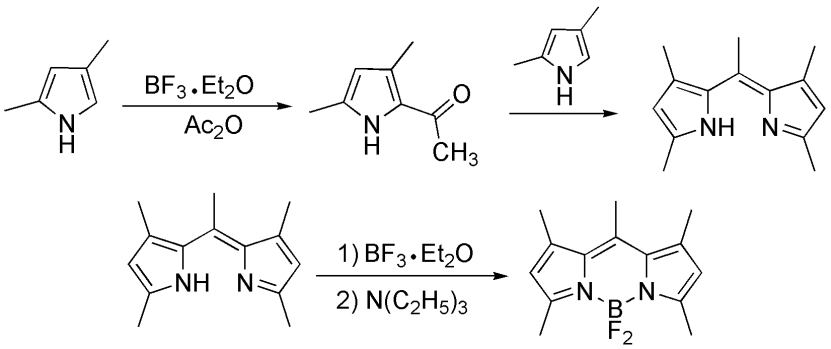

FIGURE 1.3: Treibs and Kreuzer's synthesis of the methyl substituted BODIPY.

The X-ray structure of the parent BODIPY was only revealed 41 years later by two separate groups [7, 19]. Schmitt *et al.* synthesized the parent BODIPY molecule via a one-pot condensation of 2-formyl pyrrole and 1H-pyrrole catalyzed with trifluoro acetic acid followed by deprotonation with ethyl diisopropyl amine and finally complexation of the dipyrromethene with boron trifluoro etherate (Figure 1.4) [19]. Arroyo *et al.*, on the other hand, reported the synthesis of this compound by removing the thiomethyl group from the corresponding substituted BODIPY (Figure 1.4) [7].

Although these fundamental studies were only carried out in the past five years, extensive

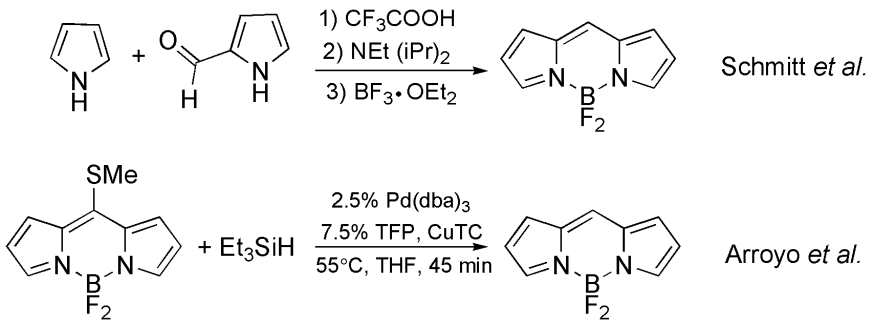

FIGURE 1.4: Syntheses of the fully unsubstituted parent BODIPY molecule.

experimental and theoretical efforts [8, 9, 13, 20–22] have been undertaken since the first reported synthesis. From the extensive work carried out, altering the size and/or number of rings in the core BODIPY system or substituting different functional groups (for instance see structures in Figure 1.5) can impart significant changes on the absorption and emission wavelengths as well as their photostabilities [23–26].

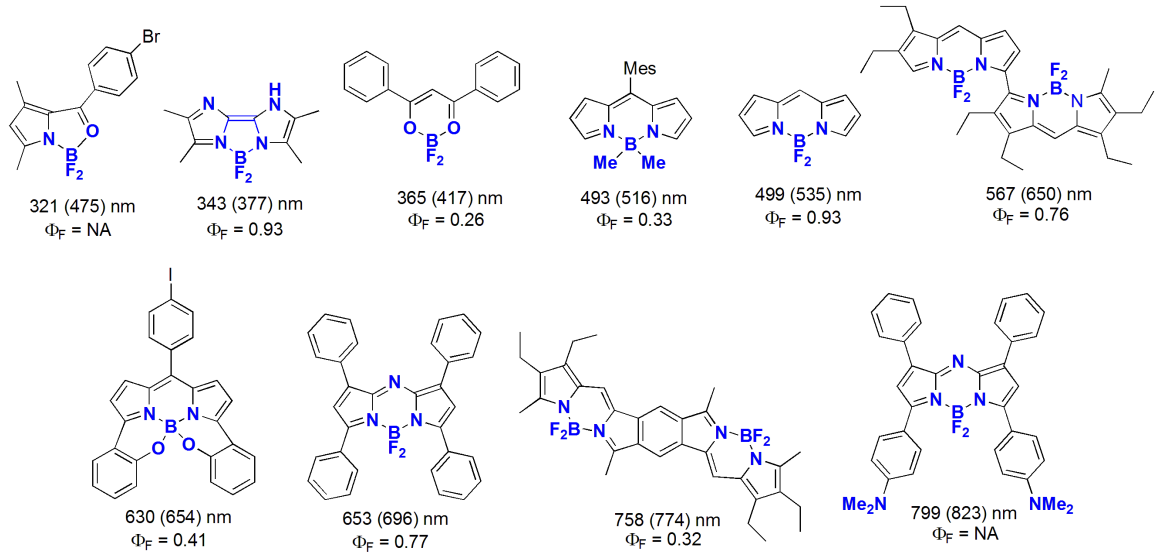

FIGURE 1.5: Experimentally determined absorption and emission (in parenthesis) wavelengths of different substituted BODIPYs along with their fluorescence quantum yields.

Extensive effort has been devoted to the design and synthesis of new BODIPY based systems with near IR absorptions and emissions [27–29]. For example, substituted aza-boron-dipyrromethene (aza-BODIPY) based systems, where the C–H group at the *meso* position in the core structure is replaced with a nitrogen atom, constitute a very important class of the red-shifted BODIPY systems [30]. The first synthesis of aza-BODIPYs was reported in the

early 1990s from reaction of tetraphenyl aza-boron-dipyrromethenes with boron electrophiles (Figure 1.6) [31].

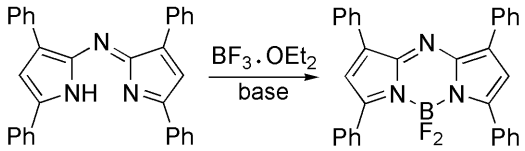

FIGURE 1.6: The first reported synthesis of the aza-BODIPY molecule.

Moreover, their photophysical properties, e.g., absorption and emission wavelengths, can be tuned via carefully chosen chemical modification (see Figure 1.5). As can be seen from Figure 1.5, changing the skeleton of BODIPYs leads to a diverse family of organic chromophores with a broad range of absorption and emission wavelengths while retaining their high fluorescence quantum yields.

1.1.2 BODIPYs and aza-BODIPYs in PDT Action

They have also been shown to be efficient singlet oxygen generators [32] and photosensitizers (PSs) in photodynamic therapy (PDT) application [1, 33, 34] (see Figures 1.7). In PDT

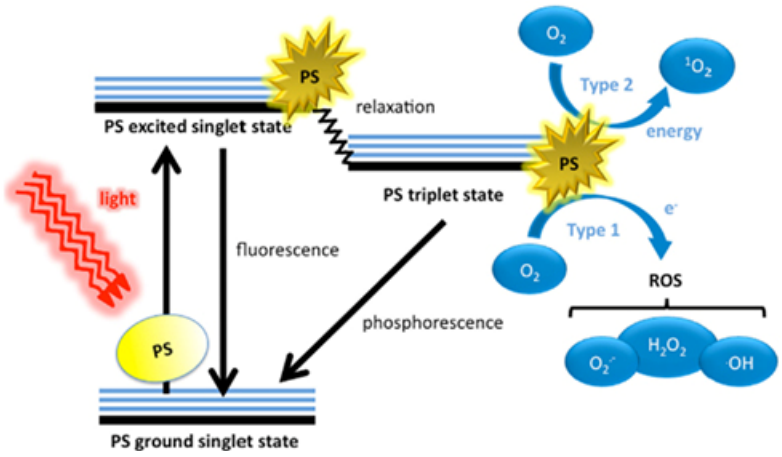

FIGURE 1.7: Schematic representation of the PDT mechanism including the Jablonski diagram. Energy transfer from PS to the $^3O_2$ molecule forms reactive oxygen species (ROS) through type 1 or $^1O_2$ species through type 2 reactions. Reprinted with permission from Ref. 1.

treatment, the PS is locally injected to the target area (cancer tissues) and a laser beam is delivered to the area through endoscopes and fiber optic catheters. After shining the light, highly reactive singlet oxygen ($^1O_2$) is generated, from already present triplet oxygen ($^3O_2$)

molecules inside cancer tissues, by an energy transfer from the excited triplet photosensitizer (^{3}PS) to the $^3O_2$ (for the structures of the commonly used PDT drugs see Figure 1.8).

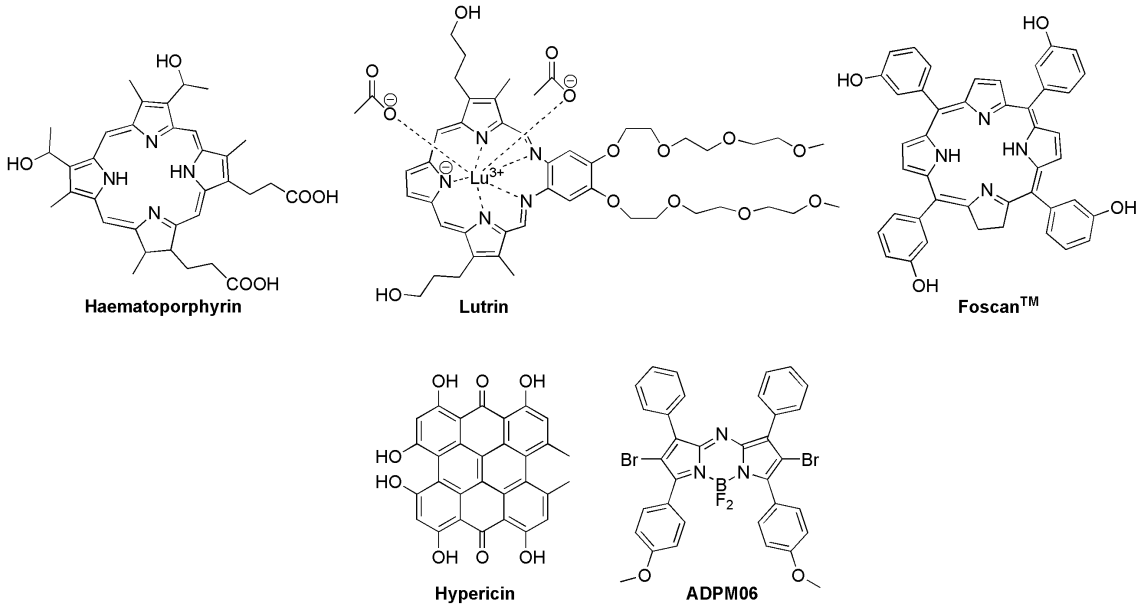

FIGURE 1.8: Structures of the some of the commonly used PDT drugs.

There are certain conditions for the PS to be used as a PDT drug including (i) low dark toxicity, i.e., the PS should be only activated by light, (ii) low photobleaching rate, (iii) a preferential uptake in target tissues, (iv) large intersystem crossing (ISC) rate and as a result, a large singlet oxygen generation quantum yield, and (v) singlet–triplet gap (ΔE [S_0–T_1]) close to that of the oxygen molecule (about 1 eV) for the energy transfer to be efficient [20, 33].

Intersystem crossing is a non-radiative transition between states of different multiplicity which involves the inversion of the spin of the excited electron which is formally forbidden. Based on the El-Sayed's rule, the ISC rate is likely to be very slow unless it involves a change of orbital configuration or orbital type. For instance, the El-Sayed's rule correctly predicts the ISC rate from a singlet excited state with $\pi \rightarrow \pi^*$ nature to a triplet excited state with n $\rightarrow$ π^* character to be large. The ISC rate is intrinsically very slow for most organic molecules because the singlet-triplet mixing is very small in them.

Determining ISC rate is not an easy task as it requires all the information regarding other competitive deactivation channels such as radiationless transition, fluorescence, etc. The

probability of ISC depends on a number of factors which are listed below:

(1) The ISC process is most favourable when vibrational levels of two excited electronic states overlap. This mechanism allows the occurrence of (a close to) an adiabatic transition (i.e., no energy must be gained or lost).

(2) The ISC rate is higher in molecules containing heavy atoms and/or transition metals. This is due to the large spin-orbit coupling between electron spin and orbital angular momentum in these compounds which ultimately leads to larger mixing of the singlet and triplet excited states. The energy shift due to spin-orbit coupling is determined to be dependent to the fourth power of the nuclear charge [35].

(3) The magnetic field originating from the paramagnetic species such as Co nanocrystals [36] can enhance the rate of ISC.

On the other hand, the singlet oxygen quantum yield can be measured using a singlet oxygen quencher such as 1,3-diphenylisobenzofurane (DPBF) or by using the singlet oxygen luminescent method. The former method monitors disappearance of the absorption of the DPBF molecule at 416 nm as an indicator of generation of singlet oxygen molecules. The fluorescence quantum yield (ϕ_F) has also been measured using comparative method of Williams [37], which uses a well characterized standard sample with a known ϕ_F value. Solutions of reference and test samples with identical absorptions at the same wavelength are assumed to absorb the same number of photons. Therefore, a simple ratio of the integrated fluorescence intensities of the two solutions under same conditions will yield the ratio of their fluorescence quantum yields. It has been shown that appropriate substitution of the BODIPY and aza-BODIPY molecules makes them ideal candidates for PDT applications [8, 9, 38]. Seminal works of ÓShea [39], Nagano [20], Akkaya [40], and Shen [41] illustrated that BODIPYs substituted with bromine and iodine atoms in the C–4 position of the dipyrromethene core are very good PSs for PDT action due to the heavy atom effect and its impact on facilitating the ISC rate (Figure 1.9).

However a major issue with *in vivo* use of these molecules is their relatively large dark toxicities due to the use of heavy atoms as stated above. Akkaya and his coworkers tackled this problem by reporting the first heavy atom free PSs based on BODIPY molecules [42] (Figure 1.9). In a joint experimental and theoretical study, they showed that BODIPY

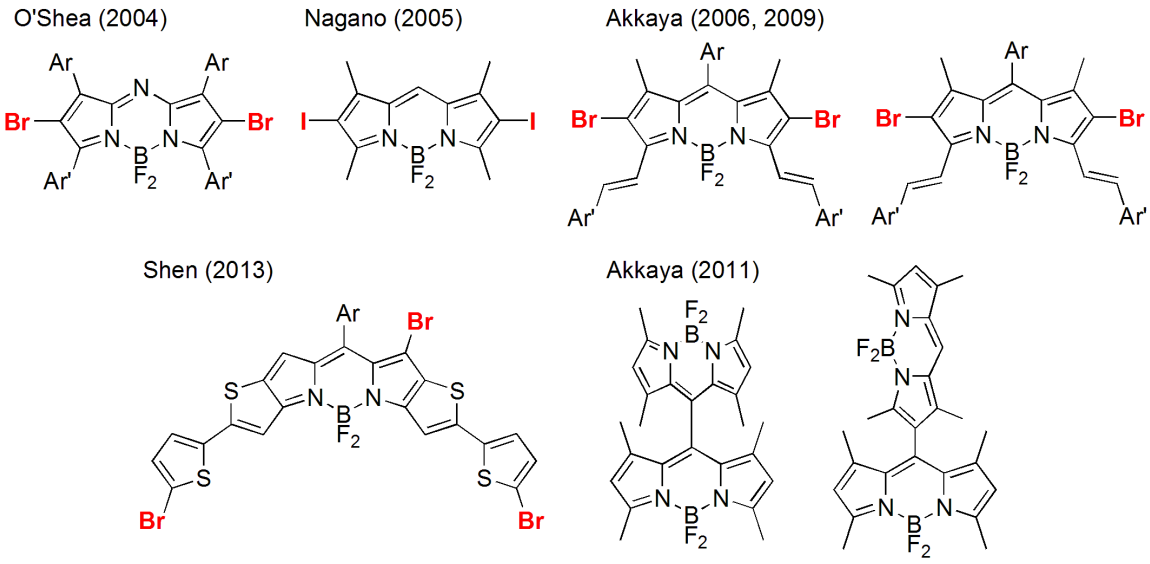

FIGURE 1.9: BODIPYs and aza-BODIPYs used in PDT.

monomers linked in the [1,4] and [1,1] positions with absorption (emission) wavelengths of 514 nm (527 nm) and 515 nm (588 nm), respectively, show high singlet oxygen generation quantum yields of 0.51 and 0.46, respectively. The photocytotoxicity of these BODIPY dimers was also successfully tested against human erythroleukemia cells. However one of the main drawbacks of these PSs are their absorption ranges which are outside the therapeutic window (i.e., 650–900 nm). Extending the conjugation length in these dyes was tested as a possible remedy but was proven to be insufficient [43].

Ideally, one would like a reliable computational approach for predicting the effects of chemical modification of BODIPYs. Time-dependent density functional theory (TD-DFT), see Chapter 2 for its theoretical background, is the computational method of choice for studying excited state properties in many systems due to its overall accuracy and efficiency [44–46]. However, several TD-DFT benchmark studies on BODIPYs illustrated that it is not a well suited approach for these compounds and the computed excitation energies are largely overestimated with respect to the experimental values [30, 47–52]. The work presented in Chapter 3 attempts to find the trends and connections between different BODIPY and BODIPY-like systems to illustrate the extent of the TD-DFT discrepancy. Therefore, 9 different TD-DFT functionals were tested for 17 different BODIPY like systems with the cc-pVTZ basis set. All TD-DFT methods were found to overestimate the experimental values (> 0.4 eV). However, due to the relatively high linear correlation of the TD-DFT results with experiment, it is

possible to empirically correct them. In an effort to understand the nature of these large deviations, several ab initio methods including TD-HF, CIS, CIS(D), CCS, EOM-CCSD, CCSDR(T), CCSDR(3), LCC2, SAC-CI, CASSCF and CASPT2 methods were benchmarked against experiment. The LCC2/cc-pVDZ method with mean absolute error (Mean AE) of 0.109 eV was found to provide the best compromise between accuracy and efficiency and was closest to the highly accurate CASPT2 method (Mean AE = 0.100 eV). However, the LCC2 method is more promising because of its applicability to much larger systems. To find the reason behind the large deviation of TD-DFT with experiment, several classical problems of TD-DFT were carefully examined such as charge transfer, multi-reference and double electron transitions. The failure of TD-DFT for the BODIPY family was attributed to multi-reference character of the wave function and also double electron transitions.

In Chapter 4 of this thesis, another benchmark study on the dimers of BODIPYs and aza-BODIPYs is presented. In this chapter, excitation energies, spin-orbit coupling matrix elements as well as singlet-triplet gaps of 36 theoretically designed BODIPY dimers are computed in an attempt to find better PSs for PDT treatment.

1.2 Carbene-bound Main Group Elements

1.2.1 Carbenes

Carbenes are referred to neutral divalent carbon-based species which contain two non-bonding electrons. Carbenes are capable of existing in either a singlet or triplet ground state depending on the nature of their substitutents [53–57]. The spin multiplicity, singlet versus triplet, is a fundamental feature of carbenes that dictates their reactivities [58]. The structure of a carbene, especially its divalent angle, is important and determines the ground state multiplicity (see Figure 1.10).

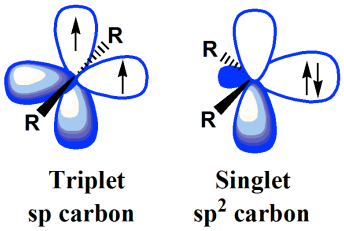

FIGURE 1.10: Electronic configuration of singlet and triplet carbenes.

Methylene (CH_2) [59], the parent of all carbenes, has been investigated in several matrix isolation experiments [60–62]. It has a triplet ground state ($^3B_1$ symmetry) with a singlet–triplet energy gap, ΔE_{S-T} of 9.05 ± 0.04 kcal/mol and a divalent angle (the H–C–H bond angle) of 136° [63–69]. The first theoretical study on methylene goes back to 1932 by Mulliken who showed that the singlet state of this molecule with $^1A_1$ symmetry has an angle of 110°. He also showed that methylene has a lower lying triplet state with $^3B_1$ symmetry. The first ab initio study on this molecule was done in 1960 and confirmed the Mulliken's prediction that the triplet state is more stable than the singlet [70]. More specifically, Foster and Boys showed that there is a ΔE_{S-T} gap of 24.5 kcal/mol between $^1A_1$ and $^3B_1$ states with divalent angles of 90° and 122°, respectively. The first experimental electron spin resonance study on triplet CH_2 was performed in 1970. The experimental measurements in a Xenon matrix at 4K confirmed the previously predicted non-linear arrangement of the $^3B_1$ methylene molecule. Dialkyl-substituted methylenes are notoriously difficult to intercept by external chemical trapping agents, and to detect by matrix isolation spectroscopy [71]. Presumably, this is due to their ability to undergo rapid intramolecular rearrangements. Evidence has been presented that singlet dimethylcarbene, the simplest dialkylcarbene, is a true intermediate with a finite

lifetime of 21 ns in pentane at room temperature [71, 72]. Earlier theoretical studies on this elusive species have been performed only at relatively low levels of theory, calculating its ΔE_{S-T} of 23.8 kcal/mol at the HF/STO-3G level [73]. In 1995, Schaefer *et al.*, using a higher level of ab initio theory (configuration interaction with singles and doubles excitations (CISD)) and larger basis sets, predicted that dimethylcarbene has a singlet ground state with a ΔE_{S-T} of 1.4 kcal/mol [74]. For the parent cyclic carbene, cyclopropylidene, several theoretical calculations are reported, showing inconsistent results [73, 75–79]. In 1984 Maier *et al.* succeeded in generating cyclopropenylidene by means of flash vacuum pyrolysis [80]. Subsequently, Thaddeus *et al.* showed that cyclopropenylidene is one of the most abundant molecules in the interstellar molecular clouds [81].

As mentioned above, the two substituents directly attached to the divalent carbon atom have significant impacts on the structures, multiplicities and reactivities of the carbenic species. It has been shown that π-electron donors such as amino and phosphino groups stabilize singlet states [82–91] while σ-donors (groups possessing elements less electronegative than carbon) stabilize triplet states [92–95]. A combination of electronic (intraring C-N π-interactions) and steric (large substituents on nitrogen) effects was assumed to be responsible for stabilization of the first isolable singlet cyclic diaminocarbene, famous as N-heterocyclic carbene (NHC), reported by Arduengo and his coworkers in 1991 (see Figure 1.11) [2]. For a collection of theoretical studies on stabilities and reactivities of carbenes see Ref. 96 and references therein.

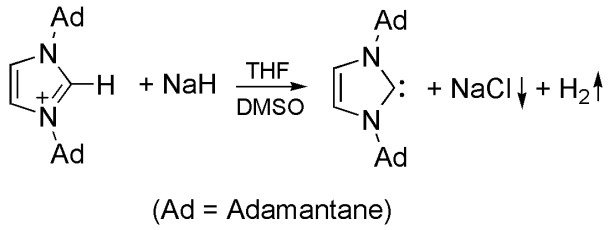

FIGURE 1.11: The first reported synthesis of a stable crystalline carbene [2].

This initial account was followed by reports of a wide variety of stable cyclic diheteroatom carbenes, including aminothio- and aminoxycarbenes (see Figure 1.12) [97–103]. In addition to nitrogen, sulfur and oxygen are also capable of stabilizing singlet carbenes, but with different steric protection [104]. Synthesis of the first stable acyclic carbene, phosphinosilylcarbene, by Bertrand *et al.* was achieved through the π-electron donation of the phosphino group as well as the π-electron acceptance of the silyl substituent [105–107]. It is now well

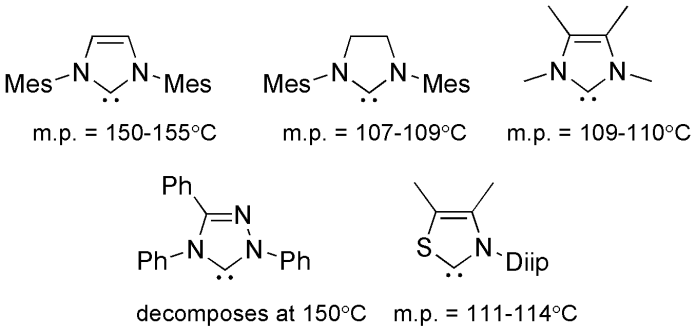

FIGURE 1.12: Stable synthesized singlet carbenes.

established that the presence of one π-electron donor heteroatom is sufficient to stabilize singlet carbenes [108–112]. After synthesis of the stable acyclic phosphinoalkylcarbenes and aminoalkyl carbenes [3, 113–116], Bertrand and his coworkers introduced cyclic aminoalkyl carbenes (CAACs) with stabilities comparable to diaminocarbenes (Figure 1.13) [109, 117–122]. The strong electron donating ability of NHCs and CAACs makes them desirable ligands

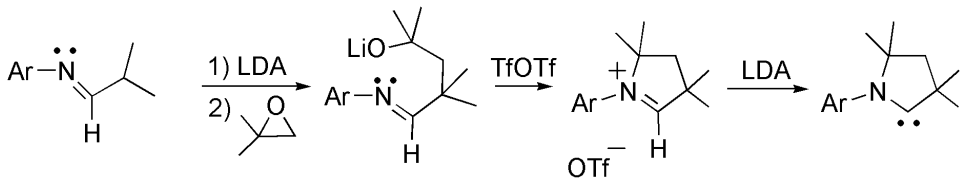

FIGURE 1.13: The first reported synthesis of a stable crystalline cyclic aminoalkyl carbene [3]. LDA = Lithium diisopropylamide.

for metal-mediated catalysis [123–127]. Owing to the strong electron donation of the CAAC ligands compared to the NHCs, low coordinated transition metal complexes are now available [118].

1.2.2 Carbenes in Complex with Other Compounds

Free carbenes have also been used to stabilize radicals and radical cations [128] as well as to instigate chemical transformations such as the cyanosilylation of unsaturated substrates [129–131] and the ring-opening polymerization of siloxanes [132–135]. In addition, NHCs and CAACs have attracted significant attention from the main group community with regard to the stabilization of reactive main group element fragments (e.g. L→Si=Si←L [136], L→Ge=Ge←L [137], L→Si←L [138], L→Ge←L [139], L→Sn=Sn←L [140], L→B≡B←L [141], L→(H)B=B(H)←L [142], L→B(H)←L [143], L→P=P←L [144], and L→As=As←L

[145], L = carbene ligands). NHC-boranes are also actively being explored as precursors to radical initiators for olefin polymerization [146, 147].

In general, NHCs and related systems such as CAACs are viewed as being resistant to degradation/bond activation processes when bound to electron deficient substrates. However recently it has been shown that Be, B and Si hydrides can undergo hydride-mediated ring expansion/atom insertion chemistry with their NHC donors [148–150]. In a computational study based on Density Functional Theory (DFT), we investigated borane and silane adducts supported by both NHC and CAAC donors (see Chapter 5). The goal of this study was to compare the hydride accepting ability of these Lewis basic donors within the context of their propensities for participating in ring expansion chemistry. Both electronic and steric effects on the formation of element hydride complexes were evaluated by examining complexes involving NHCs of different ring sizes and substituents. Moreover, a further analysis of the reported complexes using Natural Bond Orbital (NBO) and Atoms-in-Molecules (AIM) indices were performed to probe the strength and nature of the dative interactions in the preformed adducts.

1.3 Boron-nitride Compounds

The year 1985 was the milestone of a new era of materials chemistry in which the first all carbon cage like structure (C_{60} fullerene) was synthesized and characterized [151, 152]. The stabilities and reactivities of all boron fullerene cages, B_{80} [153, 154] and B_{40} [155], have also been studied both experimentally and theoretically. Discovery of the buckministerfullerenes, which are the third allotrope of pure carbon materials, was followed by the synthesis of their elongated forms, i.e., carbon nanotubes, by Iijima in 1991 [156, 157]. Similar to the fullerenes, the structure and properties of all boron nanotubes were also investigated both computationally [158, 159] and experimentally [160]. It is now well established that endohedral or exohedral substitution of fullerenes [161] and carbon nanotubes [157] can alter their structures and properties appreciably. Boron-nitride nanotubes are among the prospective materials for nano-technlogy that in opposite to their carbon counterparts their electronic properties are insensitive to their diameters.

The other two forms of pure carbon, diamond [162] and graphite [163], are also shown to possess excellent properties. For example diamond, in spite of being thermodynamically less stable than graphite, has the highest hardness and thermal conductivity of any bulk material. This interesting property in diamond is believed to arise from its strong covalent carbon-carbon (C–C) bonds. Interestingly, bringing in tiny amounts of boron or nitrogen impurities into the diamond lattice can change its colour to, respectively, blue and yellow. On the other hand graphite, the most stable form of carbon under standard conditions, has very interesting structure and properties. Graphite's honeycomb layered structure allows it to be one of the best electrical conductors and to be used as an electrode and also as a lubricant in chemical industry.

Boron nitride materials $(BN)_n$ [164–166], which are isoelectronic with various carbon allotropes mentioned above, possess vastly different properties due to the presence of polarized B-N linkages. For example, BN [166, 167] doped graphene [168, 169], the single layered form of graphite, is shown to have superior thermal and chemical properties. Because of their low electric conductivity and high thermal conductivity hexagonal BN compounds, which can have electronic band gaps as wide as 5.9 eV, are widely used material in both research and industry applications [170]. Due to the high thermal and mechanical stability and the

unsurpassed thermal shock resistance, BN ceramics have been traditionally used as parts of high-temperature equipment. There are also other significant physical properties of BN that make them suitable for various industrial applications. They are nontoxic and chemically inert, transparent to microwaves (hexagonal BN), and hard (cubic BN). The construction of devices based on BN/graphene heterostructures is also a promising recent development in electronics[171, 172].

1.3.1 Stabilizing Boron-nitride Complexes

One drawback to the widespread examination and application of BN materials is the harsh conditions required for their syntheses, i.e., heating above 900°C and/or the use of plasma conditions [164–166]. With these challenges in mind, we have embarked on a program wherein complexes of the general form $[LB{\cdot}BN]_n$ ($n \geq 1$; LB = Lewis base) might be formed with suitable carbon-based donors. Upon heating in solution, the target $[LB{\cdot}BN]_n$ complexes could afford bulk boron nitride and free Lewis base. This procedure has been successfully tested by Rivard and Veinot [173]. They showed that through microwave assisted heating of a single germanium di-hydride precursor, germanium nanocrystals can be generated [173].

To provide a solid fundamental basis for future experimental explorations, quantum mechanical computations are performed on the Lewis base stabilized linear and cyclic boron nitride species $(BN)_n$ (n = 1–3) (Chapter 6). The results presented in Chapter 6 of this thesis also include the donor-acceptor adducts $LB{\cdot}(BN)_n{\cdot}LA$ (n = 1–3, LA = Lewis acid). Recent examples of stabilizing main group element units (e.g., Si_2) with the aid of strong carbon-based donors are numerous in the literature [136, 140, 141, 143, 174–176]. Moreover, donor-acceptor stabilization has been used to great success to isolate heavier group 13–15 element species [177–182], while related computational studies have been reported [183, 184]. More specifically, DFT predicted a significant thermodynamical stabilization of group 13–15 cubane systems (e.g., B_4N_4) upon addition of NH_3 and BH_3 as donor and acceptor molecules, respectively [183].

In Chapter 6, analyses of the bonding within Lewis base-substituted boron nitride compounds in the presence and/or absence of Lewis acid are presented. Specifically we have examined the binding of the carbon-based donors, $ImMe_2$ ($ImMe_2$ = $[(HCNMe)_2C{:}]$), $ImMe_2CH_2$ and

Me_3PCH_2 to $(BN)_n$ units (n = 1–3), given the use of their sterically hindered analogues to bind/stabilize inorganic methylene and ethylene units (EH_2 and $H_2EE'H_2$; E and E′= Si, Ge and/or Sn) [175, 185–192]. Computations on LB·$(BN)_n$·BH_3 and LB·$(BN)_n$·$W(CO)_5$ adducts (n = 1–3) featuring coordinated $(BN)_n$ units are also provided. We demonstrate that this overall donor-acceptor approach is a viable means of intercepting a complex of molecular boron nitride. Finally, based on detailed EDA-NOCV computations, we will comment on the strength and nature of both the carbene–boron and nitrogen–tungsten donor acceptor bonds in the $ImMe_2$ substituted BN·$W(CO)_5$ and B_3N_3·$W(CO)_5$ adducts.

Chapter 2

Background and Theory

One of the foundations of quantum mechanics was established by introduction of the time-independent Schrödinger equation (S.E.), by Erwin Schrödinger in 1926 [193]. According to this equation, one can fully describe the behaviour of any quantum mechanical system by obtaining its many-body wave function (Ψ). However, the exact solution of this equation is only feasible for a handful of problems and one needs to make educated approximations to solve this equation for other systems. This is where *electronic structure theory* comes to existence by providing approximate solutions to the S.E. for problems related to atomic and molecular structure. One of the fundamental approximations that electronic structure takes advantage of it is called the Born-Oppenheimer approximation (B.O.). According to the B.O. approximation, because electrons move much faster than nuclei it is possible to separate these two particles from each other and solve the S.E. only for electrons (in fixed coordinates of nuclei) [194]. Through solving the electronic wave function at every fixed geometry of nuclei one can obtain the electronic energies associated with those arrangements or in other words the potential energy surface of the system. A brief review of electronic structure methods is provided here; more detailed discussion can be found in Refs. 195–198.

2.1 Slater Determinants and Restricted Hartree Fock Theory

As mentioned above, obtaining the *exact* wave function of a systems is generally not feasible save for a handful of problems. Therefore, one needs to approximate it in terms of some

other functions. The simplest representation of an N-electron wave function is to write it as a product of one particle functions, the so called *Hartree Product* (see Eq. 2.1)

$$\Psi(\mathrm{x}_1, \mathrm{x}_2, ..., \mathrm{x}_\mathrm{N}) = \psi_1(\mathrm{x}_1)\, \psi_2(\mathrm{x}_2)\, ...\, \psi_\mathrm{N}(\mathrm{x}_\mathrm{N}). \tag{2.1}$$

$\phi_i(\mathrm{x}_i)$ are spin orbitals that depend on both spatial (r: x, y, z) and spin coordinates (α and β). For simplification, the spin coordinates are not written explicitly in this thesis. An orbital, in quantum mechanics, refers to one function or a linear set of mathematical functions which are normally positioned at the center of the nucleus. The simple Hartree Product given in Eq. 2.1 is not an appropriate way of representing the wave function because it does not conform to the 6^{th} postulate of quantum mechanics. Based on this postulate, an appropriate wave function of a quantum system for fermions (e.g., electrons) must be antisymmetric with respect to exchange of any two electrons, i.e., upon exchange of two electrons, the sign of the total wave function must change. To enforce the anti-symmetry, and the Pauli exclusion principle, the approximate electronic wave function can be written as

$$\Psi(\mathrm{x}_1, \mathrm{x}_2, ..., \mathrm{x}_\mathrm{N}) = \frac{1}{\sqrt{\mathrm{N!}}} \begin{vmatrix} \psi_1(x_1) & \psi_2(x_1) & ... & \psi_N(x_1) \\ \psi_1(x_2) & \psi_2(x_2) & ... & \psi_N(x_2) \\ \vdots & \vdots & \ddots & \vdots \\ \psi_1(x_K) & \psi_2(x_K) & \cdots & \psi_N(x_K) \end{vmatrix}. \tag{2.2}$$

This determinant of $\phi_i(\mathrm{x}_i)$ orbitals is called the *Slater Determinant*, named after John C. Slater [199], and the factor in front of it is for normalizing the wave function (N is the total number of electrons and K is the number of basis functions). One can make different choices as to the form of the spatial part of the orbitals, e.g., Slater orbitals, Gaussian orbitals, etc. According to the *linear variational principle*, each trial function ($\phi_i(\mathrm{r}_i)$) can be written as linear combination of known basis functions ($\chi_i(\mathrm{r}_i)$), i.e.,

$$\psi_\mathrm{i}(\mathrm{r}_\mathrm{i}) = \sum_{\mathrm{i}}^{\mathrm{K}} \mathrm{c}_\mathrm{i}\, \chi_\mathrm{i}(\mathrm{r}_\mathrm{i}). \tag{2.3}$$

The c_i are the variational parameters in which minimization of the variational energy carries out through their optimizations.

The second postulate of quantum mechanics states: "*To every observable in classical mechanics there corresponds a linear, Hermitian operator.*" The suitable operator for obtaining the (non-relativistic) electronic energy of a system is called the *Hamiltonian operator* ($\hat{H}$) which is the sum of the kinetic and potential energy operators.

The electronic Hamiltonian operator for the ith electron shown below, in atomic units (a.u.), is comprised of all the single ($\hat{h}_{(i)}$) and all the double ($\hat{V}_{(i,j)}$) electron terms with the nuclear-nuclear repulsion potential (V_{NN}) being added as a constant value:

$$\begin{aligned} \hat{\mathrm{H}}_{(\mathrm{i})} &= \hat{h}_{(i)} + \sum_{i<j} V_{(i,j)} + V_{NN} \\ &= -\frac{1}{2}\nabla_i^2 - \sum_A \frac{Z_A}{r_{iA}} + \sum_{i<j} \frac{1}{r_{ij}} + V_{NN} \end{aligned} \tag{2.4}$$

where Z and r are nuclear charge and electron coordinates, respectively. The two electron term can be represented as sum of the Coulomb ($\hat{J}_b$ (r_i)) and exchange ($\hat{K}_b$ (r_i)) operators in the *Hartree-Fock* (HF) method. The Hamiltonian operator is called the Fock operator ($\hat{f}_{(i)}$) and is shown below:

$$\hat{f}_{(\mathrm{i})} = -\frac{1}{2}\nabla_{\mathrm{i}}^2 - \sum_{\mathrm{A}} \frac{\mathrm{Z_A}}{\mathrm{r_{iA}}} + \sum_{\mathrm{b=1}}^{\mathrm{K}} (\hat{J}_{\mathrm{b}}(\mathrm{r_i}) - \hat{K}_{\mathrm{b}}(\mathrm{r_i})) \tag{2.5}$$

where,

$$\hat{J}_{\mathrm{b}}(\mathrm{r_i}) = \int \frac{\psi_{\mathrm{b}}^*(\mathrm{r_j})\, \psi_{\mathrm{b}}(\mathrm{r_j}) \mathrm{dr_j}}{\mathrm{r_{ij}}} \text{ and } \hat{K}_{\mathrm{b}}(\mathrm{r_i}) = \int \frac{\psi_{\mathrm{b}}^*(\mathrm{r_j})\, \psi_{\mathrm{b}}(\mathrm{r_j}) \mathrm{dr_j}}{\mathrm{r_{ij}}}. \tag{2.6}$$

By substituting $\hat{f}_{(i)}$ and ψ_i into the S.E. and using the linear variational principle we obtain:

$$\begin{gathered} \hat{f}_{(\mathrm{i})} \sum_{\mathrm{i}} \mathrm{c_i}\, \chi_{\mathrm{i}}(\mathrm{r_i}) = \epsilon_i \sum_i c_i\, \chi_i(r_i), \\ \sum_j c_j\, \chi_j^*(r_j)\, \hat{f}_{(i)} \sum_i c_i\, \chi_i(r_i) = \epsilon_i \sum_j c_j \sum_i c_i\, \chi_j^*(r_j)\, \chi_i(r_i), \\ F\, C = \epsilon\, S\, C \end{gathered} \tag{2.7}$$

where F and S are called the Fock and overlap matrices and C is the matrix of coefficients. By changing the basis functions (orbitals) via changing the matrix of c coefficients one can minimize the electronic energy and obtain the one electron orbital energies (ϵ_i) through

applying the self-consistent field (SCF) procedure. This is the general formalism in the HF-Roothaan calculations.

2.2 Correlation Energy and Post-HF Methods

The HF energy provides an upper bound to the exact energy as is defined by the variational principle. Therefore the difference between the HF energy and the exact energy (E_{exact}–E_{HF}) is always negative and is called correlation energy in the limit of complete basis set. The physical meaning of the correlation energy in a system of N-electrons is that electrons are charged particles that try to avoid each other based on Coulomb's law, therefore, one can say *their motions are correlated*. In principle, inclusion of virtual orbitals in the wave function allows electrons to be further apart from each other which lowers the Coulomb repulsion and ultimately the total energy of the system. The correlation energy is in principle divided into two parts: (i) dynamical electron correlation which as we mentioned above corresponds to the Coulomb repulsion of electrons and (ii) non-dynamical or static electron correlation which is related to the inappropriateness of describing a system with using only one determinant, i.e., Slater determinant. The latter correlation becomes more important in situations where a bond is breaking or forming, diradicals, compounds involving transition metal elements, in stretched geometries and in cases where there are (close to) near-degenerate states [200]. One of the best ways of improving the HF energy is through using the configuration interaction method.

2.3 Configuration Interaction Theory

In configuration interaction (CI) theory, a linear combination of Slater determinants is considered which corresponds to a set of one to N electron excitations from the reference determinant (Eq. 2.8). One can form a linear combination of these Slater determinants to obtain configuration state functions (CSFs). Only the CSFs that have the same multiplicity and symmetry as the HF reference wave function will contribute to the total wave function and ultimately to the correlation energy. The weight of contribution of each Slater determinant to the total wave function is given by a series of coefficients (CIs). These coefficients also

ensure the normalization of the total wave function.

$$|\Psi\rangle = \sum_{i} CI_i|\Psi_i\rangle = CI_0|\Psi_0\rangle + \sum_{a}^{occ.}\sum_{r}^{virt.} CI_a^r|\Psi_a^r\rangle + \sum_{a<b}^{occ.}\sum_{r<s}^{virt.} CI_{ab}^{rs}|\Psi_{ab}^{rs}\rangle + ... \tag{2.8}$$

In Eq. 2.8, a, b subscripts and r, s superscripts denote occupied and virtual molecular orbitals (MOs), respectively, in the reference HF wave function. Additional determinants are formed by exciting electrons from occupied MOs (occ.) to virtual (virt.) ones (see Figure 2.1).

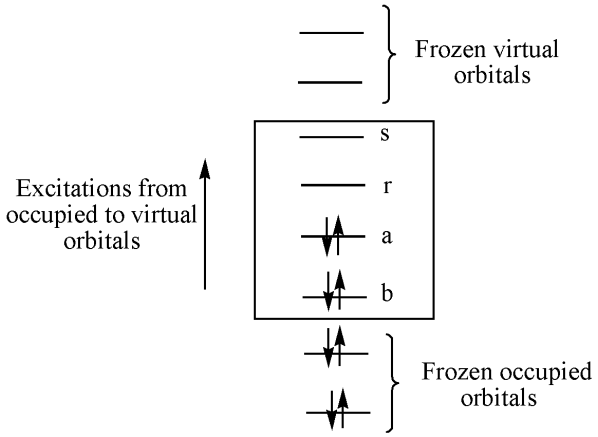

FIGURE 2.1: Schematic illustration of different MOs included in the excitation space of a CI calculation.

It has been observed in many systems that the weight of the coefficient of the HF reference wave function (i.e., CI_0) is much larger than the corresponding values in the excited determinants. Hence, the approximation to use a single Slater determinant as a representation of the total wave function is often reasonable. The variational theorem is then applied to minimize the energy with respect to the coefficients. One may obtain the exact non-relativistic electronic energy, by including all possible levels of electron excitations (i.e., full CI in the complete basis set limit). However in practice, full CI calculations scale as N! (N = number of basis functions) and, therefore, are not tractable except for very small systems (probably up to four atoms). The number of CSFs is obtained as follows:

$$N^{CSFs} = \frac{n!\,(n+1)!}{(\frac{m}{2})!\,(\frac{m}{2}+1)!\,(n-\frac{m}{2})!\,(n-\frac{m}{2}+1)!} \tag{2.9}$$

where the total number of electrons and basis functions of the system are given by m and n, respectively. For example, if we consider the carbon atom with six electrons and two basis functions for each atomic orbital plus a set of d polarization functions for a full CI calculation

we will have 63700 CSFs for which all coefficients must be determined. The number of CSFs rapidly escalates when increasing the number of electrons and basis functions. Hence, one needs to truncate the number of possible excitations to a certain level to make this method tractable for larger systems. Examples of truncated CI methods are configuration interaction singles (CIS) and configuration interaction singles and doubles (CISD) in which only singly- and doubly-excited determinants are included in the CI space. It is worthwhile mentioning that including single excitations does not improve the HF energy because based on the *Brillouin's theorem* [201, 202] the matrix elements of the Hamiltonian between the HF reference determinant and the single electron excitation determinants are zero. As it was mentioned in the case of the HF energies, in CI theory all the ground and excited state energies (E_i) are upper bounds to their corresponding exact(!) ground and excited state energies (ϵ_i) based on the variational principle [203].

2.3.1 Multi Configuration Self Consistent Field

In multi configuration self consistent field (MCSCF) theory, the wave function is constructed as a linear combination of Slater determinants (or CSFs) similar to the CI theory (see Eq. 2.8). However, in the MCSCF method both the CI and the MO coefficients are optimized. In general, this method, unlike CI and HF methods, is not "black box". The user needs to choose different occupied and virtual orbitals to be included in the excitation space, which is usually referred as the *active space*. The common notation for the active space is to show the number of electrons (m) and orbitals (n) used to construct it (i.e., [m,n], see Figure 2.2).

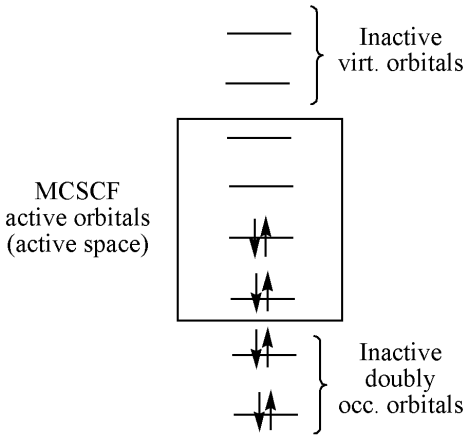

FIGURE 2.2: Illustration of a [4,4] active space in an MCSCF computation.

Choosing an appropriate active space requires care and attention especially for large molecules where one cannot include all the valence electrons, due to the cost of the calculations. There are some empirical rules that one can adopt for a suitable selection of active spaces. These rules are as follow: (i) if bond breakage or formation is happening in the system, all the involved bonding and anti-bonding orbitals must be included in the active space. (ii) If π electrons are involved in the reaction, then all the π and π^* orbitals should be included in the active space (if possible). (iii) One should run a test and check the electron occupations of the orbitals included in the active space. Based on the empirical *rule of thumb*, only MOs with occupations less than 1.98 e and larger than 0.02 e should be included in the active space. While these "rules" provide useful guidances, ultimately, choosing an appropriate active space relies on the chemistry intuition of the user.

If one considers all possible configuration state functions within a selected active space then we have a *complete active space self consistent field method* (CASSCF) which was first introduced by Roos and Taylor in 1980 [204]. CASSCF can also be considered as a full CI method within the active space. One can further improve the CASSCF wave function through addition of dynamic electron correlation from second order Møller Plesset perturbation theory (MP2) [205] to obtain *complete active space second order perturbation theory* (CASPT2) method [206]. Therefore, the CASPT2 method benefits from having both non-dynamical (static) and dynamical electron correlations from CASSCF and MP2, respectively.

2.4 Ground State Coupled Cluster Methods

In the discussion of the HF method, it was emphasized that one needs to add correlation energy to the HF energy to improve the electronic energy and bring it closer to the exact electronic energy. We discussed how one can reach this goal using a multi determinant wave function (i.e., including static electron correlation for example in the case of the CI methods). The full CI method is size extensive meaning its energy scales linearly with the number of electrons. It is also size intensive which means the energy of two identical molecules computed at large (infinite) separation is equal to the twice the energy of an individual molecule. However, as mentioned before, the full CI method is not feasible except for very small systems. Therefore truncation of the CI space to CIS, CISD, etc. was required to make

computations tractable. Although one can systematically improve the quality of the wave function by including more excitations, it becomes exceedingly more difficult to go beyond the CISD method for medium to large size molecules. Also, these truncated CI methods are neither size extensive nor intensive.

In ground state coupled cluster (CC) theory [207], the wave function is constructed using the cluster operator ($\hat{T}$), where after Taylor series expansion, one obtains

$$\Psi_0^{\mathrm{CC}} = \mathrm{e}^{\hat{\mathrm{T}}}\Psi_0 = (1 + \hat{\mathrm{T}} + \frac{\hat{\mathrm{T}}^2}{2!} + \frac{\hat{\mathrm{T}}^3}{3!} + ...)\,\Psi_0. \tag{2.10}$$

In other words, the ground state CC wave function (Ψ_0^{CC}) takes the HF reference determinant (Ψ_0) to build multi-electron wave functions using the exponential cluster operator to account for correlation energy. The choice of the exponential ansatz is critical because it guarantees the level of accuracy of the CC calculations. The cluster operator reads $\hat{T} = \hat{T}_1 + \hat{T}_2 + ...$ where $\hat{T}_1$ is the cluster of all single excitations, $\hat{T}_2$ is the cluster of all double excitations, etc. These excitation operators can be further expressed as follow:

$$\hat{\mathrm{T}}_1 = \sum_{\mathrm{a}}^{\text{occ.}} \sum_{\mathrm{r}}^{\text{virt.}} \mathrm{t}_{\mathrm{a}}^{\mathrm{r}}\, \hat{\mathrm{a}}_{\mathrm{r}}^{\dagger}\, \hat{\mathrm{a}}_{\mathrm{a}} \tag{2.11}$$

$$\hat{\mathrm{T}}_2 = \frac{1}{4} \sum_{\mathrm{a,b}}^{\text{occ.}} \sum_{\mathrm{r,s}}^{\text{virt.}} \mathrm{t}_{\mathrm{ab}}^{\mathrm{rs}}\, \hat{\mathrm{a}}_{\mathrm{r}}^{\dagger}\, \hat{\mathrm{a}}_{\mathrm{s}}^{\dagger}\, \hat{\mathrm{a}}_{\mathrm{a}}\, \hat{\mathrm{a}}_{\mathrm{b}} \tag{2.12}$$

where a, b and r, s are occupied and virtual orbitals, respectively. The $\hat{a}_r^{\dagger}$ and $\hat{a}_s^{\dagger}$ operators are creation operators while $\hat{a}_a$ and $\hat{a}_b$ operators are annihilation operators. Excitation happens through creation of spin orbitals r and s through annihilation of spin orbitals a and b. The t_a^r and t_{ab}^{rs} quantities are, respectively, single and double electron excitation amplitudes which show the probability of their corresponding excitations. When $\hat{T}_1$ and $\hat{T}_2$ operators act on the reference HF wave function they form, respectively, single and double excited determinants as

$$\hat{\mathrm{T}}_1|\Psi_0\rangle = \sum_{\mathrm{a}}^{\text{occ.}} \sum_{\mathrm{r}}^{\text{virt.}} \mathrm{t}_{\mathrm{a}}^{\mathrm{r}}\, \Psi_{\mathrm{a}}^{\mathrm{r}} \tag{2.13}$$

$$\hat{\mathrm{T}}_2|\Psi_0\rangle = \frac{1}{4} \sum_{\mathrm{a,b}}^{\text{occ.}} \sum_{\mathrm{r,s}}^{\text{virt.}} \mathrm{t}_{\mathrm{ab}}^{\mathrm{rs}}\, \Psi_{\mathrm{ab}}^{\mathrm{rs}}. \tag{2.14}$$

By substituting Eq. 2.10 into the S.E. and multiplying on the left side by reference (ψ_0) and excited ($\psi_{abc...}^{rst...}$) determinants, one can obtain, respectively, energy and cluster amplitudes (see Eqs. 2.15 and 2.16). Also, Eq. 2.16 corresponds to the matrix elements between excited determinants in the bra part of the equation and reference HF wave function in the ket part. That is,

$$\langle \Psi_0 | e^{-\hat{T}} \, (\hat{H} \, e^{\hat{T}}) \, | \Psi_0 \rangle = E \tag{2.15}$$

$$\langle \Psi_{abc...}^{rst...} | e^{-\hat{T}} \, (\hat{H} \, e^{\hat{T}}) | \Psi_0 \rangle = 0. \tag{2.16}$$

The excited determinants in the bra part are all coupled and are non-linear in the excitation amplitudes. Inclusion of all levels of electron excitations provides the full CC method which is both size extensive and size intensive. In spite of providing the exact answer to the non-relativistic electronic S.E., this method is not computationally feasible and similar to the full CI method truncation of the excitation space is needed. Therefore, one can truncate the full CC cluster operator to a cluster of only singles (CCS), singles and doubles (CCSD), etc. In the next section, we will discuss two of the currently employed approximations to the ground state CC methods.

2.4.1 Approximations to the Ground State CC Theory

The CC methods have a steep scaling with the number of basis functions, for example, the CCSD method scales as N^6, CCSDT as N^7, and so on (N denotes the number of basis functions). To decrease the burden of the CC computations, there exist many approximations two of which are listed below [207].

(i) One of the main variants of the standard CC methods, or canonical CC methods discussed so far, is to utilize their local versions (abbreviated as LCC methods) [208–215]. Within the local approximation, localized orbitals (basis functions) are used which allows a drastic increase in the speed of the CC computations. In these orbitals, the two electron integrals decay faster than the canonical orbitals with the distance from nuclei and therefore the distant integrals are neglected which saves a lot of computing time.

(ii) The other approximations for the CC methods are mainly used to include the weight of the CC triples excitations ($\hat{T}_3$) which are shown to be crucial for accurate calculations and also

for strongly correlated systems. Accordingly, one can estimate the weight of the connected triples contributions through (i) iterative (ii) non-iterative (or perturbative) and (iii) active space approximations. In the iterative approximation to the triples, the $\hat{T}_3$ equations are truncated so that the most expensive terms are not included. One example is the CC3 [216] method which is the approximated version of the CCSDT [217, 218] method. The connected triples can also be obtained non-iteratively using the Møller Plesset perturbation theory, i.e., through evaluating perturbation energy at the third order level. This approach which is generally faster than the iterative methods forms the basis for the CCSD(T) [219] method (i.e., coupled cluster method with full singles and doubles and non-iterative (perturbative) treatment of triples). This method is famous as the *gold standard* [220] of computational chemistry because of providing very good descriptions for closed shell systems near their equilibrium geometries. However, as is expected from the single reference based approaches, the CCSD(T) method starts to perform poorly in the cases that static electron correlation becomes important.

In the active space approximated version of the CC theory (e.g., CCSDt method [221–233]), excitations are limited to a subspace of occupied and virtual MOs.

2.5 Equation of Motion (EOM) Coupled Cluster Theory for Excited States

The wave function for the excited state (Ψ_k) is written as the action of an excitation operator ($\hat{R}_k$) on the ground state CC wave function (Eq. 2.17)

$$\Psi_{\mathrm{k}} = \hat{\mathrm{R}}_{\mathrm{k}}\, \mathrm{e}^{\hat{\mathrm{T}}}\, \Psi_0. \tag{2.17}$$

The $\hat{R}_k$ is a general excitation operator that reads

$$\hat{\mathrm{R}}_{\mathrm{k}} = \mathrm{t}_0(\mathrm{k}) + \sum_{\mathrm{a}}^{\mathrm{occ.}} \sum_{\mathrm{r}}^{\mathrm{virt.}} \mathrm{t}_{\mathrm{a}}^{\mathrm{r}}(\mathrm{k})\, \hat{\mathrm{a}}_{\mathrm{r}}^{\dagger}\, \hat{\mathrm{a}}_{\mathrm{a}} + \frac{1}{4} \sum_{\mathrm{a,b}}^{\mathrm{occ.}} \sum_{\mathrm{r,s}}^{\mathrm{virt.}} \mathrm{t}_{\mathrm{ab}}^{\mathrm{rs}}(\mathrm{k})\, \hat{\mathrm{a}}_{\mathrm{r}}^{\dagger}\, \hat{\mathrm{a}}_{\mathrm{s}}^{\dagger}\, \hat{\mathrm{a}}_{\mathrm{a}}\, \hat{\mathrm{a}}_{\mathrm{b}}. \tag{2.18}$$

Similar to the ground state approach, the excitation amplitudes can be obtained by diagonalizing the matrix elements of the Hamiltonian in an appropriate space of excited state

determinants (see Eqs. 2.19–2.21)

$$\hat{\mathrm{H}}\,\hat{\mathrm{R}}_{\mathrm{k}}\,\mathrm{e}^{\hat{\mathrm{T}}}\,\Psi_0 = \mathrm{E}_{\mathrm{k}}\,\hat{\mathrm{R}}_{\mathrm{k}}\,\mathrm{e}^{\hat{\mathrm{T}}}\,\Psi_0. \tag{2.19}$$

Since $\hat{R}_k$ and $\hat{T}$ commute,

$$\mathrm{e}^{-\hat{\mathrm{T}}}\,\hat{\mathrm{H}}\,\mathrm{e}^{\hat{\mathrm{T}}}\,\hat{\mathrm{R}}_{\mathrm{k}}\,\Psi_0 = \mathrm{E}_{\mathrm{k}}\,\mathrm{e}^{-\hat{\mathrm{T}}}\,\mathrm{e}^{\hat{\mathrm{T}}}\,\hat{\mathrm{R}}_{\mathrm{k}}\,\Psi_0 = \mathrm{E}_{\mathrm{k}}\,\hat{\mathrm{R}}_{\mathrm{k}}\,\Psi_0 \tag{2.20}$$

and if we subtract E_0 from both sides we obtain

$$\mathrm{e}^{-\hat{\mathrm{T}}}\,(\hat{\mathrm{H}} - \mathrm{E}_0)\,\mathrm{e}^{\hat{\mathrm{T}}}\,\hat{\mathrm{R}}_{\mathrm{k}}\,\Psi_0 = (\mathrm{E}_{\mathrm{k}} - \mathrm{E}_0)\,\hat{\mathrm{R}}_{\mathrm{k}}\,\Psi_0 \tag{2.21}$$

where E_k - E_0 corresponds to the required energy for excitation of one electron from ground state to the k^{th} excited state.

Approximations to the doubles and triples excitations in the EOM-CC theory can be made similar to the ground state approach. As mentioned before, the full versions of CI and CC are equivalent and provide exact solution for the non-relativistic electronic energy however the truncated versions of the EOM-CC method are found to be more accurate than their CI analogues, assuming all other conditions, such as number of basis functions, are the same.

2.6 Density functional theory

Density functional theory (DFT) is an alternative to wave function based methods, such as HF, CI, CC, etc, for solving the S.E. [234]. The cost of DFT calculations is usually lower or equal to the HF method (i.e., N^4) depending on whether an exact HF exchange or an approximated version of it is utilized. One can also use some numerical methods and approximations such as density fitting basis sets to lower the cost to N (i.e., linear scaling). According to the DFT formalism, the electron density (ρ (r)) contains all the required information for describing all the properties of a quantum mechanical system. As such, one can substitute the many body wave function [Ψ (x_1, x_2, ..., x_N] of a system which is a function of 4×N coordinates (x, y, z, and spin (σ) coordinates), where N denotes the number of particles, with only three coordinates of the electron density (or four coordinates

if we include spin). Therefore no matter how large the system is we only need to consider three variables which simplifies the problem appreciably. Hohenberg and Kohn formulated the DFT principles in two theorems [235]. The first Hohenberg-Kohn (H-K) theorem states that *the external potential and hence the total energy is a unique functional of the electron density.* The second theorem says that *the ground state energy can be obtained variationally; the density that minimizes the total energy is the exact ground state density.* In other words, there exists a density functional (a function of a function) where by inputing the density the total energy of the system can be obtained that corresponds to that density (i.e., ϵ_{tot} = F $[\rho(\mathrm{r})]$). By minimizing the density one can minimize the energy of the system. The energy functional can be expanded similar to expanding the electronic Hamiltonian as the sum of a kinetic energy density functional, the electron-nuclear attraction and the electron-electron repulsion density functionals:

$$\mathrm{F}\left[\rho(\mathrm{r})\right] = \mathrm{T}\left[\rho(\mathrm{r})\right] + \mathrm{V_{eN}}\left[\rho(\mathrm{r})\right] + \mathrm{V_{ee}}\left[\rho(\mathrm{r})\right]. \tag{2.22}$$

Based on Coulomb's law, one can substitute the last two expressions with the following:

$$\mathrm{V_{eN}}\left[\rho(\mathrm{r})\right] = -\sum_{\mathrm{A}} \int \frac{\mathrm{Z_A}\rho(\mathrm{r})}{|\mathrm{r}-\mathrm{R_A}|}\mathrm{dr} \tag{2.23}$$

$$\mathrm{V_{ee}}\left[\rho(\mathrm{r})\right] = \frac{1}{2}\int\int \frac{\rho(\mathrm{r})\,\rho(\mathrm{r}')}{|\mathrm{r}-\mathrm{r}'|}\mathrm{dr}\mathrm{dr}'. \tag{2.24}$$

On the other hand, the kinetic energy functional (T $[\rho(\mathrm{r})]$) is not directly dependent on the electron density and its solution is not as straightforward as the other two expressions. Kohn and Sham in 1965 (famous as the Kohn-Sham formulation of DFT (KS-DFT)) suggested the use of the HF formalism for determination of the kinetic energy by assuming that electrons are non interacting single particles:

$$\mathrm{T_S}[\rho] = \sum_{\mathrm{i}} \langle \phi_{\mathrm{i}}(\mathrm{r})| -\frac{1}{2}\nabla_{\mathrm{i}}^2 |\phi_{\mathrm{i}}(\mathrm{r})\rangle \tag{2.25}$$

where the sum over all one electron orbitals gives us back the electron density itself,

$$\rho(\mathrm{r}) = \sum_{\mathrm{i}} |\phi_{\mathrm{i}}(\mathrm{r})|^2 \;\text{ and }\; \int \rho(\mathrm{r})\,\mathrm{dr} = \mathrm{N} \tag{2.26}$$

where N is the number of electrons. In KS-DFT, the anti-symmetrization is still missing which in HF theory arises in the exchange term. Also, since electrons are not truly non-interacting particles, we are also missing a correlation term. These two missing pieces can be included in a term called the *exchange-correlation (xc) functional*. Therefore, the final form of the density functional is

$$\mathrm{F}\left[\rho(\mathrm{r})\right] = \mathrm{T_S}\left[\rho(\mathrm{r})\right] + \mathrm{V_{eN}}\left[\rho(\mathrm{r})\right] + \mathrm{V_{ee}}\left[\rho(\mathrm{r})\right] + \mathrm{V_{xc}}\left[\rho(\mathrm{r})\right]. \tag{2.27}$$

KS-DFT is formally an exact theorem which would give the exact energy if, and only if, the exact form of the xc term could be found. However the exact form of this functional is not known and most theoretical chemists believe that even if it was known it would be too difficult to use. Therefore this term needs to be approximated and different approximations provide different flavours of DFT (the rest of the terms do not change). In practice, one can approximate the exchange and correlation functionals separately. For example, one of the most common exchange functionals is named Becke's 1988 exchange functional (shortened to B88 or simply B) which can be mixed with Lee-Yang-Parr correlation functional (abbreviated as LYP) to form the BLYP xc density functional [236–238]. Becke's exchange term, which is a function of both electron density ($\rho(r)$) and its gradient ($\nabla\rho(r)$), reads

$$\mathrm{E_X^{B88}}[\rho(\mathrm{r}), \nabla\rho(\mathrm{r})] = \mathrm{E_X^{LSDA}}[\rho(\mathrm{r})] - \beta\,\rho^{1/3}(\mathrm{r})\,\frac{\mathrm{x}^2(\mathrm{r})}{1 + 6\,\beta\,\mathrm{x(r)}\,\sinh^{-1}\left[\mathrm{x(r)}\right]},\ \text{where}\ \mathrm{x(r)} = \frac{|\nabla\rho(\mathrm{r})|}{\rho^{4/3}(\mathrm{r})} \tag{2.28}$$

and the parameter $\beta = 0.0042$ is determined by fitting to the HF exchange energies of the first six noble gas atoms. The first term in Eq. 2.28 is called the local spin density exchange energy functional (only depends on the local density of α and β electrons) which is also called Slater exchange (abbreviated as S) and is expressed as

$$\mathrm{E_X^{LSDA}} = \mathrm{C_X}\int\left[\rho^{4/3}(\mathrm{r})\right]\mathrm{dr} \tag{2.29}$$

where C_X is a constant and ρ(r) is the density of a homogenous electron gas found by Monte Carlo calculations. In DFT computations, one starts with an initial guess for ρ(r) by choosing a set of basis functions, determines the electron-nuclear and electron-electron potentials and

solves the KS-DFT equation

$$\hat{\mathrm{F}}^{\mathrm{KS}}(\mathrm{r_i})\,\phi_{\mathrm{i}}^{\mathrm{KS}}(\mathrm{r_i}) = \epsilon_{\mathrm{i}}^{\mathrm{KS}}(\mathrm{r_i})\,\phi_{\mathrm{i}}^{\mathrm{KS}}(\mathrm{r_i}). \tag{2.30}$$

In this equation, $\hat{F}^{KS}$ is the one-electron Kohn-Sham operator which for the i^{th} electron can be shown as

$$\hat{\mathrm{F}}^{\mathrm{KS}}(\mathrm{r_i}) = -\frac{1}{2}\nabla_{\mathrm{i}}^2 - \sum_{\mathrm{A=1}}^{\mathrm{P}} \frac{\mathrm{Z_A}}{\mathrm{r_{iA}}} + \sum_{\mathrm{j>i}}^{\mathrm{N}} \int \frac{\rho(\mathrm{r_j})}{\mathrm{r_{ij}}} \mathrm{dr_j} + \mathrm{V_{xc}}. \tag{2.31}$$

From the solution of Eq. 2.30, one can calculate a new density and then start again until convergence is reached in a SCF (iterative) way similar to the HF method. The optimized orbitals (ϕ_i^{KS}) that are the lowest energy solutions of Eq. 2.30 are called Kohn-Sham orbitals. One can improve the choice of the xc functional by including a dependence on the gradient of the electron density ($\nabla\rho(\mathrm{r})$). This modification of the xc functional yields gradient corrected xc density functionals (also referred to as generalized gradient approximation or GGA density functionals). We can continue by adding the second derivative of the electron density as well ($\nabla^2\rho(\mathrm{r})$) to obtain meta-GGA functionals (some meta-GGAs also include corrections for the kinetic term). Examples for LSDA, GGA and meta-GGA density functionals are, respectively, S-VWN [239], BLYP [236–238], and M06-L [240]. One can also add some HF exact exchange to the xc density functional to obtain hybrid density functionals such as B3LYP [241, 242] and M06-2X [243]. It is worthwhile mentioning that while DFT usually provides better answers when going from LSDA to meta-GGA and hybrid density functionals (or by climbing the Jacob's ladder [244]), this is not in general always true.

2.7 Time Dependent DFT for Excited States

According to the 5^{th} postulate of quantum mechanics, the time-dependent S.E. (in a.u.) can be written as

$$\hat{\mathrm{H}}(\mathrm{r,t})\,\Psi_{\mathrm{n}}(\mathrm{r,t}) = \mathrm{i}\,\frac{\partial}{\partial \mathrm{t}}\,\Psi_{\mathrm{n}}(\mathrm{r,t}) \;\text{ where }\; \Psi_{\mathrm{n}}(\mathrm{r,t}) = \mathrm{e}^{-\mathrm{iE_n t}/\hbar}\,\Psi_{\mathrm{n}}(\mathrm{r}). \tag{2.32}$$

To determine excited electronic states for a molecule, we can begin by considering the interaction of a time-dependent electric field (laser) with the system. In the corresponding Hamiltonian operator, Eq. 2.33, the electric field acts as an external potential (V_{ext} (r,t),

the only term which varies in time) that can excite inner or outer electrons depending on its strength. The Hamiltonian is given by

$$\begin{aligned}\hat{\mathrm{H}}(\mathrm{r},\mathrm{t}) &= \hat{T}(r) + \hat{V}_{ee}(r) + \hat{V}_{ext}(r,t) \\ &= -\frac{1}{2}\sum_i \nabla_i^2 + \sum_{i<j}\frac{1}{r_{ij}} - \sum_{iA}\frac{Z_A}{r_{iA}} + E\, f(t)\sin(\omega\, t)\sum_i r_i\,\alpha\end{aligned} \tag{2.33}$$

where α is polarization of the laser light, ω is its frequency, E is its amplitude and f corresponds to an envelope that shapes the laser field during time. Similar to the time-independent approach, an exact solution of this equation is not possible except for mono-electronic systems such as H, He^+, H_2^+, and H_3^{+2}. Time-dependent DFT (TD-DFT) provides an alternative pathway for solving this many body equation just as the DFT did for the time-independent problem. Hereafter, we focus on the use of linear response TD-DFT for solving the time-dependent S.E. In the following section, a very brief review of TD-DFT is provided. However, for further technical details, and a more in-depth discussion, the interested reader is referred to Refs. 44, 245–248 and references therein. The Marques and Gross chapter [44] is used for the following section.

2.7.1 Linear Response Theory

If the laser light (external time-dependent potential) is weak one can treat the external potential as a small perturbation. Therefore, the many-body perturbation formalism can be used such that the time-dependent electron density can be written as

$$\rho(\mathrm{r},\mathrm{t}) = \rho^{(0)}(\mathrm{r}) + \rho^{(1)}(\mathrm{r},\mathrm{t}) + \rho^{(2)}(\mathrm{r},\mathrm{t}) + ... \tag{2.34}$$

where $\rho^{(0)}$(r) is the ground state electron density, and $\rho^{(1)}$(r,t) and $\rho^{(2)}$(r,t) are the components of the total electron density (ρ(r,t)) which depend, respectively, linearly and quadratically on the external potential. If the perturbation is weak, one can truncate the above equation to linear response (i.e., up to the $\rho^{(1)}$(r,t) term) to calculate, for instance, excitation energies, optical spectra, etc. First order response of the exact density to the external potential can be determined by using the energy-dependent density-density response function

of the full interacting system (χ (r,r′,ω)):

$$\rho^{(1)}(\mathrm{r},\omega) = \int \chi(\mathrm{r},\mathrm{r}',\omega)\, \mathrm{V}^{(1)}(\mathrm{r}',\omega)\, \mathrm{dr}' \tag{2.35}$$

where $\mathrm{V}^{(1)}$(r′,ω) term contains variation of the external potential evaluated to the first order. For further simplification, one can replace the response function with the Kohn-Sham function of non-interacting electrons

$$\rho^{(1)}(\mathrm{r},\omega) = \int \chi_{\mathrm{KS}}(\mathrm{r},\mathrm{r}',\omega)\, \mathrm{V}^{(1)}_{\mathrm{KS}}(\mathrm{r}',\omega)\, \mathrm{dr}'. \tag{2.36}$$

In the above equation, the exact density response ($\rho^{(1)}$(r,ω)) is illustrated as the response of the non-interacting KS system in which

$$\chi_{\mathrm{KS}}\,(\mathrm{r},\mathrm{r}',\omega) = \lim_{\eta\to 0^+} \sum_{\mathrm{jk}} (f_{\mathrm{k}} - f_{\mathrm{j}})\, \frac{\phi_{\mathrm{j}}(\mathrm{r})\, \phi^*_{\mathrm{j}}(\mathrm{r}')\, \phi_{\mathrm{k}}(\mathrm{r}')\, \phi^*_{\mathrm{k}}(\mathrm{r})}{\omega - (\epsilon_{\mathrm{j}} - \epsilon_{\mathrm{k}}) + \mathrm{i}\,\eta} \tag{2.37}$$

where η is an infinitesimal real number, f_k and f_j are the occupation numbers of the k and j orbitals in the Kohn-Sham ground state. The first order change in the time-dependent KS potential ($\mathrm{V}^{(1)}_{KS}$ (r,ω) term in Eq. 2.36) can be represented (in the time domain) as

$$\mathrm{V}^{(1)}_{\mathrm{KS}}\,(\mathrm{r},\mathrm{t}) = \mathrm{V}^{(1)}\,(\mathrm{r},\mathrm{t}) + \mathrm{V}^{(1)}_{\mathrm{H}}\,(\mathrm{r},\mathrm{t}) + \mathrm{V}^{(1)}_{\mathrm{xc}}\,(\mathrm{r},\mathrm{t}) \tag{2.38}$$

where the $\mathrm{V}^{(1)}_{H}$ is the change in the Hartree electron-electron repulsion potential and is represented as

$$\mathrm{V}^{(1)}_{\mathrm{H}}\,(\mathrm{r},\mathrm{t}) = \int \frac{\rho^{(1)}(\mathrm{r}',\mathrm{t})}{|\mathrm{r}-\mathrm{r}'|}\, \mathrm{dr}'. \tag{2.39}$$

The change in the xc potential can be viewed as

$$\mathrm{V}^{(1)}_{\mathrm{xc}}\,(\mathrm{r},\mathrm{t}) = \int \mathrm{dt}' \int \mathrm{dr}'\, f_{\mathrm{xc}}(\mathrm{rt},\mathrm{r}'\mathrm{t}')\, \rho^{(1)}(\mathrm{r}',\mathrm{t}') \tag{2.40}$$

where f_{xc} is called the xc kernel which includes all the important many body interactions:

$$f_{\mathrm{xc}}\,(\mathrm{rt},\mathrm{r}'\mathrm{t}') = \frac{\delta \mathrm{V}_{\mathrm{xc}}\,(\mathrm{r},\mathrm{t})}{\delta\rho(\mathrm{r}',\mathrm{t}')}. \tag{2.41}$$

Finally, the first order response of the electron density can be represented (in the frequency domain) as

$$\begin{aligned}\rho^{(1)}(\mathrm{r},\omega) = &\int \chi_{KS}(r,r',\omega)\, V^{(1)}(r',\omega)\, dr' \\ &+ \int dx \int dr'\, \chi_{KS}(r,x,\omega) \left[\frac{1}{|x-r'|} + f_{xc}(x,r',\omega)\right] \rho^{(1)}(r',\omega).\end{aligned} \tag{2.42}$$

Both the response function and the density response have poles at true excitation energies and the residues represent their corresponding transition amplitudes. The exact form of f_{xc} is not known and approximations similar to the ground state DFT approach are needed to be employed. One can use adiabatic LDA as one of the simplest approximations for the f_{xc} in which we assume that the xc potential at point r and time t is equal to the static LDA xc potential of density ρ (r). This dramatic assumption stays valid if the laser beam is weak and therefore the system stays close to its equilibrium geometry. Similar to the DFT ground state approach, one can add first and second derivatives of the electron density to the xc kernel to obtain, respectively, GGA and meta-GGA xc functionals.

2.7.1.1 Matrix Formulation of the Linear Response TD-DFT

The matrix formulation of the linear-response TD-DFT was first introduced by Casida in 1995 [245]. The matrix non-Hermitian pseudo-eigenvalue problem is

$$\begin{pmatrix} A & B \\ B^* & A^* \end{pmatrix} \begin{pmatrix} X \\ Y \end{pmatrix} = \begin{pmatrix} \omega & o \\ 0 & -\omega \end{pmatrix} \begin{pmatrix} X \\ Y \end{pmatrix}. \tag{2.43}$$

A and B are Hessian matrices, X and Y are their eigenfunctions and the ω matrix contains excitation energies. The A and B matrices are given by

$$\mathrm{A_{ia,jb}} = \delta_{\mathrm{ij}}\, \delta_{\mathrm{ab}}\, (\epsilon_{\mathrm{a}} - \epsilon_{\mathrm{i}}) + \langle \mathrm{ia}|\frac{1}{\mathrm{r_{12}}}|\mathrm{jb}\rangle - \mathrm{a_x}\, \langle \mathrm{ij}|\frac{1}{\mathrm{r_{12}}}|\mathrm{ab}\rangle + (1-\mathrm{a_x})\, \langle \mathrm{ia}|f_{\mathrm{xc}}|\mathrm{jb}\rangle \tag{2.44}$$

and,

$$\mathrm{B_{ia,jb}} = \langle \mathrm{ia}|\frac{1}{\mathrm{r_{12}}}|\mathrm{bj}\rangle - \mathrm{a_x}\, \langle \mathrm{ib}|\frac{1}{\mathrm{r_{12}}}|\mathrm{aj}\rangle + (1-\mathrm{a_x})\, \langle \mathrm{ia}|f_{\mathrm{xc}}|\mathrm{bj}\rangle \tag{2.45}$$

where ϵ_i and ϵ_a are the orbital energies of the occupied and virtual orbitals, respectively, obtained from ground state HF or KS-DFT calculations, a_x is the amount of HF non-local

exchange combined with the xc functional used (if $a_x = 1$, the above equation corresponds to TD-HF and if a_x =0 it corresponds to TD-DFT semi-local method). The anti-symmetrized two-electron integrals ($\langle ia|\frac{1}{r_{12}}|jb\rangle$) are given by

$$\langle \mathrm{ia}|\frac{1}{\mathrm{r_{12}}}|\mathrm{jb}\rangle = \int \mathrm{dr_1} \int \mathrm{dr_2}\Big[\frac{\phi_\mathrm{i}(\mathrm{r_1})\phi_\mathrm{a}(\mathrm{r_1})\phi_\mathrm{j}(\mathrm{r_2})\phi_\mathrm{b}(\mathrm{r_2}) - \phi_\mathrm{i}(\mathrm{r_1})\phi_\mathrm{j}(\mathrm{r_1})\phi_\mathrm{a}(\mathrm{r_2})\phi_\mathrm{b}(\mathrm{r_2})}{|\mathrm{r_1} - \mathrm{r_2}|}\Big]. \tag{2.46}$$

The response within the adiabatic approximation is given by the $\langle ia|f_{xc}|jb\rangle$ and $\langle ia|f_{xc}|bj\rangle$ integrals

$$\langle \mathrm{ia}|f_\mathrm{xc}|\mathrm{jb}\rangle = \int \mathrm{dr_1} \int \mathrm{dr_2}\, \phi_\mathrm{i}^*(\mathrm{r_1})\, \phi_\mathrm{a}(\mathrm{r_2})\, \frac{\partial^2 \mathrm{E_{xc}}}{\partial\rho(\mathrm{r_1})\, \partial\rho(\mathrm{r_2})}\, \phi_\mathrm{b}^*(\mathrm{r_1})\, \phi_\mathrm{j}(\mathrm{r_2}). \tag{2.47}$$

Eq. 2.43 for the TD-HF method is also well known as the random phase approximation eigenvalue problem (RPA). Hirata and Head-Gordon [249] introduced the Tamm-Dancoff approximation [250] to TD-DFT (abbreviated as TDA-DFT) in 1999. In TDA-DFT, matrix B is neglected and Eq. 2.43 is simplified to

$$\mathrm{A\,X} = \omega_\mathrm{TDA}\,\mathrm{X}. \tag{2.48}$$

With $a_x = 1$ and by using a HF reference determinant, this equation will correspond to a CIS calculation. In general, TDA-DFT and TD-DFT yield similar results [251, 252], the former approach has advantages such being faster and hence applicable to relatively larger systems. Very recently, Moore and Autschbach [253] and Ziegler and his coworkers [254] have shown that using TDA instead of the full TD approach could lead to relatively large errors, up to 0.3 eV, for linear cyanine dyes.

2.7.1.2 Failures of the Linear Response TD-DFT

In general TD-DFT is a practical method that can provide relatively good agreement with respect to experiment (excitation energy errors less than 0.3 eV). TD-DFT's applicability to large systems has made it a favourable choice over other rather expensive post-HF methods

such as CI and CC. However, TD-DFT has some well known problems that are addressed briefly below:

(i) The first failure of TD-DFT is when it encounters systems that are dominated by static correlation such as singlet trimethylenemethane [255] or twisted ethylene [256]. In this case, TD-DFT along with all other single-determinant based methods fail and one has to use multi-determinant methods such as CASSCF or CASPT2.

(ii) TD-DFT yields poor results when treating Rydberg [257] and charge transfer [258, 259] states. This classical TD-DFT failure leads to underbinding, up to 5 eV for the N_2 molecule, as well as excitation energies that are underestimated with respect to experiment. This failure is due to the incorrect asymptotic behaviour of LDA, GGA and even meta-GGA density functionals [246]. The errors have been (somewhat) corrected through development of range separated (or long-range corrected) density functionals [260] such as CAM-B3LYP [261]. Long-range corrected (LC) density functionals have been developed based on (almost) any pure GGA density functional, e.g., LC-BLYP, LC-PBE, etc. In these methods, the electron-electron repulsion potential is separated into short (SR) and long (LR) range parts:

$$\begin{aligned}\left[\frac{1}{\mathrm{r}_{12}}\right] &= \left[\frac{1}{r_{12}}\right]_{SR} + \left[\frac{1}{r_{12}}\right]_{LR} \\ &= \frac{1 - erf\,(\mu r_{12})}{r_{12}} + \frac{erf\,(\mu r_{12})}{r_{12}}.\end{aligned} \tag{2.49}$$

Here, *erf* is the standard error function and μ is a parameter that determines the ratio of these two parts. In general, the short-range part is evaluated using the DFT xc potential, while the long-range part is calculated with the exact HF exchange.

(iii) In general, the exact energy-dependent density-density response function of the full interacting system (χ (r,r$'$,ω) can treat both single and multiple excited states. However, since this function is replaced with the response of the single particle KS excitations therefore the TD-DFT cannot treat multiply excited states.

(iv) The final TD-DFT failure that we discuss here is called *scale-up catastrophe* meaning that accuracy of TD-DFT decreases by increasing the size of the system. In other words, the usual xc kernel that is used is not non-local enough to capture all the behaviours of a

very large system such as proteins and periodic systems [262, 263]. Therefore one needs to improve the quality of the employed f_{xc} to correct for the system size effect [264–268].

2.8 UV-Vis Spectroscopy and TD-DFT Computations

Ultraviolet-visible spectroscopy probes excited electronic states in the 200-800 nm wavelength region. This part of the spectroscopic window is connected to a variety of important processes such as photosynthesis, vision (the colour that we see), and so on. The UV-Vis light is responsible for electron excitations from occupied MOs (namely σ or π) to virtual ones (σ^* and π^*) in organic compounds or ligand to metal/metal to ligand charge transfer (LMCT/MLCT) and d-d transitions in transition metal complexes. Rules such as the Beer-Lambert law (A = $\log \frac{I_0}{I} = \epsilon\ \ell\ \mathrm{C}$) determine the correspondence between the intensity of the light and absorption. Here A, $\mathrm{I_0}$ I, are absorbance, intensity of the incident light, and intensity of the transmitted light, respectively. The quantity ϵ is the molar absorptivity (or molar extinction coefficient with units of $\mathrm{mol^{-1}L^{-1}cm^{-1}}$). ϵ is a fundamental property of the molecule and depends on temperature, pressure, and the type of solvent used. Also, ℓ and C are path length of the light and concentration of the solution, respectively.

Woodward-Fieser rules on the other hand, can qualitatively correlate the maximum absorption wavelength (λ_{max}^{abs}) of different organic molecules to their structural factors such as extent of conjugation and type of auxiliary groups. In addition to absorption, which corresponds to excitation of an electron from the ground state to the excited state, one can have emission which is related to the return of the electron to the ground state. If the latter occurs from a singlet excited state, it is called fluorescence and if triplet excited states are involved, it is called phosphorescence. The time scales for absorption, fluorescence and phosphorescence phenomena are (approximately) 10^{-15}, 10^{-9}, and 10^{-4} seconds, respectively. The time scale for phosphorescence is much slower because the electron needs to change its spin orientation (through intersystem crossing (ISC) mechanism) which is formally a forbidden process. Also, vibrational relaxation usually happens on a time scale of 10^{-12}–10^{-14} seconds. Based on the Frank-Condon (F-C) principle because the time scale of absorption is much faster than that of molecular vibration or nuclear motion, $\approx 10^{-12}$ seconds, the transition between ground and excited states (and similarly between excited and ground states for emission) occurs while

the nuclear geometry is unchanged. The resulting absorption (emission) is called a *vertical transition.*

An absorption spectrum is normally generated by measuring the absorbance or ϵ of a molecule against the wavelength (in nm) of the exciting field. The intensities of the vibronic transitions (vibrational states involved with the electronic excitation) are governed by the F-C principle. According to the F-C rule, vibrational levels in the ground and excited states are favoured that correspond to a minimal change in nuclear coordinates (because of the time scale difference stated above). In other words, those vibronic transitions are favoured that have the most positive overlap between their vibrational wave functions (e.g., from $\nu_0 \rightarrow \nu_2$ in Figures 2.3 and 2.4). From the quantitative viewpoint, the intensity of the transition from state a to

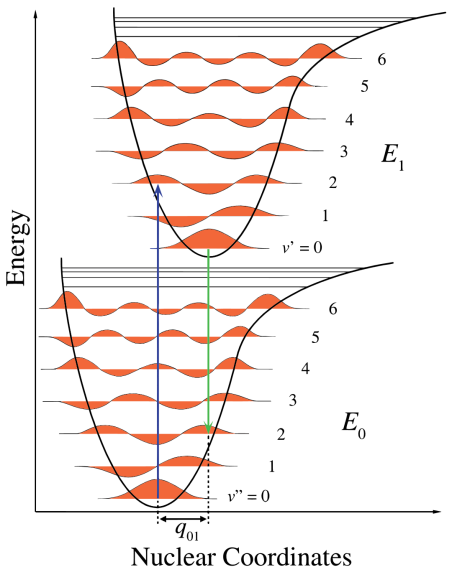

FIGURE 2.3: Schematic representation of a typical vibronic absorption spectrum. Reprinted with permission from Ref. 4.

state r is defined by the absorption oscillator strength (f) as

$$f_{\mathrm{ar}} = \frac{2}{3} \left(\mathrm{E_r} - \mathrm{E_a}\right) \mu_{\mathrm{ar}}. \tag{2.50}$$

The quantity μ_{ar} is the transition dipole moment (the electric dipole moment vector associated with the electron transition from state a to state r) which is defined, for a single particle, as

$$\mu_{\mathrm{ar}} = \mathrm{q} \left\langle \Psi_{\mathrm{a}} | \mathrm{r} | \Psi_{\mathrm{r}} \right\rangle \tag{2.51}$$

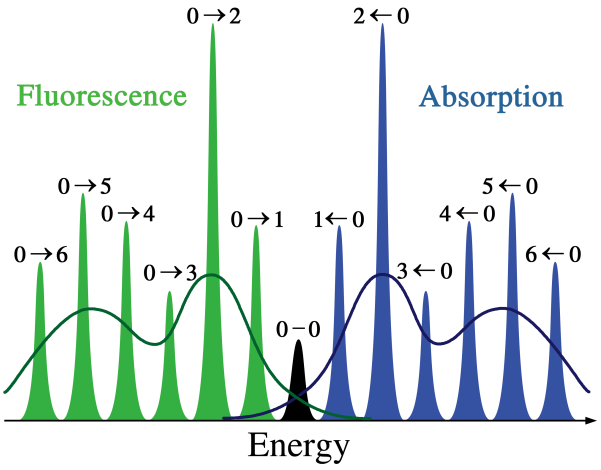

FIGURE 2.4: Vibronic absorption and emission spectra. Intensities of the transitions are governed by the Frank-Condon principle. Reprinted with permission from Ref. 4.

where q is the charge of the particle and r is its position relative to its equilibrium geometry. Similarly, for a multiply charged system, μ_{ar} can be expressed as

$$\mu_{\mathrm{ar}} = \langle \Psi_{\mathrm{a}} | \mathrm{qr}_1 + \mathrm{qr}_2 + ... | \Psi_{\mathrm{r}} \rangle. \tag{2.52}$$

The transition dipole moment, with unit of C.m or Debye, forms the basis for the spectroscopic selection rules that constrain possible transitions in a system. In general, if the value of the transition dipole moment is zero then the transition is forbidden and does not occur. Other selection rules, in the harmonic approximation, are as follows: $\Delta\nu = \pm 1$, $\Delta \mathrm{J} = 0, \pm 1, ...$ ($\mathrm{J} = \ell + \mathrm{s}$), and $\Delta \mathrm{s} = 0$ where ν, s and ℓ are, respectively, vibrational states, spin and orbital quantum numbers. Often, we do not need to solve Eqs. 2.51 or 2.52, instead it is sometimes sufficient to determine if the integral is zero or not (i.e., odd/even integrals). For example, based on selection rules, a $\pi \rightarrow \pi^*$ transition is allowed because the overall integrand is even (i.e., even $\times$ odd $\times$ odd = even) and integration over all space yields a nonzero value for μ.

The common practice in TD-DFT calculations of the absorption and emission energies is to utilize the adiabatic approximation in which one uses the optimized geometry of the molecule in its singlet ground state (S_0) to compute the excitation energies (also known as the vertical excitation energies). Although this approach does not require geometry optimization and Hessian determination for the excited state, and hence is quite computationally expedient, the computed energies are usually on the upper side of the experimental (reference) values.

The reason is because the effect of geometric relaxation of the excited state is ignored (see Figure 2.5) [5].

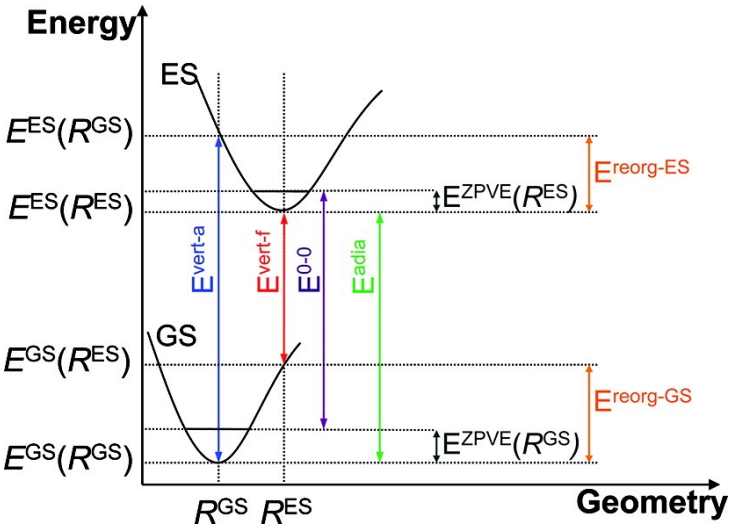

FIGURE 2.5: Comparison between TD-DFT vertical (E^{vert}), 0-0 (E^{0-0}), and adiabatic (E^{adia}) excitation energies. Reprinted with permission from Ref. 5. Copyright 2015 American Chemical Society.

The more accurate and at the same time more computationally expensive approach is to optimize geometries of both the ground (GS) and excited (ES) states and then subtract the energies to find the adiabatic excitation energies (E^{adia}) (see Eq. 2.53 and Figure 2.5):

$$\mathrm{E^{adia}} = \mathrm{E^{ES}(R^{ES})} - \mathrm{E^{GS}(R^{GS})}. \tag{2.53}$$

One can also add the zero point vibrational energy differences (ΔE^{ZPVE}) to the total electronic energies to obtain the 0-0 excitation energies (i.e., E^{0-0}) (see Eq. 2.54 and Figure 2.5):

$$\mathrm{E^{0-0}} = \mathrm{E^{adia}} + \Delta\mathrm{E^{ZPVE}} \text{ where } \Delta\mathrm{E^{ZPVE}} = \mathrm{E^{ZPVE}(R^{ES})} - \mathrm{E^{ZPVE}(R^{GS})}. \tag{2.54}$$

2.9 Natural Bond Orbital and Quantum Theory of Atoms in Molecules

As mentioned before, a single Slater determinant offers a very simple picture of the true wave function of the system since only occupied orbitals are considered and the virtual ones are neglected. While this representation is qualitatively correct (most of the time), it often fails quantitatively. A more rigorous and accurate picture is provided by the N^{th} order density matrix [269] which is defined as

$$\Gamma^{(\mathrm{N})} = \Psi_{\mathrm{N}}\left(\mathrm{r}_1, \mathrm{r}_2, ..., \mathrm{r}_{\mathrm{N}}\right) \Psi^*_{\mathrm{N}}\left(\mathrm{r}_1, \mathrm{r}_2, ..., \mathrm{r}_{\mathrm{N}}\right). \tag{2.55}$$

If we limit the number of electrons to a {P} subspace then we obtain the reduced density matrix:

$$\Gamma^{(\mathrm{P})} = \left[\frac{\mathrm{N!}}{\mathrm{P!}}\left(\mathrm{N}-\mathrm{P}\right)!\right] \int ... \int \Gamma^{(\mathrm{N})}\, \mathrm{dr}_{\mathrm{N}}\, \mathrm{dr}_{\mathrm{N}-1} ... \mathrm{dr}_{(\mathrm{N}-\mathrm{P}+1)}. \tag{2.56}$$

The binomial coefficient in front of the integral represents the indistinguishability of electrons. In this approach, the dependency on all electrons except the electrons in the {P} subspace are averaged by integrating over N-P electron coordinates. Because the Hamiltonian only depends on one-electron and two-electron operators, therefore only first ($\Gamma^{(1)}$) and second ($\Gamma^{(2)}$) order reduced density matrices are needed for evaluation of every measurable quantity of the system (see Eqs. 2.57 and 2.58):

$$\begin{aligned} \Gamma^{(1)}(\mathrm{r}_1) &= N \int ... \int \Psi_N(r_1, ..., r_N)\, \Psi^*_N(r_1, ..., r_N)\, dr_2 ... dr_N \\ &= N \int ... \int \Gamma^{(N)}(r_1, ..., r_N)\, dr_2 ... dr_N \end{aligned} \tag{2.57}$$

$$\begin{aligned} \Gamma^{(2)}(\mathrm{r}_1, \mathrm{r}_2) &= \frac{N(N-1)}{2} \int ... \int \Psi_N(r_1, ..., r_N)\, \Psi^*_N(r_1, ..., r_N)\, dr_3 ... dr_N \\ &= \frac{N(N-1)}{2} \int ... \int \Gamma^{(N)}(r_1, ..., r_N)\, dr_3 ... dr_N. \end{aligned} \tag{2.58}$$

Löwdin [270] in 1955 found that the eigenfunctions of the first order reduced density matrix correspond to unique orbitals called *natural orbitals* (θ_i):

$$\int \Gamma^{(1)}(\mathrm{r}_1)\, \theta_{\mathrm{i}}(\mathrm{r}_1) = \mathrm{n}_{\mathrm{i}}\, \theta_{\mathrm{i}}(\mathrm{r}_1),\ \mathrm{i} = 1, 2, ..., \infty \tag{2.59}$$

where n_i is the natural orbital occupation number (which represents population of the natural orbitals) of the eigenfunction θ_i which can be obtained as

$$\mathrm{n_i} = \int \theta_\mathrm{i}^* \, \Gamma^{(1)} \, \theta_\mathrm{i} \, \mathrm{d}\tau \text{ where } 0 \leq \mathrm{n_i} \leq 2. \tag{2.60}$$

Natural orbitals are the unique and accurate orbitals of the system because they only depend on the wave function (Ψ) itself. Natural bond orbitals (NBOs) are an *orthonormal set of localized maximum occupancy orbitals whose leading N/2 members (or N in the case of open-shell systems) give the most accurate possible Lewis-like description of the total N-electron density.* NBOs can be obtained from the linear combination of their corresponding natural atomic orbitals (NAOs, in which are localized one center orbitals). For more details regarding the transformations consult Refs. 271, 272 and references therein.

Another theory based on electron density (ρ(r)), and not the many body wave function, is called atoms in molecules (AIM) developed by Bader [273–275], also referred to as the quantum theory of atoms in molecules (QTAIM). Based on this theory, the geometric picture of any system can be revealed from the stationary points of ρ(r) and its gradient ($\nabla\rho$(r)). In other words, by obtaining ρ(r) (or molecular charge distribution) of a molecular system one can calculate the associated gradient and consequently find the maxima where the atoms are located. Accordingly, all trajectories of the gradient vectors start at infinity and end at the nuclei. The points where $\nabla\rho(\mathrm{r}) = 0$ are called critical points which are characterized by the number of eigenvalues of their associated Hessian matrix (λ_x, λ_y, λ_z) and the algebraic sum of their signs. Then, when one of the three eigenvalues of $\nabla^2\rho$(r) is positive and the other two are negative the critical point is denoted by (3,-1) and is called a bond critical point (BCP). When one is negative and the other two are positive it is denoted as (3,+1) and is called a ring critical point (RCP) which indicates a ring structure exists in the molecule. The sign of $\nabla^2\rho$(r) is also indicative of the nature of the bond; if $\nabla^2\rho(\mathrm{r}) < 0$ the bond is a covalent bond but when $\nabla^2\rho(\mathrm{r}) > 0$ the bond has (somewhat) ionic character.

Cremer and Kraka in 1984 showed that the Laplacian of the electron density is not a good indicative of a covalent/ionic bond [276]. Through systematic examination of the covalent nature of the C–C, C–N, C–O, C–F, O–O and F–F bonds, they found that one needs to take into account the energetic aspects in addition to the electrostatic consideration (i.e., $\nabla^2\rho$(r))

to obtain a clear picture of the bond [276]. For example an ionic bond for the F–F bond in the F_2 molecule was found based on the $\nabla^2\rho(r)$ index which is not in accordance with the MO picture of this compound. On the other hand, they found that the local energy density is always negative (stabilizing) at sites where $\rho(r)$ is maximum. Therefore they recommended the use of sum of the kinetic (V(r)) and potential (G(r)) energies, i.e., H(r) = V(r) + G(r), instead of $\nabla^2\rho(r)$ for studying the covalent/ionic nature of a bond. This index is used throughout Chapter 6 of this thesis for studying C–B and B–N bonds in novel boron-nitride complexes.

Chapter 3

Why Do TD-DFT Excitation Energies of BODIPY/Aza-BODIPY Families Largely Deviate from Experiment? Answers from Electron Correlated and Multireference Methods

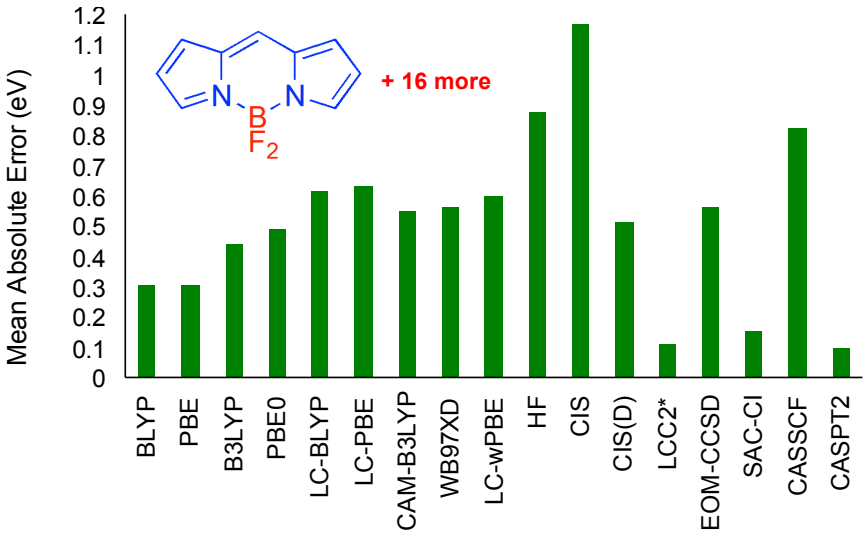

As mentioned in the Introduction (Chapter 1), absorption and fluorescence of the boron-dipyrromethene (BODIPY) fluorophores are easily tuneable and because of that they have found many applications in chemistry and medicine (e.g., see Ref. 8 and references therein). On the other hand, these relatively simple organic compounds have become a challenge for theoretical chemists. Recent benchmark studies have shown that there is a large deviation (> 0.3 eV) between the computed TD-DFT excitation energies and experiment [30, 47, 49, 50, 52]. The present work aims to fill the gap between theory and experiment through systematic investigation of excitation energies computed using different ab initio and TD-DFT methods. In the search for alternatives to TD-DFT, the performance of TD-HF, CIS, CIS(D), SAC-CI, LCC2, CASSCF, and CASPT2 methods for excited states of (aza-)BODIPY molecules is studied. Moreover, some of the well known failures of TD-DFT such as excitations with charge transfer and multi-reference characters have been studied extensively.

The structure of this chapter is such that first the BODIPY molecules included in the benchmark set will be introduced and then the results of the ab initio and TD-DFT benchmark computations will be discussed. The diagnostic tests performed on these molecules will be presented in the next stage to probe the problem(s) of TD-DFT methods with these compounds.

3.1 Excited State Properties of (aza-)BODIPY Families

A set of 17 BODIPY based structures was chosen for examination starting from the head of the family, i.e., BODIPY itself (**1**), see Figure 3.1 for all structures considered.

Substituting the carbon atom of BODIPY in the *meso* position with nitrogen produces aza-BODIPY (**2**) which provides a promising building block for the generation of new near IR emitting chromophores [277]. The carbon substituted boron 2-(2-pyridyl)imidazole (BOPIM) complex (**3**) and BOPIM itself (**4**) are next; (**3**) has not yet been synthesized. Despite the fact that (**1**) and (**3**) along with (**2**) and (**4**) are isomers and all four of them are iso-electronic, we will see later they have very different photophysical properties. The strongly fluorescent biimidazol-2-yl-BF2 complex (**5**) and its hydrogenated form ($\mathbf{5}_H$) have a common feature with (**3**) and (**4**); all have a central five-membered ring rather than a six-membered one as

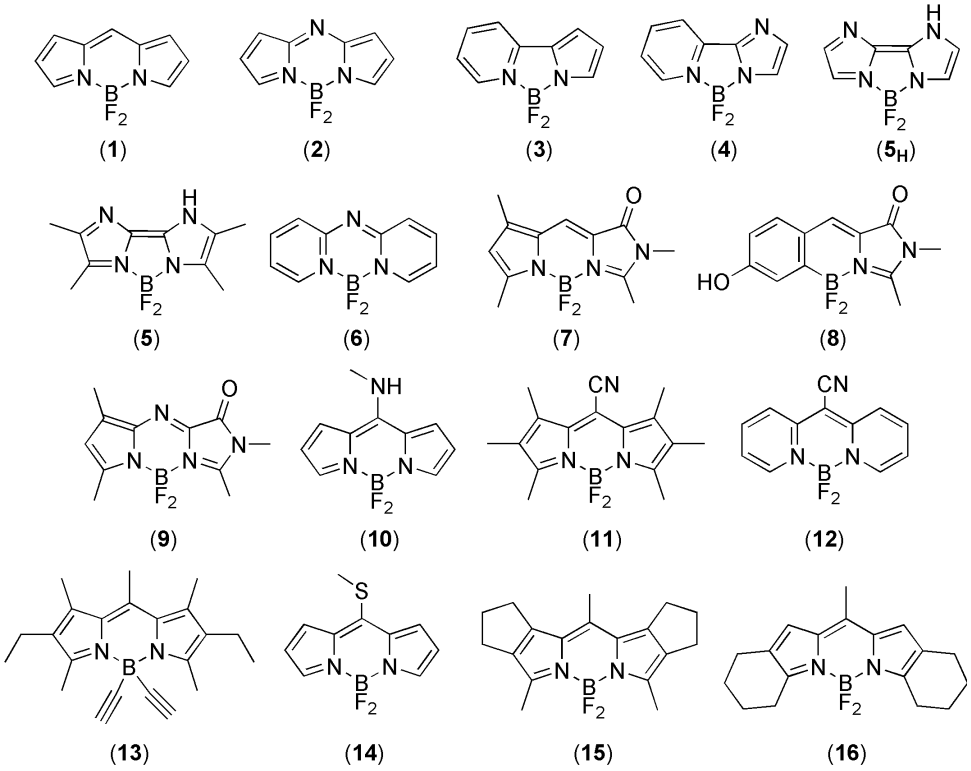

FIGURE 3.1: The first set of structures considered in this study.

in the other compounds. Difluoro-boron-triaza-anthracene (**6**), BF_2 linked green fluorescent protein (GFP) chromophore analogs (**7**) and (**9**), and the BF_2 linked GFP chromophore itself (**8**) are also in the set of structures considered in this work; for the benchmark study on the GFP chromophore itself see the work of Uppsten and Durbeej [278]. In addition, substituted complexes of (**1**) and (**6**) were chosen to show the impact of substitution of both electron donor (amino (**10**) and thio (**14**)) and acceptor (cyano (**11**) and (**12**)) groups on the photophysical properties of these compounds. Moreover in order to investigate the effect of replacing the fluorine atoms and fusing different carbocyclic rings compounds (**13**), (**15**), and (**16**) were chosen to be examined.

Time-dependent density functional theory (TD-DFT) is the computational method of choice for studying excited state properties in many systems due to its overall accuracy and efficiency, i.e., in most cases, TD-DFT provides adequate accuracy for relative energies (0.1–0.3 eV difference with experiment) within a reasonable amount of time even for large molecules. However, the TD-DFT approach has some well-known difficulties. For example, TD-DFT results based on standard functionals are often poor when dealing with excitations involving

charge transfer (CT), or, more generally, long-range excitations, e.g., in conjugated systems with attached electron donor and acceptor groups. Some of these problems have been mitigated through the introduction of range separated functionals such as CAM–B3LYP and ωB97X–D. Secondly, DFT and, hence, TD-DFT, encounters difficulties when the ground (and/or excited state) has multi-reference character. Finally, as TD-DFT is a single-electron theory, it cannot handle double excitations in its standard form. Many of the issues with TD-DFT can be attributed to the underlying approximations, i.e., the adiabatic approximation and the requisite use of approximate exchange correlation functionals [279]. Alternatively, highly correlated multi-reference techniques, such as CASSCF as well as methods built from the CASSCF reference including CASPT2 and multi-reference CI (MRCI), can be utilized to determine the excited states. These methods work well and are able to account for the difficulties with TD-DFT. However, these multi-reference techniques are not "black box" as one must choose an adequate active space, and, more importantly for BODIPYs, they are not particularly well-suited for large systems. On the other hand, one can tackle excited states using other ab initio methods such as CIS, CIS(D), EOM-CC, SAC-CI, and LCC2. In general, these single reference techniques are reliable, have reasonable accuracy, and can be applied to (relatively) large molecular systems. In the present work, we will assess the relative merits of both TD-DFT and ab initio approaches for determining the lowest-lying excited state energy for BODIPYs.

In the search for the best choice of functional to use within TD-DFT for these systems, there have been several TD-DFT benchmark studies on BODIPYs [30, 47–52]. To the best of our knowledge, two very recently published works of Jacquemin *et al.* are the only cases in the literature that tried to provide accurate theoretical estimates and to address the systematic shift (> 0.3 eV) of TD-DFT results compared to experiment for a large subclass of BODIPYs [280, 281]. In the first study, they proposed a combination of the Bethe–Salpeter approach with TD-DFT for computing vertical absorption and emission energies of oxygen substituted BODIPYs (NBOs) [280]. Using this approach they succeeded to decrease the Mean AE from 0.25–0.45 eV in the raw TD-DFT to 0.07–0.18 eV in the combined approach for the studied molecules. In the second study, they suggested the use of the scaled opposite-spin variant CIS(D) (SOS-CIS(D) method) for screening both BODIPYs and aza-BODIPYs [281, 282]; for seminal works on the spin-component scaled SCS-CIS(D) and SOS-CIS(D) methods see references [283, 284]. More specifically, TD-DFT 0–0 energies were corrected with vertical

CIS(D) and SOS-CIS(D) energies in which the Mean AE was reduced from ca. 0.4 eV for raw 0–0 energies to ca. 0.2 eV for CIS(D) and ca. 0.1 eV for the SOS–CIS(D) approaches. In another very recent study, Petrushenko and Petrushenko studied the effect of substitution in the *meso* position with using TD-DFT and RI-CC2 methods [285].

The present work attempts to find the trends and connections between different BODIPY and BODIPY-like systems to illustrate the extent of the TD-DFT discrepancy and to understand its source. With these goals in mind, TD-DFT and ab initio, including CASSCF, computations for molecules within these families are presented and compared and contrasted to each other as well as to published experimental measurements. Through evaluation of CT and multi-reference indices, comparison of methods systematically including higher levels of electron correlation, along with examination of the CASSCF wave functions, the nature of the difficulties with TD-DFT for BODIPYs will be addressed. To reach this goal, a set of 17 different BODIPY systems is chosen to be investigated where 13 of them have been synthesized and experimentally characterized, see Figure 3.1. A summary of the computational methods utilized is provided in the next section. Computational results including optimized ground and excited state geometries, excitation energies, and CT and multi-reference indices are provided in the results section. TD-DFT vertical excitation energies for all systems are compared and contrasted with the experimental results to show the extent of the difference for each of the nine functionals considered. Since all TD-DFT results are systematically shifted from, but highly correlated to, the experimental measurements, linear fit equations are derived using the nine DFT functionals to provide empirical corrections to the theoretical predictions. To assess the error introduced by comparing vertical adiabatic excitation energies to the experimental absorption maxima, the 0–0 transition energies are also determined utilizing the CAM–B3LYP functional. As a further point of comparison, the computed spectra of compounds (**1**) and (**14**) using all nine different functionals are compared to the available experimental ones. In addition, the computed CAM–B3LYP CT parameters, q^{CT} (amount of the transferred charge) and d^{CT} (CT distance based on the hole-electron distance), along with the electron density difference (EDD) plots are discussed for all species to determine the role of CT in the systematic differences observed for TD-DFT. As a comparison to TD-DFT, vertical excitation energies are computed using ab initio TD-HF, CIS, CIS(D), EOM-CCSD, SAC-CI, LCC2* and multi-reference CASSCF and CASPT2 methods. For a smaller subset of the test molecules, the effects of increasing correlation are examined

by determining the excitation energies with CCS, CC2, CCSD, CCSDR(T), an CCSDR(3) methods. To test the best methods (i.e., LCC2* and empirically corrected TD-DFT in terms of accuracy and computational efficiency), eight larger conjugated BODIPYs are examined. Finally, the CASSCF wave functions are used to provide insight into the multi-reference character in these BODIPYs. Finally, the nature of transitions in these systems are addressed and suggestions provided on the best choice of theoretical approach for examining excitation energies for BODIPYs.

3.2 Computational Methods

Geometry optimizations were performed using density functional theory (DFT) with the PBE0 [286–288] and CAM–B3LYP [261] functionals and the cc-pVTZ [289, 290] basis set in the gas phase. It's been shown previously that PBE0 is a very good functional for ground state (GS) optimization of BODIPY based compounds [30]. The excited state (ES) geometries were determined using TD-DFT with the CAM–B3LYP functional as suggested by the benchmark studies of Jacquemin *et al.* [5, 291]. Tight convergence criteria, i.e., maximum force = 1.5×10^{-5} a.u., RMS force = 1.0×10^{-5} a.u., max displacement = 6.0×10^{-5}, and RMS displacement = 4.0×10^{-5} were applied for both GS and ES optimizations. The grid used for numerical integration in DFT was set to "Ultrafine," i.e., a pruned grid of 99 radial shells and 590 angular points per shell. Harmonic vibrational frequencies were computed at the same level of theory for both S_0 and S_1 states in order to characterize the stationary points as true minima, representing equilibrium structures on the potential energy surfaces. In order to assess the effects of solvent environment on the optimized geometry, the GS and ES structures of (**1**) and (**2**) were re-optimized using the polarizable continuum model (IEF-PCM [292, 293], and universal force field (UFF) atomic radii) with parameters for methanol ($\epsilon = 32.613$). Not surprisingly, the solvent had no significant impact on geometries of both the S_0 and S_1 states (see Figure 3.2). Experimentally obtained excitation energies for the BODIPY molecule (**1**) are 2.460 and 2.485 eV in cyclohexane and ethanol, respectively [7]. In agreement with experiment, the PBE0/cc-pVTZ computed excitation energy of 3.186 eV for the BODIPY molecule in the gas phase slightly decreases to 3.082 eV in methanol and to 3.042 eV in cyclohexane; i.e., no significant change in excitation energy due to solvent.

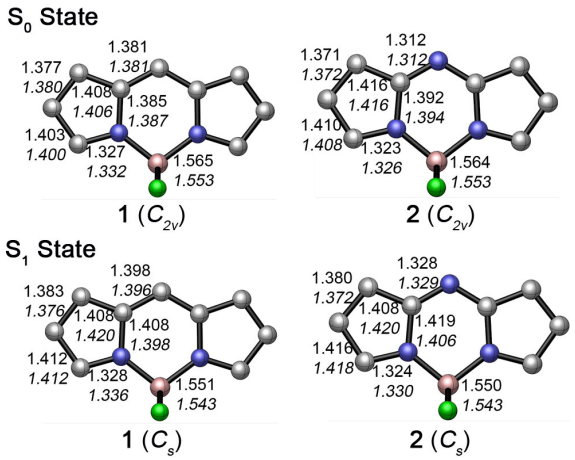

FIGURE 3.2: Comparison of the geometrical parameters of (**1**) and (**2**) in the S_0 ground and S_1 excited states in the gas phase and methanol (italicized) obtained at the CAM-B3LYP/cc-pVTZ level of theory. (C-H bonds are omitted for clarity).

While it has been shown by Chibani *et al.* that the corrected linear-response (cLR) and state-specific (SS) PCM solvation models are in most cases superior to the linear-response PCM (LR-PCM) results for the BODIPY molecules [48, 49], they have demonstrated that the gas-phase results are, in general, close to those determined using the superior solvation models. Therefore, gas phase results will be discussed throughout the text. Symmetry was used whenever possible to simplify calculations, and this was crucially important for MRSCF computations. Nine different DFT functionals, BLYP [236–238], PBE [286, 287], B3LYP [241, 242], PBE0 [286–288], LC-BLYP [294], LC-PBE [294, 295], CAM–B3LYP [261], ωB97X–D [296], and LC-ωPBE [297–299], from generalized gradient approximations (GGA) to range-separated hybrids were used to obtain vertical transitions for 10 singlet ESs (S_1-S_{10}) using the PBE0 optimized geometries. 0–0 transition energies were also obtained for all species using the range separated CAM–B3LYP functional as recommended by the benchmark study of Jacquemin *et al.* [5]. The 0–0 transition energy is determined as $\Delta E^{0-0} = E^{adia} + \Delta E^{ZPE}$ where E^{adia} is the energy difference between the optimized S_1 and S_0 states and the latter is the corresponding zero point energy difference of those two states.

TD-DFT results were compared and contrasted with configuration interaction (CI) results determined using single excitations (CIS)[300] and including perturbative corrections for double excitations (CIS(D)) [301]. Electron correlated equation of motion coupled cluster with singles and doubles (EOM-CCSD) [302–305] along with Laplace transformed density fitting local coupled-cluster singles and approximate doubles (LT-DF-LCC2 abbreviated LCC2*

hereafter) [213, 306] and symmetry adapted cluster/configuration interaction (SAC–CI) [307] methods were utilized for all studied structures. The efficient direct algorithm was utilized for all the SAC–CI computations which corresponds to the conventional SAC–CI with NoUnlinkedSelection keywords (all other options set to default values). To account for effect of the electron correlation and also to understand the convergence of the CC methods better, coupled cluster CCS, CC2, LR-CCSD, CCSDR(T), and CCSDR(3) computations were performed for the vertical excitation energies of the smallest BODIPYs, i.e., (**1**) to ($\mathbf{5}_H$).

Multi-reference complete active space self-consistent field (CASSCF) [308] and complete active space second-order perturbation (CASPT2) [309] computations were accomplished for all systems. The CASPT2 computations utilized the internally contracted RS2C program [309]. The CASSCF wavefunctions were constructed by using equal weights of the S_0 and S_1 states. The CASPT2 computations used an IPEA shift, which is a correction to the zeroth order Hamiltonian, of 0.3 [310]. In order to investigate the effect of altering active spaces on the vertical transition energies, six different active spaces were considered starting from including just the highest occupied molecular orbital (HOMO) and the lowest unoccupied molecular orbital (LUMO) (CAS[2,2]) to including all the π electrons and the nitrogen lone pair (CAS[12,11]) for the first compound (Table 3.1). Not surprisingly, selecting an appropri-

TABLE 3.1: CASSCF/CASPT2(n,m) vertical excitation energies[(a)] (in eV) for different active spaces of compound (**1**) using the cc-pVTZ basis set in the gas phase. Deviations from the experimental value of 2.460 eV are also presented. Total number of configuration state functions (CSFs) are also listed for each active space.

CASSCF	[2,2]	[4,4]	[6,6]	[8,8]	[10,10]	[12,11]
energy	3.743	3.717	3.464	3.623	2.837	2.829
deviation	+1.283	+1.257	+1.004	+1.163	+0.377	+0.369
CASPT2	[2,2]	[4,4]	[6,6]	[8,8]	[10,10]	[12,11]
energy	2.056	2.133	2.364	2.416	2.407	2.450
deviation	-0.404	-0.395	-0.096	-0.044	-0.053	-0.010
CSF	48799602	101987231	107681216	112955078	120443466	127339954

[(a)] For details of the active spaces see Appendix A.

ate active space has a critical impact on the absolute value of the CASSCF transition energy. However, the effect of enlarging the active space was not as significant for the CASPT2 energies. Since enlarging the active space has a significant impact on the CASSCF transition energy, all π electrons and lone pairs were included in the active space, whenever possible, as the least amount of error was observed for that case. Also the effect of enlarging the basis set from cc-pVXZ [289] to aug-cc-pVXZ [290, 311] (X = D and T) on the excitation energy

was investigated and the corresponding results are provided in Table 3.2. Increasing the

TABLE 3.2: CASSCF/CASPT2(12,11) vertical excitation energies (in eV) of (**1**) along with deviations from the experimental value of 2.460 eV using (aug)-cc-pVXZ (X = D, T) basis sets in the gas phase. Total number of configuration state functions (CSFs) are also listed for each basis set.

CASSCF	cc-pVDZ	cc-pVTZ	aug-cc-pVDZ	aug-cc-pVTZ
energy	2.857	2.841	2.820	2.834
deviation	+0.383	+0.369	+0.360	+0.374
CASPT2	cc-pVDZ	cc-pVTZ	aug-cc-pVDZ	aug-cc-pVTZ
energy	2.539	2.452	2.441	2.415
deviation	+0.078	-0.010	-0.021	-0.045
CSF	17629314	127339954	57729570	127570949

size of the basis from cc-pVDZ to cc-pVTZ does not have a major impact on accuracy nor has including diffuse functions. Overall, cc-pVDZ seems to be a suitable and cost efficient basis set and was utilized for CASSCF/CASPT2 computations throughout this work unless otherwise stated.

Very recently proposed charge transfer (CT) indices, q^{CT} (amount of the transferred charge) and d^{CT} (CT distance based on the hole-electron distance), by Ciofini and co-workers [312, 313] are also reported for all compounds. Moreover, in order to predict reliability of using a single-reference based method, three different diagnostic tests were carried out by performing CCSD [314–317], CCSD(T) [318], and CASSCF computations for all the systems. It is worthwhile mentioning that all of these tests refer to the multi-reference character of the ground state not the excited state. First, the T_1 diagnostic test of Lee and Taylor, which is based on the norm of the vector of single-excitation amplitudes from CCSD in a closed shell system [319], was utilized. If the T_1 value is smaller than 0.02, the system is considered to be dominated by a single-reference but if it is larger than 0.02, the system is considered to have (most likely) multi-reference character. Secondly, the %TAE[T] diagnostic test related to percent atomization energy due to triples was computed for all the BODIPY species as

$$\%\text{TAE[T]} = 100\left(\frac{\text{AE[CCSD(T)} - \text{CCSD]}}{\text{AE[CCSD(T)]}}\right) \tag{3.1}$$

where AE is the atomization energy of the system under consideration using either CCSD or CCSD(T) methods [320]. If %TAE[T] is smaller than 2%, the system is considered as a single-reference system; otherwise, it is considered as a multi-reference system. Finally, the

M diagnostic test is computed for all BODIPY systems [321]. For a closed shell system in its equilibrium geometry, M is defined as

$$M = \frac{1}{2}\left(2 - [n(MCDONO) - n(MCUNO)]\right) \tag{3.2}$$

where n(j) is a natural orbital occupation number computed as the eigenvalue of the first order density matrix of a CASSCF wave function. More specifically, n(MCDONO) and n(MCUNO) are respectively the natural occupation numbers of the most correlated doubly occupied natural orbital and the most correlating unoccupied natural orbital. Based on the work of Truhlar and co-workers who introduced the M parameter [321], if it is larger than 0.04, then the system is considered as a multi-reference system; otherwise, it is considered to be a single-reference system.

All DFT, TD-DFT, CIS, CIS(D) SAC-CI, CCSD, CCSD(T), and EOM-CCSD computations were performed using Gaussian 09 [322]. LCC2* and MRSCF computations were accomplished using the 2010 and 2012 Molpro packages [323]. Also, coupled cluster CCS, CC2, LR-CCSD, CCSDR(T) and CCSDR(3) excitation energies were computed using the DALTON program package [324, 325].

3.3 Results and Discussion

3.3.1 S_0 and S_1 Optimized Geometries

The PBE0 and CAM–B3LYP functionals were used for the S_0 GS (Figures 3.3 and 3.4) and CAM–B3LYP for the S_1 ES (Figure 3.5) geometry optimizations.

The optimized CAM–B3LYP geometry for the S_0 state is very similar to the parameter free PBE0 one with only 0.001 to 0.003 Å bond length differences for (**1**). The largest deviation from the X-ray structure for (**1**) [7] relates to the B-N bond for which both PBE0 and CAM–B3LYP exhibit a 0.021 and 0.020 Å elongation, respectively. This can most likely be attributed to the fact that experimental geometry is obtained in the solid state but our optimizations are done in vacuum. Therefore, relatively speaking, both PBE0 and CAM–B3LYP geometries are in very good agreement with the available experimental data.

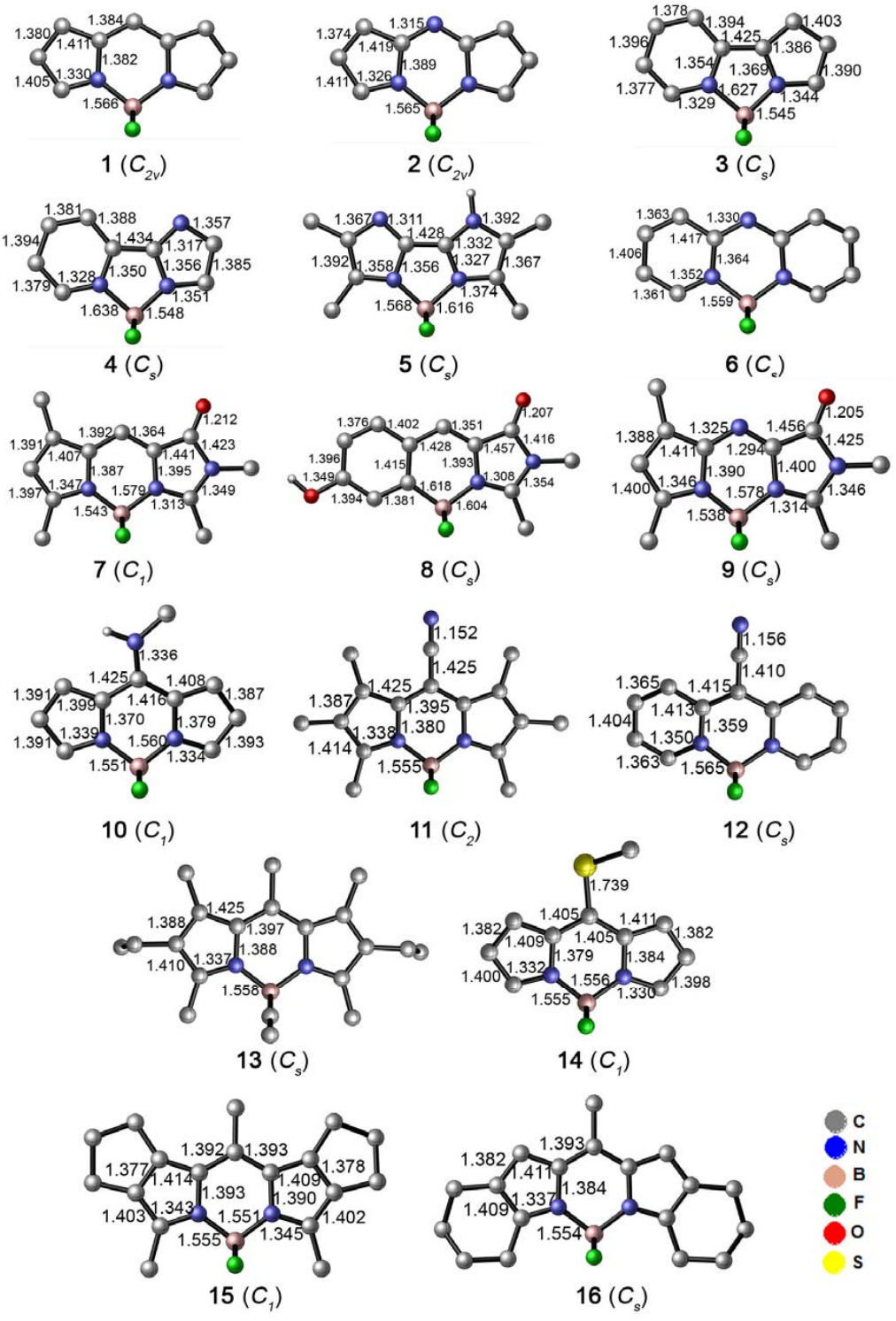

FIGURE 3.3: Optimized gas phase structures in the S_0 state obtained at the PBE0/cc-pVTZ level of theory. (C-H bonds are omitted for clarity).

Hence for the sake of consistency, PBE0 geometries for the GS are used for the rest of the computations. Despite differences in the size of their rings or substituents, the GS

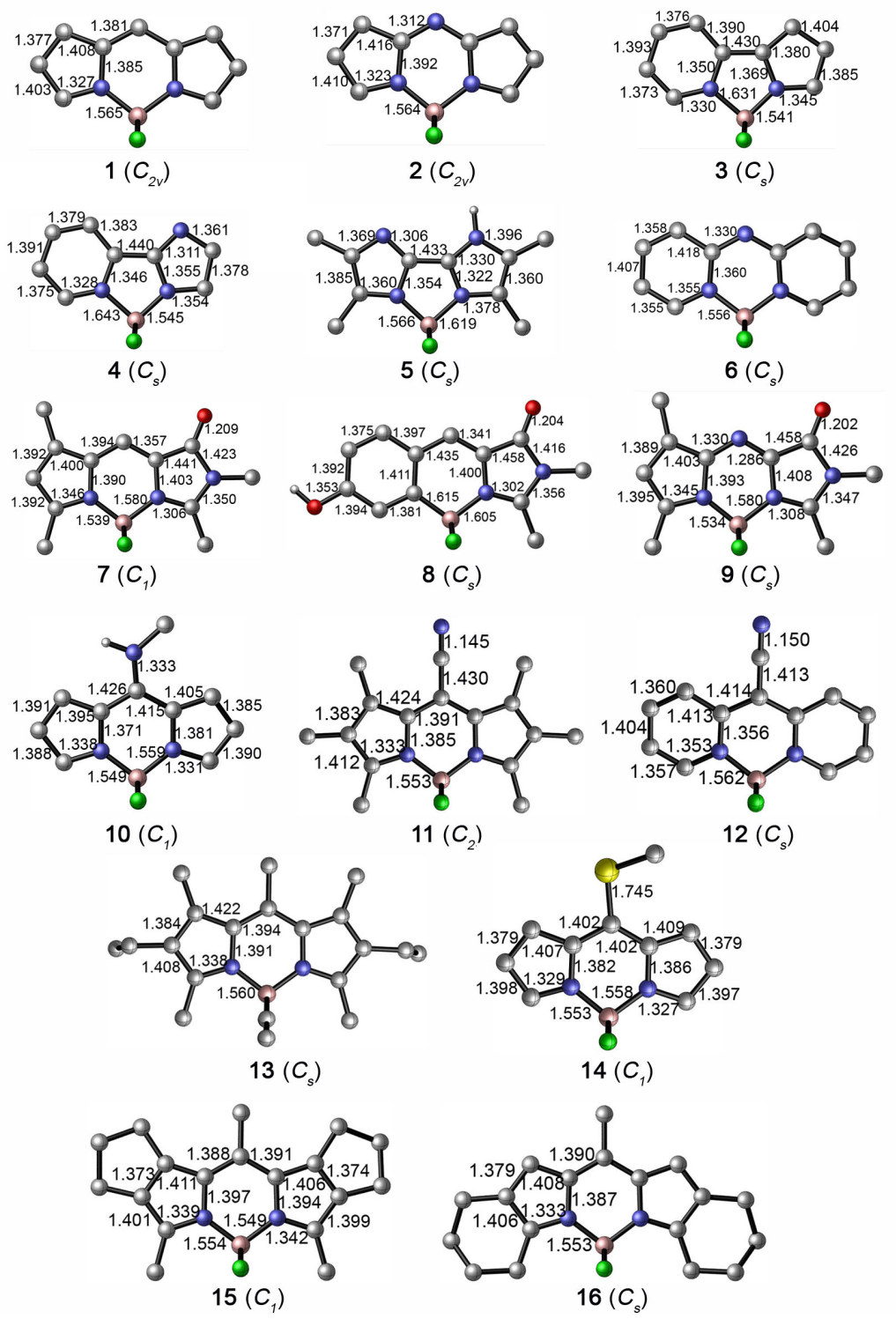

FIGURE 3.4: Optimized gas phase structures in the S_0 state obtained at the CAM-B3LYP/cc-pVTZ level of theory. (C-H bonds are omitted for clarity).

of all structures, excluding the BF_2 groups, is planar and this is most likely due to high degrees of conjugation and resonance. Expectedly, bond lengths and relative positions of the

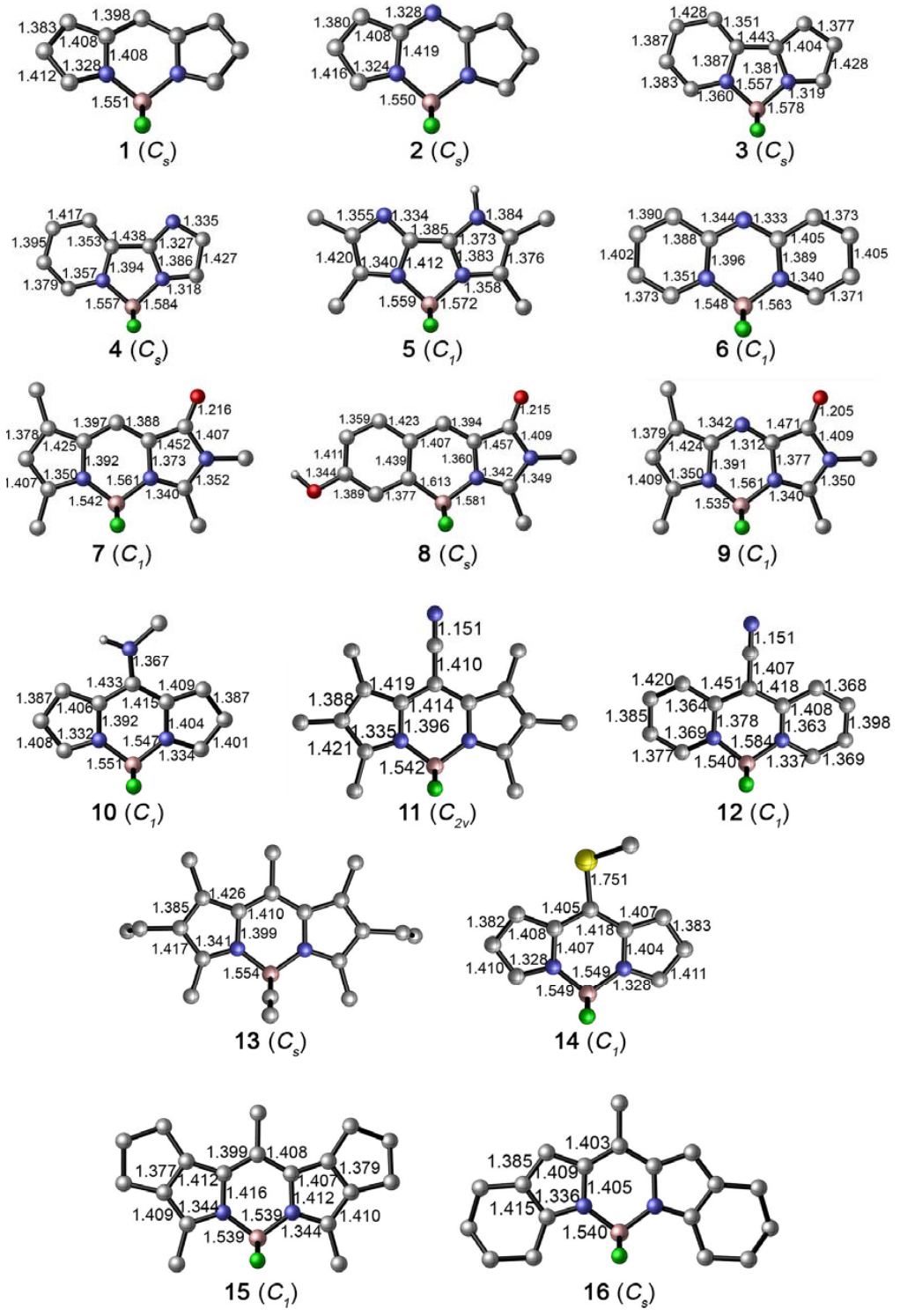

FIGURE 3.5: Optimized gas phase structures in the S_1 state obtained at the CAM-B3LYP/cc-pVTZ level of theory. (C-H bonds are omitted for clarity).

substituents to the plane of the molecule change by going from the S_0 to S_1 state. It is also worthwhile mentioning that the C=O, C-OH, and C-NH(CH_3) bond elongations are the most

important geometrical impact of the electronic excitation (Figures 3.4 and 3.5). Moreover, in some molecules such as in (**1**) and (**2**), the BF_2 unit goes out of the plane in the ES and therefore reduces the symmetry from C_{2v} to C_s (Figure 3.5).

3.3.2 TD-DFT Vertical Excitations versus 0–0 Transitions (ΔE^{0-0})

TD-DFT absorption energies (in eV) for all 17 compounds are presented in Table 3.3; all excitations correspond to $\pi \rightarrow \pi^*$ transitions. Despite the differences between structures and substituents, there is a hypsochromic shift for the TD-DFT absorption energies with respect to the experimental (CASPT2 for (**2**), (**3**), ($\mathbf{5}_H$) and (**9**)) data for all the functionals considered.

TABLE 3.3: Vertical excitation energies (in eV) using nine different functionals and the cc-pVTZ basis set in the gas phase. Experimental values (Exp., including fluorescence in parenthesis)[a] are tabulated for comparison. absolute errors (AE) (Mean AE, Max AE, and Min AE), SD and linear determination coefficient (R^2) are also shown for each functional.

Type	GGA		HGGA		RSH					Exp.
Functional	BLYP	PBE	B3LYP	PBE0	LC-BLYP	LC-PBE	CAM–B3LYP	ωB97X–D	LC-ωPBE	–
1	3.006	3.020	3.154	3.186	3.073	3.084	3.145	3.147	3.077	[7]2.460 (2.407)
2	2.732	2.743	2.889	2.916	2.714	2.723	2.853	2.852	2.733	[b]2.252 (–)
3	2.803	2.824	3.223	3.337	3.930	3.956	3.649	3.690	3.893	[b]3.259 (–)
4	2.837	2.854	3.280	3.397	4.104	4.128	3.756	3.801	4.051	[326]4.175 (3.679)
$\mathbf{5}_H$	4.078	4.109	4.285	4.366	4.726	4.764	4.489	4.497	4.686	[b]4.138 (–)
5	3.664	3.687	3.884	3.961	4.348	4.384	4.101	4.122	4.318	[327]3.712 (3.289)
6	3.254	3.273	3.598	3.680	3.942	3.964	3.808	3.830	3.907	[328]3.125 (3.112)
7	2.993	3.007	3.122	3.161	3.230	3.239	3.180	3.178	3.204	[329]2.583 (2.525)
8	3.020	3.032	3.262	3.328	3.674	3.687	3.470	3.486	3.622	[330]2.995 (2.605)
9	2.851	2.865	2.953	2.979	2.946	2.953	2.959	2.953	2.932	[b]2.479 (–)
10	3.262	3.282	3.445	3.504	3.697	3.719	3.583	3.596	3.670	[6]2.963 (2.678)
11	2.423	2.425	2.615	2.646	2.587	2.594	2.638	2.636	2.589	[331]2.109 (2.026)
12	2.813	2.827	3.170	3.254	3.608	3.625	3.430	3.452	3.565	[332]2.755 (2.719)
13	2.755	2.770	2.904	2.933	2.896	2.905	2.925	2.925	2.886	[333]2.412 (2.322)
14	2.954	2.968	3.101	3.137	3.111	3.125	3.132	3.136	3.106	[334]2.353 (2.300)
15	2.725	2.726	2.920	2.955	2.941	2.950	2.962	2.968	2.932	[335]2.422 (2.317)
16	2.718	2.724	2.839	2.867	2.819	2.830	2.857	2.866	2.820	[335]2.317 (2.214)
Mean AE	0.364	0.367	0.470	0.513	0.587	0.605	0.545	0.556	0.572	
Mean AE[c]	0.303	0.308	0.444	0.492	0.624	0.635	0.553	0.563	0.600	
Max AE	1.338	1.321	0.895	0.778	0.853	0.839	0.779	0.783	0.810	
Min AE	0.025	0.025	0.036	0.008	0.071	0.047	0.184	0.206	0.124	
SD[c]	0.364	0.371	0.499	0.541	0.652	0.669	0.574	0.593	0.631	
R^2[c]	0.793	0.797	0.905	0.923	0.963	0.964	0.961	0.961	0.966	

[a] All the transitions correspond to HOMO → LUMO ($\pi \rightarrow \pi^*$)(details of the HOMO and LUMO states for all structures can be found in Figure 3.6). Experiments carried out in different solvents but, when determined, solvent-induced shifts are small. [b] CASPT2 value was used. [c] Determined excluding compound (**4**) that has the highest Max AE for GGA and HGGA functionals.

Table 3.3 also presents a statistical analyses of the TD-DFT results, i.e., mean absolute error (Mean AE), maximum absolute error (Max AE), and minimum absolute error (Min AE). All

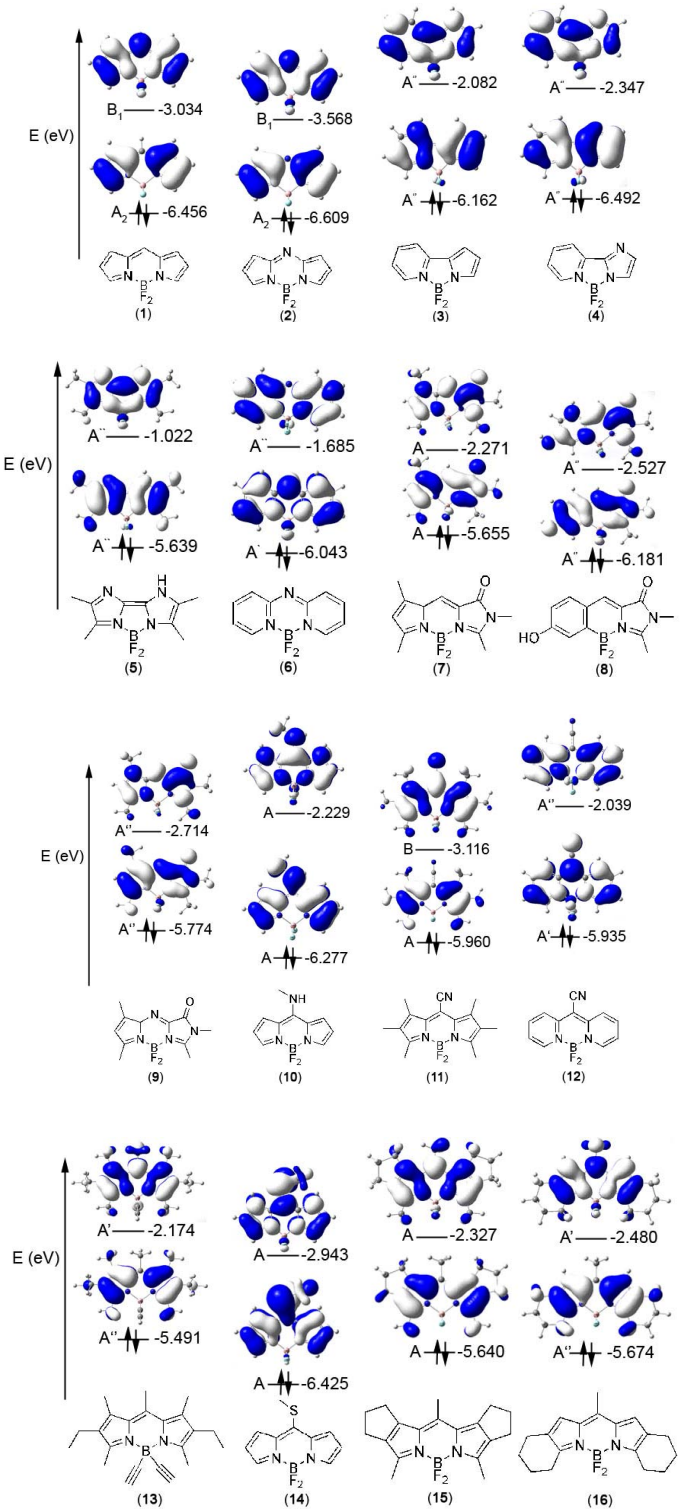

FIGURE 3.6: Frontier molecular orbitals of all the structures with isovalue of 0.02 e/Å^3 computed at the PBE0/cc-pVTZ level of theory.

functionals, regardless of family, have Mean AEs greater than 0.36 eV; this is outside the range of deviation (0.1–0.3 eV) typically reported for TD-DFT methods. The Mean AE is slightly reduced for GGA and HGGA functionals if we exclude compound (**4**) and thus most statistical analyses are reported excluding compound (**4**). Surprisingly, pure GGA BLYP and PBE functionals seem to be the best TD-DFT functionals in terms of the absolute values and deviations from the experiment. The agreement is most likely due to cancellation of errors. This phenomenon is reported previously in the benchmark study of Walczak *et al.* on retinal analogues [336]. All range separated hybrid functionals provide poorer accuracies compared to GGA and HGGA functionals and are rather close to each other. However, based on Mean AE, CAM–B3LYP works slightly better. Although HGGA B3LYP and PBE0 functionals are slightly better than the RSH functionals in terms of the Mean AEs, they provide very poor transition energies overall which are in some cases $\sim$ 0.8-0.9 eV blue shifted. The standard deviation (SD) confirms the deficiency of HGGA functionals compared to pure hybrids. However, based on values of the linear coefficients of determination (R^2), range separated hybrid methods are predictive if scaled and shifted appropriately and therefore can provide consistent predictive results (see Table 3.4 for linear fitting coefficients of all methods).

These results are in agreement with previous extensive benchmarks of the BODIPY monomers and dimers [52] and aza-BODIPYs [30] performed by Jacquemin and co-workers. In their papers, the M06-2X functional was recommended for the BODIPY molecules along with accounting for state-specific solvation and ZPE corrections. On the other hand, one can see similar statistical parameters for the B3LYP, PBE0, CAM–B3LYP, and ωB97X–D functionals used in the both studies even though except five molecules the rest of the systems are different [52]. Finally, the benchmark of Jacquemin *et al.* with an almost identical set of functionals, on the vertical excitation energies of relatively large aza-BODIPYs provided another set of interesting results. They proposed the BMK//PBE0 quick recipe for large systems but they also emphasized the necessity of geometric relaxation of the excited state and vibrational corrections whenever it is computationally possible.

The impact of ring size and substituent is also apparent from Table 3.3. For structures (**3**)-(**5**), which have a five membered ring in the middle instead of six, all TD-DFT functionals are able to predict the significant blue-shift with respect to (**1**). The effect of substituents,

TABLE 3.4: Linear fitting coefficients of all the ab initio and TD-DFT methods considered in this work. The computed values are on the X axis while the experimental ones are on the Y axis (Y = mX + b). All fits exclude compound **(4)**.

Methods	Slope (m)	Y-Intercept (b)	R^2
BLYP/cc-pVTZ	1.2407	–0.9551	0.7935
PBE/cc-pVTZ	1.2237	–0.9218	0.7968
B3LYP/cc-pVTZ	1.2678	–1.2990	0.9051
PBE0/cc-pVTZ	1.2268	–1.2323	0.923
B2PLYP/cc-pVTZ	1.0592	–0.8434	0.9550
LC-BLYP/cc-pVTZ	0.8897	–0.2452	0.9635
LC-PBE/cc-pVTZ	0.8773	–0.2174	0.9640
CAM-B3LYP/cc-pVTZ	1.0941	–0.8659	0.9615
ωB97XD/cc-pVTZ	1.0784	–0.8238	0.9612
LC-ωPBE/cc-pVTZ	0.9143	–0.3116	0.9663
TD-HF/cc-pVDZ	0.7984	–0.1429	0.9122
TD-HF/cc-pVTZ	0.7947	–0.0828	0.9154
CIS/cc-pVDZ	0.8404	–0.5382	0.9402
CIS/cc-pVTZ	0.8510	–0.5266	0.9367
CIS(D)/cc-pVDZ	0.9459	–0.3352	0.9835
CIS(D)/cc-pVTZ	0.9970	–0.4240	0.9852
RI-CC2/cc-pVDZ	0.9536	+0.0641	0.9542
RI-CC2/cc-pVTZ	1.0200	–0.0516	0.9495
EOM-CCSD/cc-pVDZ	0.9010	–0.2309	0.9832
SAC-CI/cc-pVDZ	0.7964	+0.6150	0.9327
CASSCF/cc-pVDZ	0.7543	+0.0936	0.8024
CASPT2/cc-pVDZ	0.9891	+0.0448	0.9542

which play a large role in shifting the wavelength of the maximum absorption, are also well predicted by most of the functionals. For the following comparison with experiment, the LC-ωPBE functional is used since it shows the highest R^2 value among all (although the value of R^2 is probably not statistically different from the other range-separated hybrids), see Figure 3.7; LCC2* results will be discussed in the ab initio section.

The electron donating aminomethyl group in (**10**) decreases the experimental (LC-ωPBE) maximum absorption of (**1**) (in nm) by as much as 86 (65) while the cyano (**11**) and thio (**14**) groups increase this value 84 (76) and 23 (-3.8), respectively. Attaching five and six membered rings to (**1**) results in formation of (**15**) and (**16**) which also show a bathochromic shift for the maximum absorption. For (**15**) and (**16**), LC-ωPBE can successfully predict the direction and magnitude of this shift (experimental (LC-ωPBE) shifts from **1)** in nm are 7.9 (19.9) and 31.1 (36.7), respectively). Overall, it seems that TD-DFT is able to reproduce the trends whenever the shift due to substitution is quite high and this is one of the strengths of

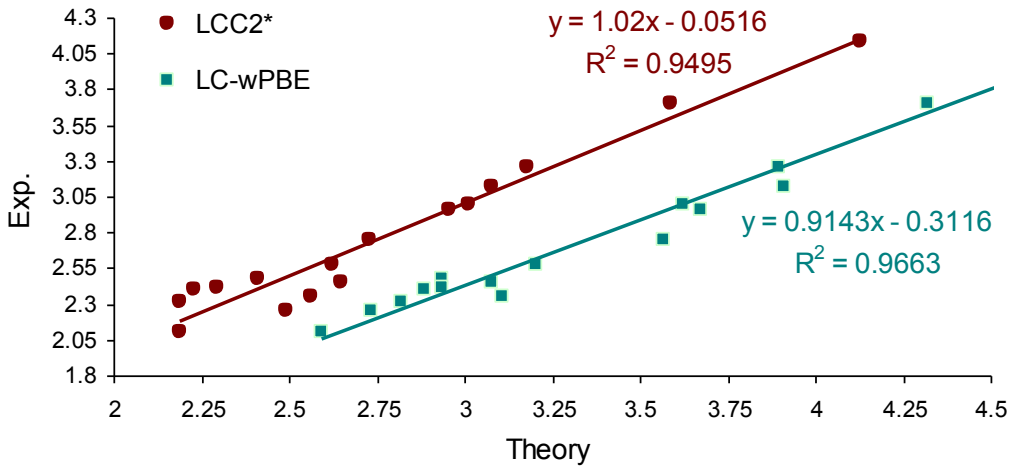

FIGURE 3.7: Comparison between LCC2* and LC-ωPBE computed vertical excitation energies and experiment (Exp.) for all the studied species except (**4**). The cc-pVTZ basis set is used for both methods.

the TD-DFT methods. However when the shift is small, TD-DFT methods have problems determining the correct shift direction.

To assess the impact of the vertical approximation on the theoretically determined absorption maxima, ΔE^{0-0} energies were obtained using the range separated hybrid CAM–B3LYP method; the RSH with the smallest Mean AE. It has been shown that this approach can provide more reliable and accurate data rather than raw vertical transition energies [5, 47–49, 284, 337–339]. Results of these calculations along with the regular vertical absorption and emission energies and oscillator strengths are provided in Table 3.5. Theoretical 0–0 energies are compared to the experimental energies at the absorption maximum rather than the absorption and emission crossing point as suggested previously [5, 52, 284, 338]; this should not strongly impact the statistical analysis. One can't see a major improvement in the agreement with the experimental measurements for the 0–0 computations, i.e., the Mean AE and SD are improved modestly while the linear coefficient of determination is significantly decreased (Mean AE = 0.379, Max AE = 0.804 eV, Min AE = 0.022 eV, SD = 0.397 eV and R^2 = 0.862). However, this method is certainly capable of removing some of error cancellations that exist in the vertical approach. Overall, the least amount of improvement is obtained for (**1**), (**2**), and (**15**), probably due to the stiffness of their structures. Their absorption values are 0.152, 0.157, and 0.152 eV, respectively, lower than their vertical excitation energies, i.e., they still overestimate the experiment by respectively, 0.533, 0.444, and 0.521 eV. Results become slightly better in the case of (**3**), and ($\mathbf{5}_H$) (0.367, and 0.455 eV shifts, respectively).

TABLE 3.5: CAM–B3LYP/cc-pVTZ computed maximum absorption and fluorescence energies (ΔE^{abs} and ΔE^{flu}, in eV, respectively) and their oscillator strengths (f^{abs} and f^{flu}) along with the 0–0 transition energies (ΔE^{0-0}) in the gas phase. Stokes shifts (Shift) for CAM–B3LYP as well as experiment (in parenthesis) are also provided in eV. See Table 3.3 for the experimental values.

Species	State	ΔE^{abs}	f^{abs}	ΔE^{0-0}	ΔE^{flu}	f^{flu}	Shift
1	B_2	3.145	0.507	2.993	3.013	0.430	0.152 (0.053)
2	B_2	2.853	0.462	2.696	2.722	0.387	0.157 (–)
3	A′	3.649	0.236	3.282	3.055	0.129	0.367 (–)
4	A′	3.756	0.233	3.371	3.145	0.150	0.385 (0.496)
$\mathbf{5}_H$	A′	4.489	0.382	4.034	3.815	0.369	0.455 (–)
5	A′	4.101	0.485	3.699	3.473	0.469	0.402 (0.423)
6	A″	3.808	0.399	3.552	3.579	0.362	0.256 (0.013)
7	A	3.180	0.668	2.972	2.938	0.611	0.208 (0.058)
8	A′	3.470	0.685	3.244	3.120	0.646	0.226 (0.390)
9	A′	2.959	0.657	2.787	2.748	0.597	0.172 (–)
10	A	3.583	0.424	3.346	3.223	0.342	0.237 (0.285)
11	B	2.638	0.541	2.496	2.532	0.482	0.142 (0.083)
12	A″	3.430	0.356	3.213	3.085	0.219	0.217 (0.036)
13	A″	2.925	0.567	2.835	2.790	0.527	0.090 (0.090)
14	A	3.132	0.432	2.874	2.871	0.368	0.258 (0.053)
15	A	2.962	0.573	2.806	2.869	0.509	0.156 (0.105)
16	A″	2.857	0.635	2.699	2.769	0.582	0.158 (0.103)

Comparing fluorescence energies with the experimentally available ones for our systems show similar range of errors, see Table 3.3 and Table 3.5. For fluorescence, the Mean AE is 0.479 eV and the SD is 0.678 eV. The R^2 value of 0.924 is slightly better than the corresponding value for the 0–0 energies but worse than that for the adiabatic absorption energies (Table 3.3). However, the CAM–B3LYP functional seems to predict the Stokes shift (the difference between the absorption and emission energies) quite reasonably. For example, within ~ 0.05 eV for compounds (**5**), (**13**), (**15**) and (**16**) but with approximately 0.2 eV difference with experiment for compounds (**6**), (**7**), (**12**), and (**14**) (Table 3.5).

Figure 3.8 compares and contrasts the spectral shapes for (**1**) and (**14**) obtained using all nine TD-DFT functionals with the experimental ones obtained in cyclohexane solutions [6]; these are chosen as examples for which we had access to the experimental spectra.

For simulation of the spectral shape, the AOMix program [340, 341] was used in which the default value of 3000.0 cm^{-1} for the bandwidth was utilized. In terms of the positions of the peaks, all TD-DFT methods tend to overestimate the absorption energies for these BODIPYs. The shift between the TD-DFT and experimental results for both the peak at

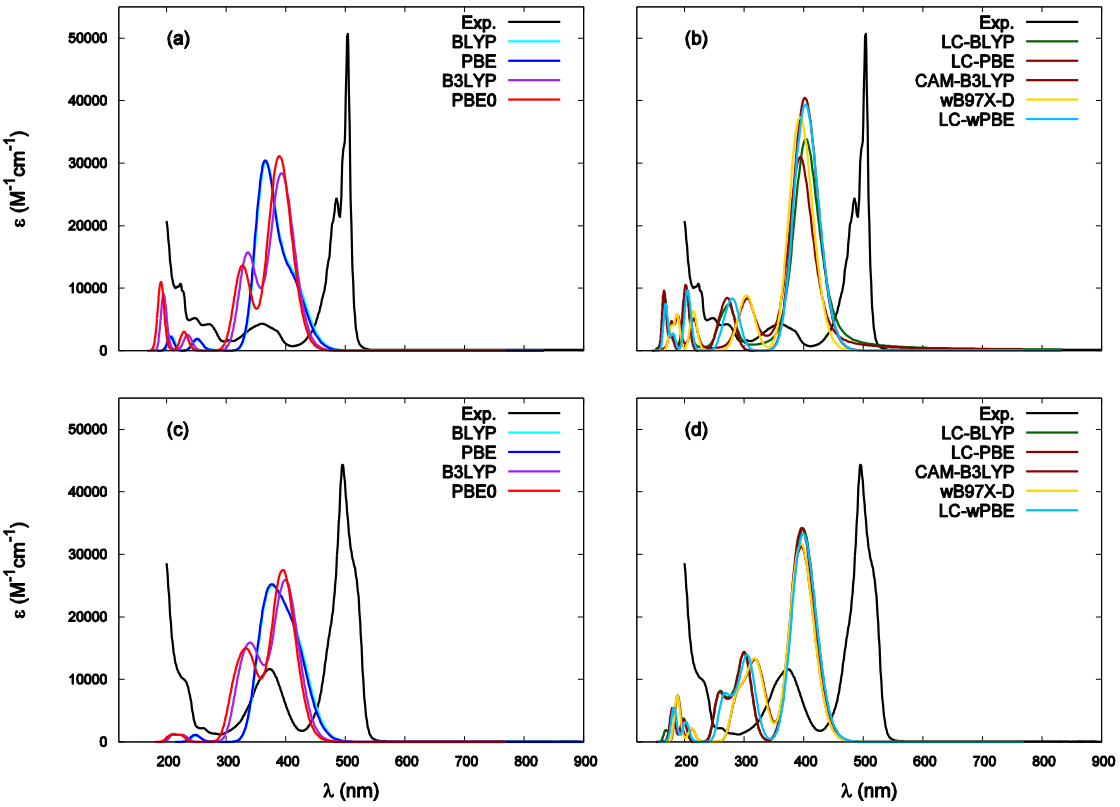

FIGURE 3.8: TD-DFT computed absorption spectra of (**1**) ((a) and (b)) and (**14**) ((c) and (d)) using nine different functionals in the gas phase. Experimental spectra (Exp.) are obtained in cyclohexane solution [6].

higher wavelength (located at approximately 500 nm in the spectra) and the one at the lower wavelength (at $\sim$ 350–370 nm in the spectra) are nearly the same and approximately 100 nm for all functionals. The simulated intensity of the lowest energy peaks for both (**1**) and (**14**) are also a bit lower than the obtained experimental ones specifically for the CAM–B3LYP functional in case of compound (**1**) and also the GGA functionals in both cases; the agreement could be modestly improved by narrowing the simulated bandwidth. Overall, based on the relative peak positions and intensities, LC-ωPBE and ωB97X–D seem to be reasonably reliable functionals for simulating the absorption spectra of these compounds and GGA and HGGA ones seem to be among the worst.

3.3.3 Charge Transfer Parameters and Electron Density Difference Plots

Depending on the nature of the excitation (valence, CT, ...) or whether (or not) there are push-pull substituents in the system of interest, different TD-DFT methods should be applied

to determine accurately the excitation energies. More important is to determine measures to assess the nature of the transition. For example, the range separated hybrid methods, like CAM–B3LYP, have been designed to correct some of deficiencies of their hybrid ancestors with respect to long-range excitations. Table 3.6 provides the computed CT parameters for all species using the range separated hybrid CAM–B3LYP functional in the gas phase. Electron

TABLE 3.6: Computed CT parameters (q^{CT} and d^{CT}), along with GS/ES (μ^{grd}/μ^{exc}) and CT (μ^{CT}) dipole moments at the CAM–B3LYP/cc-pVTZ level of theory.

Species	q^{CT}	d^{CT}	μ^{grd}	μ^{exc}	μ^{CT}
1	0.351	0.232	4.327	4.116	0.391
2	0.340	0.057	2.303	2.327	0.092
3	0.609	1.772	5.610	4.691	5.182
4	0.634	1.913	5.074	2.711	5.824
$\mathbf{5}_H$	0.460	1.072	5.751	5.043	2.369
5	0.486	1.154	5.713	4.545	2.692
6	0.427	0.091	2.020	2.493	0.187
7	0.382	0.792	2.315	1.235	1.454
8	0.437	1.594	2.822	1.502	3.343
9	0.354	0.866	3.783	2.804	1.471
10	0.441	0.824	7.770	5.717	1.745
11	0.358	0.638	0.234	1.330	1.098
12	0.460	0.636	3.001	3.777	1.405
13	0.383	0.441	3.322	2.605	0.810
14	0.370	0.554	5.480	3.495	0.985
15	0.396	0.385	4.412	3.866	0.733
16	0.382	0.444	3.379	2.719	0.816

density difference (EDD) plots are also useful for assessing the nature of the excitation and are given for all species in Figure 3.9.

The least amount of transferred charge (q^{CT}) and the CT distance (d^{CT}) correspond to the heads of the family, i.e., (**1**) and (**2**) as well as the six-membered analogue of (**2**), i.e., (**6**). The order for the least amount of CT dipole moment is also the same (Table 3.6). On the other hand, the five membered rings (**3**-**5**) have the highest values for these indices (the BF_2 linked GFP chromophore (**8**) with a six-membered ring also has significant values for these indices). EDD plots also confirm this finding as the density difference between the GS and ES is delocalized over the molecules (**3**-**5**) compared to the rest of the systems where the EDD is only distributed on the upper part of them (excluding the BF_2 unit and nitrogens attached to them) (see Figure 3.9).

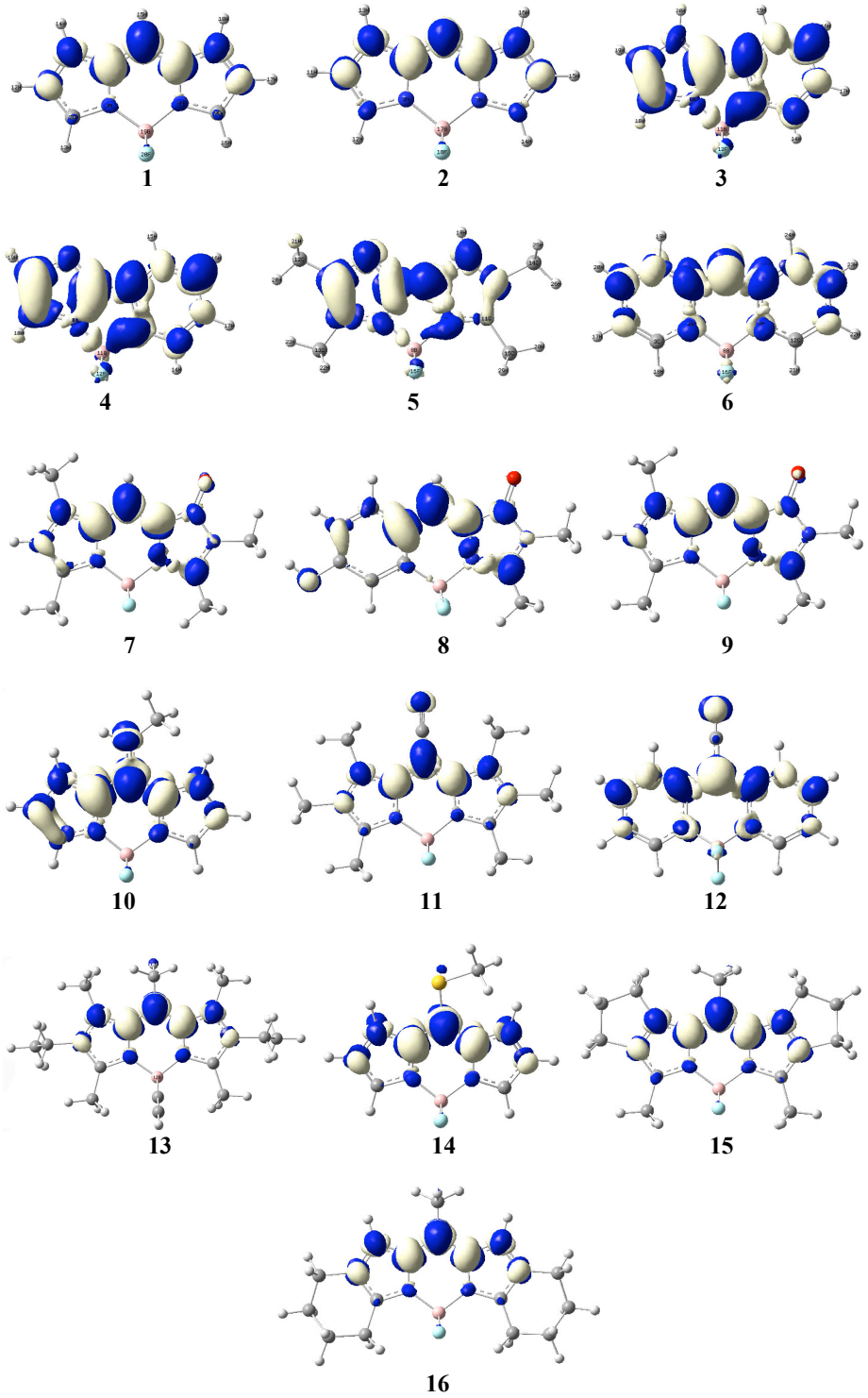

FIGURE 3.9: Electron density difference (EDD) between the excited state and ground state with isovalue of 0.002 a.u. computed at the CAM-B3LYP/cc-pVTZ level of theory. White and blue regions correspond to density increase and decrease, respectively, upon electron excitation.

Participation of the functional groups in the transitions is also evident, for example, see compound (**8**) that shows values of 0.437 e, 1.594 Å and 3.343 D for q^{CT}, d^{CT} and μ^{CT}, respectively. The phenomenon can be observed to some extent in other substituted species such as (**7**), (**9**), (**10**), and (**12**).

From the CT indices, although CT is somewhat significant in compounds (**3**)-(**5**), it is most likely not large enough to be solely responsible for the problems of TD-DFT inaccurately reproducing the the absolute vertical excitation energies for these systems nor does it explain problems for the other compounds where the CT indices have lower values. Importantly, compounds (**1**) and (**2**), for which TD-DFT also exhibits large deviations from experiment, show negligible CT characteristics. This agrees with the seminal works of Tozer [342], Dreuw and Head-Gordon [343] that CT (in most cases) is reflected in an underestimations of the TD-DFT excitation energies (rather than the overestimation observed here). We will discuss the reasons behind the TD-DFT failures for these compounds at the end of the next section where CI vectors from CASSCF computations are considered.

3.3.4 Benchmarking Ab initio and MRSCF Methods

All ab initio, including MRSCF, results using both cc-pVDZ and cc-pVTZ basis sets are depicted in Table 3.7 along with the corresponding statistical analyses. First of all, enlarging the basis set from cc-pVDZ to cc-pVTZ shifts the energy less than 0.1 eV (red shift) except 0.204 eV for LCC2* of (**5**)) for all methods (see also Table 3.8 for EOM-CCSD, CASSCF, and CASPT2 results for (**1**)-(**5**) with the cc-pVTZ basis set).

The size consistent configuration interaction with singles only (CIS) method shows the poorest agreement with experiment among all methods applied in this study (even poorer than TD-HF) with the largest Mean AE, Max AE, and SD (Table 3.7). On the other hand, although TD-HF exhibits a smaller Mean AE than CIS, its R^2 value is also (slightly) smaller than corresponding CIS results with values of 0.912 (0.915) for cc-pVDZ (cc-pVTZ) basis sets. However, the TD-HF and CIS results demonstrate that it is possible to get rough estimates of excitation energies for extremely large BODIPY systems, for which electron correlated methods are not applicable due to system size, by correcting the results of either TD-HF or CIS methods (see Table 3.4 for linear fitting coefficients of all methods).

TABLE 3.7: Vertical excitation energies using different ab initio methods and the cc-pVDZ (DZ) and the cc-pVTZ (TZ, except EOM-CCSD, SAC-CI, CASSCF[(a)], and CASPT2[(a)] methods) basis sets in the gas phase. Mean AE, Max AE, Min AE, SD and R^2 are also listed for each method. See Table 3.3 for the experimental values.

Method	TD-HF		CIS		CIS(D)		LCC2*		EOM-CCSD	SAC-CI	CASSCF	CASPT2
Basis	DZ	TZ	DZ	TZ	DZ	TZ	DZ	TZ	DZ	DZ	DZ	DZ
1	3.266	3.206	3.578	3.519	3.021	2.968	2.679	2.647	2.973	2.657	2.829	2.538
2	2.846	2.762	3.225	3.146	2.846	2.788	2.531	2.492	2.725	2.425	2.565	2.344
3	4.225	4.159	4.471	4.407	3.744	3.655	3.269	3.176	3.777	3.310	3.730	3.129
4	4.378	4.311	4.622	4.558	3.876	3.776	3.399	3.308	3.936	3.464	3.933	3.278
$\mathbf{5}_H$	4.898	4.898	5.255	5.167	4.713	4.564	4.283	4.125	4.751	4.331	4.933	4.104
5	4.650	4.550	4.902	4.806	4.294	4.136	3.791	3.587	4.393	3.764	4.704	3.726
6	4.398	4.355	4.619	4.577	3.607	3.555	3.149	3.074	3.747	3.177	3.904	2.821
7	3.535	3.472	3.823	3.762	3.090	3.004	2.653	2.623	3.206	2.424	3.510	–
8	4.033	3.979	4.293	4.242	3.555	3.458	3.011	3.011	3.697	2.959	4.313	3.142
9	3.184	3.099	3.526	3.446	2.921	2.822	2.468	2.408	3.029	2.299	3.277	2.479
10	3.998	3.922	4.232	4.160	3.537	3.440	3.058	2.953	3.579	2.967	3.627	3.055
11	2.733	2.682	3.072	3.023	2.640	2.579	2.242	2.187	2.626	2.015	2.998	1.957
12	4.047	3.990	4.250	4.193	3.254	3.181	2.816	2.726	3.395	2.700	3.485	2.693
13	3.083	3.043	3.380	3.343	2.783	2.735	2.278	2.226	2.815	1.966	3.647	–
14	3.328	3.261	3.614	3.548	2.996	2.921	2.631	2.560	3.002	2.342	2.924	2.448
15	3.153	3.110	3.447	3.407	2.825	2.773	2.339	2.294	2.846	2.043	2.887	–
16	3.015	2.967	3.314	3.269	2.742	2.692	2.216	2.187	2.746	1.932	3.457	–
Mean AE	0.839	0.780	1.124	1.061	0.500	0.431	0.148	0.145	0.542	0.187	0.747	0.161
Mean AE[(b)]	0.879	0.820	1.167	1.104	0.513	0.434	0.109	0.100	0.561	0.154	0.778	0.100
Max AE	1.292	1.235	1.495	1.438	0.643	0.568	0.776	0.867	0.702	0.711	1.318	0.897
Min AE	0.594	0.510	0.963	0.894	0.371	0.323	0.010	0.010	0.403	0.004	0.313	0.014
SD[(b)]	0.886	0.830	1.152	1.090	0.509	0.428	0.135	0.119	0.558	0.206	0.831	0.126
$R^{2(b)}$	0.912	0.915	0.940	0.937	0.983	0.985	0.954	0.949	0.983	0.933	0.802	0.954

[(a)]For details of the computations see methods section.
[(b)]Determined excluding compound (**4**).

TABLE 3.8: EOM-CCSD, CASSCF, and CASPT2 vertical transition energies for the first 5 structures using cc-pVTZ basis set in the gas phase.

Species	EOM-CCSD	CASSCF	CASPT2
1	2.944	2.829	2.450
2	2.686	2.565	2.252
3	3.714	3.699	3.208
4	3.869	3.933	3.352
$\mathbf{5}_H$	4.636	4.933	4.138

Applying the perturbative doubles (D) correction significantly improves the CIS results where for cc-pVDZ (cc-pVTZ), the mean AE (in eV) decreases from 1.167 (1.104) to 0.513 (0.434), the SD from 1.152 (1.090) to 0.509 (0.428) and also R^2 has the largest value among all the wavefunction-based (and TD-DFT) methods. The smallest computed shift (in eV) toward the red region as compared to the experimental measurements is found for compound (**2**), 0.379 (0.368), and the most for compounds (**12**) and (**6**), 0.996 (1.012) and 1.012 (1.022), respectively, using cc-pVDZ (cc-pVTZ) basis sets (Table 3.7). These results are in line with the work of Grimme and Neese in which the importance of perturbative doubles corrections

(D) is emphasized for developing the superior double hybrid methods [344].

By going from CIS(D) to the local coupled cluster second order LCC2* method, one can see another improvement in the agreement (due to an approximately 0.3-0.5 eV red shift for each compound) and the results are indeed closest to the highly accurate and sophisticated CASPT2 method; most likely due to cancellation of errors. Of course, the LCC2* approach is more applicable for larger substituted BODIPY systems. Even though R^2 slightly decreases for the LCC2* results compared to those from CIS(D) computations, the Mean AE, SD and Max AE decrease by (approximately) a factor of 3-5 (Table 3.7).

Coupled cluster EOM-CCSD computations were carried out using the cc-pVDZ basis set for all species and compared to all other methods. Surprisingly, a small shift from the results determined with the CIS(D)/cc-pVDZ method was found only for compounds (**1**) and (**2**) (0.048 and 0.121 eV red shift, respectively) and the EOM-CCSD/cc-pVDZ results were poorer than CIS(D)/cc-pVDZ for all other species (Table 3.7). Even though it is believed that this method is the more accurate version of the LCC2* method (and also SAC–CI) but except for R^2, the rest of the statistical indices suggest that EOM-CCSD method with the small cc-pVDZ basis is not a good choice for examining the excited states of BODIPY compounds. The SAC-CI method with the cc-pVDZ basis set was also computed for all systems and the results are presented in Table 3.7. The Mean AE decreases from 0.561 eV for the EOM-CCSD method to 0.154 eV with SAC-CI; SD decreases from 0.558 eV to 0.205 eV and R^2 slightly decreases from 0.983 to 0.933. Overall, the LCC2* and SAC-CI methods seem to be very good choices for studying excited state properties of the BODIPY systems.

In order to better understand the effect of electron correlation and also the convergence of the coupled cluster methods, a series of CCS, CC2, LR-CCSD, CCSDR(T), and CCSDR(3) computations were undertaken for the smallest BODIPYs, i.e., (**1**) to ($\mathbf{5}_H$), see Table 3.9. There is a clear trend in the convergence going from CCS to CCSDR(T). However, the trend is broken when going to CCSDR(3); these results highlight the extreme sensitivity of the vertical excitation energies to the differences in electron correlation between the ground and excited states. The canonical CC2 results reported in Table 3.9 are different than their corresponding local LCC2* results reported in Table 3.7 and strongly suggest that the excellent performance of LCC2* is due to the cancellation of errors.

TABLE 3.9: Computed coupled cluster vertical excitation energies (in eV) for the compounds (**1**)–(**5**$_H$) using the cc-pVDZ basis set. Deviations from experiment (CASPT2 for compounds (**2**)–(**5**$_H$)) are also given in parentheses.

Species	CCS	CC2	CCSD	CCSDR(T)	CCSDR(3)
(**1**)	3.578 (+1.118)	3.017 (+0.557)	2.973 (+0.513)	2.380 (–0.080)	2.895 (+0.435)
(**2**)	3.225 (+0.881)	2.800 (+0.456)	2.725 (+0.381)	2.074 (–0.270)	2.658 (+0.314)
(**3**)	4.471 (+1.212)	3.586 (+0.327)	3.777 (+0.527)	3.155 (-0.095)	3.624 (+0.495)
(**4**)	4.621 (+1.343)	3.713 (+0.435)	3.936 (+0.660)	3.297 (+0.019)	3.770 (+0.492)
(**5**$_H$)	5.255 (+1.117)	4.609 (+0.471)	4.751 (+0.613)	4.176 (+0.038)	4.628 (+0.390)

Multi-reference CASSCF and CASPT2 computations are also undertaken for all compounds using the cc-pVDZ basis set; CASPT2 computations are not carried out for compounds (**7**), (**13**), (**15**), and (**16**) that represent some of the largest molecules in the set. The related cc-pVTZ data for compounds (**1**)-(**5**$_H$) can be found in the Table 3.8. In most cases, the CASSCF vertical excitation energies are worse than CIS(D) and EOM-CCSD data. The discrepancies can be readily related to the lack of dynamic electron correlation in CASSCF and also the fact that we weren't able to include all the π electrons and the nitrogen lone pairs in the active space for the larger systems (For details of the CASSCF computations see the theoretical methods section). Expectedly, CASPT2 is found to be the most reliable method as the Mean AE (SD) slightly improves from 0.109 eV (0.135 eV) for the LCC2* method to 0.100 eV (0.126 eV) for the CASPT2 method both with cc-pVDZ basis set. There are some examples of applying CASSCF and/or CASPT2 methods for studying BODIPYs in the literature[42, 345, 346] but they have focussed only on a small number of examples. For instance, Briggs *et al.* have reported a value of 2.62 eV for the vertical excitation energy of the BODIPY parent molecule (**1**) at the CASPT2/6-31G* level of theory [345]. Valiev *et al.* have used the extended multi-configuration quasi-degenerate second order of perturbation theory (XMCQDPT2) and CC2 methods to examine a series of 5 BODIPYs [347]. The differences for their CC2 energies (overestimated by 0.42–0.59 eV) are in keeping with the present CC2 results, see Table 3.9; interestingly, they attribute this difference due to substantial contributions of double excitations to the excited states (> 10%).

3.3.5 Conjugated BODIPYs and aza-BODIPYs

In order to expand our study to larger conjugated molecules and also to find out the impact of enlarging the conjugation length on the accuracies of the LCC2* and TD-DFT methods, four extended BODIPYs (**I**–**IV**) and four aza-BODIPYs (**V**–**VIII**) were considered (Figure 3.10).

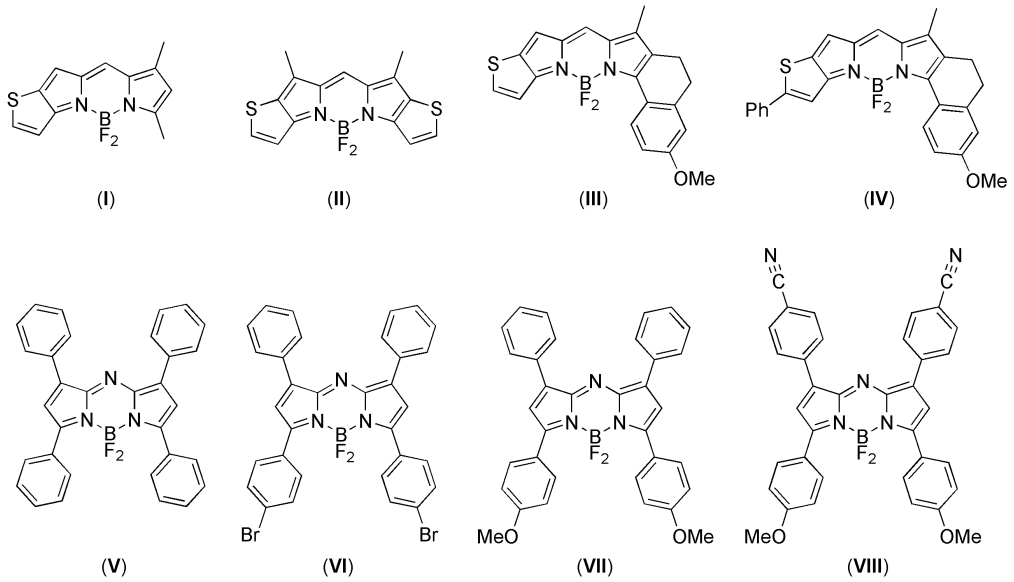

FIGURE 3.10: Conjugated BODIPYs (**I**–**IV**) and aza-BODIPYs (**V**–**VIII**) studied in this work.

Similar to our previous approach they were first optimized with the PBE0/cc-pVTZ functional in the gas phase and then their vertical excitation energies were determined by the LCC2*/cc-pVDZ method as well as PBE0, CAM–B3LYP, and LC–ωPBE functionals using the cc-pVTZ basis set, see Table 3.10. As can be seen from Table 8, the error for the TD-DFT functionals is 0.273–0.537 eV and it is greater ca. 0.1–0.2 eV for the BODIPYs compared to the aza-BODIPYs. The results determined using the PBE0 functional show the lowest absolute deviations from the experimental values for all the BODIPYs and aza-BODIPYs considered herein except (**V**) and (**VI**); however, the AE still exceeds ca. 0.3 eV. On the other hand, The LCC2* method shows relatively small (absolute) errors for the BODIPYs, i.e., $\leq$ 0.113 eV for the uncorrected values, but it increases for the aza-BODIPYs up to the 0.223 eV possibly because of enlarging the conjugation length and decreasing of the HOMO–LUMO gap. The LC–ωPBE and LCC2* corrected values are also depicted in Table 3.10; this functional is

TABLE 3.10: Computed vertical excitation energies (in eV) for the extended BODIPYs (**I**–**IV**) and aza-BODIPYs (**V**–**VIII**). Deviation from experiment is shown in parenthesis. For the LC-ωPBE density functional and the LCC2* method the corrected values (corr.) based on the correlation shown in Table 3.4 are also given.

Species	Exp.	PBE0	CAM–B3LYP	LC-ωPBE	LCC2*	LC-ωPBE$^{(corr)}$	LCC2*$^{(corr)}$
I	[348]2.331	2.801 (+0.470)	2.864 (+0.533)	2.824 (+0.493)	2.401 (+0.070)	2.270 (–0.061)	2.354 (+0.023)
II	[349]2.206	2.572 (+0.366)	2.743 (+0.537)	2.691 (+0.485)	2.253 (+0.047)	2.149 (–0.057)	2.213 (+0.007)
III	[349]2.049	2.521 (+0.472)	2.547 (+0.498)	2.544 (+0.495)	1.999 (–0.050)	2.014 (–0.035)	1.970 (–0.079)
IV	[349]1.922	2.327 (+0.405)	2.376 (+0.454)	2.392 (+0.470)	1.809 (–0.113)	1.875 (–0.047)	1.789 (–0.133)
V	[350, 351]1.907	2.234 (0.327)	2.240 (0.333)	2.190 (0.283)	1.825 (–0.082)	1.691 (–0.216)	1.804 (–0.103)
VI	[352]1.884	2.170 (0.286)	2.199 (+0.315)	2.159 (+0.275)	1.737 (–0.147)	1.662 (–0.222)	1.721 (–0.163)
VII	[39, 350, 351]1.802	2.106 (+0.304)	2.143 (+0.341)	2.107 (–0.305)	1.608 (–0.194)	1.615 (–0.187)	1.597 (–0.205)
VIII	[353]1.732	2.005 (+0.273)	2.063 (+0.331)	2.036 (+0.304)	1.509 (–0.223)	1.550 (–0.182)	1.503 (–0.229)

used because it showed a higher correlation with experiment than the PBE0 functional. Empirical corrections seem to overcome some of the TD-DFT overestimations and therefore it is recommended for both BODIPY and aza-BODIPY molecules. However, the LCC2* values do not show a major improvement upon empirical correction except for (**I**) and (**II**) and hence correction is not required, nor recommended, for this method.

3.3.6 Multi-reference versus Double Transitions

In order to test the reliability of single reference electron correlated/uncorrelated methods applied in this study, three different diagnostic tests, i.e., T_1, %TAE[T], and M, are computed for all systems and the results are depicted in Table 3.11. These three diagnostic tests provide insight into the multi-reference character of the ground electronic state and, hence, possible difficulties in using the DFT ground state as a reference for TD-DFT. Both T_1 and %TAE[T] tests suggest that the BODIPY molecules can be treated with coupled cluster methods. In other words, treating BODIPY systems with these methods should lead to no significant error in the results due to the use of a single reference method. On the contrary, based on the M diagnostic test, see Eq. 3.2, all the systems exhibit a significant amount of multi-reference character since all have M values larger than 0.04 electron. To further investigate this matter, CASSCF CI vectors (> 0.05 for at least one state) of all the GSs and ESs of the structures studied in this work were examined. For the parent BODIPY, an active space comprising of six B_1 and five A_2 symmetry orbitals was considered (12 electrons in 11 orbitals). As can be seen from Appendix A for the ground state of compound (**1**), the two dominant configurations $|\phi_1\rangle = |(\text{core})^n\ (5B_1)^2\ (2A_2)^2\ (6B_1)^2\ (7B_1)^2\ (3A_2)^2\ (4A_2)^2\ (8B_1)^0\rangle$ and $|\phi_2\rangle =$

TABLE 3.11: Computed T_1, %TAE, and M diagnostic tests using the cc-pVDZ basis set. Square of the dominant configuration coefficients for the ground states ($|CI|^2_{S0}$) and first excited states ($|CI|^2_{S1}$) are also listed using the state averaged CASSCF method and the cc-pVDZ basis set.

Species	T_1	%TAE	M	$\|CI\|^2_{S0}$	$\|CI\|^2_{S1}$
1	0.014	1.47	0.114	0.812	0.592
2	0.015	1.43	0.147	0.792	0.721
3	0.013	1.41	0.100	0.824	0.744
4	0.013	1.31	0.100	0.828	0.743
$\mathbf{5}_H$	0.013	1.07	0.079	0.872	0.796
5	0.013	1.04	0.079	0.872	0.805
6	0.015	1.34	0.087	0.826	0.726
7	0.015	1.14	0.097	0.865	0.806
8	0.015	1.20	0.106	0.847	0.823
9	0.015	1.10	0.139	0.800	0.762
10	0.014	1.27	0.080	0.877	0.808
11	0.013	1.33	0.106	0.852	0.816
12	0.015	1.45	0.063	0.856	0.777
13	0.013	1.38	0.054	0.929	0.916
14	0.014	1.42	0.110	0.825	0.753
15	0.013	1.33	0.112	0.837	0.766
16	0.012	1.32	0.091	0.871	0.826

$|(\text{core})^n\ (5B_1)^2\ (2A_2)^2\ (6B_1)^2\ (7B_1)^2\ (3A_2)^2\ (4A_2)^0\ (8B_1)^2\rangle$ contribute 81.3% and 1.6% to the wavefunction (Table 3.11). The rest of the contributions corresponds to other configurations resulting from single or double electron excitations within the active space. On the other hand, the S_1 ES of this molecule has two major configurations $|\phi_1\rangle = |(\text{core})^n\ (5B_1)^2\ (2A_2)^2\ (6B_1)^2\ (7B_1)^2\ (3A_2)^2\ (4A_2)^1\ (8B_1)^1\rangle$ and $|\phi_2\rangle = |(\text{core})^n\ (5B_1)^2\ (2A_2)^2\ (6B_1)^2\ (7B_1)^2\ (3A_2)^1\ (4A_2)^2\ (8B_1)^1\rangle$, which contribute 59.2% and 13.7%, respectively. However, configurations corresponding to double excitations have a contributions of 7.6%.

The same active space for compound (**2**), i.e., head of the aza-BODIPY molecules, yields 79.2% of GS contribution to the S_0 wavefunction which is slightly smaller than compound (**1**). However, for the S_1 ES one can see 72.1% single electron transition from HOMO to LUMO, 3.5% double transition comprising of one HOMO to LUMO and one HOMO-2 to LUMO, and 1.6% double transitions from HOMO-1 to LUMO and from HOMO to LUMO+3. Compounds (**3**), (**4**), (**6**), (**9**), (**12**), (**14**), (**15**) and (**8**) have somewhat similar weightings for the dominant CI eigenvector for both their S_0 and S_1 states, i.e. ∼83% and ∼75%, respectively. Compounds ($\mathbf{5}_H$), (**5**), (**7**), (**10**), (**11**), and (**16**) form another group which show slightly higher values for

those eigenvectors; about 87% and 81%, respectively. In complete contrast to compounds (**1**) and (**2**), which showed the smallest values, compound (**13**) exhibits the largest weightings for the dominant CI eigenvector; 92.9% and 91.2%, respectively. As discussed above, only one index, i.e., M index, illustrates a MR character for BODIPYs and two other indices show a single-reference character for them. Therefore, one cannot attribute the TD-DFT problem solely to the MR nature of these dyes. On the other hand, the CI eigenvectors are suggestive that double excitations play an important role in the BODIPY family and hence contribute to the systematic deviation of TD-DFT results from the experimental measurements. The importance of double excitations for BODIPYs has been reported previously [347] and is also in line with previous reports for cyanine dyes in which the importance of double corrections are emphasized [253, 344].

3.4 Conclusions

From a quantitative point of view, all TD-DFT functionals overestimate the experimental absorption maxima by more than 0.3 eV for all 17 species that are investigated in this work. Therefore, the use of TD-DFT is not recommended unless the results are corrected empirically in an appropriate manner (see Table 3.4). Pure BLYP and PBE functionals show promising Mean AEs, but, since their R^2 values are very low (0.797 and 0.793, respectively), their use is not recommended. Based on R^2 values (> 0.96), all the range separated hybrid functionals appear moderately superior to the hybrid GGA functionals ($R^2 > 0.9$); therefore, most can be used if corrected appropriately. Similar TD-DFT results for BODIPYs and aza-BODIPYs have been reported previously.[52, 281]

It was found that from both accuracy and efficiency viewpoints, the LCC2* method with the cc-pVTZ or even the cc-pVDZ basis set seems to be a very good and reliable alternative candidate to either TD-DFT or high level (computationally expensive or even intractable) multi-reference approaches for determining vertical excitation energies of the BODIPY systems. The SAC-CI method with the cc-pVDZ basis set can be seen as the next best alternative to LCC2* as it gives a Mean AE of 0.154 eV, which is almost as accurate as the CASPT2

method with the same basis set. However, compared to CASPT2, LCC2* and SAC-CI methods have the advantage of applicability for large substituted BODIPY systems. Therefore, the author highly recommend using these methods for the study of BODIPYs.

Vertical excitation energies of the extended BODIPYs and aza-BODIPYs were also computed using some of our best methods, i.e., LCC2*, PBE0, CAM–B3LYP, and LC-ωPBE methods. Absolute errors up to +0.495 eV were found for the LC–ωPBE method and the maximum error was reduced to +0.222 eV by empirical correction. Also, the LCC2* method showed a very good performance for both BODIPYs (AE $\leq$ 0.113 eV) and aza-BODIPYs (AE $\leq$ 0.223 eV). Importantly, empirical correction is not required, nor recommended, for this method.

The obtained CT parameters and EDD plots demonstrate that compounds (**3**)–(**5**) exhibit CT characteristics; however, not all the studied species exhibit significant CT, see Table 3.6. The lack of significant CT is also suggested because there are not significant improvements in absolute performance when moving from GGA and HGGA functionals to range-separated ones. However, this may have been anticipated as problems with CT normally manifest themselves in an underestimation of the TD-DFT excitation energies [342, 343], while in the present work the use of GGA and HGGA functionals leads to a significant overestimation of the vertical excitation energies. Therefore, the problems with the predictions of TD-DFT, i.e., Mean AE $\gtrsim$ 0.3–0.6 eV, can't be attributed to the CT issue.

From the CASSCF computations, it was found that the major problem in these compounds, and, in particular, for the heads of the family, i.e. compounds (**1**) and (**2**), arises because of the multi-reference nature of the transitions. For instance, the dominant CSF for the first excited state corresponding to HOMO to LUMO excitation contributed 59.2% for compound (**1**) and 72.1% for compound (**2**). Similarly, the contributions belonging to double excitations, which in some cases make moderate 5–10% contributions (see Table A.1, Appendix A), can't be captured by TD-DFT.

This study hopes to encourage future complementary ab initio and TD-DFT benchmarks on these problematic chromophores. Importantly, the results presented and BODIPYs in general can serve as excellent test cases for the development of new functionals and methods for TD-DFT. However, until then, useful empirical corrections can be employed for existing techniques in order to make accurate predictions of vertical excitation energies for new BODIPYs.

Chapter 4

A Local CC2 and TDA-DFT Double Hybrid Study on BODIPY/Aza-BODIPY Dimers As Heavy Atom Free Triplet Photosensitizers for Photodynamic Therapy Applications

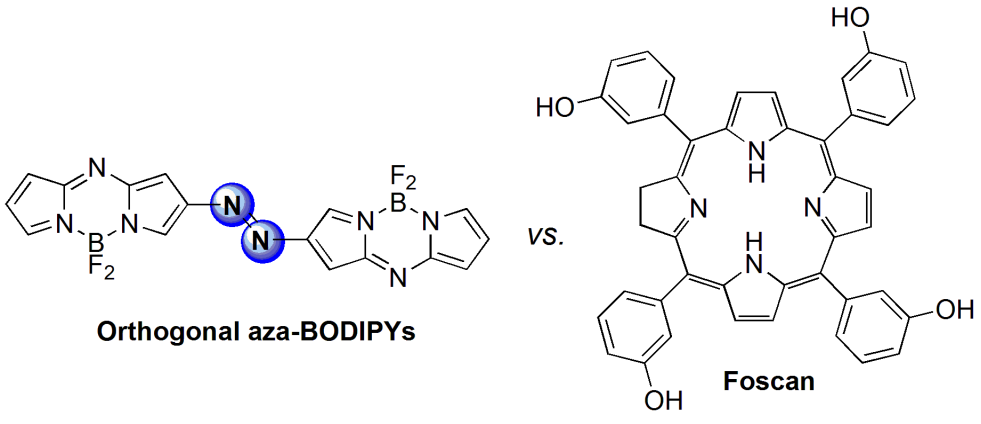

4.1 BODIPY and Aza-BODIPY Dimers in Photodynamic Therapy

It is been shown that appropriate substitution of the BODIPY and Aza-BODIPY molecules makes these molecules ideal candidates for PDT application [8, 9, 38, 354]. In PDT treatment, the PS is locally injected to the target area (cancer tissues) and laser beam is delivered to the area through endoscopes and fiber optic catheters. After shining the light, carcinogenic singlet oxygen ($^1O_2$) is generated, from already present triplet oxygen ($^3O_2$) molecules inside cancer tissues, by an energy transfer from the excited triplet photosensitizer (^{3}PS) to the $^3O_2$. As stated in the Introduction, a major issue with in vivo use of heavy atom substituted BODIPYs, [20, 39–41] is their relatively large dark toxicities due to use of heavy metal atom. Akkaya and his coworkers showed that BODIPY monomers linked in the [1,1] and [1,4] positions possess high singlet oxygen generation quantum yields of 0.51 and 0.46, respectively [42]. However they found that the absorption ranges of these PSs are outside the therapeutic window (i.e., 650–900 nm). Extending the conjugation length in these dyes was tested as a possible remedy but was proved to be not efficient [43].

Through a detailed benchmark study (see Chapter 3) [355] we showed that all time-dependent density functional theory (TD-DFT) methods systematically overestimate excitation energies of BODIPYs and Aza-BODIPY monomers. In search of the reason of this large error, we found that these systems suffer from significant amounts of double electron excitations which in principle single electron based methods such as TD-DFTs are not able to capture them [355]. Through systematic increase of the level of excitation in a series of coupled cluster calculations and also by careful examination of the configuration interaction vectors obtained from multi-reference computations we showed that these molecules are highly electron correlated and one needs an appropriate level of electron correlation to tackle them (Chapter 3) [355]. Our comprehensive benchmark of ab initio methods on the other hand showed that local coupled cluster with singles and approximate doubles (LCC2) method is a very good compromise between accuracy and efficiency and can provide excitation energies with mean absolute errors (Mean AE) of $\sim$ 0.1 eV [355]. Jacquemin and his coworkers on the other hand, have shown that combining scaled opposite spin configuration interaction singles and perturbative doubles (SOS-CIS(D)) with the TD-DFT polarizable continuum model (PCM) reduces the

Mean AE to 0.197 eV [281]. In another study they showed that use of wave function based Bethe-Salpeter approach reduces the Mean AE to 0.18 eV for these systems [356].

To test the performance of TD-DFT and ab initio methods on BODIPY and Aza-BODIPY dimers, a benchmark study is performed on a test set comprised of 11 different dimeric species. A special attention is paid to the double hybrid functionals (DH-DFs) in which a fraction of perturbative doubles correction (D) is added to them by definition that could account for some of the needed electron correlation in these compounds. Next, a series of theoretically designed BODIPY/Aza-BODIPY dimers are constructed by connecting two monomer molecules through ethylene, benzyl, acetyl and azo bridges. Previous experimental studies have shown that linking two BODIPY monomers through different heteroatoms leads to vastly different photophysical properties (e.g., see Refs. 357–359). The possible application of these dyes in PDT were also studied through computing their spin-orbit coupling matrix elements (SOCs). Finally, based on our findings on different linked dimers, a series of 36 different azo-bridged BODIPY dimers, depending on the position of the linkage unit, were examined and some of them are introduced as PSs for PDT application.

4.2 Computational Methods

Geometry optimizations were performed using density functional theory (DFT) with the meta hybrid M06-2X [243] functional and the cc-pVDZ [289, 290] basis set in the gas phase. Since the impact of basis set size is moderate for geometry optimizations with density functional theory methods, [360] cc-pVDZ is a suitable choice for the purpose of this work. "Tight" convergence criteria, i.e., maximum force $= 1.5 \times 10^{-5}$ a.u., RMS force $= 1.0 \times 10^{-5}$ a.u., max displacement $= 6.0 \times 10^{-5}$, and RMS displacement $= 4.0 \times 10^{-5}$ were applied for all ground state (S_0) and excited state (S_1 and T_1) optimizations. An "Ultrafine" grid, i.e., a pruned grid of 99 radial shells and 590 angular points per shell, was used for numerical integration as results utilizing the M06-2X functional are shown to be strongly grid dependent [361, 362]. Harmonic vibrational frequencies were computed at the same level of theory for the ground and excited states in order to characterize the stationary points as true minima, representing equilibrium structures on the potential energy surfaces. Symmetry was utilized whenever possible to expedite calculations especially for multi-reference methods. 15 different

density functionals were used for computing vertical excitation energies of three different singlet excited states. Pure BLYP [236–238] and PBE [286, 287] functionals as well as the revised form of the PBE functional (revPBE) [363] with no HF exchange along with their corresponding three parameter B3LYP [364] and one parameter PBE0 [288] and revPBE0 [288] hybrid functionals with 20% and 25% HF exchange, respectively, were utilized. It is been shown by benchmark study of Truhlar and his coworkers that using revPBE functional leads to more reliable energetic results than the PBE itself [365]. Also, from range-separated hybrid functionals LC-BLYP [294] and CAM-B3LYP [261] functionals were chosen.

The idea of mixing MP2 electron correlation with non-local BLYP in DFT and building double hybrid density functionals was first introduced by Truhlar and coworkers in 2003 [366]. However, the first practical DH-DF was proposed three years later by Grimme which was a B88 two parameter functional with HF exchange of $a_x = 0.53$ and MP2 correlation of $a_c = 0.27$ mixed with LYP correlation named B2-PLYP (Eq. 4.1) [367].

$$E_{XC} = a_x E_x^{HF} + (1 - a_x) E_x^{GGA} + (1 - a_c) E_c^{GGA} + a_c E_c^{MP2} \tag{4.1}$$

In the excited state DH-DF, the excitation energy ω which is calculated from the singles based TD(A)-DFT computations is added with a fraction (a_c) of double corrections (D) to the CIS method (Eq. 4.2).

$$\omega_{TD(A)-B2PLYP} = \omega + a_c \Delta_{(D)} \tag{4.2}$$

Grimme also reported the mPW2-PLYP [368] functional which was shown to yield good energetic results in the case of weak interactions. Since then many more DH-DFs are being added to this family based on different amounts of HF exchange (a_x), MP2 correlation (a_c) and the type of the GGA exchange correlation functional employed (Eq. 4.1). Notably, Martin [369] re-optimized the B2-PLYP functional for general purpose (B2GP-PLYP) [369], kinetics (B2K-PLYP) [369], and thermochemistry (B2T-PLYP)[369] applications. Also Sancho reported a DH-DF with $a_x = 0.602$ and $a_c = 0.273$ for π-conjugated systems (B2π-PLYP) [370]. Several benchmark studies have proven the superiority of these DH-DFs over their hybrid, range separate hybrid and meta-hybrid ancestors [361, 371]. Herein, we employ two different classes of DH-DFs based on the type of the GGA exchange correlation functional used; one group based on the BLYP functional, i.e., B2-PLYP, B2GP-PLYP, B2π-PLYP, and mPW2-PLYP functionals, and another group based on the PBE exchange correlation, namely

PBE0-2 [372] and PBE0-DH [373], developed by Mao and Adamo, respectively. For all 15 DFT methods employed in this study, Resolution of Identity with chain of sphere algorithm (RIJCOSX) [374] was used for approximating Coulomb and exchange type integrals in the SCF cycles. This approach can expedite calculations up to two orders of magnitude without significantly losing accuracy when auxiliary basis sets are used [375, 376]. The correlation fitting basis set, cc-pVDZ/C, developed by Hättig *et al.* was used for all the calculations [377], unless noted otherwise. All the TD-DFT computations were performed with Tamm-Dancoff and also frozen core approximations. Grimme and Neese have previously shown that excitation energies computed using the Tamm-Dancoff approximation are very similar to the full time-dependent calculations and in the cases of purely valence excitations and even difficult cases such as transition metals and large conjugated systems they are superior to the full TD results [344]. They also showed that their basis set dependences are very similar and inseparable. It has been shown by Grimme *et al.* that DH-DF results are strongly basis set dependent and one should use a large basis set specially due to the MP2 perturbation part of the calculation [361]. Therefore the effect of enlarging the basis set from cc-pVXZ [289] to aug-cc-pVXZ (X = D and T) [290, 311] on the excitation energy of compound (**I**) was investigated and the results are provided in Table 4.1. The effect of using density fitting basis sets, i.e., def2-TZVPP and def2-QZVPP [379], were investigated and compared and contrasted to the former Dunning correlation consistent ones. The results of the def2-QZVP basis set are shown to fall within 1-2 kcal/mol of the complete basis set limit [361, 380, 381]. As can be seen from Table 4.1, adding diffuse and polarization functions to the cc-pVDZ basis set to form aug-cc-pVTZ only lowers the S_1 excitation energy by 0.079 eV. Going from the cc-pVDZ basis set to def2-QZVPP lowers the energy only by 0.074 eV. Overall, increasing the size of the basis set by adding more polarization and diffuse functions slightly lowers the excitation energy but has no major impact on the accuracy of our results. Hence, cc-pVDZ seems to be a suitable and cost efficient basis set and was utilized for our computations throughout this work unless otherwise stated.

0-0 transition energies were also determined using the M06-2X functional, recommended by Jacquemin *et al.* [5], as $E^{0-0} = E^{adia} + \Delta E^{ZPE}$ where E^{adia} is the energy difference between the optimized S_1 and S_0 states and the latter is the corresponding zero point energy difference of those two states. In order to predict reliability of using a single-reference based method,

TABLE 4.1: Computed B2-PLYP vertical excitation energies (in eV) using (aug)-cc-pVXZ (X = D, T), def2-TZVPP and def2-QZVPP basis sets for compound (**I**).[(a)] The same type of auxiliary basis set is utilized for each basis. Also provided are the dominant contributions where H = HOMO and L = LUMO.

	S_1	S_2	S_3
cc-pVDZ	2.937 H → L (0.961)	3.288 H-1 → L (0.838)	3.626 H-3 → L (0.539) H → L+1 (0.351)
aug-cc-pVDZ	2.860 H → L (0.957)	3.228 H-1 → L (0.847)	3.553 H-3 → L (0.504) H → L+1 (0.384)
cc-pVTZ	2.884 H → L (0.959)	3.233 H-1 → L (0.846)	3.555 H-3 → L (0.522) H → L+1 (0.366)
aug-cc-pVTZ	2.858 H → L (0.957)	3.220 H-1 → L (0.849)	3.538 H-3 → L (0.500) H → L+1 (0.388)
def2-TZVPP	2.872 H → L (0.959)	3.227 H-1 → L (0.847)	3.548 H-3 → L (0.515) H → L+1 (0.373)
def2-QZVPP	2.862 H → L (0.958)	3.218 H-1 → L (0.848)	3.535 H-3 → L (0.506) H → L+1 (0.382)

[(a)] The Experimental value for the first excited state of this compound is 2.868 eV [378].

the T_1 diagnostic test of Lee and Taylor, which is based on the norm of the vector of single-excitation amplitudes from CCSD in a closed shell system [319], was utilized. If the T_1 value is smaller than 0.02, the system is considered to be dominated by a single-reference but if it is larger than 0.02, the system is considered to have (most likely) multi-reference character. According to this diagnostic test, no multi-reference character was found for the ground state of the studied species in the benchmark test (i.e., $T_1 < 0.02$) (see Figure 6.1).

TD(A)-DFT results were compared and contrasted with electron correlated Laplace transformed density fitting local coupled-cluster singles and approximate doubles (LT-DF-LCC2, abbreviated as LCC2 in the text) [213, 306], Laplace transformed density fitting local algebraic diagrammatic construction second order (LT-DF-LADC(2), abbreviated as LADC(2) in the text) [382, 383], and symmetry adapted cluster/configuration interaction (SAC–CI)

[307] methods. The efficient direct algorithm was utilized for all the SAC–CI computations which corresponds to the conventional SAC–CI with NoUnlinkedSelection keywords (all other options set to default values). Multi-reference complete active space self-consistent field (CASSCF) [308] and complete active space second-order perturbation (CASPT2) [309] computations were accomplished for all systems (except CASPT2 for **X** and **XI**, see Figure 4.1). The CASPT2 computations utilized the internally contracted RS2C program [309]. The

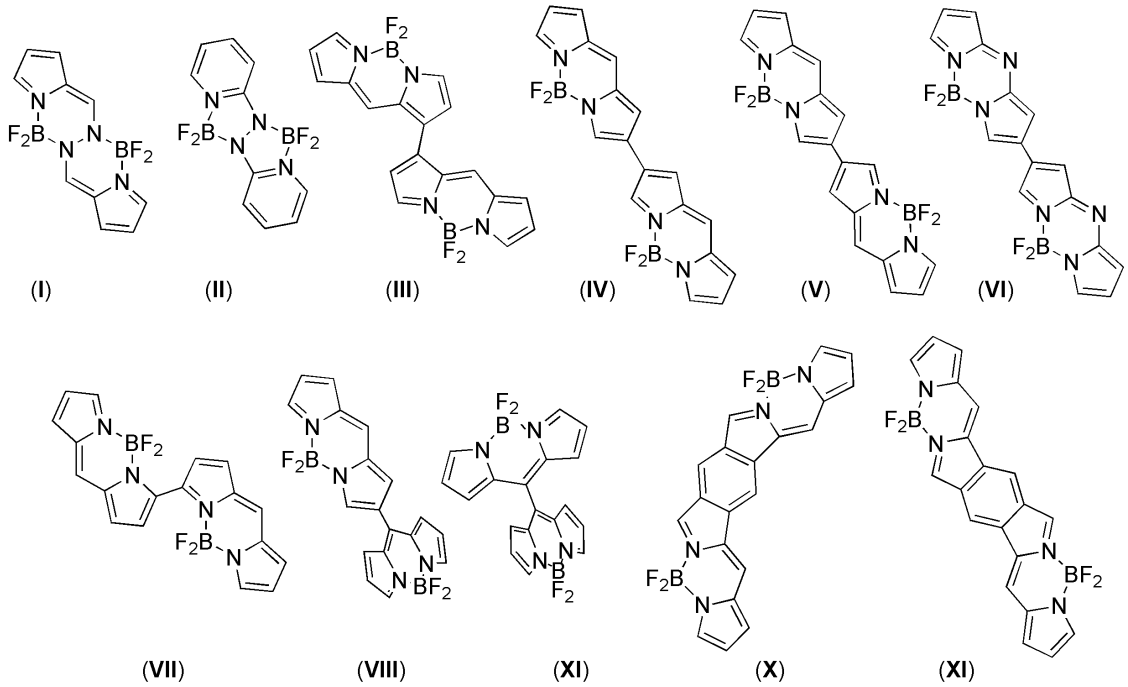

FIGURE 4.1: Structures of the benchmark set considered in this study.

CASSCF wave functions were constructed by using equal weights of the S_0 and S_1 states. The CASPT2 computations used an IPEA shift, which is a correction to the zeroth order Hamiltonian, of 0.3 [310].

According to the Fermi Golden rule [384, 385], the rate of non-radiative transition from any singlet excited state (S_n) to any triplet excited state (T_m) is expressed as

$$k_{\mathrm{ISC}} = \frac{2\pi}{\hbar} \langle \mathrm{S_n}|\hat{\mathrm{H}}_{\mathrm{SO}}|\mathrm{T_m}\rangle^2 \times \mathrm{FCWD} \tag{4.3}$$

where $\langle S_n|\hat{H}_{SO}|T_m\rangle$ are the spin-orbit coupling (SOC) integrals between pure spin states of S_n and T_n and FCWD is the Franck-Condon weighted density of states which is close to unity for a set of similar species. Determination of the ISC rate is extremely challenging for

large molecules as it requires accurate assignment of different deactivation channels [386]. Instead chemists usually rely on semi-quantitative approaches for such investigations [387]. Therefore, SOC matrix elements are computed as a representative of ISC rates for these systems (see Eq. 4.3). The SOCs were computed for three different excited singlet (S_n) and triplet (T_m) states using the T_1 optimized geometry and the CAM-B3LYP/cc-pVDZ//UM06-2X/cc-pVDZ density functional. The spin-orbit mean-field (MNF-SO) quadratic response approach was used for SOCs calculations which utilizes an effective one-electron operator in which the two electron terms are evaluated as a sum over all α and β spin orientations [388, 389]; For a comparison between different approaches for computing SOCs see Ref. 386 and references therein. Previous benchmark studies have demonstrated the accuracy and efficiency of this approach for transition metal complexes [388]. An error of less than 5% has been obtained for the one-electron MNF-SO method compared to the full Breit-Pauli (BP) SOC Hamiltonian approach (using CASSCF and MR-CI methods) in the case of light element (organic) compounds [390, 391] which are subject of the current study. For DFT computations of SOCs using these two approaches see Ref. 392 and references therein.

All the M06-2X ground and excited state geometry optimizations along with the SAC-CI computations were performed using the Gaussian 09 package [322]. LCC2, LADC(2), and MRSCF computations were accomplished using the 2010 and 2012 versions of MOLPRO [323, 393]. All the TDA-DFT computations were accomplished using the ORCA 3.0.2 package [394, 395]. All the SOC calculations were performed using the DALTON 2015.0 code [325].

4.3 Results and Discussion

For benchmarking purposes, a set of 11 different BODIPY/Aza-BODIPY based dimers are considered where the corresponding experimental data are available (Figure 4.1). Iso-electronic five and six membered fused bis BODIPYs (**I** and **II**) as well as BODIPY dimers (**III**–**V** and **VII**–**IX** and Aza-BODIPY, **VI**) in which BODIPY monomers are attached in different positions are considered in the test set. Benzene fused near IR (NIR) light emitting BODIPY dimers (**X** and **XI**) were also included as these types of chromophores are well known to be challenging due to their low highest occupied (HOMO) and lowest unoccupied (LUMO) molecular orbital gap (for the S_0 optimized geometries and singlet–triplet gaps see

Table 4.2). Compounds **I** and **II** are both isomers and isoelectronic, **IV** and **V** as well as **X**

TABLE 4.2: M06-2X/cc-pVDZ selected geometrical parameters for the S_0 ground state along with the HOMO–LUMO (ΔE_{H-L}) and singlet–triplet (ΔE_{S-T}, ΔE_{S-T}+ZPE, and ΔG_{S-T}) gaps (in eV) for all the studied species.

Species	$(C–C)_{bridge}$[a]	$(C–C–C–C)_{bridge}$	N–C	N–B	ΔE_{H-L}	ΔE_{S-T}	ΔE_{S-T}+ZPE	ΔG_{S-T}
I	1.384	24.3	1.381	1.539 (1.608)	5.451	2.312	2.197	2.035
II	1.406	36.2	1.355	1.559 (1.593)	6.122	2.685	2.567	2.364
III	1.455	40.8	1.384 (1.389)	1.568 (1.569)	4.421	1.607	1.536	1.421
IV	1.457	9.1 (9.5)	1.388 (1.389)	1.567 (1.571)	4.206	1.828	1.785	1.744
V	1.457	8.5	1.388 (1.389)	1.566 (1.571)	4.347	1.955	1.904	1.861
VI	1.456	5.0 (5.3)	1.396 (1.397)	1.567 (1.571)	3.806	1.352	1.317	1.252
VII	1.457	33.2	1.334–1.387	1.562 (1.574)	3.887	1.232	1.185	1.113
VIII	1.462	43.3 (44.3)	1.328–1.391	1.562–1.571	4.286	1.780	1.691	1.558
XI	1.485	65.1 (66.5)	1.388 (1.332)	1.565 (1.567)	4.420	1.680	1.637	1.601
X	1.393 (1.394)	179.27 (179.77)	1.313–1.401	1.548, 1.592	3.910	1.602	1.549	1.399
XI	1.391 (1.395)	179.72 (179.48)	1.315–1.397	1.548, 1.594	3.695	1.303	1.230	1.128

[a] $(N–N)_{bridge}$ in the case of the compounds (**I**) and (**II**).

and **XI** are *syn* and *anti* isomers, **VI** is the aza-substituted isomer of **IV** and **III**–**V**. Also, **VII**–**IX** are isomers which are different in the position of connection. As is shown in the next section, these structurally similar BODIPY dimers illustrate very different photophysical properties that could be challenging for benchmarking purposes.

4.3.1 Benchmark of Ab initio and TDA-DFT Excitation Energies

Two different pure DFT functionals, Perdew, Burke and Ernzerhof (PBE and revPBE) and Becke exchange and Lee, Yang and Parr correlation functional (BLYP), and their hybrid (PBE0, revPBE0 and B3LYP) and range separated hybrid (RSH: LC-BLYP and CAM-B3LYP) functionals along with their double hybrid counterparts (B2-PLYP, B2GP-PLYP, B2π-PLYP, mPW2-PLYP, PBE0-2 and PBE0-DH) were chosen for computing vertical excitation energies of all the chromophores considered in the test set (Table 4.3). Mean deviation (MD), mean absolute deviation (MAD), maximum-minimum deviation difference (Max-Min) and root-mean-square deviation (RMSD) of all methods are presented in Table 4.3. In close agreement with our previous findings on BODIPY monomers [355], the least MAD is found for the pure functionals and the highest for the RSH functionals (Table 4.3). The hybrid B3LYP functional is slightly better than PBE0 (ΔMAD = 0.069 eV) however their pure versions are almost identical from accuracy viewpoints. Also, the revised forms of the PBE functional give similar results to their PBE ancestors. The RSH LC-BLYP and CAM-B3LYP functionals with MADs of 0.823 eV and 0.772 eV provide the worst results. Inclusion of geometric relaxation of the ground and excited electronic states of BODIPY dimers in the 0-0

TABLE 4.3: Computed TDA-DFT and ab-initio vertical excitation energies (in eV) using the cc-pVDZ basis set in the gas phase. M06-2X 0-0 excitation energies (M06–2X$^{(0-0)}$) are also provided.

Method	**I**	**II**	**III**	**IV**	**V**	**VI**	**VII**	**VIII**	**IX**	**X**	**XI**	MD	MAD	Max-Min	RMSD
[(a)]Exp.	2.868	2.638	2.214	2.357	2.036	1.781	2.194	2.450	2.407	1.792	1.636				
BLYP	3.170	2.922	2.058	2.038	1.981	1.777	2.153	1.522	2.015	1.922	1.984	–0.076	0.269	0.924	0.364
B3LYP	3.490	3.488	2.592	2.421	2.459	2.186	2.538	2.130	2.422	2.434	2.332	0.374	0.433	0.786	0.497
LC-BLYP	3.773	4.155	2.999	2.826	2.916	2.556	2.616	3.188	3.149	2.685	2.564	0.823	0.823	1.095	0.867
CAM-B3LYP	3.740	4.041	2.989	2.773	2.884	2.513	2.618	3.148	2.980	2.689	2.525	0.772	0.772	0.957	0.813
B2LYP	3.407	3.503	2.772	2.437	2.551	2.226	2.416	2.510	2.669	2.432	2.248	0.436	0.436	0.805	0.498
B2-PLYP	2.937	2.702	2.508	2.070	2.173	1.924	2.184	1.874	2.299	2.128	1.951	0.034	0.213	0.566	0.265
B2GP-PLYP	2.958	2.800	2.566	2.127	2.247	2.004	2.192	2.546	2.372	2.126	1.967	0.139	0.188	0.350	0.221
B2π-PLYP	3.104	3.019	2.630	2.218	2.335	2.064	2.264	2.454	2.465	2.224	2.055	0.224	0.249	0.428	0.291
mPW2-PLYP	3.053	2.909	2.584	2.168	2.277	2.010	2.240	2.079	2.400	2.202	2.024	0.143	0.246	0.403	0.278
PBE	3.185	2.924	2.068	2.052	1.995	1.786	2.165	1.533	2.022	1.934	1.998	–0.065	0.267	0.912	0.362
revPBE	3.190	2.933	2.072	2.055	2.000	1.788	2.167	1.540	2.028	1.939	2.001	0.060	0.267	0.903	0.361
PBE0	3.566	3.621	2.703	2.513	2.572	2.266	2.574	2.294	2.524	2.569	2.386	0.474	0.502	0.866	0.571
revPBE0	3.569	3.629	2.705	2.516	2.575	2.269	2.574	2.300	2.528	2.573	2.387	0.477	0.505	0.870	0.574
PBE0-DH	3.399	3.462	2.759	2.431	2.540	2.217	2.420	2.445	2.636	2.435	2.246	0.420	0.421	0.819	0.486
PBE0-2	2.967	2.900	2.574	2.157	2.280	2.066	2.187	2.561	2.426	2.099	1.965	0.164	0.202	0.353	0.234
M06–2X$^{(0-0)}$	3.162	2.872	2.356	2.348	2.444	2.076	2.232	2.433	2.480	2.344	2.162	0.231	0.235	0.543	0.302
SAC–CI	2.769	3.034	2.078	1.817	1.964	1.625	1.605	2.070	2.106	1.704	1.595	–0.182	0.254	0.548	0.316
LCC2	3.006	3.150	2.394	1.972	2.104	1.795	1.867	2.398	2.296	1.897	1.828	0.030	0.189	0.498	0.240
LADC(2)	2.982	3.121	2.370	1.939	2.061	1.742	1.861	2.380	2.279	1.894	1.786	–0.004	0.183	0.458	0.236
CASSCF	3.755	5.013	3.477	2.776	2.918	2.615	2.392	2.891	3.357	3.072	2.934	0.984	0.984	2.177	1.133
CASPT2	2.881	2.915	2.080	1.910	1.972	1.721	1.924	–	–	–	–	–0.062	0.118	0.434	0.185

[(a)]Experimental (Exp.) data are taken from Refs. 42, 378, 396–403.

M06-2X computations (M06–2X$^{(0-0)}$) removes some of the errors in the vertical approximation approach and decreases the MAD to 0.235 eV and RMSD to 0.302 eV. Comparing B2LYP (a hybrid functional without (D) correction) with its DH version (i.e., B2-PLYP with 0.27 fraction of (D) correction) clearly illustrates the impact of electron correlation from a wave function based method to a TD-DFT functional as the MAD drops by more than a factor of two (from 0.436 eV to 0.213 eV) (Table 4.3). The MAD further drops to 0.188 eV in the B2GP-PLYP DH-DF but slightly increases in the cases of B2π-PLYP and mPW2-PLYP (0.249 and 0.246 eV, respectively). Going from hybrid PBE0 to DH PBE0-DH the MAD decreases only by 0.081 eV but it significantly drops by 0.300 eV for the PBE0-2 method. Therefore, it seems that a balance between the amount of HF exact exchange and MP2 correlation is more important in the case of the PBE based DH-DFs than BLYP based ones. Overall, B2GP-PLYP and PBE0-2 DH-DFs provide the lowest MADs among all 15 different TD-DFT methods studied herein and therefore are highly recommended for these systems.

Five different ab initio methods were tested for these molecules and the excitation energies and statistical evaluations are depicted in Table 4.3 along with the TDA-DFT and 0-0 results. Expectedly, the CASSCF method significantly overestimates the excitation energies

and yields the highest MAD and RMSD of 0.984 and 1.133 eV among all the studied methods most likely due to lack of dynamic electron correlation (For details of active spaces of all species see Figures B.2–B.12, Appendix B). On the other hand, the CASPT2 method provides the best estimate to the experiment with MAD = 0.118 eV and RMSD = 0.185 eV. Local CC2 and ADC(2) methods with MADs of 0.189 and 0.183 eV are closest to the highly sophisticated and accurate CASPT2 method. SAC-CI with MAD = 0.254 eV and RMSD = 0.316 eV is poorer than both best estimates of DH-DFs (i.e., B2GP-PLYP and PBE0-2) and ab initio (LCC2 and LADC(2)) methods. Overall, based on our statistical analyses and for the sake of consistency with our previous study [355], the LCC2 method seems to be a good compromise between accuracy and efficiency. Therefore, LCC2 is employed hereafter unless otherwise stated (For the graphs of statistical analyses of all methods see Figure 4.2).

4.3.2 Linkage Control Over Excitation Energies and Intersystem Crossing

As stated in the original paper [42], BODIPY dimers attached in the [1,1] and [1,4] positions (molecules **VIII** and **IX**, Figure 4.3) possess singlet oxygen generation abilities due to the orthogonal arrangement of the monomers (For the effect of methyl substitution on the vertical excitation energies of these species see Table 4.4).

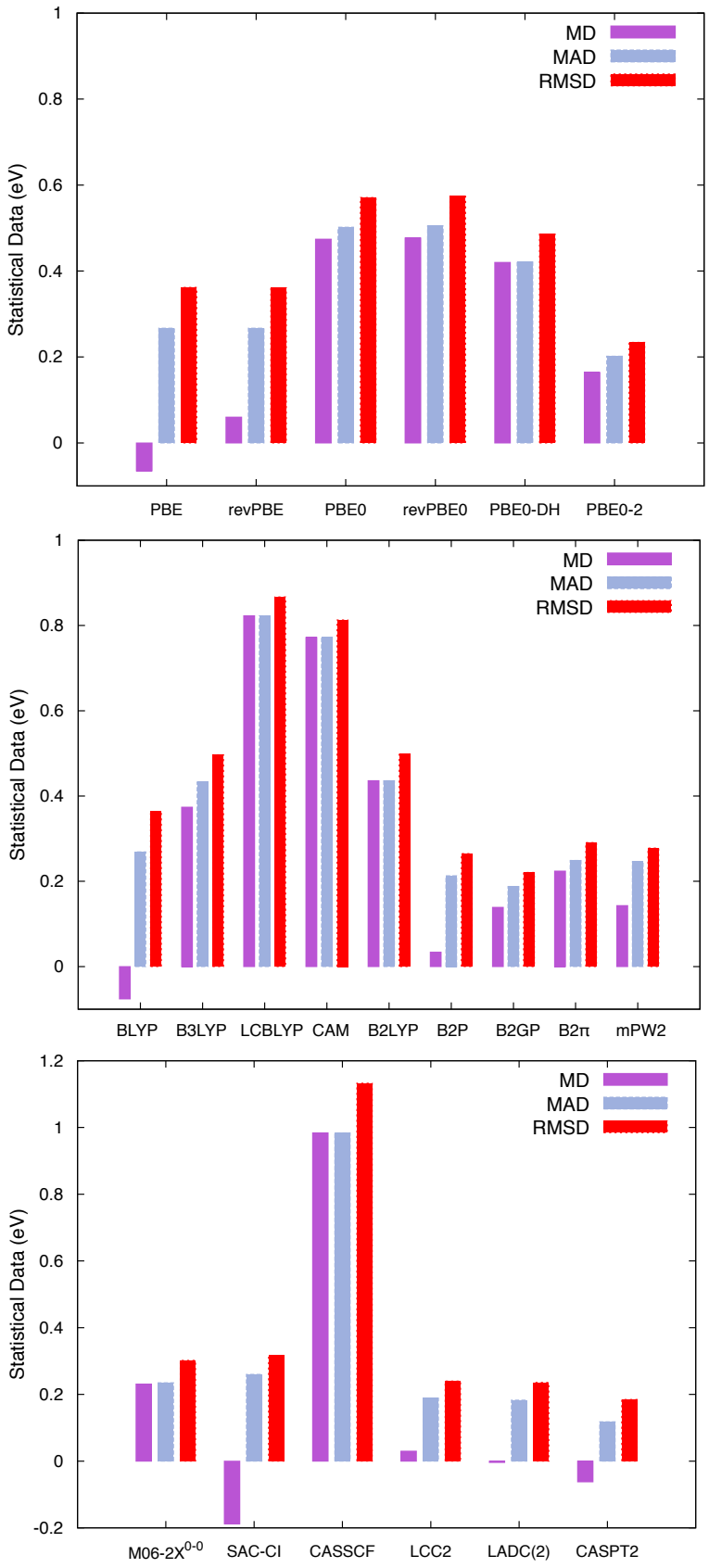

FIGURE 4.2: Graphs of the computed vertical excitation energies (in eV) of all the studied methods in this work.

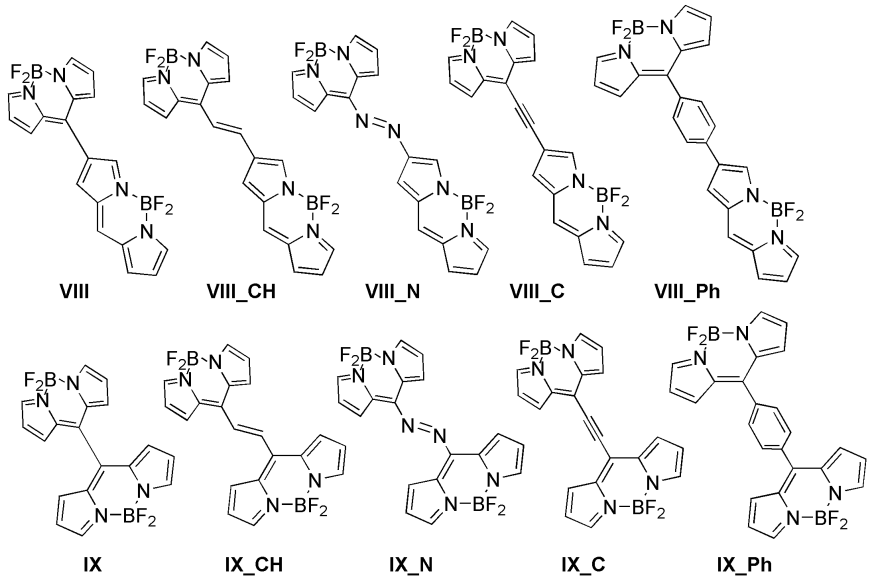

FIGURE 4.3: Linked BODIPY dimers considered in this study.

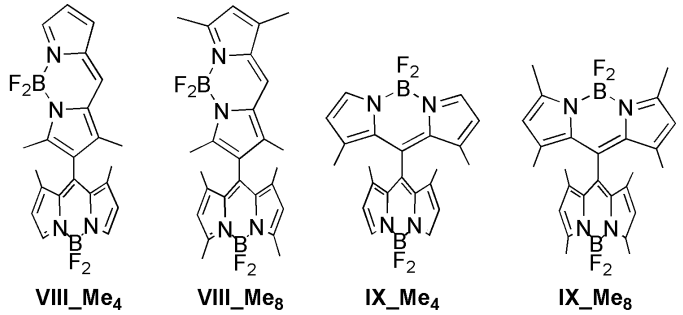

TABLE 4.4: Computed M06-2X/cc-pVDZ vertical excitation energies of the methyl substituted dimers (**VIII_Me**$_4$, **VIII_Me**$_8$, **IX_Me**$_4$, and **IX_Me**$_8$) compared to their unsubstituted forms (**VIII_H**$_8$ and **IX_H**$_8$) in the gas phase. Oscillator strengths are also provided in parenthesis.

Species	S_1	S_2	S_3	T_1	T_2	T_3
VIII_H$_8$ (C_1)	2.924 (0.287)	2.983 (0.734)	3.260 (0.639)	1.576	1.621	3.037
	π_H–π^*_L (^{1}A)	π_{H-1}–π^*_L (^{1}A)	π_H–π^*_{L+1} (^{1}A)	π_{H-1}–π^*_L (^{3}A)	π_H–π^*_{L+1} (^{3}A)	π_{H-4}–π^*_L (^{3}A)
VIII_Me$_4$ (C_1)	3.006 (0.704)	3.063 (0.370)	3.249 (0.088)	1.523	1.571	3.014
	π_{H-1}–π^*_L (^{1}A)	π_H–π^*_{L+1} (^{1}A)	π_H–π^*_L (^{1}A)	π_{H-1}–π^*_L (^{3}A)	π_H–π^*_{L+1} (^{3}A)	π_{H-2}–π^*_L (^{3}A)
VIII_Me$_8$ (C_1)	2.916 (0.775)	2.937 (0.396)	3.086 (0.102)	1.460	1.479	3.050
	π_{H-1}–π^*_L (^{1}A)	π_H–π^*_{L+1} (^{1}A)	π_H–π^*_L (^{1}A)	π_{H-1}–π^*_L (^{3}A)	π_H–π^*_{L+1} (^{3}A)	π_H–π^*_L (^{3}A)
IX_H$_8$ (C_2)	2.784 (0.253)	2.989 (0.131)	3.030 (0.139)	1.366	1.502	2.925
	π_H–π^*_L (^{1}A)	π_H–π^*_L (^{1}B)	π_H–π^*_L (^{1}B)	π_H–π^*_L (^{3}A)	π_H–π^*_L (^{3}B)	π_H–π^*_L (^{3}B)
IX_Me$_4$ (C_2)	2.965 (0.109)	2.998 (0.004)	3.066 (0.410)	1.546	1.555	2.902
	π_H–π^*_L (^{1}B)	π_H–π^*_L (^{1}A)	π_H–π^*_L (^{1}A)	π_H–π^*_L (^{3}B)	π_H–π^*_L (^{3}A)	π_H–π^*_L (^{3}A)
IX_Me$_8$ (D_2)	2.768 (0.201)	2.808 (0.158)	2.995 (0.247)	1.425	1.457	2.857
	π_H–π^*_L (^{1}B$_2$)	π_H–π^*_L (^{1}B$_3$)	π_H–π^*_L (^{1}B$_3$)	π_H–π^*_L (^{3}B$_2$)	π_H–π^*_L (^{3}B$_3$)	π_H–π^*_L (^{3}B$_3$)

This orthogonality results in a tetra-radical electronic configuration in which four electrons are

distributed between four molecular orbitals (HOMO-1, HOMO, LUMO, and LUMO+1) which ultimately leads to ISC rate enhancement [43]. However, as mentioned in the Introduction section, these BODIPY dimers absorb light outside the therapeutic window (650 $\sim$ 900 nm) and therefore are not applicable for PDT applications [42]. In search for heavy atom free NIR BODIPY dimer based PSs, two BODIPY monomers were connected through an auxiliary group: ethylene, azo, acetylene, and phenyl moieties (Figure 4.3). CASSCF occupancies, for the two highest occupied (HOMO and HOMO-1) and two lowest unoccupied (LUMO and LUMO+1) molecular orbitals (MOs) were computed for all species (Table 4.6, for the MOs of all species see Figures 4.4).

	HOMO-1	**HOMO**	**LUMO**	**LUMO+1**
VIII	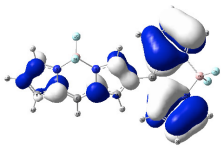	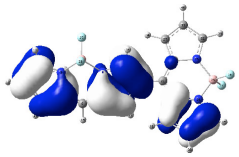	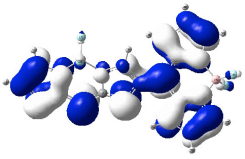	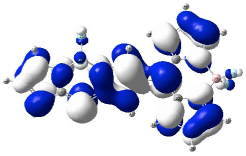
	A (-7.679)	A (-7.193)	A (-2.906)	A (-2.209)
VIII_CH	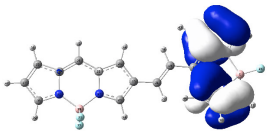	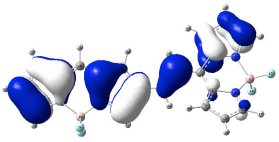	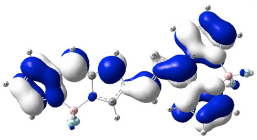	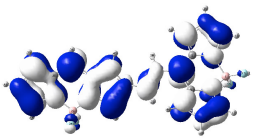
	A (-7.420)	A (-7.111)	A (-2.924)	A (-2.290)
VIII_N	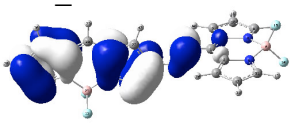	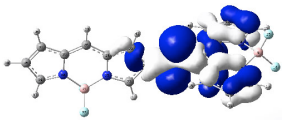	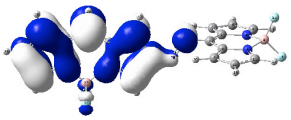	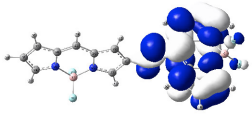
	A (-7.829)	A (-7.183)	A (-2.987)	A (-2.096)
VIII_C	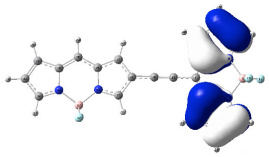	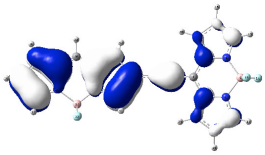	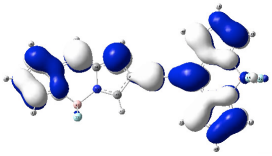	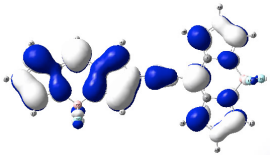
	A (-7.559)	A (-7.150)	A (-2.999)	A (-2.434)
VIII_Ph	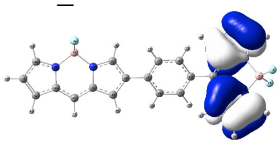	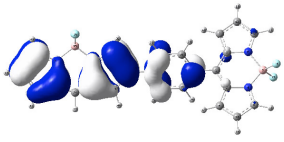	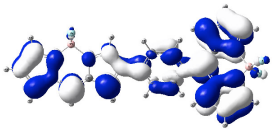	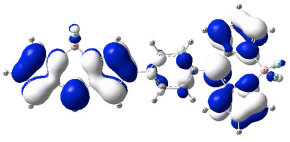
	A (-7.295)	A (-7.172)	A (-2.669)	A (-2.299)

IX

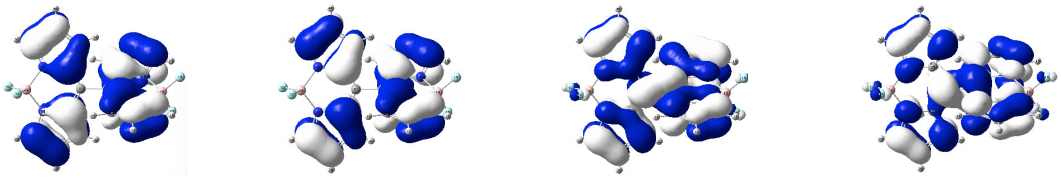

A (-7.661) | B (-7.347) | B (-2.927) | A (-2.405)

IX_CH

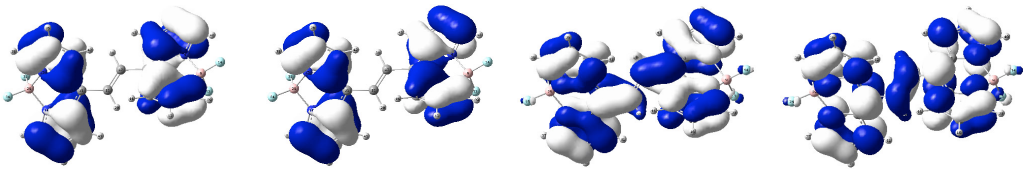

B (-7.459) | A (-7.449) | B (-3.199) | A (-2.173)

IX_N

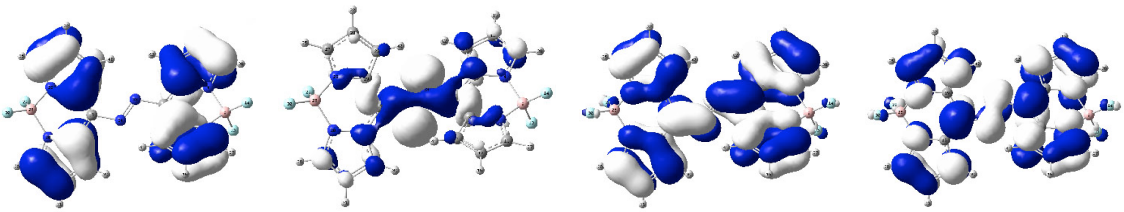

B (-7.516) | A (-7.490) | B (-3.701) | A (-2.285)

IX_C

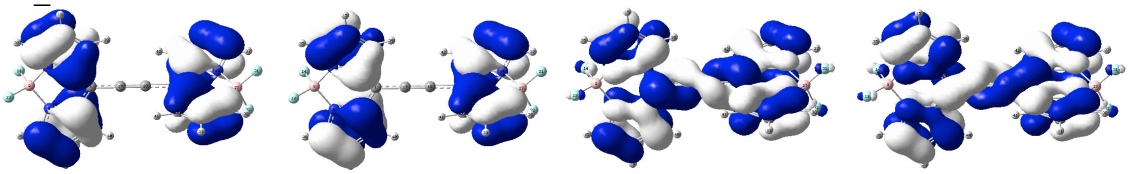

A (-7.519) | B (-7.516) | A (-2.974) | B (-2.943)

IX_Ph

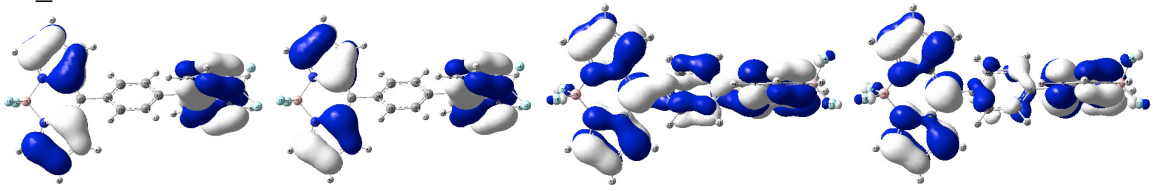

A (-7.396) | B (-7.386) | B (-2.748) | A (-2.371)

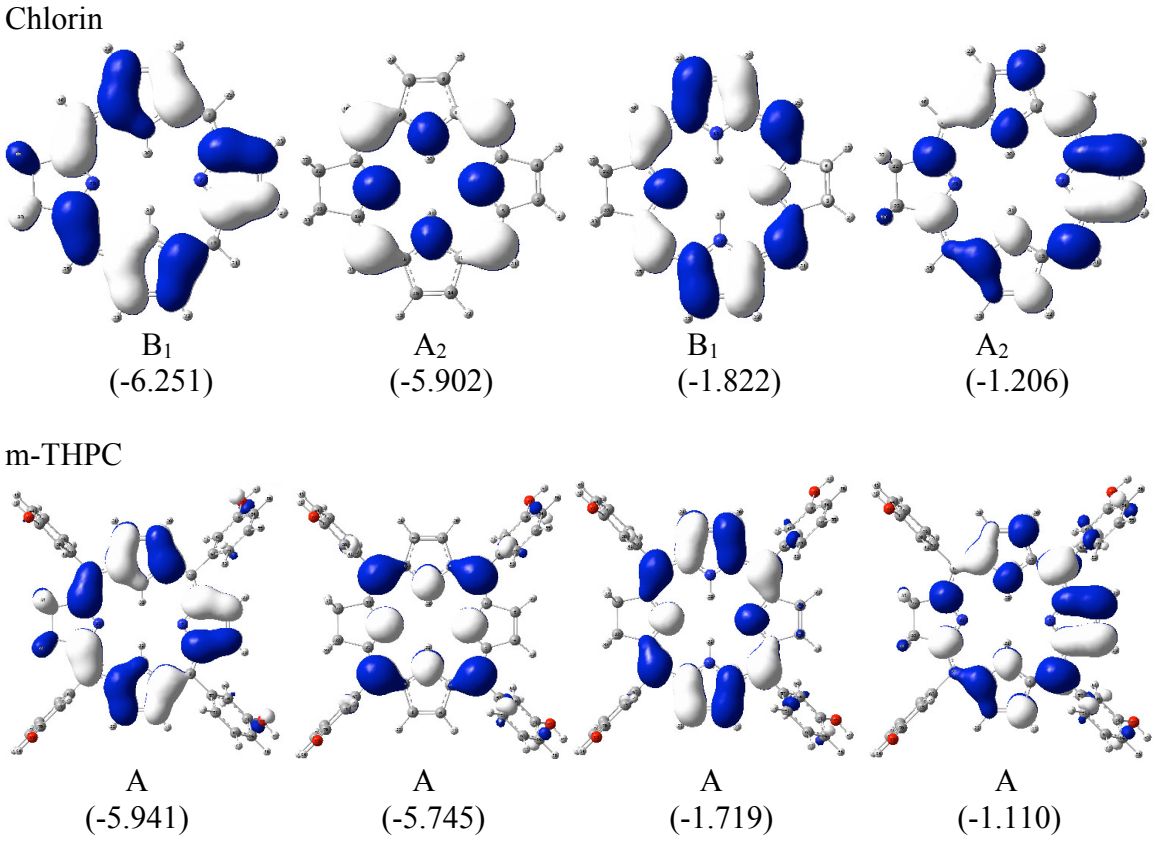

FIGURE 4.4: Optimized MOs (with isovalue of 0.02 e/Å^3) of all the studied linked dimers. Symmetries as well as energies (in eV) are also shown.

The same active space was used for all species to ensure the equal footing of our computations. SOCs for the X, Y, and Z components were computed using the M06-2X T_1 optimized geometries and vertical LCC2 excitation energies using their corresponding ground state S_0 geometries. Singlet-triplet energy gaps (ΔE [S_0–T_1]s and ΔE [S_1–T_n]s) were also computed for all species using the M06-2X and LCC2 methods (see Table 4.6). For a comparison between the LCC2 and M06-2X computed S_1–S_3 and T_1–T_3 vertical excitation energies of all species see Table 4.5.

The results are compared and contrasted to the BODIPY monomer itself as well as to the chlorin molecule as the truncated model of the *meta*-tetrahydroxyphenyl chlorin (m-THPC) as a commercially available PDT agent. We note that our computed SOC value of –0.5 cm^{-1} for the chlorin molecule at the CAM-B3LYP/cc-pVDZ level is close to the reported value of +0.3 cm^{-1} for the m-THPC molecule at the B3LYP/6-31+G(d) level of theory[392]. All the studied linked dimers show tetra-radical character in which dimer **VIII_N** possess the highest and **IX_N** the lowest amount among all (Table 4.6).

TABLE 4.5: Computed singlet (S_1–S_3) and triplet (T_1–T_3) vertical excitation energies of the studied linked dimers using the cc-pVDZ basis set in the gas phase.

Type	LCC2						M06-2X					
Species	S_1	S_2	S_3	T_1	T_2	T_3	S_1	S_2	S_3	T_1	T_2	T_3
VIII	2.388	2.433	2.973	1.686	1.701	2.836	2.924	2.983	3.260	1.576	1.621	3.037
VIII_CH	2.193	2.383	3.045	1.629	1.680	2.314	2.750	2.892	3.078	1.531	1.588	2.427
VIII_N	2.432	2.656	2.992	1.763	1.880	2.225	2.717	3.015	3.096	1.605	1.792	2.085
VIII_C	2.344	2.418	3.210	1.645	1.718	2.583	2.840	2.886	3.112	1.453	1.575	2.552
VIII_Ph	2.276	2.538	3.165	1.592	1.736	2.668	2.883	3.083	3.205	1.510	1.612	2.881
IX	2.288	2.406	2.728	1.436	1.580	2.638	2.784	2.989	3.030	1.366	1.502	2.925
IX_CH	2.285	2.292	3.234	1.536	1.546	2.694	2.762	2.765	3.013	1.403	1.412	2.781
IX_N	1.720	1.864	2.006	1.040	1.167	1.440	1.991	2.299	2.394	0.965	1.030	1.584
IX_C	2.420	2.424	3.053	1.508	1.509	2.795	2.916	2.919	3.049	1.324	1.324	2.960
IX_Ph	2.509	2.547	3.489	1.713	2.863	2.872	3.044	3.065	3.228	1.563	1.565	3.128
BODIPY	2.650	3.848	3.946	1.748	3.084	3.290	3.149	4.092	4.293	1.545	3.172	3.385
Chlorin	1.749	2.059	3.016	1.470	1.570	1.942	2.249	2.655	3.724	1.526	1.598	2.180

TABLE 4.6: Computed CASSCF occupancies, LCC2 excitation energies (in eV), SOCs (in cm^{-1}), and adiabatic and vertical singlet-triplet gaps (in eV) of the studied BODIPY dimers using the cc-pVDZ basis set in the gas phase.

	CASSCF Occupancies				ΔE [S_0-S_1]	$\langle S_1\|\hat{H}_{SO}\|T_n\rangle$ (cm^{-1})				$\Delta(E+ZPE)$ [S_0-T_1]	ΔE [S_1-T_n]
Species	HOMO-1	HOMO	LUMO	LUMO+1	LCC2 (eV)	Involved States	X	Y	Z	M06-2X (eV)	LCC2 (eV)
VIII	1.71	1.29	0.64	0.36	2.388	$S_1 \rightarrow T_2$	0.47	–0.44	–1.35	1.691	–0.687
VIII_CH	1.65	1.30	0.68	0.38	2.193	$S_1 \rightarrow T_1$	0.04	–0.19	–0.68	1.649	–0.564
VIII_N	1.27	1.02	1.00	0.71	2.432	$S_1 \rightarrow T_2$	–1.19	–4.04	0.00	1.707	–0.552
VIII_C	1.64	1.29	0.69	0.38	2.344	$S_1 \rightarrow T_2$	–0.15	0.00	–0.61	1.686	–0.626
VIII_Ph	1.61	1.29	0.71	0.39	2.276	$S_1 \rightarrow T_2$	3.14	4.94	9.27	1.642	–0.540
IX	1.54	1.35	0.67	0.44	2.288	$S_1 \rightarrow T_2$	–0.16	0.29	0.00	1.637	–0.708
IX_CH	1.79	1.44	0.58	0.19	2.285	$S_1 \rightarrow T_1$	0.83	–2.69	0.00	1.621	–0.749
IX_N	1.84	1.38	0.65	0.13	1.720	$S_1 \rightarrow T_2$	0.00	0.00	0.57	1.089	–0.553
IX_C	1.61	1.60	0.40	0.38	2.420	$S_1 \rightarrow T_1$	–0.02	–1.47	0.00	1.579	–0.912
IX_Ph	1.46	1.43	0.59	0.51	2.509	$S_1 \rightarrow T_2$	–0.07	–0.07	0.00	2.381	0.354
Bodipy	1.87	1.36	0.73	0.08	2.650	$S_1 \rightarrow T_1$	0.00	0.00	0.00	1.674	–0.902
Chlorin	1.90	1.36	0.64	0.11	1.749	$S_1 \rightarrow T_1$	0.03	–0.50	–0.05	1.409	–0.279

The computed LCC2 excitation energies for the S_1 state shows that the excitation energy for the former molecule is 0.044 eV higher than the unsubstituted dimer (**VIII**) whereas the latter with excitation energy of 1.720 eV shows a significant red shift of 0.568 eV and is closest to that of the chlorin molecule. The excitation energies for all the other species fall close to or above the unlinked molecules. The largest computed SOC belongs to the **VIII_Ph** species with 9.27 cm^{-1} for its <Z> component compared to –1.35 cm^{-1} for the <Z> component of the reference molecule (**VIII**). The azo-linked dimers (**VIII_N** and **IX_N**) possess large SOCs compared to their reference species (–4.04 and 0.57 cm^{-1}, respectively). Overall, except dimer **IX** and **IX_Ph** the rest of the species have SOCs larger than the chlorin molecule whereas the BODIPY monomer itself shows SOC values of zero (Table 4.6). As mentioned before, the singlet-triplet gap of the photosensitizer needs to be equal or greater than the

energy required for exciting the $^3O_2$ molecule to its excited singlet state. As can be seen from Table 4.6, all the studied BODIPY dimers possess gaps higher than 1 eV with the smallest gap belonging to the **IX_N** molecule and the largest to the **IX_Ph** compound. For comparison, the singlet-triplet gap for the chlorin molecule is computed to be 1.409 eV at the same level. Also, the energy differences between different deactivation channels are computed using the LCC2 method and shown in Table 4.6. The [S_1–T_n] gaps of the two azo-substituted dimers (**VIII_N**, **IX_N**) are almost the same and are comparable to their corresponding reference species and are also closest to the chlorin molecule (–0.274 eV difference) among all. Except **XI_Ph** and **XI_C** the [S_1–T_n] gaps for the rest of molecules fall close to each other and stay $\sim$ 0.5 eV below that of the chlorin molecule.

4.3.3 Azo-substituted BODIPY/Aza-BODIPY Dimers

It was found in the previous section that substituting two BODIPY monomers through an azo linkage in compound **IX_N** shifts the absorption value of the unlinked BODIPY dimer up to $\sim$ 130 nm towards the red region which is beneficial for the PDT purpose. To further investigate the effect of azo substitution on the excited state properties of the BODIPY as well Aza-BODIPY dimers, a series of 36 different (Aza-)BODIPY based dimers, depending on the position of the connection of two monomers, were systematically investigated. Vertical excitation energies of three different singlet excited states (S_1–S_3) were computed using the LCC2 method and the cc-pVDZ basis set in the gas phase (see Tables 4.7 and 4.8 for the excitation values and their corresponding assignments).

Position of connection of two monomers has a remarkable impact on the excitation energies of the formed dimers. The trend of excitation energies to S_1 for BODIPY substituted dimers is as following: **Bo[3,3]** > **Bo[3,1]** > **Bo[4,1]** > **Bo[1,1]** > **Bo[5,1]** > **Bo[4,3]** > **Bo[5,3]** > **Bo[4,4]-Anti** > **Bo[4,4]-Syn** > **Bo[5,4]** > **Bo[5,5]** (Table 4.7). Similar to the BODIPY dimers, the **Az[3,3]** dimer possesses the largest excitation energy and **Az[5,4]** and **Az[5,5]** the smallest ones (Table 4.8). Overall, absorptions in the Aza-BODIPY dimers are red shifted compared to their BODIPY dimer analogues; the maximum red shift of 1.132 eV corresponds to the [3,3] position and the minimum of 0.177 eV to the [4,4]-Syn position (Tables 4.7 and 4.8). Linking BODIPY and Aza-BODIPY dimers with an N_2 group leads to a new class of azo-substituted BODIPY (**Bo[n,n]-N_2**, n = 1–5) and aza-BODIPY (**Az[n,n]-N_2**, n = 3–5)

TABLE 4.7: Effect of N_2 substitution on the vertical excitation energies (S_1–S_3, in eV) of the BODIPY (Bo) dimers computed at the LCC2/cc-pVDZ level for different positions (1–5) in gas phase (see Figure 1.1 for the numberings). Weights and natures of excitations are also provided in parenthesis.

Species	**Bo[1,1]**	**Bo[3,1]**	**Bo[3,3]**	**Bo[4,1]**	**Bo[4,3]**	**Bo[4,4]-Syn**
S_1	2.296 (0.9341) ($\pi \rightarrow \pi^*$)	2.526 (0.2919) ($\pi \rightarrow \pi^*$)	3.176 (0.9618) ($\pi \rightarrow \pi^*$)	2.400 (0.3920) ($\pi \rightarrow \pi^*$)	2.191 (0.7881) ($\pi \rightarrow \pi^*$)	1.972 (0.8990) ($\pi \rightarrow \pi^*$)
S_2	2.413 (0.7210) ($\pi \rightarrow \pi^*$)	2.505 (0.5991) ($\pi \rightarrow \pi^*$)	4.007 (0.9033) ($\pi \rightarrow \pi^*$)	2.514 (0.6386) ($\pi \rightarrow \pi^*$)	2.657 (0.5761) ($\pi \rightarrow \pi^*$)	2.469 (0.8403) ($\pi \rightarrow \pi^*$)
S_3	2.730 (0.8020) ($\pi \rightarrow \pi^*$)	3.037 (0.7749) ($\pi \rightarrow \pi^*$)	4.463 (0.9073) ($\pi \rightarrow \pi^*$)	2.965 (0.6576) ($\pi \rightarrow \pi^*$)	2.932 (0.5861) ($\pi \rightarrow \pi^*$)	3.340 (0.7924) ($\pi \rightarrow \pi^*$)
Species	**Bo[1,1]-N_2**	**Bo[3,1]-N_2**	**Bo[3,3]-N_2**	**Bo[4,1]-N_2**	**Bo[4,3]-N_2**	**Bo[4,4]-N_2-Syn**
S_1	1.720 (0.7792) (n $\rightarrow \pi^*$)	2.030 (0.5052) (n $\rightarrow \pi^*$)	2.167 (0.8876) (n $\rightarrow \pi^*$)	2.135 (0.5384) (n $\rightarrow \pi^*$)	2.170 (0.8046) (n $\rightarrow \pi^*$)	2.124 (0.8236) (n $\rightarrow \pi^*$)
S_2	1.864 (0.8915) ($\pi \rightarrow \pi^*$)	2.216 (0.4131) ($\pi \rightarrow \pi^*$)	2.499 (0.3676) ($\pi \rightarrow \pi^*$)	2.282 (0.3820) ($\pi \rightarrow \pi^*$)	2.550 (0.6390) ($\pi \rightarrow \pi^*$)	2.499 (0.7675) ($\pi \rightarrow \pi^*$)
S_3	2.006 (0.2588) ($\pi \rightarrow \pi^*$)	2.378 (0.2454) ($\pi \rightarrow \pi^*$)	2.751 (0.8915) ($\pi \rightarrow \pi^*$)	2.388 (0.2520) ($\pi \rightarrow \pi^*$)	2.652 (–) ($\pi \rightarrow \pi^*$)	2.818 (0.0571) ($\pi \rightarrow \pi^*$)
Species	**Bo[4,4]-Anti**	**Bo[5,1]**	**Bo[5,3]**	**Bo[5,4]**	**Bo[5,5]**	
S_1	2.104 (0.8640) ($\pi \rightarrow \pi^*$)	2.289 (0.7179) ($\pi \rightarrow \pi^*$)	2.113 (0.8847) ($\pi \rightarrow \pi^*$)	1.913 (0.9132) ($\pi \rightarrow \pi^*$)	1.867 (0.9338) ($\pi \rightarrow \pi^*$)	
S_2	2.368 (0.8652) ($\pi \rightarrow \pi^*$)	2.474 (0.7829) ($\pi \rightarrow \pi^*$)	2.564 (0.7334) ($\pi \rightarrow \pi^*$)	2.622 (0.7898) ($\pi \rightarrow \pi^*$)	2.691 (0.6235) ($\pi \rightarrow \pi^*$)	
S_3	3.363 (0.7666) ($\pi \rightarrow \pi^*$)	2.797 (0.74407) ($\pi \rightarrow \pi^*$)	3.013 (0.7234) ($\pi \rightarrow \pi^*$)	3.233 (0.7273) ($\pi \rightarrow \pi^*$)	3.100 (0.69481) ($\pi \rightarrow \pi^*$)	
Species	**Bo[4,4]-N_2-Anti**	**Bo[5,1]-N_2**	**Bo[5,3]-N_2**	**Bo[5,4]-N_2**	**Bo[5,5]-N_2**	
S_1	2.070 (0.8450) (n $\rightarrow \pi^*$)	1.861 (0.6824) (n $\rightarrow \pi^*$)	1.951 (0.9013) (n $\rightarrow \pi^*$)	1.947 (0.8539) (n $\rightarrow \pi^*$)	1.753 (0.9246) (n $\rightarrow \pi^*$)	
S_2	2.478 (0.7660) ($\pi \rightarrow \pi^*$)	1.989 (0.2877) ($\pi \rightarrow \pi^*$)	2.470 (0.7885) ($\pi \rightarrow \pi^*$)	2.482 (–) ($\pi \rightarrow \pi^*$)	2.579 (0.6881) ($\pi \rightarrow \pi^*$)	
S_3	3.429 (0.6729) ($\pi \rightarrow \pi^*$)	2.158 (0.8999) ($\pi \rightarrow \pi^*$)	2.917 (0.7309) ($\pi \rightarrow \pi^*$)	2.559 (0.7135) ($\pi \rightarrow \pi^*$)	3.006 (0.7484) ($\pi \rightarrow \pi^*$)	

dimers. In all 18 different azo-substituted structures studied in this work, the S_1 excited state corresponds to a transition from HOMO $\rightarrow$ LUMO which is related to an $n_N \rightarrow \pi^*$ transition. In general, N_2 substitution shifts the absorption energies of all the BODIPY and Aza-BODIPY dimers more to the red region; except in compounds **Bo[4,4]-Syn**, **Az[4,3]** and **Az[5,4]**. The SOCs were computed for all species possessing excitation energies lower than 2 eV or wavelengths longer than 620 nm (i.e., close to the therapeutic window) and the selected results are provided in Table 4.9.

Except **Az[5,3]** and **Bo[5,1]-N_2** molecules with [S_0–T_1] gaps of 0.637 and 0.915 eV, respectively, the rest of the dimers shown in Table 4.9 possess gaps higher than 1 eV required

TABLE 4.8: Effect of N_2 substitution on the vertical excitation energies (S_1–S_3, in eV) of the Aza-BODIPY (Az) dimers computed at the LCC2/cc-pVDZ level for different positions (1–5) in gas phase (see Figure 1.1 for the numberings). Weights and natures of excitations are also provided in parenthesis.

Species	**Az[3,3]**	**Az[4,3]**	**Az[4,4]-Syn**	**Az[4,4]-Anti**	**Az[5,3]**	**Az[5,4]**	**Az[5,5]**
S_1	2.044 (0.9042) ($\pi \rightarrow \pi^*$)	1.838 (0.8387) ($\pi \rightarrow \pi^*$)	1.795 (0.8805) ($\pi \rightarrow \pi^*$)	1.911 (0.8563) ($\pi \rightarrow \pi^*$)	1.804 (0.9261) ($\pi \rightarrow \pi^*$)	1.621 (0.9201) ($\pi \rightarrow \pi^*$)	1.668 (0.9347) ($\pi \rightarrow \pi^*$)
S_2	2.273 (0.8220) ($\pi \rightarrow \pi^*$)	2.390 (0.5078) ($\pi \rightarrow \pi^*$)	2.287 (0.8124) ($\pi \rightarrow \pi^*$)	2.151 (0.8372) ($\pi \rightarrow \pi^*$)	2.351 (0.7504) ($\pi \rightarrow \pi^*$)	2.382 (0.8343) ($\pi \rightarrow \pi^*$)	2.520 (0.5882) ($\pi \rightarrow \pi^*$)
S_3	2.492 (0.3325) ($\pi \rightarrow \pi^*$)	2.511 (0.7885) ($\pi \rightarrow \pi^*$)	3.136 (0.7439) ($\pi \rightarrow \pi^*$)	3.154 (0.7109) ($\pi \rightarrow \pi^*$)	2.689 (0.7658) ($\pi \rightarrow \pi^*$)	2.901 (0.7820) ($\pi \rightarrow \pi^*$)	2.746 (0.7917) ($\pi \rightarrow \pi^*$)
Species	**Az[3,3]-N_2**	**Az[4,3]-N_2**	**Az[4,4]-N_2-Syn**	**Az[4,4]-N_2-Anti**	**Az[5,3]-N_2**	**Az[5,4]-N_2**	**Az[5,5]-N_2**
S_1	2.044 (0.8771) (n $\rightarrow \pi^*$)	1.875 (0.7778) (n $\rightarrow \pi^*$)	1.942 (0.7987) (n $\rightarrow \pi^*$)	1.843 (0.8282) (n $\rightarrow \pi^*$)	1.755 (0.8975) (n $\rightarrow \pi^*$)	1.694 (0.8380) (n $\rightarrow \pi^*$)	1.574 (0.9247) (n $\rightarrow \pi^*$)
S_2	2.256 (0.2724) ($\pi \rightarrow \pi^*$)	2.353 (0.5168) ($\pi \rightarrow \pi^*$)	2.318 (0.7439) ($\pi \rightarrow \pi^*$)	2.224 (0.7519) ($\pi \rightarrow \pi^*$)	2.236 (0.7515) ($\pi \rightarrow \pi^*$)	2.319 (0.7359) ($\pi \rightarrow \pi^*$)	2.411 (0.6509) ($\pi \rightarrow \pi^*$)
S_3	2.416 (0.2725) ($\pi \rightarrow \pi^*$)	2.579 (0.6408) ($\pi \rightarrow \pi^*$)	2.730 (–) $\pi \rightarrow \pi^*$	3.167 (0.6880) ($\pi \rightarrow \pi^*$)	2.646 (0.7059) ($\pi \rightarrow \pi^*$)	2.905 (0.7289) ($\pi \rightarrow \pi^*$)	2.695 (0.8014) ($\pi \rightarrow \pi^*$)

for exciting the oxygen molecule. The lowest [S_1–T_n] gap corresponds to the **Bo[4,4]-Syn** molecule and the highest to the **Az[5,3]** molecule. The [S_1–T_n] gaps of the rest are close to each other and around 0.6–0.7 eV. All the species grouped in Table 4.9 show significant SOCs compared to their corresponding directly linked and experimentally verified molecules. As mentioned before, the orthogonal arrangement of the BODIPY monomers in **VIII** and **IX** was responsible for their tetra-radical behaviour and ultimately their applicability in PDT. Similarly, the linked **Az[4,4]-N_2-Anti** and **Bo[5,4]-N_2** dimers with non-planar geometries possess the highest SOC values (125.01 cm^{-1} for the <Y> component of the **Az[4,4]-N_2-Anti** dimer and –8.97 cm^{-1} for the <X> component of the **Bo[5,4]-N_2** molecule. Hence, considering the computed vertical excitation energies, [S_0–T_1] and [S_1–T_n] gaps and SOCs, compounds **Az[4,3]**, and **Az[4,4]-Syn**, and **Az[4,4]-N_2-Anti** with excitation energies of 1.838 eV (675 nm) 1.795 eV (691 nm), and 1.843 eV (673 nm), respectively, look promising candidates for PDT action. Our results are in close agreement with previous experimental findings that substituting BODIPY and Aza-BODIPY monomers in the C–4 position is crucial for having a large ISC rate and therefore a good triplet PS [20, 39–41].

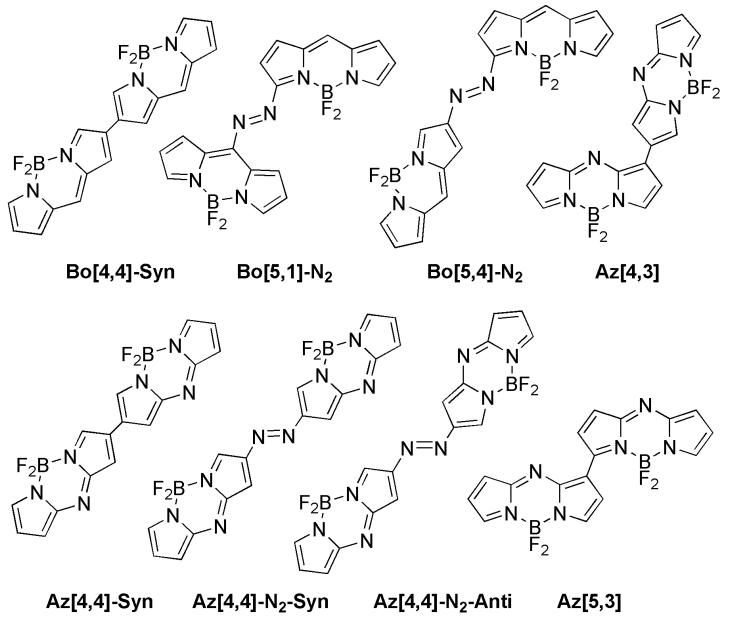

TABLE 4.9: Computed photophysical properties of selected linked dimers using the cc-pVDZ basis set.

Species	ΔE [S_0-S_1] LCC2 (eV)	[a]$\langle S_1\|\hat{H}_{SO}\|T_n\rangle$ (cm^{-1}) X	Y	Z	$\Delta(E+ZPE)$ [S_0-T_1] M06-2X (eV)	[a]ΔE [S_1-T_n] LCC2 (eV)
Bo[4,4]-Syn	1.972	0.00	0.00	–5.15	1.785	–0.493
Bo[5,1]-N_2	1.861	–4.80	0.13	0.81	0.915	–0.647
Bo[5,4]-N_2	1.947	–8.97	–0.55	1.65	1.141	–0.582
Az[4,3]	1.838	0.02	0.00	5.80	1.139	–0.721
Az[4,4]-Syn	1.795	4.19	0.00	0.00	1.317	–0.692
Az[4,4]-N_2-Syn	1.942	0.09	0.04	–5.22	1.157	–0.754
Az[4,4]-N_2-Anti	1.843	–29.96	125.01	0.00	1.210	–0.621
Az[5,3]	1.804	0.00	0.00	–2.99	0.637	–0.885

[a]All excitations correspond to $S_1 \rightarrow T_1$ except for **Az[4,4]-N_2-Anti** with a $S_1 \rightarrow T_2$ transition.

4.4 Concluding remarks

An extensive benchmark study on vertical excitation energies of 11 different BODIPY and Aza-BODIPY dimers was performed using 15 different TDA-DFT functionals. 0-0 excitation energies were also obtained for all structures using the M06-2X meta hybrid functional. Among all the TDA-DFT functionals used, B2GP-PLYP and PBE0-2 double hybrid density functionals were found to yield the least amounts of mean absolute deviations (0.188 and 0.202 eV, respectively). Also, from the different ab initio methods tested in this work, the local coupled cluster method with singles and approximate doubles along with local algebraic diagrammatic construction second order yielded the best results and were closest to the CASPT2 method. In the search for near IR heavy atom free triplet photosensitizers based on

BODIPY dimers, two of the previously proposed dimers for PDT action were further modified using different auxiliary groups (ethylene, acetylene, azo and phenyl moieties). Spin-orbit coupling matrix elements and CASSCF occupancies were computed for all species along with the LCC2 vertical excitation energies and [S_1–T_n] singlet-triplet gaps. Finally, a systematic study on all possible azo-linked BODIPY and Aza-BODIPY dimers was performed and triplet photosensitizers based on these molecules were introduced.

Chapter 5

Carbene-bound Borane and Silane Adducts: A Comprehensive DFT Study on their Stability and Propensity for Hydride-mediated Ring Expansion

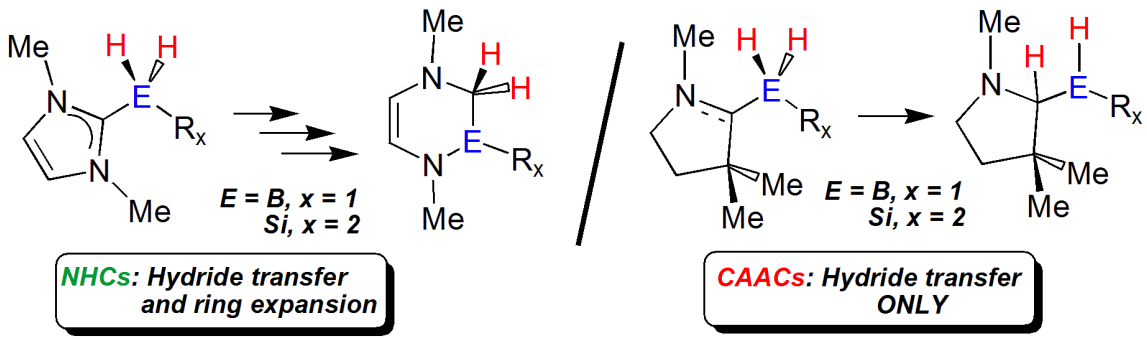

5.1 Bonding Properties of Carbene Substituted Be, B and Si Main Group Element Adducts

N-heterocyclic carbenes (NHCs) and related systems such as cyclic alkyl-amino carbenes (CAACs) are viewed as being resistant to degradation/bond activation processes when bound to electron deficient substrates. However recently it has been shown that Be, B and Si hydrides can undergo hydride-mediated ring expansion/atom insertion chemistry with their NHC donors [148–150]. The first report of NHC-based ring expansion chemistry was by Hill and coworkers who noted that warming an in situ generated beryllium adduct (proposed to be) IPr-BeH_2 (IPr = [(HCNDipp)$_2$C:]; Dipp = 2,6-^{i}Pr$_2$C$_6$H$_3$) results in $C_{carbene}$-N bond cleavage and expansion of the five-membered NHC ring to give a six-membered one with inclusion of a beryllium atom in the resulting heterocycle (see Figure 5.1). Later the groups of Radius and Rivard noted similar results when arylsilane and aminoborane-carbene adducts were heated to 100 °C in toluene [149, 150]. The similar nature of each of these ring expansion reactions led us to consider the possibility that a general ring expansion mechanism was operational. A very recent theoretical study by the Dutton group on the mechanism of silicon hydride-mediated activation of NHCs confirmed the previously proposed mechanism by Radius and coworkers, and revealed that the first step, hydride migration/C-H bond formation, is favourable and is likely the rate determining step [404]. In the report by Dutton, NHCs adducts of $SiHPh_3$, SiH_2Ph_2, and their methylated and chlorosilane analogues were investigated at the MP2/TZVP//M06-2X/6-31G(d) level of theory.

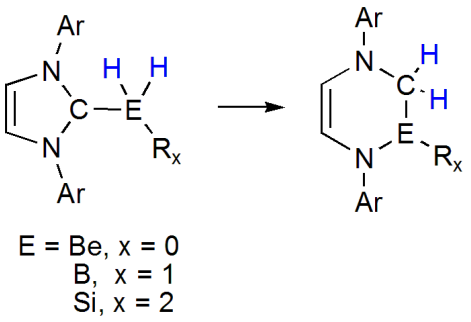

FIGURE 5.1: General NHC-based ring expansion reaction.

The postulated mechanism of the above mentioned rearrangements includes three steps: hydride migration from the element hydride to the carbene center (E-H bond activation), followed by $C_{carbene}$-N bond cleavage/ring expansion, and finally another hydride migration to generate an intraring methylene, CH_2, unit. The initial hydride transfer from an E-H residue to a carbon center of an NHC is related to bond activation chemistry demonstrated by cyclic aminoalkyl carbenes (CAACs) [117], which can instigate the scission of H-H, N-H [119], B-H, Si-H, and P-H bonds [405]. Mézailles and coworkers have also shown that related carbenoids can activate boranes under mild conditions [406].

In this computational study based on Density Functional Theory (DFT), we expand upon the work of Dutton and coworkers [404] on NHC-silane complexes to include additional silane and borane adducts supported by both NHC and CAAC donors; the goal of this study is to compare the hydride accepting ability of these Lewis basic donors within the context of their propensities for participating in ring expansion chemistry. Both electronic and steric effects on the formation of element hydride complexes were evaluated by examining complexes involving NHCs of different ring sizes and substituents. Moreover, a further analysis of the reported complexes using Natural Bond Orbital (NBO) and Atoms-in-Molecules (AIM) indices was performed in order to probe the strength and nature of the dative interactions in the preformed adducts.

Bonding properties and reactivities of different series of N-heterocyclic carbene ($ImMe_2$) and cyclic aminoalkyl carbene (^{Me}CAAC) substituted BH_3, BH_2NHMe, SiH_nPh_{n-1} (n = 1–4) are studied quantum mechanically (see Figure 5.2). Mechanism of C-N bond cleavage in $ImMe_2$ substituted complexes are extensively examined and compared and contrasted to their ^{Me}CAAC analogues.

5.2 Methods

Geometry optimizations to determine both equilibrium and transition state structures were performed using density functional theory (DFT) with the M06-2X functional [243] and the cc-pVDZ [289, 290] basis set. Harmonic vibrational frequencies were computed at the same level of theory in order to characterize the stationary points as minima, representing equilibrium structures, or transition states (TSs). The vibrational frequencies were also

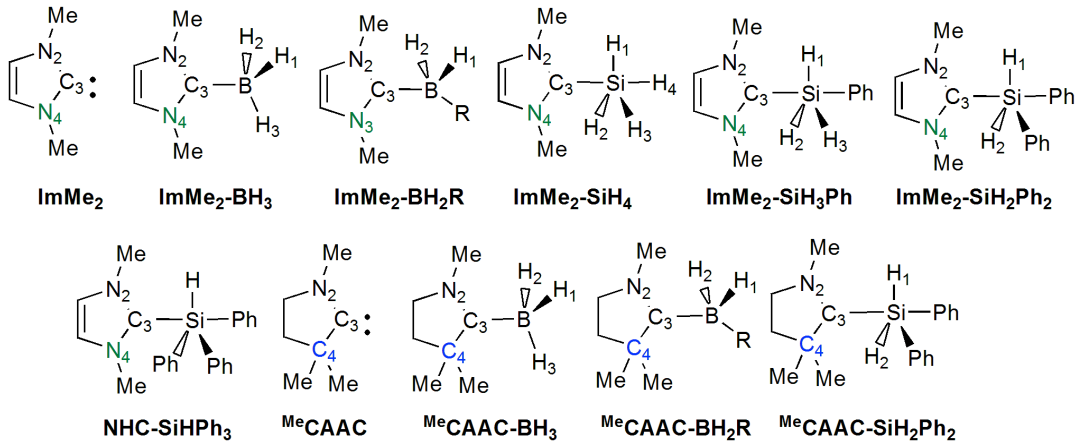

FIGURE 5.2: All the carbene-borane and silane adducts along with their atom numberings considered in this study (R = NHMe).

utilized to evaluate the corresponding zero-point vibrational energies and thermochemical data (within the harmonic limit and determined at 1 atmosphere and 298 K). In order to assess the M06-2X/cc-pVDZ energetics, single point computations were performed at the CCSD(T)[219, 316]/cc-pVDZ//M06-2X/cc-pVDZ and CCSD(T)/cc-pVTZ//M06-2X/cc-pVDZ levels of theory for the smallest NHC compounds, i.e., $ImMe_2$-BH_3, $ImMe_2$-BH_2NHMe, and $ImMe_2$-SiH_4 ($ImMe_2$ = [(HCNMe)$_2$C:]), and at the CCSD(T)/cc-pVDZ//M06-2X/cc-pVDZ level of theory for $ImMe_2$-SiH_3Ph. In addition to computations in the gas-phase, the majority of optimized geometries and frequencies were determined using the polarizable continuum model (IEF-PCM) [292, 293] with parameters for toluene (ϵ = 2.3741). In all optimizations, no restrictions or constraints were enforced for any of the computed structures. For all TSs, intrinsic reaction coordinates computations [407–409] were carried out to ensure the connectivity between the local minima along the reaction path. All the electronic structure computations were performed using Gaussian 09, Revision C.01 [322]. The nature of the bonding in the NHC and CAAC adducts was assessed using both Natural Bond Orbital (NBO) and Atoms-in-Molecules (AIM) analyses. NBO [410] population analyses were done at the M06-2X/cc-pVDZ level of theory by using the NBO suite available in Gaussian 09. The AIM [273] analysis was carried out at the same level of theory using the AIMAll software package [411].

5.3 Optimized Geometries of the Reported Element Hydride Carbene Adducts

The M06-2X/cc-pVDZ optimized geometries of the free carbenes $ImMe_2$ and ^{Me}CAAC along with their complexes with the boranes and silanes are depicted in Figure 5.3.

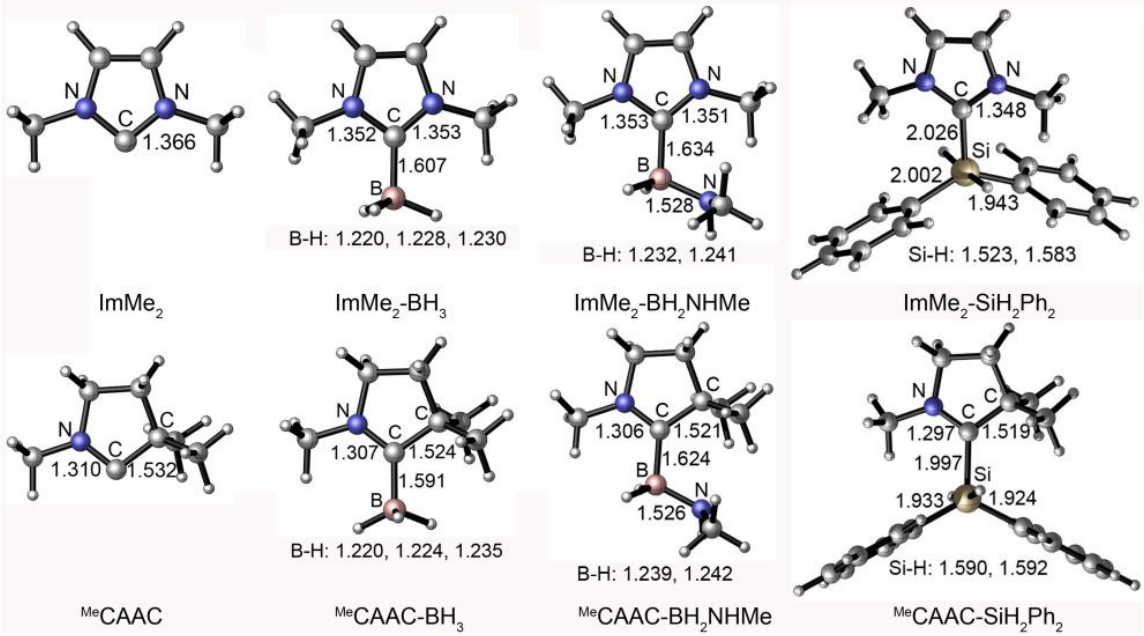

FIGURE 5.3: Optimized structures of the borane and silane $ImMe_2$ and ^{Me}CAAC adducts obtained at the M06-2X/cc-pVDZ level of theory in toluene (polarizable continuum model, PCM).

The analogous ImH_2-BH_3 complex has been studied by Tonner and Frenking previously [412]. All the complexes studied adopted non-planar C_1 symmetries. The intraring N-$C_{carbene}$ bond within free CAAC, and in its corresponding element hydride complexes are shorter in relation to the N-$C_{carbene}$ bond lengths in free $ImMe_2$ and its adducts by ca. 0.05 Å. This observation can be rationalized by the competition of two adjacent π-donors for the empty p-orbital at the carbene carbon in $ImMe_2$, which leads to each N-C interaction being weakened in relation to the solitary N-C π-bond in ^{Me}CAAC.

Comparing $ImMe_2$-BH_2NHMe to $ImMe_2$-BH_3 one finds that the $C_{carbene}$-B bond is longer in the former complex as a result of π-electron donation from the amino group attached to the boron atom which reduces the Lewis acidity of the BH_2NHMe group in relation to BH_3 (Figure 5.3). The $C_{carbene}$-B bonds are also shorter in the ^{Me}CAAC complexes compared

to the $ImMe_2$ adducts, confirming the previous observation that CAAC ligands are both stronger σ-donors and π-acceptors in relation to N-heterocyclic carbenes [119]. The Si-H bonds are also slightly longer in CAAC complexes and comment with respect to the ability of these bonds to undergo hydride transfer chemistry to the adjacent carbene carbon centers will follow. The $C_{carbene}$-Si bonds of $ImMe_2$-SiH_2Ph_2 and ^{Me}CAAC-SiH_2Ph_2 (2.026 and 1.997 Å, respectively) are considerably longer than the covalent C^{sp2}-Si bonds in SiH_2Ph_2 (1.885 Å) calculated at the same level of theory. This observation can be rationalized from two cumulative effects: i) an increase in coordination number generally leads to longer bonds, thus longer C-Si interactions are anticipated in the five-coordinate adduct $ImMe_2$-SiH_2Ph_2; ii) the dative nature of $C_{carbene}$-Si bonds (e.g. in $ImMe_2$-SiH_2Ph_2) generally leads to longer bonds in relation to their covalently bonded counterparts. Similarly, the Si-H bonds in the $ImMe_2$ complexes are elongated, up to 1.583 Å, compared to the covalent Si-H bonds in SiH_2Ph_2 (1.494 Å avg.). There is also a significant change in the NBO partial charges of the hydrogen atoms in SiH_2Ph_2 and $SiHPh_3$ when going from the free species (ca. –0.164) to the adduct (–0.321 and –0.295, respectively); the change for the hydrogens in the SiH_4 and SiH_3Ph units upon complexation is much more modest (see Tables in Appendix C). The Si-H bond lengthening likely triggers the hydride mediated ring-expansion chemistry that will be discussed in detail later on in this chapter.

5.4 Complexation (E_c) and Bond Dissociation Energies (BDEs) for Various Element Hydride Carbene Complexes

The relative electronic (ΔE_c) and Gibbs free energies (ΔG_c) for the reactions of NHCs and CAACs with both boranes and silanes, as well as the bond dissociation energies (BDEs) of the B-H and the Si-H bonds in toluene are provided in Table 5.1.

In order to assess the accuracy of the M06-2X/cc-pVDZ approach used, single point computations at the CCSD(T)[219, 316]/cc-pVDZ//M06-2X/cc-pVDZ and CCSD(T)/cc-pVTZ//M06-2X/cc-pVDZ levels of theory were undertaken for the smallest NHC compounds, i.e., $ImMe_2$-BH_3, $ImMe_2$-BH_2NHMe, and $ImMe_2$-SiH_4 ($ImMe_2$ = [(HCNMe)$_2$C:), and at the CCSD(T)/cc-pVDZ//M06-2X/cc-pVDZ level of theory for $ImMe_2$-SiH_3Ph (Table 5.2).

TABLE 5.1: Relative electronic energies (ΔE_c, kcal/mol) and Gibbs free energies (ΔG_c) of complexation[(a)] as well as bond dissociation energies[(b)] for several $ImMe_2$ and ^{Me}CAAC adducts. All values are determined at the M06-2X/cc-pVDZ level of theory in toluene. ΔE_c and E_{BDE} are given with and without (in parentheses) the inclusion of zero point energy, ZPE.

Systems	ΔE_c	ΔG_c	E_{BDE}	ΔG_{BDE}
$ImMe_2$-BH_3	-56.5[(c)] (–60.9)	–46.9	+133.2 (+137.8)	+127.7
$ImMe_2$-BH_2NHMe	–22.2 (–24.7)	–9.2	+101.4 (+101.4)	+92.0
$ImMe_2$-SiH_2Ph_2	+6.0 (+4.4)	+20.1	+72.8 (+76.0)	+67.1
^{Me}CAAC-BH_3	–60.7 (–65.0)	–50.8	+139.0 (+144.6)	+132.5
^{Me}CAAC-BH_2NHMe	–25.3 (–27.2)	–13.6	+97.8 (+101.9)	+91.5
^{Me}CAAC-SiH_2Ph_2	–0.9 (–2.2)	+11.7	+78.4 (+81.8)	+73.6

[(a)]For reactions: $ImMe_2 + BR_2H \rightarrow ImMe_2\text{-}BR_2H$ or $ImMe_2 + SiR_4 \rightarrow ImMe_2\text{-}SiR_4$
[(b)]For reactions: $ImMe_2\text{-}BR_2H \rightarrow [ImMe_2\text{-}BR_2]^+ + H^-$ or $ImMe_2\text{-}SiR_3H \rightarrow [ImMe_2\text{-}SiR_3]^+ + H^-$
[(c)]Values for ImH_2-BH_3 at the BP86/SVP optimized geometry are –58.6 kcal/mol, –57.3 kcal/mol, and –53.2 kcal/mol at the BP86/TZVPP, MP2/TZVPP, and SCS-MP2/TZVPP levels of theory.

TABLE 5.2: Comparison of relative electronic energies of complexation[(a)] (ΔE_c, kcal/mol) and bond dissociation energies[(b)] (E_{BDE}, kcal/mol) for $ImMe_2$-BH_3, $ImMe_2$-BH_2NHMe, $ImMe_2$-SiH_4, and $ImMe_2$-SiH_3Ph as determined at the M06-2X/cc-pVDZ and CCSD(T)/cc-pVDZ and CCSD(T)/cc-pVTZ (in parentheses) levels of theory in the gas-phase.

System	ΔE (gas) M06-2X	ΔE (gas) CCSD(T)	E_{BDE} (gas) M06-2X	E_{BDE} (gas) CCSD(T)
$ImMe_2$-BH_3	–59.2	-56.4 (–57.4)	216.2	215.2 (206.3)
$ImMe_2$-BH_2NHMe	–24.7	–22.6 (–23.2)	179.2	178.2 (169.4)
$ImMe_2$-SiH_4	–5.0	-4.0 (-3.8)	172.0	173.7 (162.0)
$ImMe_2$-SiH_3Ph	–5.4	-4.4 (–)	165.3	166.5 (–)

[(a)]For reactions: $ImMe_2 + BR_2H \rightarrow ImMe_2\text{-}BR_2H$ or $ImMe_2 + SiR_4 \rightarrow ImMe_2\text{-}SiR_4$
[(b)]For reactions: $ImMe_2\text{-}BR_2H \rightarrow [ImMe_2\text{-}BR_2]^+ + H^-$ or $ImMe_2\text{-}SiR_3H \rightarrow [ImMe_2\text{-}SiR_3]^+ + H^-$.

The relative energetics determined by M06-2X/cc-pVDZ are very close to those from CCSD(T)/cc-pVDZ (ca. 1-3 kcal/mol difference) and CCSD(T)/cc-pVTZ (ca. 1-2 kcal/mol difference for complexation and 10 kcal/mol for BDEs). Therefore the less computationally demanding M06-2X/cc-pVDZ method was used to compute the larger phenyl-substituted systems (e.g., $ImMe_2$-SiH_2Ph_2 and ^{Me}CAAC-SiH_2Ph_2). From these results, it can also be seen that there is almost no difference between the energetics in the gas-phase and in toluene solvent, and so for convenience we will restrict our discussions to the ΔG_c data from computations (M06-2X/cc-pVDZ) in toluene (polarizable continuum model, PCM).

The $ImMe_2$-BH_3 complex is 46.9 kcal/mol more stable relative to its dissociated Lewis base/acid components ($ImMe_2$ and BH_3). This can be compared to the value of 25.9 kcal/mol determined at the CCSD(T)/CBS level of theory for the classical H_3BNH_3 donor-acceptor complex [413]. In the case of $ImMe_2$-BH_2NHMe, this value is only 9.2 kcal/mol (Table 5.1).

The large difference in complexation energy clearly shows the effect of the neighbouring π-donating amino group on the Lewis acidity of the boron center, which restricts the degree of electron flow from the carbene carbon of the N-heterocyclic carbene (NHC) to the boron atom.

While the Gibbs free energies of complexation (ΔG_c) for the carbene-borane complexes are negative, each of the carbene-silane adducts studied gave positive values for the Gibbs free energies of complexation (ΔG_c), (see Table 5.1). The ΔG_c value of $ImMe_2$-SiH_4 is +6.6 kcal/mol (Figure 5.4) followed by increasing ΔG_c values as the number of silicon-bound phenyl rings increases (up to +15.6 kcal/mol for $ImMe_2$-$SiHPh_3$, Figures 5.5-5.8). No stable complex was found for the tetraphenyl substituted silane (i.e., $ImMe_2$-$SiPh_4$) because of the increased steric hindrance around the silicon atom (Figure 5.8).

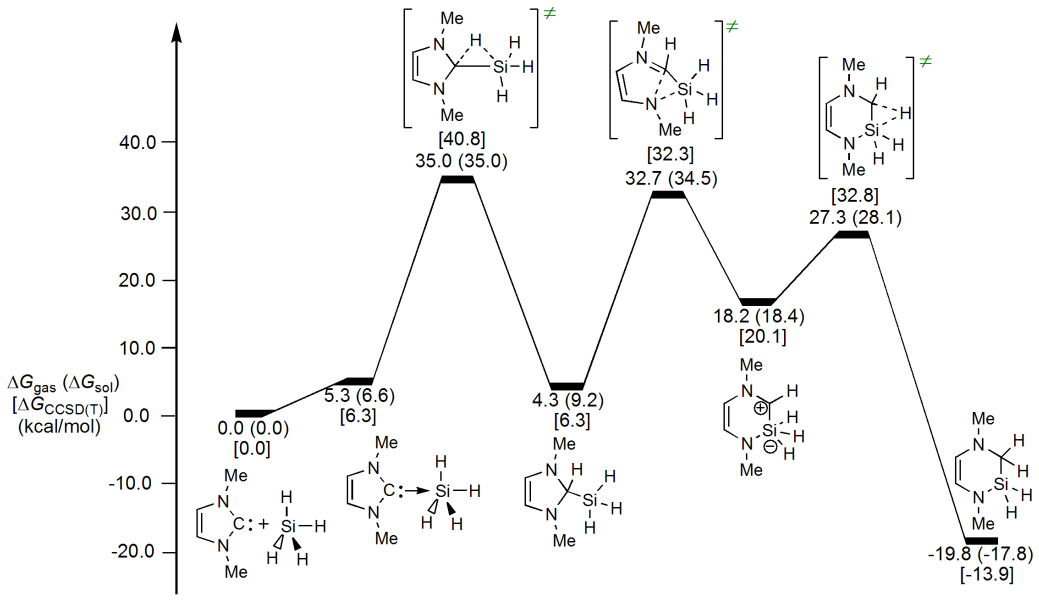

FIGURE 5.4: Mechanistic scheme for the ring expansion of $ImMe_2$-SiH_4, including the relative Gibbs free energies as determined at the M06-2X/cc-pVDZ level of theory in the gas-phase, ΔG_{gas}, and in PCM toluene (ΔG_{sol} given in parenthesis). CCSD(T)/cc-pVDZ gas-phase Gibbs free energies (determined using M06-2X/cc-pVDZ frequencies) are provided in brackets [ΔG CCSD(T)].

To determine the bond dissociation energies of the B–H and Si–H bonds (ΔG_{BDE}), the relative stabilities of boron and silicon cations were evaluated after abstraction of a hydride group (i.e. heterolytic E-H bond cleavage), and the results are summarized in Table 5.1. Upon placing an amino group at the boron atom or by incorporating additional phenyl rings on silicon, the ΔG_{BDE} values for the E-H bonds decrease (127.7 kcal/mol for $ImMe_2$-BH_3

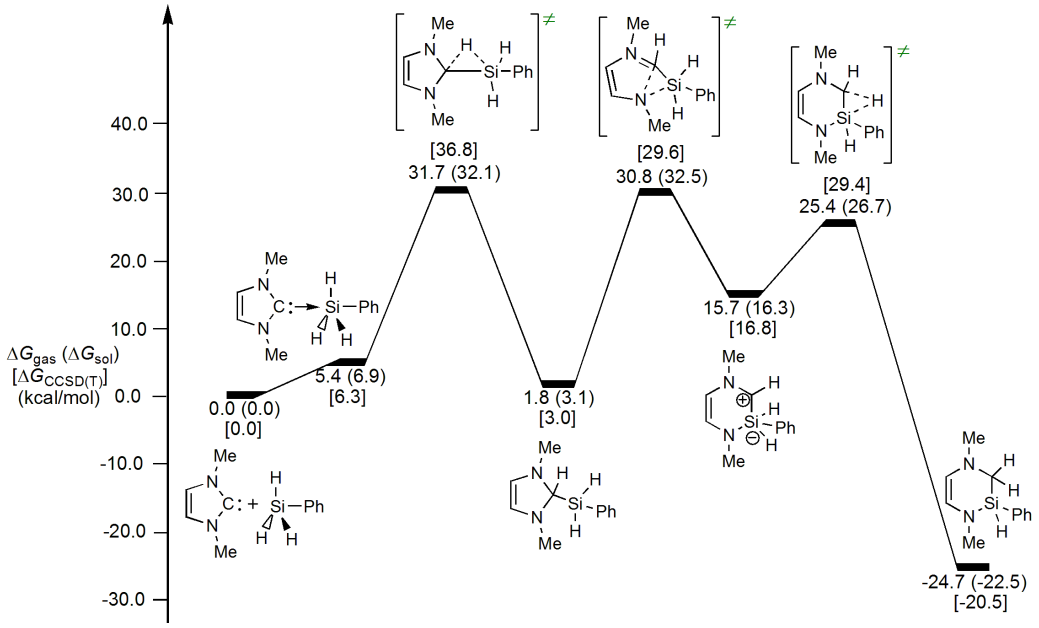

FIGURE 5.5: Mechanistic scheme for the ring expansion of $ImMe_2$-SiH_3Ph, including the relative Gibbs free energies as determined at the M06-2X/cc-pVDZ level of theory in the gas-phase, ΔG_{gas}, and in PCM toluene (ΔG_{sol} given in parenthesis). CCSD(T)/cc-pVDZ gas-phase Gibbs free energies (determined using M06-2X/cc-pVDZ frequencies) are provided in brackets [$\Delta G_{CCSD(T)}$].

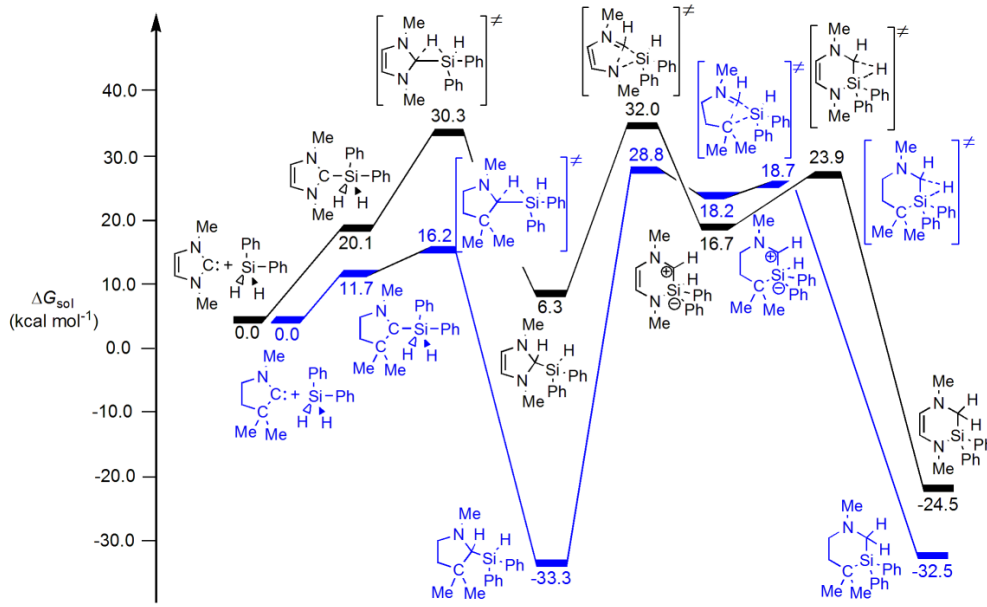

FIGURE 5.6: Mechanistic scheme for the ring expansion of $ImMe_2$-SiH_2Ph_2 (black) and ^{Me}CAAC-SiH_2Ph_2 (blue), including the relative Gibbs free energies as determined at the M06-2X/cc-pVDZ level of theory in PCM toluene (ΔG_{sol}).

vs. 92.0 kcal/mol for $ImMe_2$-BH_2NHMe; 85.9 kcal/mol for $ImMe_2$-SiH_4 *vs.* 64.7 for $ImMe_2$-$SiHPh_3$). It is worthwhile mentioning that there is a close relationship between ΔG_{BDE} and

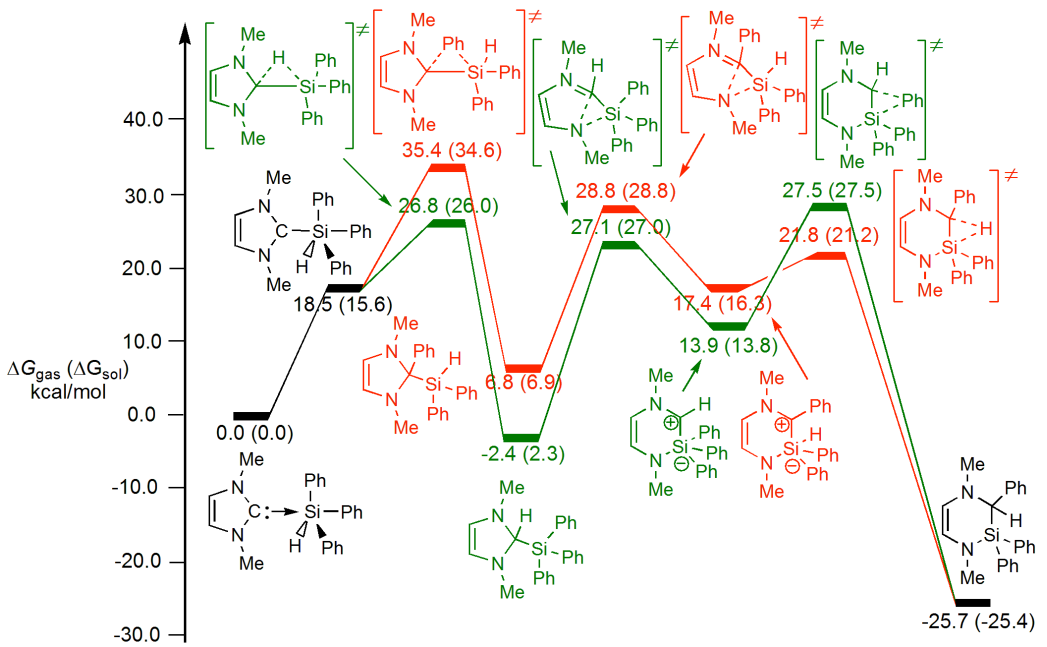

FIGURE 5.7: Mechanistic schemes for the ring expansion of $ImMe_2$-$SiHPh_3$, including the relative Gibbs free energies as determined at the M06-2X/cc-pVDZ level of theory in the gas-phase, ΔG_{gas}, and in PCM toluene (ΔG_{sol} given in parenthesis). The two pathways of hydrogen (green) *vs.* kinetically unfavourable phenyl (red) migration both leading to the same product are highlighted.

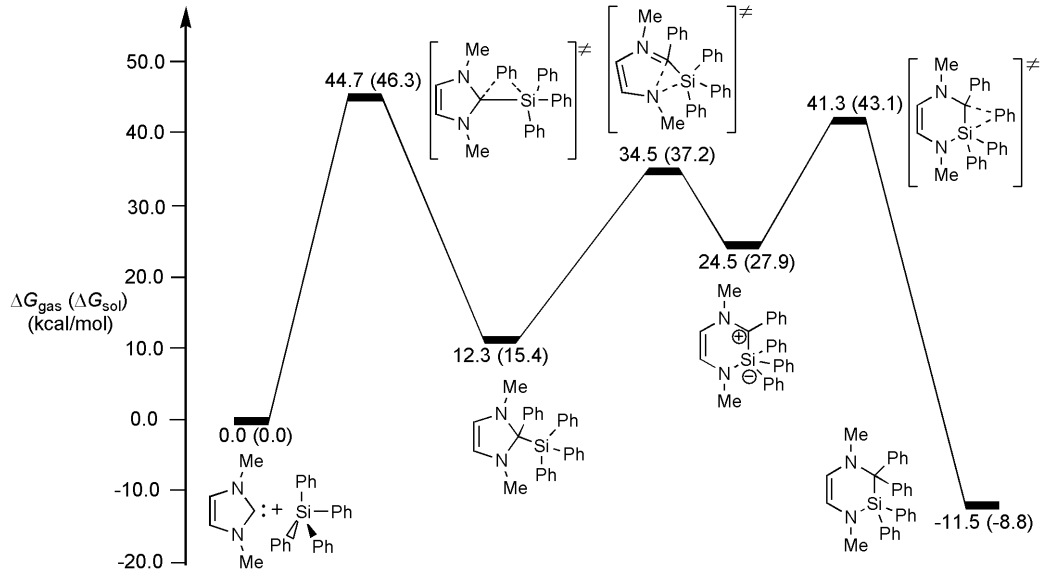

FIGURE 5.8: Mechanistic scheme for the ring expansion of $ImMe_2$-$SiPh_4$, including the relative Gibbs free energies as determined at the M06-2X/cc-pVDZ level of theory in the gas-phase, ΔG_{gas}, and in PCM toluene (ΔG_{sol} given in parenthesis).

ΔG_C as any change of ΔG_{BDE} is concurrent with a change in ΔG_C. In other words, more energy is required to heterolytically cleave the B-H or Si-H bonds within the more stable complexes (see Table 5.1).

5.5 Natural Bond Orbital and Atoms in Molecules Analysis

NBO and AIM analyses were performed to understand the nature of the bonding in these adducts (see the NBO tables and AIM figures in Appendix C; NBO partial charges and AIM results have been determined previously for the ImH_2-BH_3 complex [412]. The NBO analysis shows the existence of a dative σ bond between $C_{carbene}$ and B atoms with similar bond polarities (ca. 70 % electron density towards the donor C atoms) in all borane complexes shown in Figure 5.3. Notably a higher Wiberg bond index (WBI) was found for the $C_{carbene}$-B bond in $ImMe_2$-BH_3 (0.902) in relation to in $ImMe_2$-BH_2NHMe (0.840). A similar trend in the WBIs is obtained for the $C_{carbene}$-B interactions in the analogous CAAC complexes (0.932 in ^{Me}CAAC-BH_3 compared to 0.856 in ^{Me}CAAC-BH_2NHMe). According to the topological analysis of electron density in the theory of AIM, if $\nabla^2\rho > 0$, the bond can be classified as being predominantly ionic in nature. Our AIM analysis also supports the assignment of the carbene-borane interactions as having ionic character with values of +0.364 and +0.292 for the $C_{carbene}$-B bond in $ImMe_2$-BH_3 and $ImMe_2$-BH_2NHMe, respectively, and +0.376 and +0.291 for the corresponding bonds in ^{Me}CAAC complexes. Furthermore, the corresponding AIM electron density ρ(r) values for these complexes (0.137 and 0.132 for the $C_{carbene}$-B bond in $ImMe_2$-BH_3 and $ImMe_2$-BH_2NHMe, respectively), are similar, while the ^{Me}CAAC-BH_3 and ^{Me}CAAC-BH_2NHMe adducts show comparable trends in ρ(r) values (0.145 and 0.138, respectively).

5.6 Mechanistic Study of the Ring Expansion Reaction Involving N-heterocyclic Carbenes

As demonstrated by Rivard and coworkers [150], heating the NHC-borane adduct IPr-$BH_2NHDipp$ at 100°C in toluene results in $C_{carbene}$-N bond cleavage and expansion of the five-membered ring to a six-membered heterocycle incorporating the boron atom. The Radius group have

observed a related ring expanded product from NHC-silane adducts under similar experimental conditions [148]. Although different Lewis acidic element hydride adducts have been studied by the two groups, the parallel formation of ring expanded products, and the fact that boron and silicon are diagonal elements in the second and third periods of the periodic table [414], suggest that there may be similar mechanisms and even adduct stabilities in both systems.

The mechanism of the carbene activation/ring expansion transformation, has been postulated to occur in three discrete steps: (i) hydride migration from a main group hydride to a carbene center, (ii) $C_{carbene}$-N bond cleavage/ring expansion, and (iii) a second hydride migration to the carbon atom. In very recent computational work exploring the NHC-silicon-containing species complexes, Dutton confirmed this three-step mechanism and revealed that the first step in this process, i.e. hydride migration/C-H bond formation, is rate-determining [404]. Here, the rearrangement mechanisms for carbene borane and additional NHC-silane adducts were examined along with the respective transition states and intermediates for each key step in the ring expansion transformation. Importantly, we compare the reactivity of NHC with model adducts featuring CAAC donors to provide a more general picture of the reactivity of carbenes with coordinated element hydrides.

The reaction mechanisms for ring expansion in $ImMe_2$-BH_2NHMe and ^{Me}CAAC-BH_2NHMe are presented in Figure 5.9. As in the silicon-containing complexes [404], the first step (hydride transfer) is the rate-determining step for the overall ring expansion of $ImMe_2$-BH_2NHMe; the energy barrier is 26.1 kcal/mol for the ring-activation/atom insertion step (step 2), while only 14.6 kcal/mol is required for the final hydride transfer (third step). For ^{Me}CAAC-BH_2NHMe, the situation is drastically altered as the first step requires only 5.7 kcal/mol while the second step needs 44.5 kcal/mol. Therefore, step two is rate-determining, and, more importantly, ring-expansion chemistry will likely not be feasible under previously attempted experimental conditions (i.e., heating at 100 °C); therefore in solution, the reaction will cease after the first hydride migration occurs [119, 415, 416]. For the CAAC adducts, there are two different pathways for ring expansion, i.e., C-C bond breakage can occur instead of C-N breakage. The present computations show that C-C bond cleavage is preferred over C-N cleavage in all complexes. Also, all efforts to optimize minima and transition states (TS) encountered in the C-N bond breakage pathway failed.

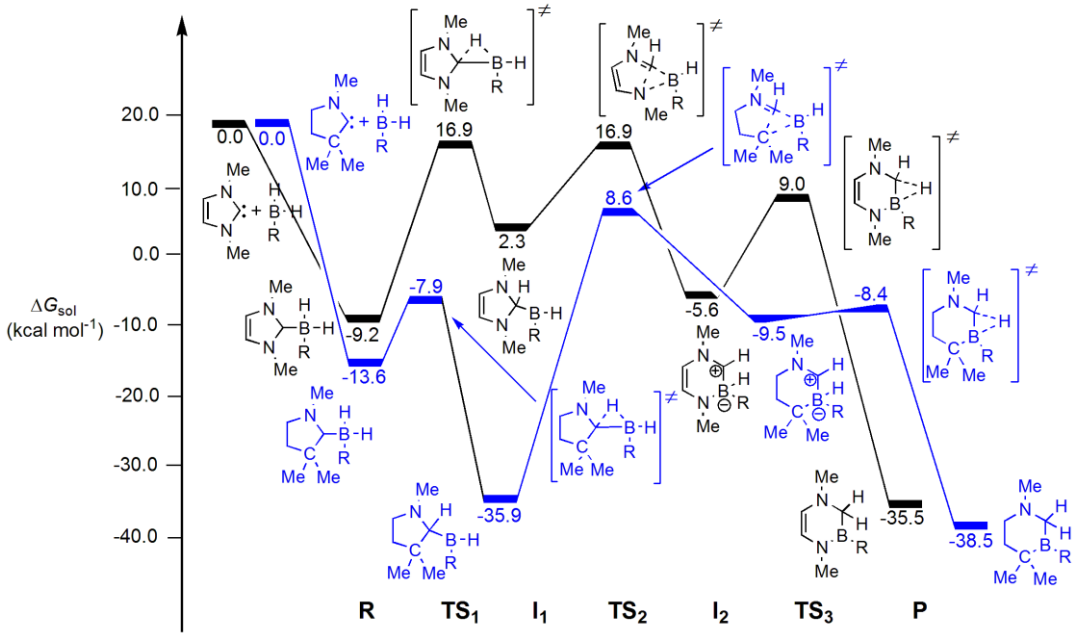

FIGURE 5.9: Mechanistic scheme for the ring expansion of $ImMe_2$-BH_2R (black) and ^{Me}CAAC-BH_2R (blue) with R = NHMe, including the relative Gibbs free energies as determined at the M06-2X/cc-pVDZ level of theory in PCM toluene (ΔG_{sol}).

While heating IPr-BH_2NHDipp to 100 °C leads to a ring expanded product, experiments by Rivard and coworkers show that heating IPr-BH_3 (up to 140 °C) [149] did not lead to any observable reaction. Accordingly ring expansion chemistry for the borane-capped adducts $ImMe_2$-BH_3 and ^{Me}CAAC-BH_3 were investigated and the results are depicted in Figure 5.10. The computations are in agreement with these experimental findings as intramolecular hydride transfer from B to C in $ImMe_2$-BH_3 requires 46.0 kcal/mol energy and hence would not occur under the previously examined experimental conditions.

On the other hand, ^{Me}CAAC-BH_3 requires only 5.7 kcal/mol energy for hydride migration leading to an intermediate (^{Me}CAACH)-BH_2 that is 2.7 kcal/mol more stable than the initial BH_3 complex (Figure 5.10). However, the second step (ring expansion) requires 34.3 kcal/mol of energy and therefore is not likely to happen. While Dutton and coworkers recently explored the ring expansion mechanism for silicon-substituted NHCs [404], here we studied complexes of all possible phenyl silane (SiH_nPh_{4-n}, n = 0-4) adducts with $ImMe_2$ (see Figures 5.4-5.8); this includes a re-examination at the M06-2x/cc-pVDZ level of theory of the $ImMe_2$-SiH_3Ph and $ImMe_2$-SiH_2Ph_2 complexes previously reported [404]. By having a closer look into the reaction mechanisms, one can find the effect of the phenyl rings on the rate-determining step. Here relative energies are given from separated reactants to the hydride transfer transition

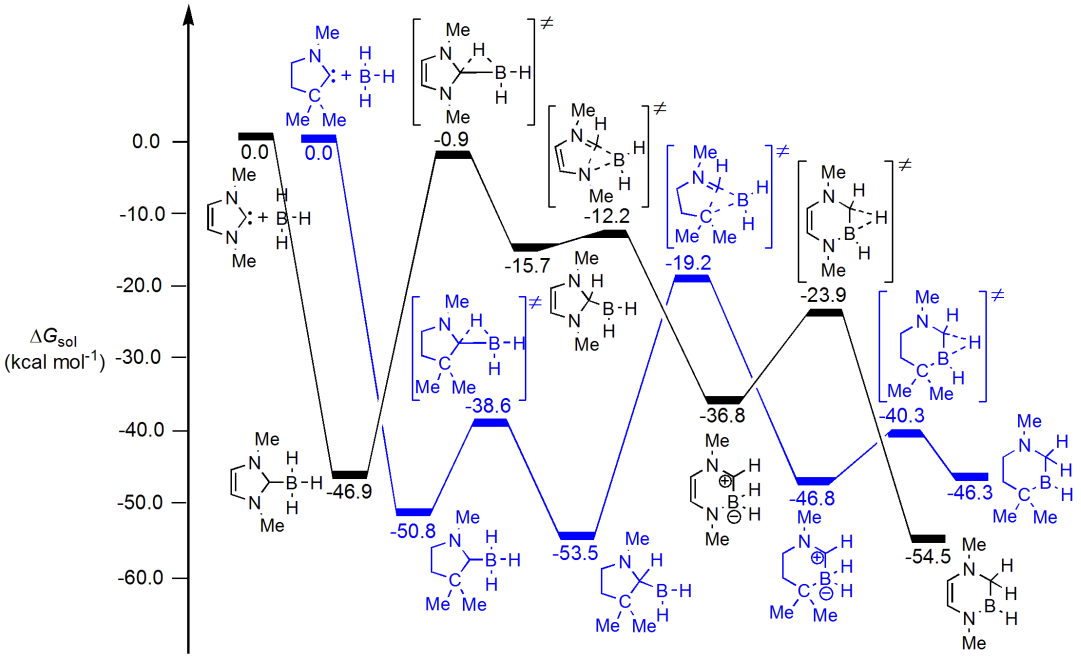

FIGURE 5.10: Mechanistic scheme for the ring expansion of $ImMe_2$-BH_3 (black) and ^{Me}CAAC-BH_3 (blue), including the relative Gibbs free energies as determined at the M06-2X/cc-pVDZ level of theory in PCM toluene (ΔG_{sol}).

state rather than from the stable adduct (R) to TS_1 (Figures 5.4-5.8) since no stable $ImMe_2$-$SiPh_4$ complex could be found as discussed earlier. While $ImMe_2$-SiH_4 requires considerable energy input (35.0 kcal/mol) for Si to C hydride transfer (first step); additional phenyl groups on the silicon center cause a reduction in the energy barrier: from 32.1 to 30.3 to 26.0 upon sequential replacement of hydrogen with phenyl groups. An exceptionally high energy barrier (44.7 kcal/mol) is calculated for phenyl group migration from Si to C in the model complex $ImMe_2$-$SiPh_4$ (Figure 5.8). For example, for $ImMe_2$-$SiHPh_3$, the energy barrier for phenyl migration is 34.6 kcal/mol compared to a smaller barrier of 26.8 kcal/mol for the migration of hydride to carbene, see Figure 5.7. Overall, we have confirmed Dutton's findings on the critical role of hydrogen atom migration and C-H bond formation in the ring expansion mechanism. Moreover, by examining adducts of SiH_4 and showing that these species will likely resist hydride transfer chemistry, the importance of the phenyl groups in instigating ring expansion chemistry has been emphasized. In addition to examining the NHC complexes, the results for the diphenylsilane adduct of ^{Me}CAAC are compared to its $ImMe_2$ analog in Figure 5.6.

The first step (hydrogen-atom migration) for the rearrangement of ^{Me}CAAC-SiH_2Ph_2 can

readily happen as it requires only 16.2 kcal/mol of energy. However, the second ring-activation step needs 62.1 kcal/mol, and therefore is prohibitive energetically. For this reason, the ring expansion mechanisms of the other CAAC-silane complexes were not explored further. In conclusion, although the rearrangement of both ^{Me}CAAC-SiH_2Ph_2 and ^{Me}CAAC-BH_2NHMe are exothermic by 32.5 and 38.5 kcal/mol, both are strongly disfavored on kinetic grounds.

5.6.1 Diphenylsilane Complexes with Sterically and Electronically Modified NHCs

Lastly, the effects of altering the NHC backbone and modifying the flanking N-bound substitutents on the complexation ability of the resulting NHC with diphenylsilane were probed. Diphenylsilane has been chosen for this study because of the similarity in function to the rest of the silane species and also to BH_2NHMe. Moreover, aromatic silanes play an important role in synthetic chemistry and have been used in conjunction with NHCs to promote organic transformations [417]. The electronic and steric effects on the coordination chemistry of NHCs were studied by modifying three different functional groups about the NHC ring. The first change involved placing electron donating (Me and NMe_2) or electron accepting (CN and NO_2) residues on the C=C double bond backbone of an NHC (Figure 5.11). In the second

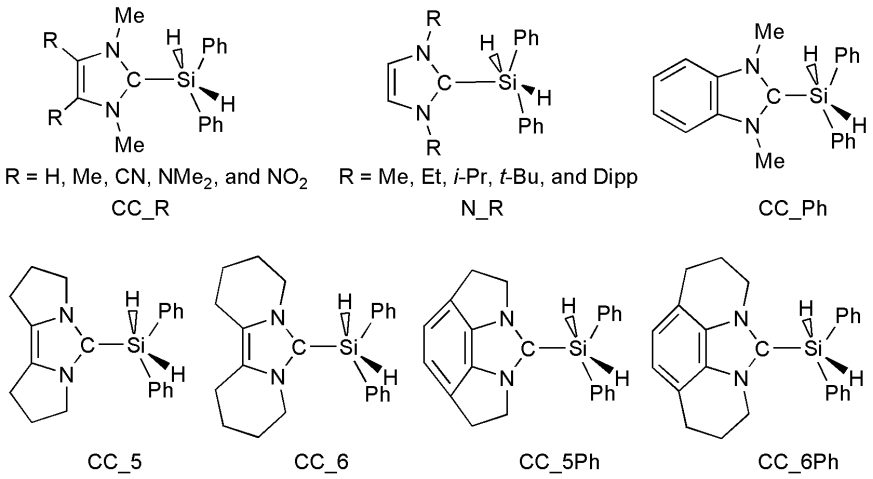

FIGURE 5.11: Different substituted NHC complexes with diphenylsilane.

alteration, the effect of steric hindrance on the coordination ability of an NHC was studied via replacing the nitrogen-bound Me substituents in $ImMe_2$ by Et, *i*-Pr, *t*-Bu, and Dipp.

TABLE 5.3: Relative Gibbs free energies (kcal/mol) for the corresponding ring expansion mechanisms of substituted $ImMe_2$ with SiH_2Ph_2 computed at the M06-2X/cc-PVDZ level of theory in PCM toluene.[a]

Species	NHC+SiH_2Ph_2	R	TS_1	I_1	TS_2	I_2	TS_3	P
CC-Me	0.0	14.3	30.4	5.0	33.6	27.0	33.1	–15.3
CC-NMe_2	0.0	10.1	24.5	–2.2	29.9	19.4	23.4	–25.1
CC-CN	0.0	23.9	34.0	2.5	24.6	17.0	22.7	–28.4
CC-NO_2	0.0	26.1	33.4	–3.0	10.6	7.6	18.0	–34.8
N-Me	0.0	20.1	30.3	6.3	32.0	16.7	23.9	–24.5
N-Et	0.0	13.1	29.8	3.9	28.7	14.0	20.7	–25.6
N-^{i}Pr	0.0	15.0	35.9	9.8	34.0	18.7	25.7	–21.7
N-^{t}Bu[b]	0.0	8.3	44.3	8.8	33.1	27.2	30.1	–20.3
N-Dipp	0.0	12.6	27.2	11.5	32.4	13.8	20.6	–29.2
CC-5	0.0	12.2	27.0	–1.1	25.4	4.7	11.1	–37.1
CC-5Ph	0.0	15.5	21.5	–25.7	–4.8	–38.4	–32.5	–83.2
CC-6	0.0	12.6	28.9	–3.2	32.2	24.1	30.1	–19.7
CC-6Ph	0.0	14.3	25.2	–5.4	25.4	14.1	16.7	–35.1
CC-Ph	0.0	18.6	29.7	–4.8	30.6	23.5	25.0	–27.4

[a]For the definition of the species (R, TS_1, I_1, TS_2, I_2, TS_3, P) along the reaction path see Figure 5.9.
[b]N-^{t}Bu only forms a weakly bonded complex with the silane compound.

Finally, the effect of ring fusion was studied by choosing different five- and six-membered backbones attached to the main NHC framework (Figure 5.11).

The energetic profiles associated with the ring expansion chemistry for all three families of compounds are given in Table 5.3, while the geometries of the optimized complexes are provided in Figure 5.12. It is readily apparent that the presence of electron donating groups (Me and NMe_2) on the C=C bond and phenyl ring fusion to an NHC backbone, all facilitate formation of stable SiH_2Ph_2 complexes (Table 5.3) in comparison to $ImMe_2$ (Figure 5.12).

Ring expansion chemistry for all the carbene-diphenylsilane complexes listed in Table 5.3 was found to be exothermic. As with $ImMe_2$-SiH_2Ph_2, the hydrogen migration/C-H bond formation, is the rate-determining step for each modified carbene except for the dimethylamino-appended donor, CC-NMe_2 $[(Me_2N)CNMe]_2C$:, where the second step, i.e. ring expansion, requires more energy. The most stable complex of the series in relation to ring expansion is N-^{t}Bu-SiH_2Ph_2 (N-^{t}Bu = $[(HCN^tBu)_2C:]$) with an energy barrier for the hydrogen-atom migration of 44.3 kcal/mol. On the other hand, the CC-5Ph complex with diphenylsilane seems to be very unstable as it shows the smallest barrier for the first step and also a highly thermodynamically favored ring expansion reaction.

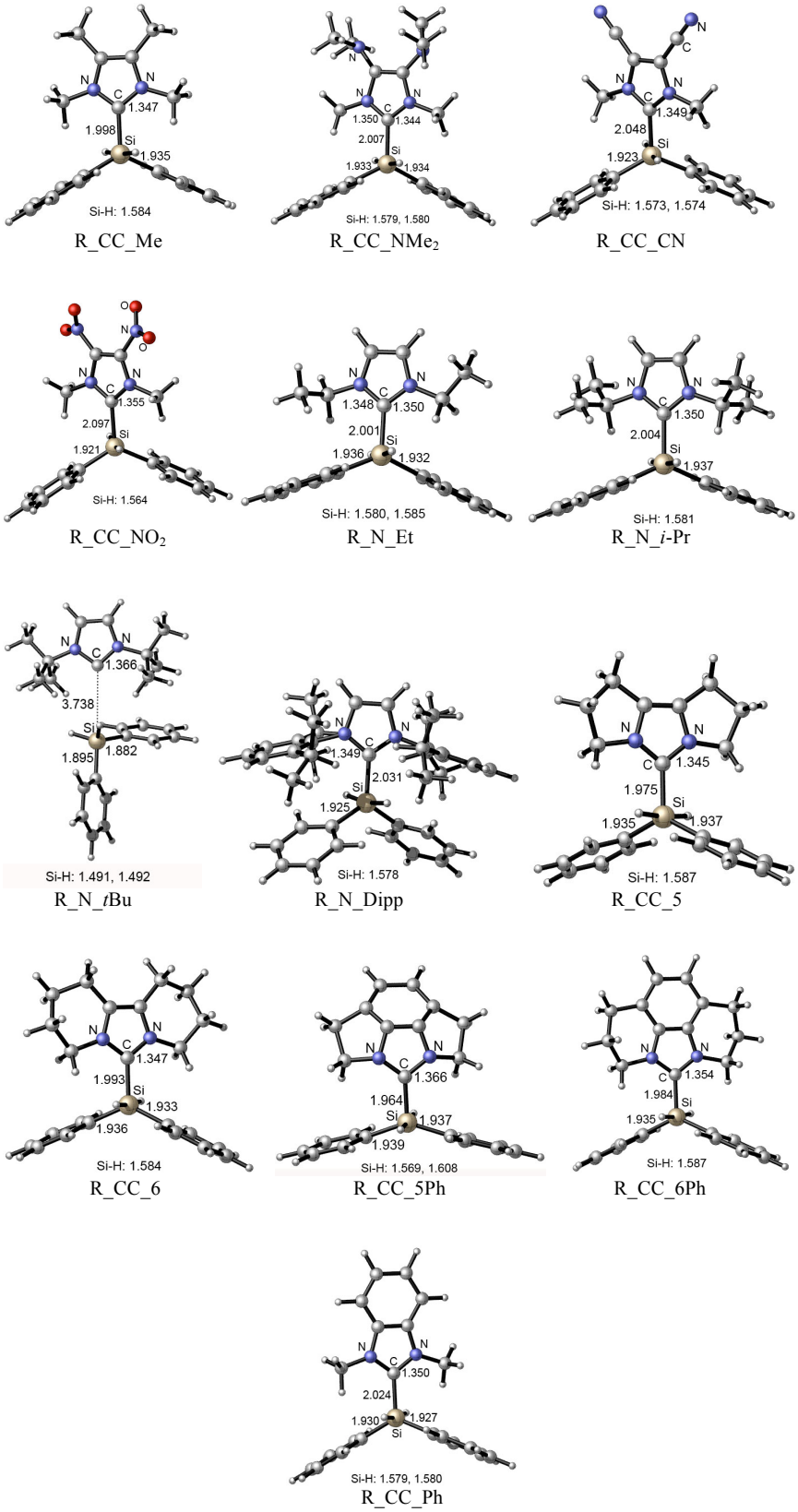

FIGURE 5.12: Optimized structures of substituted NHC complexes with SiH_2Ph_2 obtained at the M06-2X/cc-pVDZ level of theory in PCM toluene.

5.7 Conclusions

In summary, the abilities of different borane and silane adducts with $ImMe_2$ to undergo ring expansion chemistry have been studied using density functional theory computations in both the solution and gas phase. These results were compared with those obtained with the related cyclic alkyl amino carbene donor (^{Me}CAAC). A significant difference has been observed between these two carbenes in terms of the propensity of their element hydride complexes to participate in ring expansion chemistry, with the ^{Me}CAAC analogues showing facile hydride transfer chemistry from E-H bonds to carbon but with prohibitively high activation energies associated with subsequent ring expansion. In addition, the present computations show that formation of the ring expanded product from $ImMe_2$-BH_3 is kinetically unfavourable due to the high energy barrier for the H-atom migration from boron to carbon. The presence of a boron-bound π-donating amino group in $ImMe_2$-BH_2NHMe significantly decreases the energy barrier required for hydride transfer, leading to an energetically feasible ring opening reaction. These results are in good agreement with the experimental results of Rivard and coworkers, who reported no reaction for $ImMe_2$-BH_3 even after heating at 100 °C in toluene for three days. In the case of the silane adducts with NHC, the simultaneous presence of at least one hydrogen atom and one phenyl ring is crucial as ring expansion reaction is not likely to happen in the case of SiH_4 and $SiPh_4$, which is in agreement with experimental findings. Finally, the electronic and steric nature of the substituents attached to an N-heterocyclic carbene are shown to have an important impact on the stability of their adducts with diphenylsilane and also the propensity for ring expansion.

Chapter 6

Interplay of Donor–acceptor Interactions in Stabilizing Boron Nitride Compounds: Insights from Theory

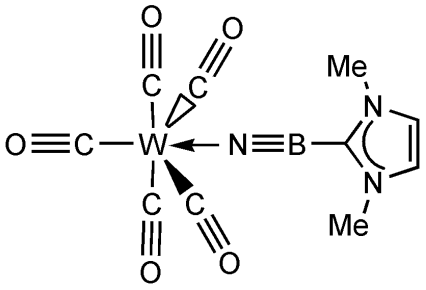

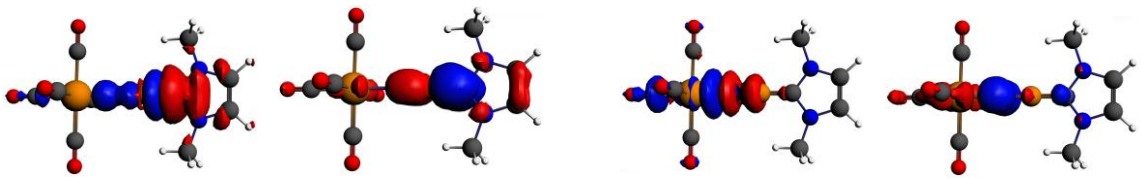

σ-donation –113.5 kcal/mol | π-backbonding –30.9 kcal/mol | σ-donation –31.6 kcal/mol | π-backbonding –10.7 kcal/mol

C–B Donor Bond | **N–W Acceptor Bond**

6.1 Boron-nitride Compounds

In this chapter we are concerned with stabilizing $(BN)_n$ (n = 1–3) compounds through Lewis base (LB) Lewis acid (LA) donor-acceptor interactions. The use of N-heterocyclic carbene (NHC) [418–420], N-heterocyclic olefin (NHO) [421–428] and Wittig ($R_3PCR'_2$) [192, 429, 430] donors is becoming prevalent in main group element chemistry. Accordingly $ImMe_2$, $ImMe_2CH_2$ and Me_3PCH_2 are chosen as donors within the boron nitride adduct series shown in Figure 6.1.

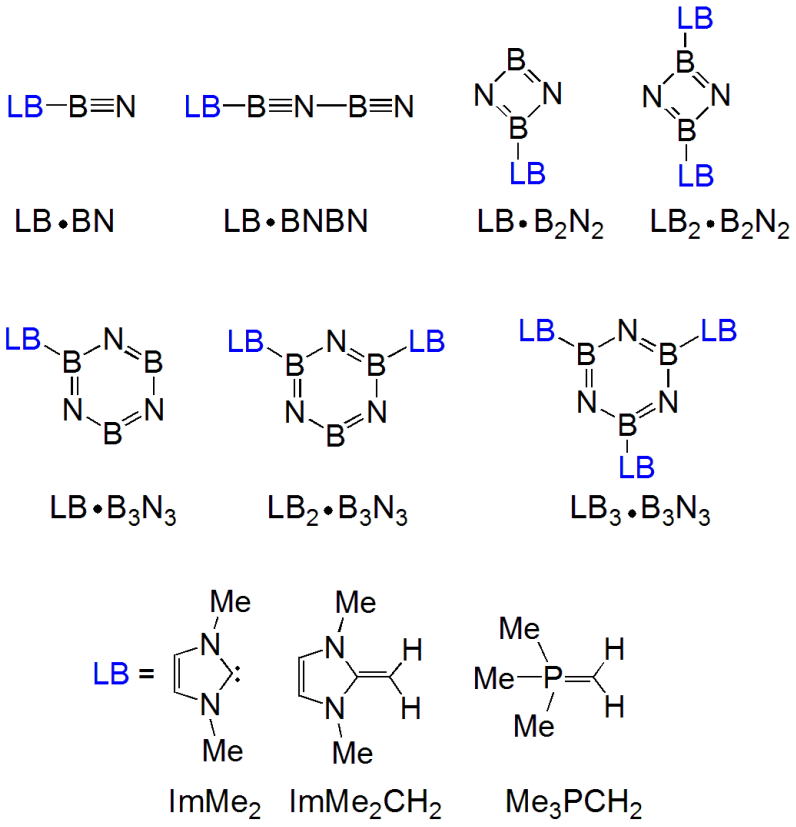

FIGURE 6.1: Lewis base (LB) bound $(BN)_n$ (n = 1–3) complexes considered in this chapter.

6.2 Methods

Geometry optimizations were performed using density functional theory (DFT) with the M05-2X [431] functional. The computations employed the following basis sets: cc-pVTZ [289, 290] for all period 1, 2 and 3 atoms and cc-pVTZ-PP [432, 433], combined with the corresponding small core (60 electrons) effective core potential (ECP) for tungsten (W). The

basis set and ECP for tungsten were obtained from the Basis Set Exchange [434, 435]. For convenience, these computations are simply labeled as M05-2X/cc-pVTZ throughout the text. Triplet states for BN, linear BNBN, and cyclic B_2N_2 were computed using an UHF reference. For geometry optimizations, "Tight" convergence criteria were applied: maximum force = 1.5×10^{-5} a.u., RMS force = 1.0×10^{-5} a.u., maximum displacement = 6.0×10^{-5}, and RMS displacement = 4.0×10^{-5}. The grid used for numerical integration in DFT was set to "Ultrafine" with a pruned grid of 99 radial shells and 590 angular points per shell. Harmonic vibrational frequencies were computed analytically at the same level of theory in order to characterize the stationary points as minima, representing equilibrium structures on the potential energy surfaces.

Energy decomposition analyses (EDA) were performed for all the mono-substituted complexes using the GGA BP86 density functional[236, 436] and the TZ2P basis set [437]; relativistic effects were considered for the tungsten atom using the ZORA approximation. As originally developed by Morokuma [438], Ziegler and Rauk [439], EDA analysis can provide valuable insight into the nature and strength of a bond. It decomposes the bond dissociation energy (D_e) between two fragments (A and B) into the interaction energy (ΔE_{int}) and the preparation energy (ΔE_{prep}):

$$D_e = \Delta E_{\text{int}} + \Delta E_{\text{prep}}. \tag{6.1}$$

The preparation energy, which pertains to the amount of energy required to distort and/or electronically excite the two fragments to their states in the complex, is defined as:

$$\Delta E_{\text{prep}} = E_A - E_A^0 + E_B - E_B^0. \tag{6.2}$$

$E_{A/B}$ and $E^0_{A/B}$ are the energies of the fragments for their geometries in the complex and as free ligands, respectively. To obtain these energies, all of the boron nitride, Lewis basic (LB) and Lewis acidic (LA) molecules as well as their complexes were re-optimized at the BP86/TZ2P level of theory. BP86/TZ2P optimized geometries show slightly (0.003-0.009 Å) shorter C–B and longer (0.001-0.029 Å) carbene attached B–N bonds compared to the geometries obtained by M05-2X. In the $ImMe_2CH_2$ and Me_3PCH_2 substituted adducts, the C–B and B–N bonds determined using BP86/TZ2P are 0.002-0.016 Å and 0.007-0.020 Å longer, respectively, than those determined using M05-2X/cc-pVTZ. Except in the case of the $ImMe_2CH_2$·BNBN and $ImMe_2CH_2$·B_3N_3 adducts, all the other BP86 optimized C-CH_2

and P-CH_2 ylidic bonds are 0.007-0.015 Å longer than the bond lengths obtained via M05-2X .

The interaction energy (ΔE_{int}) can be decomposed into three terms: (1) the Pauli exchange repulsion term (ΔE_{Pauli}), (2) the electrostatic interaction energy (ΔE_{elstat}) between charge densities of the fragments, and (3) the orbital interaction energy (ΔE_{orb}) which results from orbital mixing of the A and B fragments:

$$\Delta E_{\text{int}} = \Delta E_{\text{Pauli}} + \Delta E_{\text{elstat}} + \Delta E_{\text{orb}}. \tag{6.3}$$

The first term (ΔE_{Pauli}) is always positive while in most cases ΔE_{elstat} and ΔE_{orb} are negative. For more information regarding this method and its application in studying chemical bonds including donor-acceptor complexes the reader is referred to the literature [440–443].

The natural orbitals for chemical valence (NOCV) approach can be utilized to obtain both a qualitative and quantitative picture of the chemical bond (Eq. 6.4) [444]. In this approach, the deformation density $\Delta\rho(\text{r})$ is decomposed into pairwise ψ_k and ψ_{-k} complementary eigenfunctions (NOCVs) with eigenvalues of ν_k and ν_{-k} that have the same magnitude but opposite sign:

$$\Delta\rho(\text{r}) = \sum_{\text{k=1}}^{\text{N/2}} \nu_{\text{k}}[-\psi^2_{\text{-k}}(\text{r}) + \psi^2_{\text{k}}(\text{r})]. \tag{6.4}$$

Positive and negative values describe, respectively, density accumulation and density depletion; the bond forms through flowing electron density from the negative part of the molecule (shown later in red color) to the positive part (shown in blue). For quantitative results, one can represent the orbital interaction energy in terms of the NOCV eigenvectors:

$$\Delta E_{\text{orb}} = \sum_{\text{k=1}}^{\text{N/2}} \nu_{\text{k}}[-\text{F}^{\text{TS}}_{\text{-k,-k}} + \text{F}^{\text{TS}}_{\text{k,k}}]. \tag{6.5}$$

where $\text{F}^{TS}_{-k,-k}$ and $\text{F}^{TS}_{k,k}$ are diagonal transition state Kohn-Sham matrix elements over the corresponding NOCVs. Therefore, Eqs. 6.4 and 6.5 provide the qualitative and quantitative pictures of a chemical bond even for asymmetric complexes. For further details on this approach please see the original paper [444].

The nature of the bonding in the Lewis Base (LB) substituted adducts was also assessed using

both natural bonding orbital (NBO) [410] and atoms-in-molecules (AIM) [273] analyses. NBO population analyses were done at the M05-2X/cc-pVTZ level of theory by using the NBO suite available in Gaussian 09 [322]. AIM analyses were carried out at the same level of theory using the AIMAll software package [411]. Nucleus independent chemical shift (NICS) [445] computations were also performed using the gauge-independent atomic orbital (GIAO) method at the center of and 1 Å above the ring at the M05-2X/cc-pVTZ level of theory. All the electronic structure calculations were performed using Gaussian 09 [322] and ADF 2013 [446] packages.

6.3 Results and Discussion

6.3.1 Isolated $(BN)_n$ (n = 1–3) Molecules

The isolated $(BN)_2$ and $(BN)_3$ species, as well as higher oligomers, have been the subjects of numerous computational investigations [447–452]; monomeric BN has also been studied extensively [453–455]. Isolated BN is a challenging system as the lowest singlet and triplet states both have multi-reference character and are nearly isoenergetic [453–455]; the triplet state has been determined experimentally to be more stable by 0.71 ± 0.09 kcal/mol [456, 457]. The M05-2X/cc-pVTZ singlet-triplet gap is overestimated at 21.7 kcal/mol (with the triplet state as more stable) but this is in keeping with most DFT methods and also many ab initio approaches. However, the present work is focused on electronic and structural characterization of the singlet complexes rather than relative singlet-triplet energetics of the isolated species. For example, our computed M05-2X/cc-pVTZ bond lengths in the triplet and singlet states (1.315 Å and 1.261 Å, respectively) agree well with high-level CCSD(T)/aug-cc-pVQZ results of 1.329 Å and 1.270 Å(Figure 6.2).

Xu *et al.* have previously studied the singlet and triplet potential energy surfaces (PESs) of linear and cyclic B_2N_2 isomers by means of the coupled cluster CCSD method with the aug-cc-pVTZ basis set [447]. Cui *et al.* have recently examined the B_2N_2 isomers with CCSD(T) single point computations based on DFT geometries [448]. We will compare our results to the energies and geometries determined by Xu *et al.* as the relative stability of the linear isomers is strongly dependent on the electronic structure method used [448–450, 452]. For all the

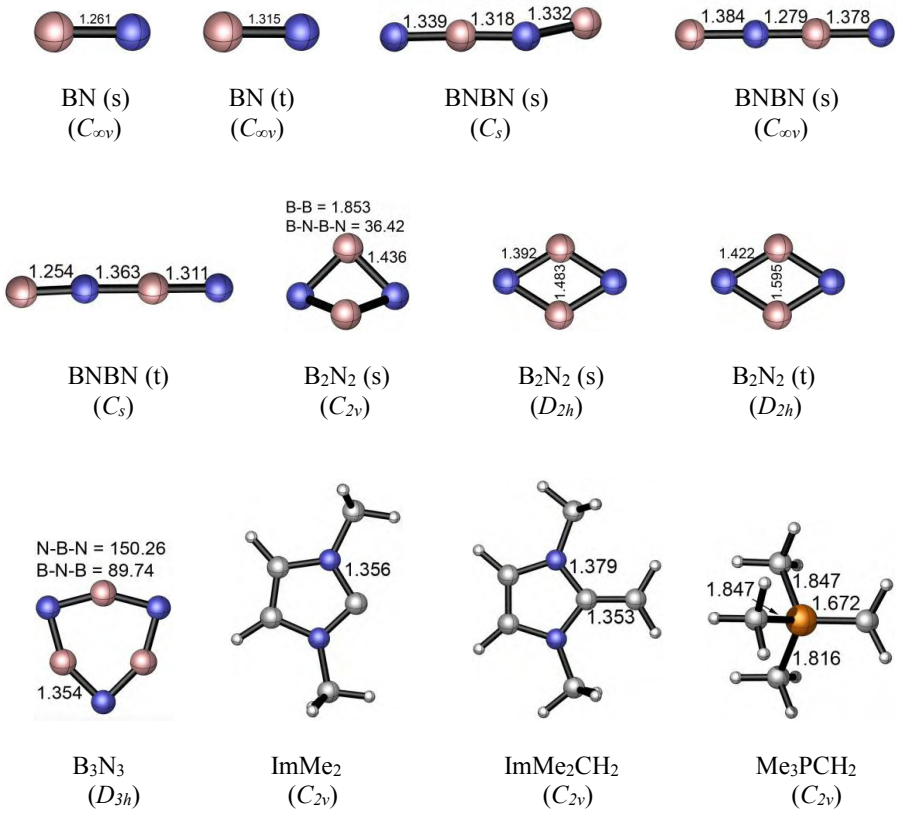

FIGURE 6.2: M05-2X/cc-pVTZ optimized structures of the isolated species in the gas phase.

B_2N_2 isomers studied, the triplet states were found to be more stable than their corresponding singlet electronic arrangements; cyclic B_2N_2 and linear BNBN in their triplet states being the two lowest energy structures and nearly isoenergetic [447, 448]. Cyclic B_2N_2 and linear BNBN will be the two B_2N_2 isomers considered in our study, where upon complexation they undergo spin-forbidden process to form the singlet complex. On the triplet PES, the cyclic isomer is 1.0 kcal/mol

(-0.3 kcal/mol) more stable than the linear form at the M05-2X/cc-pVTZ (CCSD/aug-cc-pVTZ) level of theory. On the singlet PES, the cyclic planar four-membered ring with D_{2h} symmetry is most stable and the linear $C_{\infty v}$ symmetric BNBN molecule is 25.1 kcal/mol higher in energy. The linear isomer with BNBN connectivity is 14.7, 20.9, and 46.6 kcal/mol more stable than the BNNB, NBBN, and BBNN isomers, respectively. They also concluded on the basis of short transannular B–B distances that a B–B bond exists within the singlet B_2N_2 heterocycle. Overall, our M05-2X/cc-pVTZ optimized geometries of linear BNBN and the D_{2h} symmetric B_2N_2 rings are in reasonable agreement with the CCSD geometries determined by Xu *et al.* (Figure 6.2). However, singlet BNBN was found to adopt C_s symmetry

as a global minimum instead of the reported $C_{\infty v}$ symmetry, with the former geometry being 6.3 kcal/mol more stable than the latter at the M05-2X/cc-pVTZ level of theory. The calculated B-N bond lengths of the BNBN isomer at the M05-2X/cc-pVTZ level of theory (CCSD/aug-cc-pVTZ values in parentheses), with C_s ($C_{\infty v}$) symmetries, are 1.339 (1.397), 1.318 (1.289), and 1.332 (1.381) Å, respectively. The corresponding B-N bonds within the cyclic isomer B_2N_2 are each 1.392 (1.403) Å with a computed cross-ring B$\cdots$B distance of 1.483 (1.491) Å. Additionally, the computed singlet-triplet gap (ΔE_{S-T}) value for the B_2N_2 molecule at the CCSD/aug-cc-pVTZ (20.0 kcal/mol) level of theory compares well with the ΔE_{S-T} value of 13.2 kcal/mol obtained using M05-2X/cc-pVTZ; the corresponding M05-2X (CCSD) ΔE_{S-T} values for the BNBN molecule are 40.1 (46.6) kcal/mol.

For B_3N_3, only the singlet isomer has been considered as all other isomers (regardless of spin-state) are significantly higher in energy [449, 451]; for example, linear BNBNBN in its triplet state is 75.2 kcal/mol higher in energy than the cyclic isomer in its singlet state at the CCSD(T)/cc-pVDZ level of theory [451]. The B–N bond lengths in B_3N_3 are determined in the present M05-2X/cc-pVTZ study to be 1.354 Å; this is within 0.03 Å of the 1.3763 Å computed by Martin *et al.* [451] at the CCSD(T)/cc-pVDZ level of theory. The M05-2X/cc-pVTZ computed B–N bond lengths in singlet cyclo-B_3N_3 decrease on average by 0.038 Å in relation to the intraring B–N distances in singlet cyclo-B_2N_2; this suggests a greater degree of B–N intraring resonance stabilization within B_3N_3 in relation to the B_2N_2, as later determined by NICS computations (see Table 6.1).

Overall, the optimized M05-2X/cc-pVTZ geometries and relative energies of the isolated $(BN)_n$ ($n = 1-3$) are in good agreement with available coupled cluster data, and hence we chose to conduct the remaining computations using the M05-2X/cc-pVTZ level of theory.

6.3.2 Geometries of the Lewis Base (LB) Adducts LB·$(BN)_n$ (n = 1–3)

The M05-2X/cc-pVTZ optimized geometries of the mono-ligated boron nitride oligomers, LB·$(BN)_n$ (n = 1–3), are depicted in Figure 6.3 (LB = $ImMe_2$, $ImMe_2CH_2$, and Me_3PCH_2). In each case, the carbon-based donors were bound to electron deficient boron sites, in line with prior adduct formation with amino-boranes (R_2N-BH_2) [150, 458–460]. The NHC-bound adducts of the BN chains, $ImMe_2$·BN and $ImMe_2$·BNBN, each adopt linear C_{ImMe_2}–$(BN)_n$

TABLE 6.1: Calculated NICS values of the B_2N_2 and B_3N_3 rings of the studied complexes at the M05-2X/cc-pVTZ level of theory. The corresponding values are computed for benzene (C_6H_6) and cyclobutadiene (C_2H_4) as aromatic and anti-aromatic molecules, respectively.

Species	NICS (0.0)	NICS $(0.0)_{zz}$	NICS (1.0)	NICS $(1.0)_{zz}$
B_2N_2	–44.50	–73.09	–6.28	–15.12
B_3N_3	–9.88	–7.04	–2.64	–6.51
C_2H_4	+33.58	+127.38	+20.85	+65.77
C_6H_6	–7.41	–16.09	–10.56	–31.06
$ImMe_2{\cdot}B_2N_2$	–11.03	–12.79	+1.29	+8.46
$(ImMe_2)_2{\cdot}B_2N_2$	+6.06	+36.05	+5.13	+13.74
$ImMe_2{\cdot}B_3N_3$	–6.24	+1.02	–3.52	–7.43
$(ImMe_2)_2{\cdot}B_3N_3$	–3.61	+2.42	–3.92	–8.55
$(ImMe_2)_3{\cdot}B_3N_3$	–1.02	–4.96	–3.97	–2.02
$ImMe_2CH_2{\cdot}B_2N_2$	–12.82	+25.83	+0.47	+8.60
$(ImMe_2CH_2)_2{\cdot}B_2N_2$	+4.42	+22.52	+3.06	+9.04
$ImMe_2CH_2{\cdot}B_3N_3$	–5.67	–11.08	–3.12	–0.20
$(ImMe_2CH_2)_2{\cdot}B_3N_3$	–3.56	+1.50	–3.87	–3.19
$(ImMe_2CH_2)_3{\cdot}B_3N_3$	–1.96	+2.45	–3.71	–2.37
$Me_3PCH_2{\cdot}B_2N_2$	-13.87	–19.71	–1.17	+2.55
$(Me_3PCH_2)_2{\cdot}B_2N_2$	+7.07	+36.58	+3.67	+12.62
$Me_3PCH_2{\cdot}B_3N_3$	–6.15	+1.42	–3.31	–6.95
$(Me_3PCH_2)_2{\cdot}B_3N_3$	–2.92	+5.36	–3.16	–6.39
$(Me_3PCH_2)_3{\cdot}B_3N_3$	–0.91	+4.71	–3.78	–3.37

configurations; geometry optimizations initiated with non-linear configurations return to linearity. On the other hand, appreciably bent C–B–N and intrachain N–B–N angles are found within the related $ImMe_2CH_2$ and Me_3PCH_2-capped boron nitride adducts. For example, the C–B–N angles of the $ImMe_2CH_2$ substituted BN and BNBN adducts are 162.57° and 152.26°, respectively, and the C–B–N bond angles are 156.50° and 156.32° for the corresponding Me_3PCH_2 substituted analogues. In general, within the monoadducts, the B_2N_2 and B_3N_3 rings adopt planar geometries; the B_3N_3 rings in $ImMe_2$ and $ImMe_2CH_2$ are slightly puckered. The B–N bond lengths involving the donor-bound boron atoms in these B_2N_2 and B_3N_3 rings are each *ca.* 0.12 Å longer than the remaining B–N bonds involving donor-free, two coordinate boron centers. This bond lengthening implies an increase in B–N π-interactions and/or enhanced ionic contribution to the B–N σ-bonds. Within the $ImMe_2$ monoadduct series, the formally dative C–B linkages range from 1.510 Å in the terminal

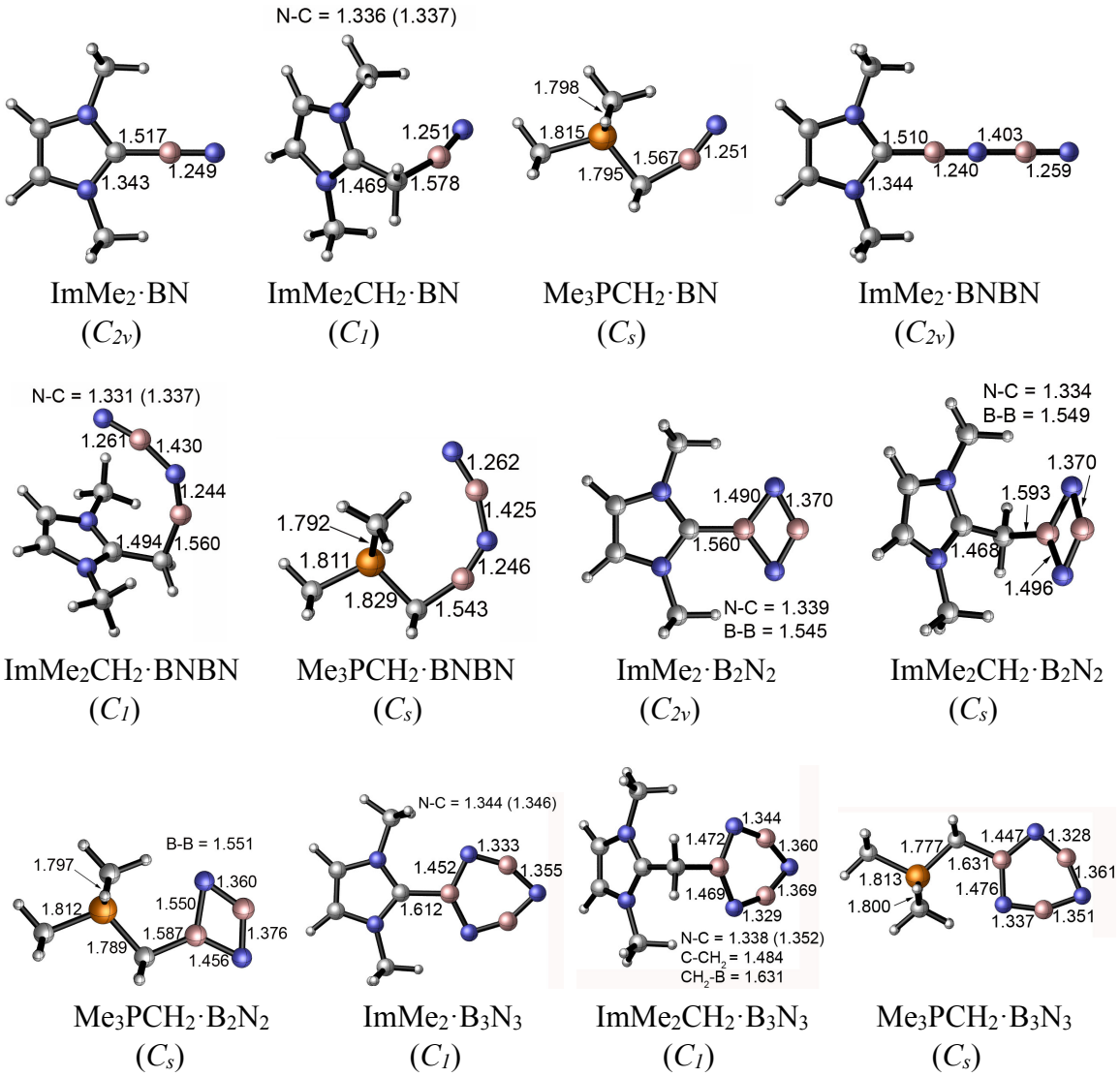

FIGURE 6.3: M05-2X/cc-pVTZ optimized geometries including important bond lengths and corresponding symmetries of the mono-substituted adducts in the gas phase.

adduct $ImMe_2$·BNBN to elongated values of 1.560 and 1.612 Å in the heterocyclic B_2N_2 and B_3N_3 adducts. For comparison, the C–B bond length in the coordinatively saturated amino-borane adduct IPr·BH_2-NHDipp (IPr = [(HCNDipp)$_2$C:]; Dipp = 2,6-^{i}Pr$_2$C$_6$H$_3$) was determined to be 1.627(4) Å [150], while in the diboryne adduct IPr·B≡B·IPr this bond length is 1.491(4) Å (avg.) [141]. In general the computed C–B bonds in the $ImMe_2$ adducts were shorter by *ca.* 0.02 to 0.05 Å compared to the corresponding $ImMe_2CH_2$ and Me_3PCH_2 complexes; of note, it has been found that *N*-heterocyclic carbenes are stronger σ-donors than their *N*-heterocyclic olefin counterparts (such as IPrCH$_2$) [424]. The coordination of

the Me_3PCH_2 units to boron leads to a large increase in the ylidic P–C bond length from 1.672 Å in the free ligand to bond length values as long as 1.829 Å in Me_3PCH_2·BNBN. This observation could be traced to a reduction of $H_2C{\rightarrow}P{-}C(\sigma^*)$ hyperconjugative interactions [192, 461] in Me_3PCH_2 as the terminal CH_2 unit participates in coordination to boron. The same phenomenon can be observed in the case of the $ImMe_2CH_2$ adducts: the terminal C–C bond length increases from 1.353 Å in the free ligand to 1.494 Å in the BNBN substituted adduct $ImMe_2CH_2$·BNBN.

The M05-2X/cc-pVTZ optimized geometries of the di- and tri-substituted adducts (LB·$(BN)_n$, n = 2 and 3) are depicted in Figure 6.4. In general, addition of a second equivalent of Lewis base to the B_2N_2 and B_3N_3 units leads to elongation of the average C–B bond length. The C–B bonds increase in length by *ca.* 0.06-0.09 Å for the B_2N_2 rings, while a more modest increase of *ca.* 0.01 to 0.04 Å was noted upon binding two donors to a B_3N_3 unit. Despite the planar nature of the B_2N_2 rings, the intraring B–N distances within the bis-adducts $(ImMe_2)_2$·B_2N_2, $(ImMe_2CH_2)_2$·B_2N_2, and $(Me_3PCH_2)_2$·B_2N_2 all lie within a narrow range of 1.440 to 1.448 Å and suggest the absence of strong B–N π-bonding. To compare, iminoboranes (RB≡NR′) have B–N triple bond lengths in the range of 1.23 to 1.26 Å [462–465], while the diborylamide anion $[Mes_2B{=}N{=}BMes_2]^-$ (Mes = 2,4,6-$Me_3C_6H_2$), which has significant B=N double bond character, has B–N lengths of 1.343(5) and 1.348(5) Å [466]. The central B_3N_3 units in each complex adopt nearly planar arrangements with intraring B–N bond lengths that are typical for short B–N single bonds (1.404 to 1.436 Å). Each of the coordinative C–B distances are slightly longer in $(ImMe_2)_3$·B_3N_3 (1.645 to 1.655 Å) in relation to the values found in the bisadduct $(ImMe_2)_2B_3N_3$ (1.622 Å). The ylide-bound tris adducts $(Me_3PCH_2)_3$·B_3N_3 and $(ImMe_2CH_2)_3$·B_3N_3 feature very long C–B bonds of 1.717–1.732 and 1.687–1.702 Å, respectively, suggesting that these species would have reduced stability.

Very recently, Tai and Nguyen have studied the stability of $(ImMe_2{\cdot}B)_n$ (n = 1–6) adducts using quantum mechanical computations with the B3LYP method [467]. They attributed the stability of these systems to the degree of π conjugation and aromatic character within the core B_n (n = 3-6) rings. In order to probe the aromaticity in the $(BN)_x$ rings, NICS analyses of the free (singlet) B_2N_2 and B_3N_3 molecules as well as their adducts were performed using the GIAO method at the M05-2X/cc-pVTZ level of theory (Table 6.1). The NICS results were compared to the corresponding values determined at the same level of theory for well

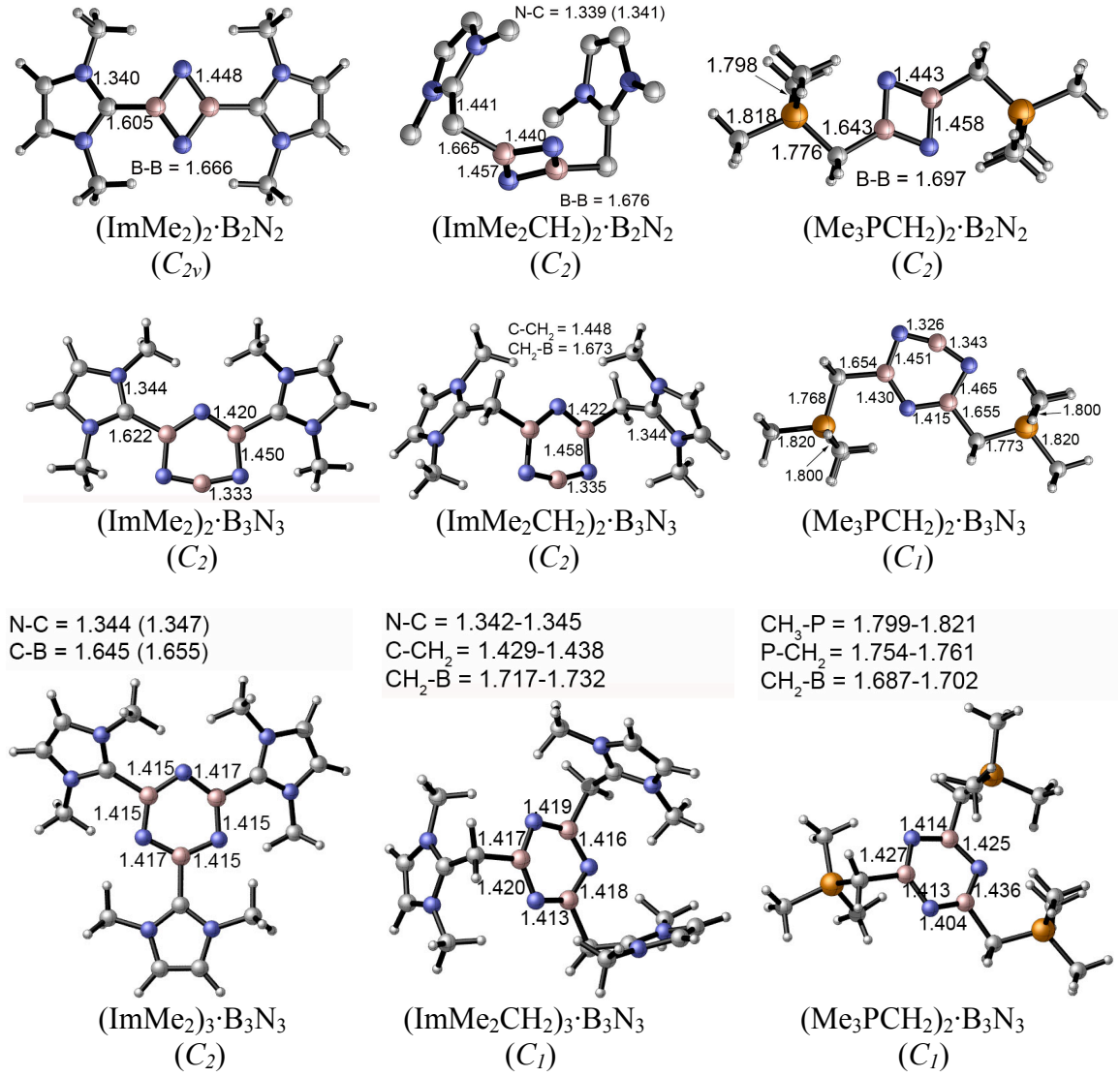

FIGURE 6.4: M05-2X/cc-pVTZ optimized geometries and symmetries of the di- and tri-substituted adducts in the gas phase (C–H bonds are omitted in the case of $(ImMe_2CH_2)_2{\cdot}B_2N_2$ for clarity).

known aromatic benzene and anti-aromatic cyclobutadiene molecules to examine changes in aromaticity upon binding of Lewis bases. NICS data are sensitive to the position at which they are evaluated and to interference from other parts of the molecule, especially for non-planar compounds [184]. The changes in aromaticity/anti-aromaticity are discussed in terms of NICS $(1.00)_{zz}$ values (see Table 6.1). Interestingly, NICS $(1.00)_{zz}$ values show aromatic character for the free B_2N_2 and B_3N_3 molecules (–15.12 and –6.51 ppm, respectively, compared to –31.06 ppm for benzene). However, the free B_2N_2 loses aromatic character upon binding of one LB ligand (i.e., NICS $(1.00)_{zz}$ values of +2.55, +8.46, and +8.60 ppm for B_2N_2 complexed with Me_3PCH_2, $ImMe_2$, and $ImMe_2CH_2$, respectively). For the doubly-bound

adducts, $(LB)_2{\cdot}B_2N_2$, the B_2N_2 unit becomes significantly anti-aromatic: +12.62, +13.94, and +9.04 ppm for the Me_3PCH_2, $ImMe_2$, and $ImMe_2CH_2$ adducts, respectively (see Table 6.1). On the other hand, B_3N_3 remains moderately aromatic upon attachment of 1, 2, or 3 equivalents of Lewis base. The NICS $(1.00)_{zz}$ decrease upon attaching two Lewis bases to the B_3N_3 ring with values of –8.55 and –3.19 ppm for $ImMe_2$ and $ImMe_2CH_2$ ligands, respectively, but slightly increases from –6.95 ppm to –6.39 ppm upon attaching the second Me_3PCH_2 ligand. For the case of the three LB bound adducts, the NICS $(1.00)_{zz}$ values all increase (–2 to –3 ppm) upon attachment of the third ligand (Table 6.1).

6.3.3 Energies of the Lewis Base (LB) Bound LB·$(BN)_n$ (n = 1–3) Adducts

The total stabilization energies and Gibbs free energies of the $(BN)_n$ (n = 1–3) molecules upon complexation with the three Lewis bases were computed using the M05-2X/cc-pVTZ level of theory and the results are summarized in Table 6.2 (for the graphs of stabilization energies see Figure 6.5). The sequential stabilization energies, $\Delta E_{seq.}$, $(\Delta E + ZPE)_{seq.}$, and $\Delta G^{\circ}_{seq.}$, which take into account the impact of adding one additional Lewis base to the existing $(LB)_x{\cdot}B_2N_2$ and $(LB)_x{\cdot}B_3N_3$ ($x = 0 - 2$) complexes were also evaluated.

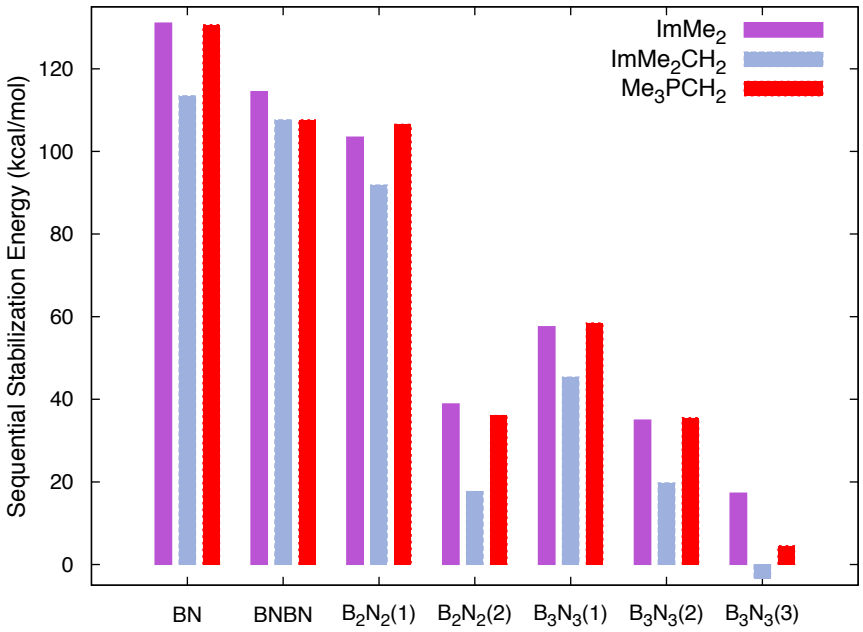

FIGURE 6.5: Graph of the computed M052X/cc-pVTZ sequential Gibbs free stabilization energies (in kcal/mol) of all the adducts studied in this work. Numbers in parenthesis denote the number of Lewis base molecules attached to the B_2N_2 and B_3N_3 molecules. See Table 6.2 for the values.

TABLE 6.2: Computed total[(a)] and sequential[(b)] stabilization energies (in kcal/mol), with *ZPE* ($\Delta E + ZPE$) and without *ZPE* (ΔE), and free energies ($\Delta G°$) at the M05-2X/cc-pVTZ level of theory.

Species	$\Delta E_{tot}{}^{(a)}$	$(\Delta E + ZPE)_{tot}{}^{(a)}$	$\Delta G°_{tot}{}^{(a)}$	$\Delta E_{seq.}{}^{(b)}$	$(\Delta E + ZPE)_{seq.}{}^{(b)}$	$\Delta G°_{seq.}{}^{(b)}$
$ImMe_2$·BN	–144.1	–140.5	–131.1	–	–	–
$ImMe_2CH_2$·BN	–128.6	–123.8	–113.5	–	–	–
Me_3PCH_2·BN	–145.7	–141.0	–130.7	–	–	–
$ImMe_2$·BNBN	–129.5	–124.9	–114.5	–	–	–
$ImMe_2CH_2$·BNBN	–126.6	–120.6	–107.7	–	–	–
Me_3PCH_2·BNBN	–145.3	–139.7	–127.0	–	–	–
$ImMe_2$·B_2N_2	–118.2	–114.8	–103.5	–118.2	–114.8	–103.5
$(ImMe_2)_2$·B_2N_2	–171.8	–165.9	–142.4	–53.6	–51.2	–38.9
$ImMe_2CH_2$·B_2N_2	–108.6	–104.0	–91.9	–108.6	–104.0	–91.9
$(ImMe_2CH_2)_2$·B_2N_2	–143.4	–136.1	–109.6	–34.8	–32.0	–17.7
Me_3PCH_2·B_2N_2	–121.8	-117.7	–106.6	–121.8	–117.7	–106.6
$(Me_3PCH_2)_2$·B_2N_2	–172.5	–166.2	–142.7	–50.7	–48.4	–36.1
$ImMe_2$·B_3N_3	–71.5	–68.7	–57.6	–71.5	–68.7	–57.6
$(ImMe_2)_2$·B_3N_3	–122.9	–117.5	–92.6	–51.4	–48.9	–35.0
$(ImMe_2)_3$·B_3N_3	–153.6	–147.4	–109.9	–30.7	–29.9	–17.3
$ImMe_2CH_2$·B_3N_3	–61.0	–57.4	–45.4	–61.0	–57.4	–45.4
$(ImMe_2CH_2)_2$·B_3N_3	–97.9	–91.2	–65.3	–36.9	–33.8	–19.8
$(ImMe_2CH_2)_3$·B_3N_3	–110.8	–102.0	–61.9	–12.9	–10.8	+3.4
Me_3PCH_2·B_3N_3	–72.8	–69.7	–58.5	–72.8	–69.7	–58.5
$(Me_3PCH_2)_2$·B_3N_3	–121.1	–116.3	–94.1	–48.4	–46.6	–35.6
$(Me_3PCH_2)_3$·B_3N_3	–141.5	–133.1	–96.3	–21.1	–18.4	–4.6

[(a)]For the reaction: $(BN)_n + x$·LB → $(LB)_x$·$(BN)_n$ (n = 1–3, x = 1–3).
[(b)]For the reaction: LB_x·$(BN)_n$ + LB → $(LB)_{x+1}$·$(BN)_n$ (n = 1–3, x = 0–2).

Notably, in two separate articles, Jones, Frenking and co-workers have studied the $ImMe_2$- and phosphine-bound Group 13 element complexes along with their possible applications for hydrogen storage [468, 469]. More specifically, they found that the Gibbs free energies of –29.8 and –45.8 kcal/mol for the Me_3P and $ImMe_2$ bound BH_3 adducts, respectively, at the RI–BP86/def2-TZVPP level of theory; which is very close to the –46.9 kcal/mol computed for the latter complex, $ImMe_2$·BH_3, at the M06-2X/cc-pVDZ level of theory [470]. In another recent study, Sarmah *et al.* examined complexes of normal and abnormal *N*-heterocyclic carbenes with Group 13 element based Lewis acids (EX_3; E = B, Al, Ga; X = H, F, Cl, OH, NH_2, CH_3, CF_3) and performed corresponding NBO and AIM analyses of the adducts [471]. They computed a complexation energy of –49.2 kcal/mol at the B3LYP/6-31+G* level of theory for the $ImMe_2$·BH_3 adduct which is close to the values found previously by Frenking, Jones and co-workers [468, 469] as well as Brown and coworkers [470]. The complexation (stabilization)

energy associated with the formation of our mono-substituted $(BN)_n$ (n = 1–3) adducts was computed to be greater than –100 kcal/mol for all species except the B_3N_3 adducts, where zero-point corrected energies (ΔE + ZPE) are in the range of –57.4 to –69.7 kcal/mol. The ZPE correction to the electronic energies changes the value of ΔE by $\sim$ 4-10 kcal/mol. The Gibbs free energy differences are also lower than the ZPE corrected values by $\sim$ 10-40 kcal/mol. For the sake of brevity and consistency, the Gibbs free energy differences will be discussed throughout the text. We will comment on the nature of the formed carbene-boron bonds including their degrees of ionic/covalent character based on EDA as well as NBO/AIM analyses. The gap between the highest occupied molecular orbital (HOMO) and the lowest unoccupied molecular orbital (LUMO) increases for most of the boron nitride species upon binding of the carbon-based ligands; the exceptions to this trend are the Lewis base bound B_3N_3 adducts (Figure 6.6).

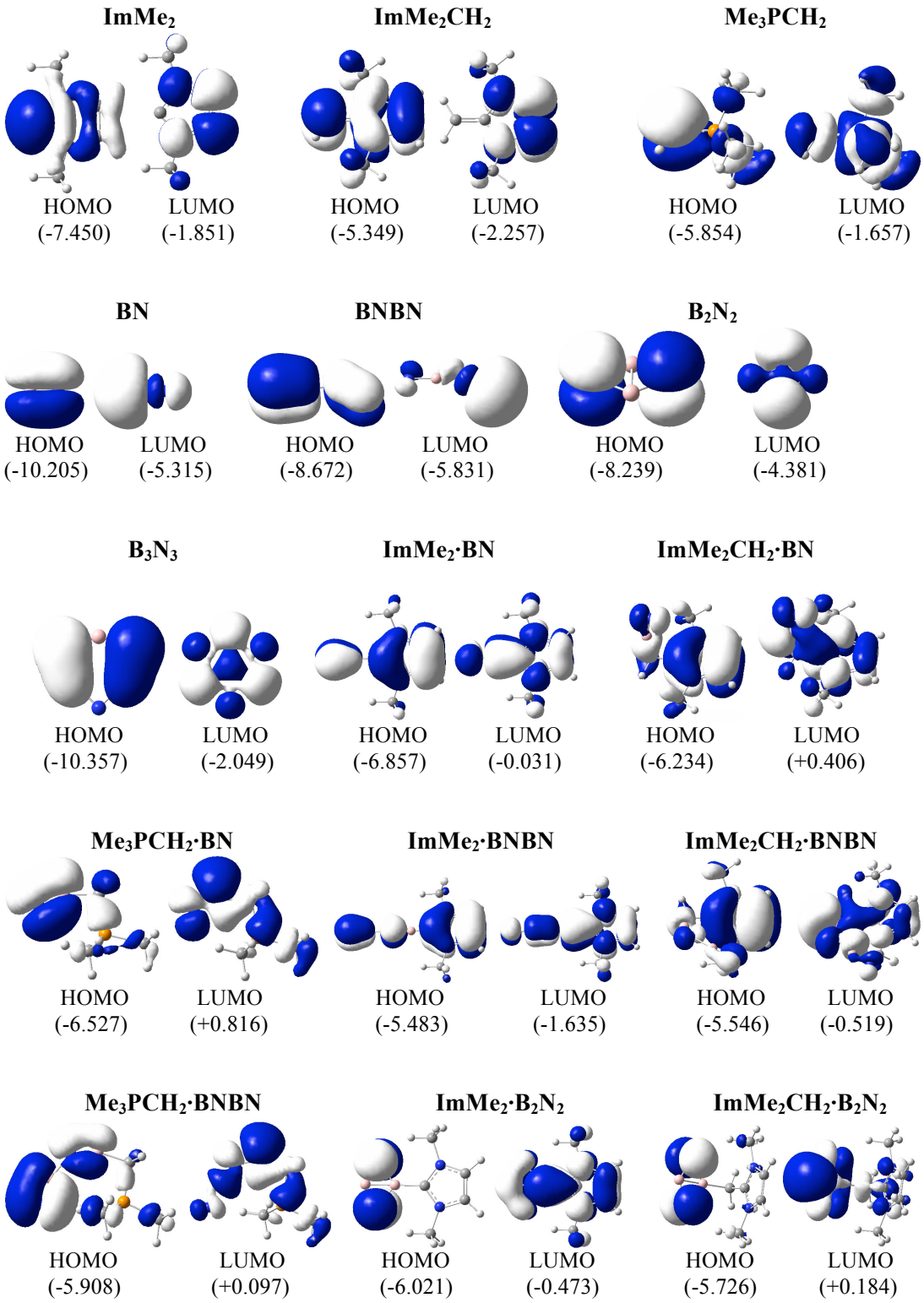
ImMe2
HOMO (-7.450)
LUMO (-1.851)
ImMe2CH2
HOMO (-5.349)
LUMO (-2.257)
Me3PCH2
HOMO (-5.854)
LUMO (-1.657)
BN
HOMO (-10.205)
LUMO (-5.315)
BNBN
HOMO (-8.672)
LUMO (-5.831)
B2N2
HOMO (-8.239)
LUMO (-4.381)
B3N3
HOMO (-10.357)
LUMO (-2.049)
ImMe2·BN
HOMO (-6.857)
LUMO (-0.031)
ImMe2CH2·BN
HOMO (-6.234)
LUMO (+0.406)
Me3PCH2·BN
HOMO (-6.527)
LUMO (+0.816)
ImMe2·BNBN
HOMO (-5.483)
LUMO (-1.635)
ImMe2CH2·BNBN
HOMO (-5.546)
LUMO (-0.519)
Me3PCH2·BNBN
HOMO (-5.908)
LUMO (+0.097)
ImMe2·B2N2
HOMO (-6.021)
LUMO (-0.473)
ImMe2CH2·B2N2
HOMO (-5.726)
LUMO (+0.184)

$Me_3PCH_2{\cdot}B_2N_2$

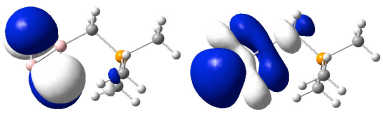

HOMO (-5.783) LUMO (+0.711)

$(ImMe_2)_2{\cdot}B_2N_2$

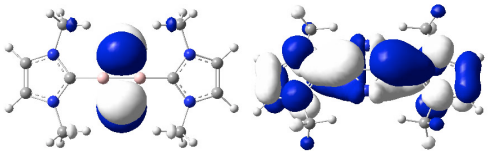

HOMO (-4.320) LUMO (+0.553)

$(ImMe_2CH_2)_2{\cdot}B_2N_2$

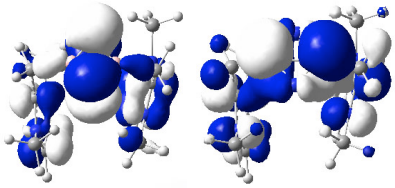

HOMO (-4.110) LUMO (+1.137)

$(Me_3PCH_2)_2{\cdot}B_2N_2$

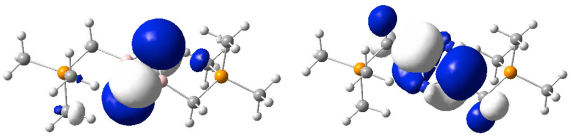

HOMO (-3.968) LUMO (+1.586)

$ImMe_2{\cdot}B_3N_3$

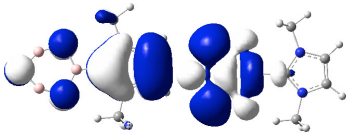

HOMO (-8.073) LUMO (-0.082)

$ImMe_2CH_2{\cdot}B_3N_3$

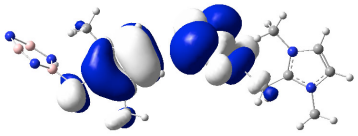

HOMO (-7.833) LUMO (+0.406)

$Me_3PCH_2{\cdot}B_3N_3$

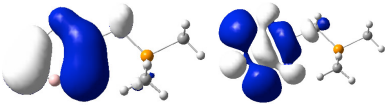

HOMO (-7.760) LUMO (+0.800)

$(ImMe_2)_2{\cdot}B_3N_3$

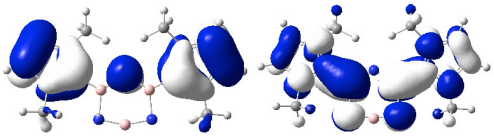

HOMO (-6.392) LUMO (+0.717)

$(ImMe_2CH_2)_2{\cdot}B_3N_3$

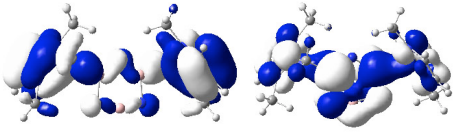

HOMO (-5.932) LUMO (+1.262)

$(Me_3PCH_2)_2{\cdot}B_3N_3$

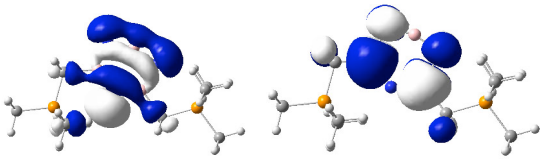

HOMO (-5.460) LUMO (+1.509)

$(ImMe_2)_3{\cdot}B_3N_3$

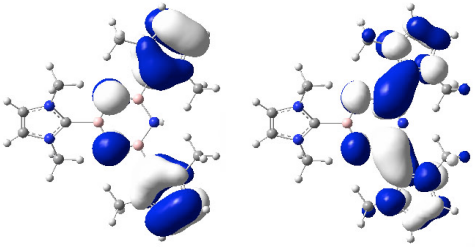

HOMO (-5.340) LUMO (+1.383)

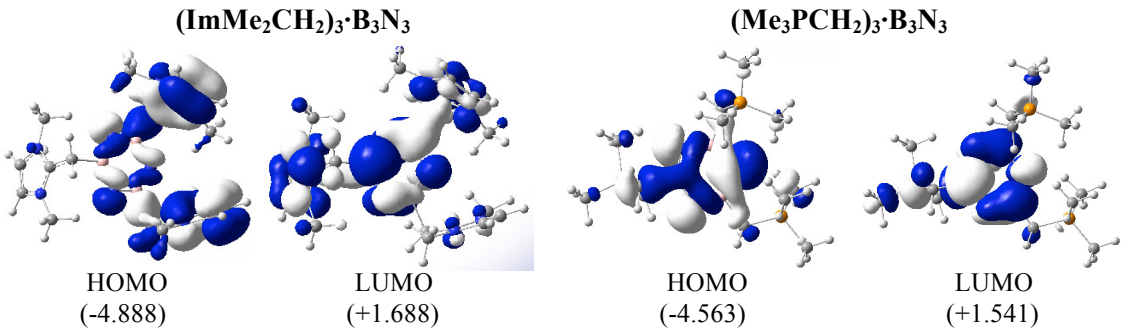

FIGURE 6.6: MOs of all the studied structures (isovalue = 0.02 e/Å^3) computed at the M05-2X/cc-pVTZ level of theory. Energies (in eV) are also given in parentheses.

The free energies associated with the sequential addition of Lewis base equivalents to molecular B_2N_2 and B_3N_3 molecules ($\Delta G^{\circ}_{seq.}$) follow the general trend that it becomes increasingly less favourable to bind multiple donors to these rings (Figure 6.5). This effect can be explained by a decrease in Lewis acidity of the $(BN)_n$ rings as electron density is being donated from the carbon-based ligands; this phenomenon can be easily observed from the gradual destabilization of the LUMO energy levels of the B_2N_2 and B_3N_3 rings after addition of the Lewis bases (Figure 6.6). Overall, the binding of subsequent equivalents of Lewis base to the BN rings is exergonic, however, a slightly disfavoured binding event was computed for the formation of the tris adduct $(ImMe_2CH_2)_3{\cdot}B_3N_3$ (+3.4 kcal/mol), placing this species on the cusp of stability.

6.3.4 Bonding Properties through NBO and AIM Analyses

NBO and AIM computations were performed on all $(BN)_n$ species including their free and as well as their ligand bound forms at the M05-2X/cc-pVTZ level of theory (Table 6.3; for the NBO and AIM analyses of all compounds see Appendix D).

TABLE 6.3: Selected NBO atomic charges of the carbene carbon and boron atoms (q_C and q_B) along with the total charge of the acceptor molecules (q_{LA}), Wiberg bond indices (WBI) of the C–B and B–N bonds, and the electron density (ρ) and energy density at the bond critical points ($H_{(C-B)}$ and $H_{(B-N)}$) for all the mono-substituted species at the M05-2X/cc-pVTZ level of theory. B–N values refer to bonds adjacent to the carbene carbon atom. Values in parentheses correspond to two different B–N bonds connected to the carbene carbon atom.

Species	q_C	q_B	q_{LA}	WBI_{C-B}	WBI_{B-N}	$\rho(r_{C-B})$	$H(r_{C-B})$	$\rho(r_{B-N})$	$H(r_{B-N})$
$ImMe_2$·BN	+0.203	+0.230	–0.524	0.944	2.622	0.179	–0.175	0.300	–0.324
$ImMe_2CH_2$·BN	–0.821	+0.367	–0.551	0.772	2.656	0.163	–0.158	0.298	–0.324
Me_3PCH_2·BN	–1.046	+0.382	–0.565	0.872	2.604	0.166	–0.162	0.299	–0.325
$ImMe_2$·BNBN	+0.140	+0.608	–0.553	0.966	2.062	0.189	–0.193	0.290	–0.295
$ImMe_2CH_2$·BNBN	–0.794	+0.838	–0.628	0.898	2.018	0.180	–0.184	0.298	–0.320
Me_3PCH_2·BNBN	–1.075	+0.858	–0.603	0.931	1.997	0.185	–0.191	0.298	–0.322
$ImMe_2$·B_2N_2	+0.235	+0.654	–0.651	0.861	0.998	0.171	–0.170	0.192	–0.199
$ImMe_2CH_2$·B_2N_2	–0.738	+0.783	–0.622	0.801	0.969	0.166	–0.168	0.189	–0.194
Me_3PCH_2·B_2N_2	–1.037	+0.769	–0.622	0.840	1.096 (0.846)	0.167	–0.168	0.204 (0.172)	–0.214 (–0.171)
$ImMe_2$·B_3N_3	+0.251	+0.749	–0.592	0.837	1.082	0.154	–0.149	0.192 (0.192)	–0.192
$ImMe_2CH_2$·B_3N_3	–0.763	+0.863	–0.578	0.749	1.022 (1.096)	0.157	–0.157	0.184 (0.185)	–0.183 (–0.182)
Me_3PCH_2·B_3N_3	–1.062	+0.690	–0.572	0.689	1.145 (1.143)	0.154	–0.152	0.194 (0.255)	–0.195 (–0.179)

The computed NBO atomic charges of the boron atoms show a significant decrease (0.5 to 0.6 e^-) upon attachment of the Lewis bases. However, the change in charge of the bonding carbon atom upon complexation is much more modest *ca.* 0.1 to 0.2 (Table 6.3 and Appendix D). The charge transfer to the boron center is highest for the $ImMe_2$ and lowest for the Me_3PCH_2 substituted BN and BNBN adducts. For both B_2N_2 and B_3N_3 adducts, the highest charge transfer to the boron atom belongs to the $ImMe_2$ and Me_3PCH_2 ligands, respectively, but the lowest to the $ImMe_2CH_2$ ligand (Table 6.3). Interestingly, the NBO analysis does not show a significant charge difference for the nitrogen atom attached to the boron center in the LB·BN adducts compared to the isolated species (see Tables in Appendix D). On the other hand, in LB·BNBN adducts, the terminal nitrogen gains about 0.4-0.8 electrons and the central N atom loses about 0.2-0.4 electrons relative to the free species. For B_2N_2, the boron loses 0.1-0.2 electrons, while the nitrogen shows a 0.4 electron gain upon complexation; the changes in partial charges of B and N in B_3N_3 are very modest (0.1-0.2 e^-). Therefore, there is stronger electronic communication in the BNBN complexes compared to the other adducts. Also, the Wiberg bond index (WBI) shows the following trend for all the C–B bonds in the mono-substituted adducts: LB·BNBN > LB·BN > LB·B_2N_2 > LB·B_3N_3; a rather similar trend can be observed for the AIM electron densities (ρ) of these bonds (Table 6.3). On the other hand, the trend of the WBI for the B–N bonds is LB·BN > LB·BNBN > LB·B_2N_2 ≈ LB·B_3N_3.

Analysis of the energy density (H(r)) at the C–B and B–N bond critical points shows that all of these bonds are predominantly covalent in character (i.e., negative values for $H_{(C-B)}$ and $H_{(B-N)}$). This data agrees well with the EDA-NOCV results which will be discussed later and points to the existence of covalent bonding between the carbon donors and boron acceptors, which is accompanied by π-backbonding in these systems as previously noted in LB·BX_3 (X = H, F, Cl) adducts [472, 473]. The computed value of the electron density (ρ) for the C–B bonds also shows that its strength decreases in the order of $ImMe_2$ > Me_3PCH_2 > $ImMe_2CH_2$ in the case of the BN, BNBN, and the B_2N_2 adducts. For the mono-substituted B_3N_3 adducts, the trend in ρ is $ImMe_2CH_2$ > $ImMe_2$ ≈ Me_3PCH_2 (Table 6.3) although the differences in ρ are very small (< 0.003 e^-). The ρ values for the B–N bonds in each of the adducts increase from 0.185 e^- to 0.300 e^- on going from the B_3N_3 adducts to the BN adducts, in line with the corresponding increase in WBI values for these species. From the optimized geometries, we found that the C–B bond length increases upon substituting more Lewis bases. AIM data are in agreement with the geometries as, for example, the ρ value for this bond decreases from 0.154 e^- in the $ImMe_2$·B_3N_3 complex to 0.136–0.139 e^- in $(ImMe_2)_3$·B_3N_3 while the C–B bond length increases from 1.612 Å to ≈ 1.650 Å (see AIM data in Appendix D, and geometries in Figures 6.3 and 6.4). This trend mirrors the variation in stabilization energies, and indicate that the interaction between the Lewis base and the boron atoms becomes weaker in the presence of added equivalents of donor. The ρ values of the C–B bonds for $(ImMe_2CH_2)_n$·B_3N_3 and $(Me_3PCH_2)_n$·B_3N_3 also decrease by going from mono- to tri-substituted adducts: from 0.157 e^- to 0.120 e^- and from 0.154 e^- to 0.127 e^-, respectively (see AIM data in Appendix D); a trend reflected in the corresponding C–B bond length.

6.3.5 Energy Decomposition Analysis (EDA-NOCV)

To understand the nature of the bonding between different Lewis bases and the cyclic and acyclic boron nitride oligomers (LB·$(BN)_n$, n = 1–3), EDA-NOCV computations were performed using the GGA BP86 functional and the TZ2P basis set (Table 6.4). For brevity, we only focus on the most stabilized and least stabilized boron nitride species, i.e., LB·BN and LB·B_3N_3, respectively. The order of bond dissociation energies (D_e) for the different Lewis bases follows the series $ImMe_2$ > Me_3PCH_2 > $ImMe_2CH_2$. More specifically, the C–B bonds

TABLE 6.4: Computed EDA–NOCV components (in kcal/mol) for the C–B bonds of the BN and B_3N_3 substituted systems at the BP86/TZ2P level of theory. The C–B bond lengths (R, in Å) are also provided for all the complexes.[a]

	$ImMe_2$·BN	$ImMe_2CH_2$·BN	Me_3PCH_2·BN	$ImMe_2$·B_3N_3	$ImMeCH_2$·B_3N_3	Me_3PCH_2·B_3N_3
ΔE_{int}	–136.1	–127.9	–135.8	–93.8	–84.5	–94.4
ΔE_{Pauli}	211.6	187.7	215.1	203.9	173.5	191.3
ΔE_{elstat}[b]	–168.3	–139.3	–168.2	–151.5	–116.2	–139.0
	(48.4%)	(44.1%)	(47.9%)	(50.9%)	(45.0%)	(48.7%)
ΔE_{orb}[b]	–179.3	–176.3	–182.7	–146.2	–141.8	–146.7
	(51.6%)	(55.9%)	(52.1%)	(49.1%)	(55.0%)	(51.3%)
$\Delta E_{orb,\sigma}$[c]	–115.8	–131.0	–130.6	–112.9	–118.9	–121.5
	(64.6%)	(74.3%)	(71.5%)	(77.2%)	(83.9%)	(82.8%)
$\Delta E_{orb,\pi}$[c]	–40.5	–33.8	–25.2	–16.7	–4.5	–7.6
	(22.6%)	(19.2%)	(13.8%)	(11.4%)	(3.2%)	(5.2%)
$\Delta E_{orb,rest}$[c]	–19.5	–11.5	–26.9	–16.6	–18.4	–17.6
	(12.8%)	(6.5%)	(14.7%)	(11.4%)	(12.9%)	(12.0%)
ΔE_{prep}	1.7	15.2	8.6	26.8	31.8	31.7
D_e	134.4	112.7	127.2	67.0	52.7	62.7
R	1.508	1.582	1.569	1.605	1.658	1.647

[a] For deformation densities see Figure 6.7.
[b] Percentage contributions to the total attractive interactions (ΔE_{elstat} + ΔE_{orb}) provided in parenthesis.
[c] Percentage contributions to the total orbital interactions ΔE_{orb} provided in parenthesis.

in the $ImMe_2$ substituted adducts are 4.3–21.7 kcal/mol stronger than their Me_3PCH_2 and $ImMe_2CH_2$ analogues. For a given boron nitride adduct, there is a clear correlation between C–B bond length on one hand and bond dissociation energy and Pauli repulsion values on the other hand (Table 6.4).

The percentage contribution of the electrostatic attraction (ΔE_{elstat}) and orbital interaction (ΔE_{orb}) terms to the total attractive energies are also provided in Table 6.4. Overall, the orbital interaction makes a significant contribution to the total attractive energy (more than 50%) in all complexes except $ImMe_2$·B_3N_3 where it is 49.1%. This high contribution indicates that C–B bonds retain substantial covalent character which is in agreement with our NBO/AIM results discussed above. The percentage contributions of the σ and π orbitals to the total orbital interaction are shown in Table 6.4 while the relevant deformation densities ($\Delta\rho$) are depicted in Figure 6.7. Notably, the $ImMe_2CH_2$·B_3N_3 adduct shows the lowest π-contribution to the C–B orbital interaction (3.2%) amongst the compounds investigated, while in contrast, the $ImMe_2$·BN and $ImMe_2CH_2$·BN adducts show the highest degree of π-character with 22.6% and 19.2% contributions, respectively. Thus from both Table 6.4 and Figure 6.7 it is evident that π-backbonding between the boron nitride oligomers and the carbon-based ligands can be quite significant in some cases. The preparation energy (ΔE_{prep}), the difference between the fragment energies in their complexed and free geometries, is the

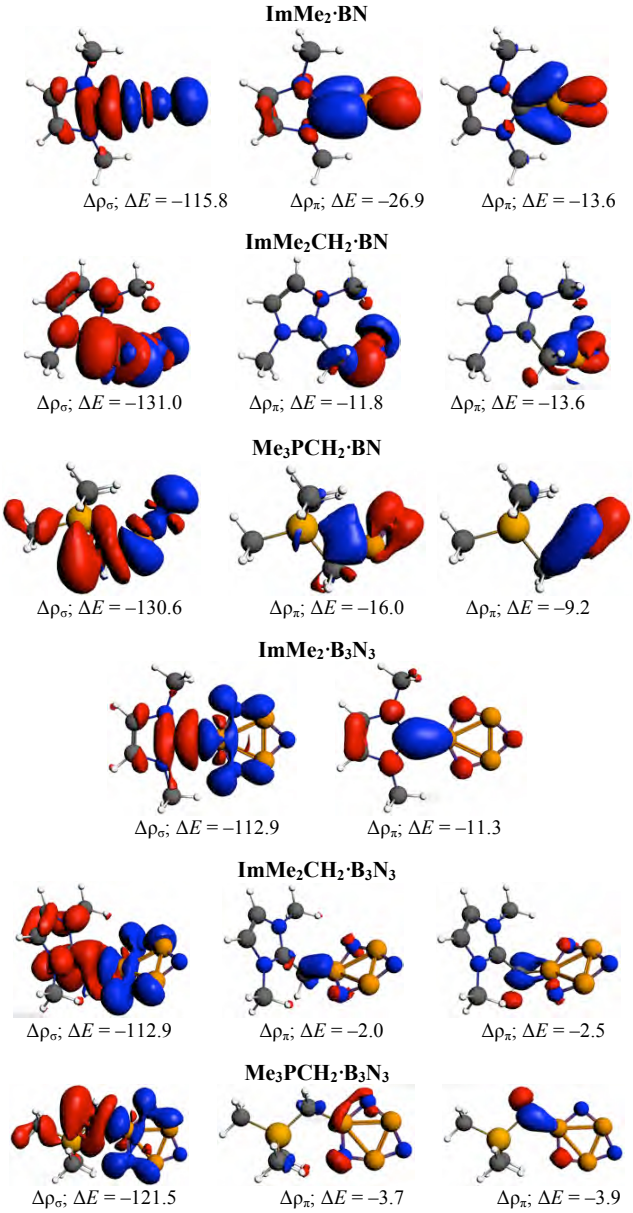

FIGURE 6.7: Deformation densities ($\Delta\rho$) associated with the most important pairwise orbital interactions for the C–B bond formation of the different Lewis base substituted BN and B_3N_3 adducts. The charge flow is from red → blue. Energies in kcal/mol are also provided.

lowest for the $ImMe_2$·BN while it is the highest for the $ImMe_2CH_2$·B_3N_3 adduct.

Our D_e values for the carbene–boron bonds are significantly more negative than the reported D_e values for the H_3B–NH_3 (31.9 kcal/mol) and H_3B–NMe_3 (36.2 kcal/mol) bonds computed at the BP86/TZ2P level of theory [472–474]. Tonner and Frenking have shown that replacing ammonia with the $ImMe_2$ ligand to form the $ImMe_2$·BH_3 adduct changes the D_e to 57.9 kcal/mol computed at the same level [412]. Also, the amount of π-backbonding in NH_3·BH_3,

$NMe_3{\cdot}BH_3$, and $ImMe_2{\cdot}BH_3$ are 10.1%, 13.0%, and 9.4%, respectively. The values are comparable to each other for all these three systems and are close to the corresponding value for the $ImMe_2{\cdot}B_3N_3$ complex (Table 6.4).

6.3.6 Stabilization through Donor-Acceptor Interactions

The HOMOs of both the $ImMe_2{\cdot}BN$ and $ImMe_2{\cdot}BNBN$ adducts have π character localized on the (terminal) BN unit as well as on the $ImMe_2$ ring (Figure 6.8). On the other hand, the HOMO-4 of both complexes shows a directional lone pair on the terminal nitrogen atom (with some mixing with a B–N σ bond) ready to be captured by a Lewis acid (LA). Herein

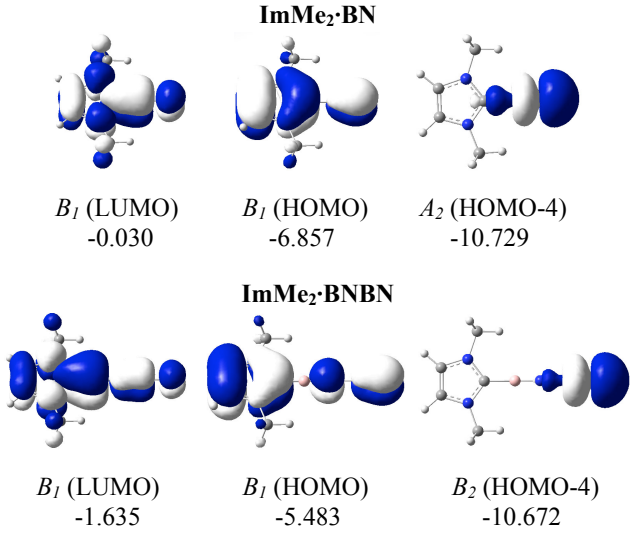

FIGURE 6.8: M05-2X/cc-pVTZ computed relevant MOs for the $ImMe_2{\cdot}BN$ and $ImMe_2{\cdot}BNBN$ substituted adducts in the gas phase. Symmetries as well as energies (in eV) are also provided.

we consider the previously employed donor-acceptor approach for stabilizing highly reactive heavier Group 14 element dihydrides [175], by using BH_3 and $W(CO)_5$ as Lewis acids (LA) and $ImMe_2$ as a Lewis base. The M05-2X optimized Lewis acid/base bound $(BN)_n$ complexes as well as their complexation Gibbs free energies are shown in Figure 6.9 (for a comparison between their electronic energies and Gibbs free energies see Table 6.5).

The C–B bond lengths in the Lewis acid bound adducts $ImMe_2{\cdot}BN{\cdot}LA$ and $ImMe_2{\cdot}BNBN{\cdot}LA$ (LA = BH_3 and $W(CO)_5$) are in the narrow range of 1.513 to 1.517 Å and are nearly identical to the values found in the Lewis acid free BN and BNBN adducts (1.517 and 1.510 Å, respectively). However, in the donor-acceptor complexes, the B–N bond lengths in BN and

TABLE 6.5: The M05-2X/cc-pVTZ computed complexation energies[(a)] (in kcal/mol) for the attachment of different $ImMe_2{\cdot}(BN)_x$ donors to the BH_3 and WCO_5 acceptor groups[(b)]

Species	ΔE_{LA}[(b)]	$(\Delta E + ZPE)_{LA}$[(b)]	$\Delta G°_{LA}$[(b)]
$ImMe_2{\cdot}BN{\cdot}BH_3$	–45.7	–42.7	–35.2
$ImMe_2{\cdot}BN{\cdot}WCO_5$	–59.0	–58.0	–46.6
$ImMe_2{\cdot}BNBN{\cdot}BH_3$	–51.9	–49.1	–41.5
$ImMe_2{\cdot}BNBN{\cdot}WCO_5$	–68.1	–67.1	–55.6
$ImMe_2{\cdot}B_2N_2{\cdot}BH_3$	–40.6	–36.8	–27.0
$ImMe_2{\cdot}B_2N_2{\cdot}WCO_5$	–51.3	–49.9	–38.1
$ImMe_2{\cdot}B_3N_3{\cdot}BH_3{\cdot}$*ortho*	–34.8	–31.4	–21.3
$ImMe_2{\cdot}B_3N_3{\cdot}WCO_5{\cdot}$*ortho*	–43.7	–42.8	–30.6
$ImMe_2{\cdot}B_3N_3{\cdot}BH_3{\cdot}$*para*	–21.7	–18.9	–10.7
$ImMe_2{\cdot}B_3N_3{\cdot}WCO_5{\cdot}$*para*	–35.3	–34.8	–26.2

[(a)]See Table 6.2 for definition of each term.
[(b)]For the reaction: $ImMe_2{\cdot}(BN)_n$ + LA → $ImMe_2{\cdot}(BN)_n{\cdot}$LA ($n$ = 1–3)

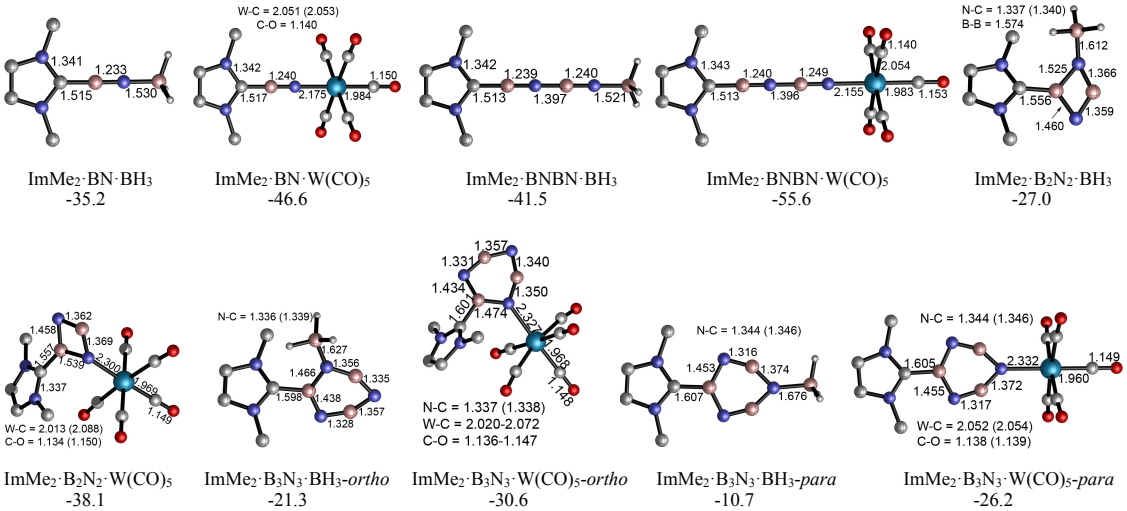

FIGURE 6.9: M05-2X/cc-pVTZ optimized geometries and Gibbs free energies of the BH_3 and $W(CO)_5$ substituted boron nitride adducts in the gas phase (C-H bonds are omitted for clarity).

BNBN slightly increase by 0.001–0.035 Å showing (modest) π-electron transfer from the B–N bond to the LA molecule. The computed N–B and N–W bond lengths for the BN and BNBN adducts (1.521–1.627 Å and 2.155–2.332 Å, respectively) are shorter than the BP86/TZ2P values for the H_3N–BH_3 and H_3N–$W(CO)_5$ complexes (1.657 and 2.350 Å, respectively) due to a change in hybridization at nitrogen from sp^3 to formally sp [474].

Overall, $W(CO)_5$ appears to be a stronger Lewis acid compared to BH_3 as the ΔG° values for the former adduct series are more favorable (negative) by 9.3–15.5 kcal/mol (Figure 6.9). These results support our experimental results within the IPr·GeH_2·LA complexes (LA = BH_3 and $W(CO)_5$) where the $W(CO)_5$ adduct is more stable [186].

The impact of complexing $ImMe_2$ and BH_3 molecules concurrently to the B_2N_2 and B_3N_3 units was studied. More specifically, the Gibbs free energies for the addition of the $ImMe_2$ ligand to the $ImMe_2{\cdot}B_2N_2{\cdot}(BH_3)_2$ and $(ImMe_2)_2{\cdot}B_3N_3{\cdot}(BH_3)_3$ adducts to form the fully saturated $(ImMe_2)_2{\cdot}B_2N_2{\cdot}(BH_3)_2$ and $(ImMe_2)_3{\cdot}B_3N_3{\cdot}(BH_3)_3$ complexes were found to be –74.2 and
–60.9 kcal/mol, respectively.

EDA-NOCV for BN and B_3N_3 LB/LA Substituted Adducts

To further study the impact of adding a Lewis acid on stabilizing BN and B_3N_3 molecules, C–B and N–W bonds in the $ImMe_2{\cdot}BN{\cdot}W(CO)_5$ and $ImMe_2{\cdot}B_3N_3{\cdot}W(CO)_5$ adducts were examined using the EDA-NOCV approach (Figure 6.10); their corresponding deformation densities are presented in Figure 6.11.

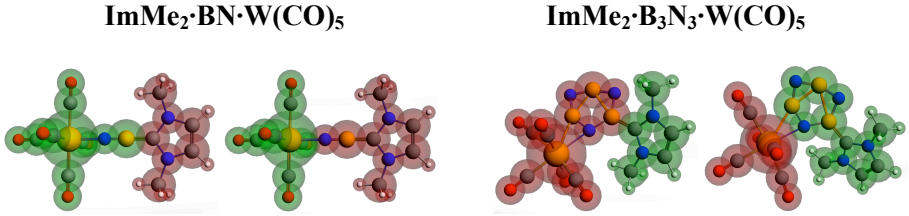

FIGURE 6.10: Different fragments (shown in green and red colors) utilized for the EDA–NOCV computations of the C–B and N–W bonds in the $ImMe_2{\cdot}BN{\cdot}W(CO)_5$ and $ImMe_2{\cdot}B_3N_3{\cdot}W(CO)_5$ adducts.

Comparing the interaction energies in the BN and the B_3N_3 adducts reveals that the C–B bond becomes 36.5 kcal/mol stronger upon $W(CO)_5$ Lewis acid attachment in the former

TABLE 6.6: Computed EDA–NOCV components (in kcal/mol) for the C–B and N–W bonds of the $ImMe_2{\cdot}BN{\cdot}W(CO)_5$ and $ImMe_2{\cdot}B_3N_3{\cdot}W(CO)_5$ adducts at the BP86/TZ2P level of theory. The analogous values for the C–B bonds without Lewis acid are also provided in parenthesis. See Figure 6.10 for the corresponding fragments.

	$ImMe_2{\cdot}BN{\cdot}W(CO)_5$		$ImMe_2{\cdot}B_3N_3{\cdot}W(CO)_5$	
	C–B	N–W	C–B	N–W
ΔE_{int}	–172.6 (–136.1)	–57.6	–92.0 (–93.8)	–45.1
ΔE_{Pauli}	151.1 (211.6)	106.5	203.9 (220.7)	113.0
ΔE_{elstat}	–154.4 (–168.3)	–105.7	–151.5 (–158.1)	–89.8
ΔE_{orb}	–169.4 (–179.3)	–58.4	–146.2 (–154.6)	–68.3
$\Delta E_{orb,\sigma}$	–113.5 (–115.8)	–31.6	–112.9 (–118.8)	–26.7
$\Delta E_{orb,\pi}$	–30.9 (–40.5)	–10.7	–16.7 (–10.9)	–26.9
$\Delta E_{orb,rest}$	–25.0 (–19.5)	–16.1	–16.6 (–24.9)	–14.7

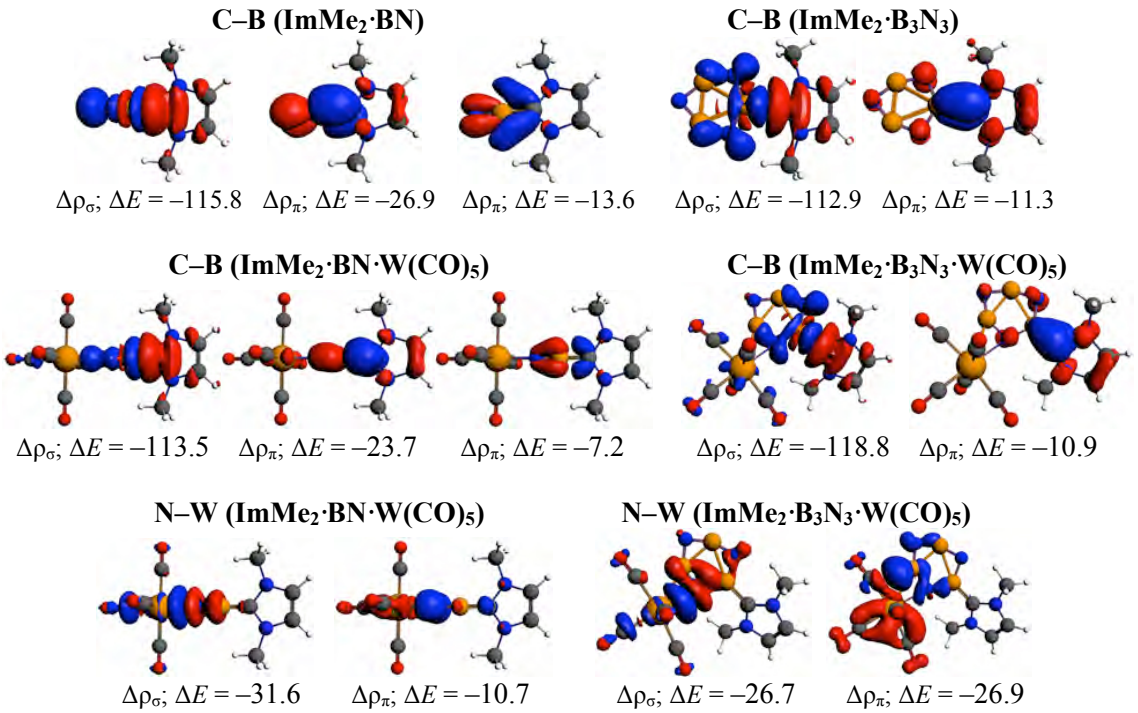

FIGURE 6.11: Deformation densities ($\Delta\rho$) associated with the most important pairwise orbital interactions for the C–B and N–W bond formations in the $ImMe_2{\cdot}BN{\cdot}W(CO)_5$ and $ImMe_2{\cdot}B_3N_3{\cdot}W(CO)_5$ adducts. The charge flow is from red→blue. Energies in kcal/mol are also provided.

adduct, but surprisingly it becomes 1.8 kcal/mol weaker in the latter (Figure 6.9). More specifically, addition of tungsten pentacarbonyl as a Lewis acid significantly decreases the Pauli repulsion portion of the C–B bond; from 211.6 kcal/mol in $ImMe_2{\cdot}BN$ to 151.1 kcal/mol in $ImMe_2{\cdot}BN{\cdot}W(CO)_5$ but increases it from 203.9 kal/mol in $ImMe_2{\cdot}B_3N_3$ to 220.7 kcal/mol in $ImMe_2{\cdot}B_3N_3{\cdot}W(CO)_5$ (Figure 6.9). Lewis acid attachment also decreases the contribution of electrostatic and orbital interactions by 13.9 and 9.9 kcal/mol for $ImMe_2{\cdot}BN$ adduct but

it increases them to 6.6 and 8.4 kcal/mol for the $ImMe_2{\cdot}B_3N_3$ adduct. An inspection of the σ and π orbital interaction components for the C–B bonds in the BN adduct proves that the decrease in ΔE_{orb} upon bonding to the Lewis acid comes mainly from the decrease of π-backbonding rather than σ-donation. Moreover, comparing the percent contribution of the ΔE_{orb} component to the total interaction energy confirms the ionic nature of the N–W bonds (35.6 % and 43.2 % for the BN and B_3N_3 adducts, respectively). It is also worthwhile mentioning that no stationary point was found for the $BN{\cdot}W(CO)_5$ or $B_3N_3{\cdot}W(CO)_5$ adducts which points towards the instability of the N–W bond in these species in the absence of the Lewis base.

Given that the free energies of complexation associated with coordinating $ImMe_2{\cdot}BN$ and $ImMe_2{\cdot}BNBN$ units by BH_3 and $W(CO)_5$ are quite favorable, Lewis acid coordination can provide even more stability for these highly elusive boron nitride species [462, 475, 476].

6.4 Conclusions

A variety of acyclic and cyclic $(BN)_n$ (n = 1–3) adducts with different Lewis bases including an *N*-heterocyclic carbene, an *N*-heterocyclic olefin and a Wittig donor were examined using M05-2X/cc-pVTZ computations. Considering the Gibbs free energies, values greater than –50 kcal/mol were found for the complexation energies. From the NBO, AIM and EDA-NOCV approaches, the existence of a polar covalent bond between carbene and boron atom was confirmed in each adduct studied. On the other hand, computed NPA charges illustrated rather significant amounts of charge transfer from the carbene center towards the boron atom upon C–B bond formation. A donor-acceptor strategy, in analogy with our synthesis of heavier group 14 element dihydride adducts,[175] show that $LB{\cdot}(BN)_nW(CO)_5$ (n = 1–3) complexes could be experimentally achievable. Finally, both the C–B donor and N–W acceptor bonds were decomposed into their σ and π bonding components in the $ImMe_2$ substituted BN and B_3N_3 adducts with and without $W(CO)_5$ as a Lewis acid. Analysis of the EDA-NOCV results in these adducts showed that the carbene–boron bonds are stronger in the presence of $W(CO)_5$ as a Lewis acid mainly because of a dramatic decrease in Pauli repulsion rather than an increase in the electrostatic/orbital attraction.

Chapter 7

Conclusion and Future Work

7.1 Excited State Properties of (aza-)BODIPY Based Cyanine Dyes

We studied the excited state properties of (aza-)BODIPY families using 9 different TD-DFT functionals (see Chapter 3). From a quantitative point of view, all TD-DFT functionals were found to overestimate the experimental absorption maxima by more than 0.3 eV (see Table 3.3). We showed that the low Mean AEs of the pure BLYP and PBE functionals is concurrent with low R^2 values (0.797 and 0.793, respectively) and hence these functionals were not recommended.

The LCC2*/cc-pVDZ method with Mean AE of 0.109 eV was found as the best compromise between accuracy and efficiency. Therefore, the author highly recommends using this method for the study of the (aza-)BODIPY molecules.

The reliability of the LCC2* and empirically corrected TD-DFT methods were tested against 8 different extended BODIPYs and aza-BODIPYs (see Table 3.10). The LCC2* method showed a very good performance for both BODIPYs (AE $\leq$ 0.113 eV) and aza-BODIPYs (AE $\leq$ 0.223 eV). In contrast to the TD-DFT methods, empirical correction was not required, nor recommended, for this method.

The obtained CT parameters and EDD plots for the 17 studied (aza-)BODIPYs demonstrated that not all the studied species exhibit CT, see Table 3.6. The lack of significant CT was also suggested because there were not significant improvements in absolute performance when

going from GGA and HGGA functionals to range-separated ones.
From the CASSCF computations, it was found that the major problem in these compounds, and, in particular, for the heads of the family, i.e. compounds (**1**) and (**2**), arises because of the multi-reference nature of the transitions (Table 3.11). Similarly, the contributions belonging to double excitations, which in some cases make moderate 5–10% contributions, can't be captured by TD-DFT.

In Chapter 4 of this thesis, the results of an extensive benchmark study on vertical excitation energies of 11 different (aza-)BODIPY dimers were presented using 15 different TDA-DFT methods. The M06-2X adiabatic excitation energies were also obtained for all structures. We found the B2GP-PLYP and PBE0-2 double hybrid density functionals with Mean AEs of 0.188 and 0.202 eV, respectively, as the best TDA-DFT methods for studying the (aza-)BODIPY dimers. Among the studied ab initio methods, the LCC2* and LADC(2) methods yielded the best results and were closest to the highly sophisticated CASPT2 method.
In the search for near IR emitting and heavy atom free triplet photosensitizers based on (aza-)BODIPY dimers, two of the previously proposed dimers for PDT action were further modified using different auxiliary groups (ethylene, acetylene, azo and phenyl moieties). Spin-orbit coupling matrix elements and CASSCF occupancies were computed for all species along with the LCC2 vertical excitation energies and [S_1–T_n] singlet-triplet gaps. A systematic study on all possible azo-linked (aza-)BODIPY dimers was performed and novel triplet photosensitizers based on these molecules were introduced.

7.2 Chemistry of NHC/CAAC Substituted Boron, Silicon, and Boron Nitride Compounds

In Chapter 5, ring expansion chemistry of different borane and silane adducts with $ImMe_2$ (NHC) was presented using density functional theory computations in both the solution and gas phase. The previously proposed mechanism for the ring expansion of borane and silane adducts with NHC carbenic donors was verified theoretically. The results were compared and contrasted with those obtained with the related cyclic aminoalkylcarbene donor (^{Me}CAAC) and a significant difference was observed. The ^{Me}CAAC adducts showed a facile hydride transfer chemistry from B–H and Si–H bonds to carbon but with prohibitively high activation

energies associated with subsequent ring expansion (see Figures 5.9 and 5.10). In good agreement with the experimental results [150], our computations showed that formation of a ring expanded product from $ImMe_2$-BH_3 is kinetically unfavourable due to the high energy barrier for the H-atom migration from boron to carbon (Figure 5.10). The presence of a boron-bound π-donating amino group in $ImMe_2$-BH_2NHMe significantly decreases the energy barrier required for hydride transfer, leading to an energetically feasible ring opening reaction (Figure 5.9). In the case of the silane adducts with NHC, the simultaneous presence of at least one hydrogen atom and one phenyl ring was found to be crucial as the ring expansion reaction is not likely to happen in the case of SiH_4 and $SiPh_4$, which is in agreement with experimental findings (see Figures 5.4-5.7). Finally, the electronic and steric nature of the substituents attached to an N-heterocyclic carbene were shown to have an important impact on the stability of their adducts with diphenylsilane and also the propensity for ring expansion (Table 5.3).

In Chapter 6 of this thesis, we were concerned with stabilization of elusive $(BN)_n$ (n = 1–3) compounds through use of Lewis base (LB)/Lewis acid (LA) donor-acceptor interaction strategies. To this end, different Lewis base donors including NHC, an *N*-heterocyclic olefin and Wittig molecules were examined using M05-2X/cc-pVTZ computations (see Chapter 6). Values greater than –50 kcal/mol were found for the complexation Gibbs free energies of all the LB substituted boron nitride compounds (Table 6.2). From the NBO, AIM and EDA-NOCV approaches, the existence of a polar covalent bond between carbene and the boron atom was confirmed in each adduct studied (see Tables 6.3 and 6.4). Computed NPA charges illustrated rather significant amounts of charge transfer from the carbene center towards the boron atom upon C–B bond formation.

A donor-acceptor strategy, in analogy with the synthesis of heavier group 14 element dihydride adducts [175], show that $LB{\cdot}(BN)_nW(CO)_5$ (n = 1–3) complexes could be experimentally achievable (see Table 6.5 and Figure 6.9). Finally, both the C–B donor and N–W acceptor bonds were decomposed into their σ and π bonding components in the $ImMe_2$ substituted BN and B_3N_3 adducts with and without $W(CO)_5$ as a Lewis acid (Table 6.6). Analysis of the EDA-NOCV results in these adducts showed that the carbene–boron bonds are stronger in the presence of $W(CO)_5$ as a Lewis acid mainly because of a dramatic decrease in Pauli repulsion rather than an increase in the electrostatic/orbital attraction.

7.3 Future Work

Complete understanding of the fate of an excited molecule necessitates studying dynamics of the photo-excited system. Kohn-Sham DFT provides an excellent tool for such studies especially when one considers the applicability of this methodology to very large systems (up to several thousands atoms) [477]. Recently, TD-DFT dynamics has been extended to the non-adiabatic regime [478–481], which makes the study of quantum dominant systems feasible. Therefore, future work could study excited state dynamics of large organic chromophores such as
(aza-)BODIPYs.

Also, very recently, new versions of local coupled cluster methods paired with density fitting basis sets have been derived and implemented for the study of ground state molecules up to 500 atoms or more than 8800 basis functions [482–489]. The main advantage of these methods is that they can bring the (full) power of quantum chemistry to large systems due to their near linear scaling properties. Work toward the implementation of their linear response and/or equation of motion versions for excited states are needed to make the study of photo-physical properties of large systems possible. Comprehensive benchmark studies are also required to test the performance of these methods for different families of molecules.

Bibliography

[1] Dai, T.; Fuchs, B. B.; Coleman, J. J.; Prates, R. A.; Astrakas, C.; St. Denis, T. G.; Ribeiro, M. S.; Mylonakis, E.; Hamblin, M. R.; Tegos, G. P. *Front. Microbiol.* **2012**, *3*, 120.

[2] Arduengo, A. J.; Harlow, R. L.; Kline, M. *J. Am. Chem. Soc.* **1991**, *113*, 361–363.

[3] Solé, S.; Gornitzka, H.; Schoeller, W. W.; Bourissou, D.; Bertrand, G. *Science* **2001**, *292*, 1901–1903.

[4] By Mark M. Somoza (Own work) [GFDL (http://www.gnu.org/copyleft/fdl.html), CC-BY-SA-3.0 (http://creativecommons.org/licenses/by-sa/3.0/) or CC BY-SA 2.5-2.0-1.0 (http://creativecommons.org/licenses/by-sa/2.5-2.0-1.0)], via Wikimedia Commons.

[5] Jacquemin, D.; Planchat, A.; Adamo, C.; Mennucci, B. *J. Chem. Theory Comput.* **2012**, *8*, 2359–2372.

[6] Osorio-Martínez, C. A.; Urías-Benavides, A.; Gómez-Durán, C. F. A.; Bañuelos, J.; Esnal, I.; López Arbeloa, I. n.; Peña Cabrera, E. *J. Org. Chem.* **2012**, *77*, 5434–5438.

[7] Arroyo, I. J.; Hu, R.; Merino, G.; Tang, B. Z.; Peña Cabrera, E. *J. Org. Chem.* **2009**, *74*, 5719–5722.

[8] Loudet, A.; Burgess, K. *Chem. Rev.* **2007**, *107*, 4891–4932.

[9] Ulrich, G.; Ziessel, R.; Harriman, A. *Angew. Chem., Int. Ed.* **2008**, *47*, 1184–1201.

[10] López Arbeloa, F.; Bañuelos, J.; Martínez, V.; Arbeloa, T.; López Arbeloa, I. *Int. Rev. Phys. Chem.* **2005**, *24*, 339–374.

[11] Duran-Sampedro, G.; Agarrabeitia, A. R.; Garcia-Moreno, I.; Costela, A.; Bañuelos, J.; Arbeloa, T.; López Arbeloa, I. n.; Chiara, J. L.; Ortiz, M. J. *Eur. J. Org. Chem.* **2012**, *2012*, 6335–6350.

[12] Baruah, M.; Qin, W.; Vallee, R.; Beljonne, D.; Rohand, T.; Dehaen, W.; Boens, N. *Org. Lett.* **2005**, *7*, 4377–4380.

[13] Boens, N.; Leen, V.; Dehaen, W. *Chem. Soc. Rev.* **2012**, *41*, 1130–1172.

[14] Gonçalves, M. S. T. *Chem. Rev.* **2009**, *109*, 190–212.

[15] Yuan, L.; Lin, W.; Zheng, K.; He, L.; Huang, W. *Chem. Soc. Rev.* **2013**, *42*, 622–661.

[16] Vendrell, M.; Zhai, D.; Er, J. C.; Chang, Y.-T. *Chem. Rev.* **2012**, *112*, 4391–4420.

[17] Erten-Ela, S.; Yilmaz, M. D.; Icli, B.; Dede, Y.; Icli, S.; Akkaya, E. U. *Org. Lett.* **2008**, *10*, 3299–3302.

[18] Treibs, A.; Kreuzer, F. *Justus Liebigs Ann. Chem.* **1968**, *718*, 208–223.

[19] Schmitt, A.; Hinkeldey, B.; Wild, M.; Jung, G. *J. Fluoresc.* **2009**, *19*, 755–758.

[20] Yogo, T.; Urano, Y.; Ishitsuka, Y.; Maniwa, F.; Nagano, T. *J. Am. Chem. Soc.* **2005**, *127*, 12162–12163.

[21] Qi, X.; Jun, E.; Xu, L.; Kim, S.; Hong, J.; Yoon, Y.; Yoon, J. *J. Org. Chem.* **2006**, *71*, 2881–2884.

[22] Baruah, M.; Qin, W.; Basaric, N.; De Borggraeve, W.; Boens, N. *J. Org. Chem.* **2005**, *70*, 4152–4157.

[23] Ni, Y.; Zeng, W.; Huang, K.-W.; Wu, J. *Chem. Comm.* **2013**, *49*, 1217–1219.

[24] Gresser, R.; Hartmann, H.; Wrackmeyer, M.; Leo, K.; Riede, M. *Tetrahedron* **2011**, *67*, 7148–7155.

[25] Hayashi, Y.; Obata, N.; Tamaru, M.; Yamaguchi, S.; Matsuo, Y.; Saeki, A.; Seki, S.; Kureishi, Y.; Saito, S.; Yamaguchi, S.; Shinokubo, H. *Org. Lett.* **2012**, *14*, 866–869.

[26] Jiang, X.-D.; Fu, Y.; Zhang, T.; Zhao, W. *Tet. Lett.* **2012**, *53*, 5703 – 5706.

[27] Yu, C.; Xu, Y.; Jiao, L.; Zhou, J.; Wang, Z.; Hao, E. *Chem. Eur. J.* **2012**, *18*, 6437–6442.

[28] Berhe, S. A.; Rodriguez, M. T.; Park, E.; Nesterov, V. N.; Pan, H.; Youngblood, W. J. *Inorg. Chem.* **2014**, *53*, 2346–2348.

[29] Sarkar, S. K.; Mukherjee, S.; Thilagar, P. *Inorg. Chem.* **2014**, *53*, 2343–2345.

[30] Le Guennic, B.; Maury, O.; Jacquemin, D. *Phys. Chem. Chem. Phys.* **2012**, *14*, 157–164.

[31] Sathyamoorthi, G.; Soong, M.-L.; Ross, T. W.; Boyer, J. H. *Heteroat. Chem.* **1993**, *4*, 603–608.

[32] Batat, P.; Cantuel, M.; Jonusauskas, G.; Scarpantonio, L.; Palma, A.; O'Shea, D. F.; McClenaghan, N. D. *J. Phys. Chem. A* **2011**, *115*, 14034–14039.

[33] Kamkaew, A.; Lim, S. H.; Lee, H. B.; Kiew, L. V.; Chung, L. Y.; Burgess, K. *Chem. Soc. Rev.* **2013**, *42*, 77–88.

[34] Awuah, S. G.; You, Y. *RSC Adv.* **2012**, *2*, 11169–11183.

[35] Winkler, R. *Spin–Orbit Coupling Effects in Two-Dimensional Electron and Hole Systems*; Springer Berlin Heidelberg, 2003; Vol. 191.

[36] Cohen, A. E. *J. Phys. Chem. A* **2009**, *113*, 11084–11092.

[37] Williams, A. T. R.; Winfield, S. A.; Miller, J. N. *Analyst* **1983**, *108*, 1067–1071.

[38] Ziessel, R.; Ulrich, G.; Harriman, A. *New J. Chem.* **2007**, *31*, 496–501.

[39] Gorman, A.; Killoran, J.; ÓShea, C.; Kenna, T.; Gallagher, W. M.; ÓShea, D. F. *J. Am. Chem. Soc.* **2004**, *126*, 10619–10631.

[40] Ozlem, S.; Akkaya, E. U. *J. Am. Chem. Soc.* **2009**, *131*, 48–49.

[41] Yang, Y.; Guo, Q.; Chen, H.; Zhou, Z.; Guo, Z.; Shen, Z. *Chem. Comm.* **2013**, *49*, 3940–3942.

[42] Cakmak, Y.; Kolemen, S.; Duman, S.; Dede, Y.; Dolen, Y.; Kilic, B.; Kostereli, Z.; Yildirim, L. T.; Dogan, A. L.; Guc, D.; Akkaya, E. U. *Angew. Chem. Int. Ed.* **2011**, *50*, 11937–11941.

[43] Duman, S.; Cakmak, Y.; Kolemen, S.; Akkaya, E. U.; Dede, Y. *J. Org. Chem.* **2012**, *77*, 4516–4527.

[44] Marques, M.; Gross, E. *Ann. Rev. Phys. Chem.* **2004**, *55*, 427–455.

[45] Stratmann, R.; Scuseria, G.; Frisch, M. *J. Chem Phys.* **1998**, *109*, 8218–8224.

[46] Furche, F.; Ahlrichs, R. *J. Chem Phys.* **2002**, *117*, 7433–7447.

[47] Chibani, S.; Le Guennic, B.; Charaf-Eddin, A.; Maury, O.; Andraud, C.; Jacquemin, D. *J. Chem. Theory Comput.* **2012**, *8*, 3303–3313.

[48] Chibani, S.; Charaf-Eddin, A.; Mennucci, B.; Le Guennic, B.; Jacquemin, D. *J. Chem. Theory Comput.* **2014**, *10*, 805–815.

[49] Chibani, S.; Charaf-Eddin, A.; Le Guennic, B.; Jacquemin, D. *J. Chem. Theory Comput.* **2013**, *9*, 3127–3135.

[50] Le Guennic, B.; Chibani, S.; Charaf-Eddin, A.; Massue, J.; Ziessel, R.; Ulrich, G.; Jacquemin, D. *Phys. Chem. Chem. Phys.* **2013**, *15*, 7534–7540.

[51] Charaf-Eddin, A.; Le Guennic, B.; Jacquemin, D. *Theor. Chem. Acc.* **2014**, *133*, 1–9.

[52] Chibani, S.; Le Guennic, B.; Charaf-Eddin, A.; Laurent, A. D.; Jacquemin, D. *Chem. Sci.* **2013**, *4*, 1950–1963.

[53] Gerbig, D.; Ley, D. *WIREs Comput. Mol. Sci.* **2013**, *3*, 242–272.

[54] Brinker, U. H. *Advances in Carbene Chemistry*; Elsevier: Amsterdam, 2001.

[55] Moss, R. A.; Platz, M. S.; Jones, J., M. *Reactive Intermediate Chemistry*; Wiley-Interscience: Hoboken, 2004.

[56] Herrmann, W. A.; Köcher, C. *Angew. Chem Int. Ed.* **1997**, *36*, 2162–2187.

[57] Bourissou, D.; Guerret, O.; Gabbaï, F. P.; Bertrand, G. *Chem. Rev.* **2000**, *100*, 39–92.

[58] Schuster, G. B. In *Structure and Reactivity of Carbenes having Aryl Substituents*; Gold, V., Bethell, D., Eds.; Advances in Physical Organic Chemistry; Academic Press, 1987; Vol. 22; pp 311–361.

[59] Kalemos, A.; Jr., T. H. D.; Mavridis, A.; Harrison, J. F. *Can. J. Chem.* **2004**, *82*, 684–693.

[60] MILLIGAN, D.; PIMENTEL, G. *J. Chem Phys.* **1958**, *29*, 1405–1412.

[61] Chang, S. C.; Kafafi, Z. H.; Hauge, R. H.; Billups, W. E.; Margrave, J. L. *J. Am. Chem. Soc.* **1987**, *109*, 4508–4513.

[62] Chang, S. C.; Kafafi, Z. H.; Hauge, R. H.; Billups, W. E.; Margrave, J. L. *J. Am. Chem. Soc.* **1985**, *107*, 1447–1448.

[63] Shavitt, I. *Tetrahedron* **1985**, *41*, 1531–1542.

[64] Goddard, W. A., III *Science* **1985**, *227*, 917–923.

[65] Schaefer, H. F., III *Science* **1986**, *231*, 1100–1107.

[66] Wasserman, E.; Yager, W.; Kuck, V. *Chem. Phys. Lett.* **1970**, *7*, 409 – 413.

[67] Bernheim, R. A.; Bernard, H. W.; Wang, P. S.; Wood, L. S.; Skell, P. *J. Chem Phys.* **1970**, *53*, 1280–1281.

[68] Herzberg, G.; Johns, J. W. C. *J. Chem. Phys.* **1971**, *54*, 2276–2278.

[69] McKellar, A. R. W.; Bunker, P. R.; Sears, T. J.; Evenson, K. M.; Saykally, R. J.; Langhoff, S. R. *J. Chem. Phys.* **1983**, *79*, 5251–5264.

[70] Foster, J. M.; Boys, S. F. *Rev. Mod. Phys.* **1960**, *32*, 305–307.

[71] Modarelli, D. A.; Platz, M. S. *J. Am. Chem. Soc.* **1991**, *113*, 8985–8986.

[72] Modarelli, D. A.; Morgan, S.; Platz, M. S. *J. Am. Chem. Soc.* **1992**, *114*, 7034–7041.

[73] Baird, N. C.; Taylor, K. F. *J. Am. Chem. Soc.* **1978**, *100*, 1333–1338.

[74] Richards, C. A.; Kim, S.-J.; Yamaguchi, Y.; Schaefer, H. F., III *J. Am. Chem. Soc.* **1995**, *117*, 10104–10107.

[75] Pasto, D. J.; Haley, M.; Chipman, D. M. *J. Am. Chem. Soc.* **1978**, *100*, 5272–5278.

[76] Minato, T.; Osamura, Y.; Yamabe, S.; Fukui, K. *J. Am. Chem. Soc.* **1980**, *102*, 581–589.

[77] Honjou, N.; Pacansky, J.; Yoshimine, M. *J. Am. Chem. Soc.* **1984**, *106*, 5361–5363.

[78] Honjou, N.; Pacansky, J.; Yoshimine, M. *J. Am. Chem. Soc.* **1985**, *107*, 5332–5341.

[79] Kakkar, R.; Garg, R.; Chadha, P. *J. Mol. Struct. THEOCHEM* **2002**, *617*, 141–147.

[80] Adam, W.; Oppenländer, T. *Angew. Chem. Int. Ed.* **1984**, *23*, 641–642.

[81] Thaddeus, P.; Vrtilek, J. M.; Gottlieb, C. A. *Astrophys. J.* **1985**, *299*, L63–L66.

[82] Gould, I. R.; Turbo, N. J.; Butcher, J. j.; Doubleday, C. j.; Hacker, N. P.; Lehr, G. F.; Moss, R. A.; Cox, D. P.; Guo, W.; Munjal, R. C.; Perez, L. A.; Fedorynski, M. *Tetrahedron* **1985**, *41*, 1587–1600.

[83] Thanh Le, H.; Lam Nguyen, T.; Lahem, D.; Flammang, R.; Tho Nguyen, M. *Phys. Chem. Chem. Phys.* **1999**, *1*, 755–760.

[84] Matus, M. H.; Nguyen, M. T.; Dixon, D. A. *J. Phys. Chem. A* **2006**, *110*, 8864–8871.

[85] Mendez, F.; Garcia-Garibay, M. A. *J. Org. Chem.* **1999**, *64*, 7061–7066.

[86] Canac, Y.; Conejero, S.; Donnadieu, B.; Schoeller, W. W.; Bertrand, G. *J. Am. Chem. Soc.* **2005**, *127*, 7312–7313.

[87] Alder, R. W.; Blake, M. E.; Oliva, J. M. *J. Phys. Chem. A* **1999**, *103*, 11200–11211.

[88] Heinemann, C.; Thiel, W. *Chem. Phys. Lett.* **1994**, *217*, 11–16.

[89] W. Alder, R.; E. Blake, M. *Chem. Comm.* **1997**, 1513–1514.

[90] Moss, R. A.; Wlostowski, M.; Shen, S.; Krogh-Jespersen, K.; Matro, A. *J. Am. Chem. Soc.* **1988**, *110*, 4443–4444.

[91] Du, X. M.; Fan, H.; Goodman, J. L.; Kesselmayer, M. A.; Krogh-Jespersen, K.; LaVilla, J. A.; Moss, R. A.; Shen, S.; Sheridan, R. S. *J. Am. Chem. Soc.* **1990**, *112*, 1920–1926.

[92] Harrison, J. F.; Liedtke, R. C.; Liebman, J. F. *J. Am. Chem. Soc.* **1979**, *101*, 7162–7168.

[93] Irikura, K. K.; Goddard, W. A.; Beauchamp, J. L. *J. Am. Chem. Soc.* **1992**, *114*, 48–51.

[94] García, V.; Castell, O.; Reguero, M.; Caballol, R. *Mol. Phys.* **1996**, *87*, 1395–1404.

[95] Nemirowski, A.; Schreiner, P. R. *J. Org. Chem.* **2007**, *72*, 9533–9540.

[96] Heinemann, C.; Müller, T.; Apeloig, Y.; Schwarz, H. *J. Am. Chem. Soc.* **1996**, *118*, 2023–2038.

[97] Arduengo, A. J.; Goerlich, J. R.; Marshall, W. J. *Liebigs Ann.* **1997**, *1997*, 365–374.

[98] Couture, P.; Terlouw, J. K.; Warkentin, J. *J. Am. Chem. Soc.* **1996**, *118*, 4214–4215.

[99] Warkentin, J. *Acc. Chem. Res.* **2009**, *42*, 205–212.

[100] Lambert, C.; Lopez-Solera, I.; Raithby, P. R. *Organometallics* **1996**, *15*, 452–455.

[101] Arduengo, A. J.; Dias, H. V. R.; Harlow, R. L.; Kline, M. *J. Am. Chem. Soc.* **1992**, *114*, 5530–5534.

[102] Arduengo, A. J.; Goerlich, J. R.; Marshall, W. J. *J. Am. Chem. Soc.* **1995**, *117*, 11027–11028.

[103] Enders, D.; Breuer, K.; Raabe, G.; Runsink, J.; Teles, J. H.; Melder, J.-P.; Ebel, K.; Brode, S. *Angew. Chem. Int. Ed.* **1995**, *34*, 1021–1023.

[104] Vignolle, J.; Cattoën, X.; Bourissou, D. *Chem. Rev.* **2009**, *109*, 3333–3384.

[105] Igau, A.; Grutzmacher, H.; Baceiredo, A.; Bertrand, G. *J. Am. Chem. Soc.* **1988**, *110*, 6463–6466.

[106] Igau, A.; Baceiredo, A.; Trinquier, G.; Bertrand, G. *Angew. Chem. Int. Ed.* **1989**, *28*, 621–622.

[107] Kato, T.; Gornitzka, H.; Baceiredo, A.; Savin, A.; Bertrand, G. *J. Am. Chem. Soc.* **2000**, *122*, 998–999.

[108] Kassaee, M.; Shakib, F.; Momeni, M.; Ghambarian, M.; Musavi, S. *Tetrahedron* **2009**, *65*, 10093–10098.

[109] Kassaee, M. Z.; Shakib, F. A.; Momeni, M. R.; Ghambarian, M.; Musavi, S. M. *J. Org. Chem.* **2010**, *75*, 2539–2545.

[110] Kassaee, M.; Momeni, M.; Shakib, F.; Ghambarian, M.; Musavi, S. *Struct. Chem.* **2010**, *21*, 593–598.

[111] Momeni, M.; Shakib, F. *Comput. Theoret. Chem.* **2011**, *965*, 101–106.

[112] Kassaee, M.; Momeni, M.; Shakib, F.; Najafi, Z.; Zandi, H. *J. Phys. Org. Chem.* **2011**, *24*, 1022–1029.

[113] Lavallo, V.; Mafhouz, J.; Canac, Y.; Donnadieu, B.; Schoeller, W. W.; Bertrand, G. *J. Am. Chem. Soc.* **2004**, *126*, 8670–8671.

[114] Buron, C.; Gornitzka, H.; Romanenko, V.; Bertrand, G. *Science* **2000**, *288*, 834–836.

[115] Despagnet, E.; Gornitzka, H.; Rozhenko, A. B.; Schoeller, W. W.; Bourissou, D.; Bertrand, G. *Angew. Chem. Int. Ed.* **2002**, *41*, 2835–2837.

[116] Canac, Y.; Soleilhavoup, M.; Conejero, S.; Bertrand, G. *J. Organomet. Chem.* **2004**, *689*, 3857–3865.

[117] Lavallo, V.; Canac, Y.; Präsang, C.; Donnadieu, B.; Bertrand, G. *Angew. Chem Int. Ed.* **2005**, *44*, 5705–5709.

[118] Lavallo, V.; Canac, Y.; DeHope, A.; Donnadieu, B.; Bertrand, G. *Angew. Chem Int. Ed.* **2005**, *44*, 7236–7239.

[119] Frey, G. D.; Lavallo, V.; Donnadieu, B.; Schoeller, W. W.; Bertrand, G. *Science* **2007**, *316*, 439–441.

[120] Jazzar, R.; Dewhurst, R.; Bourg, J.-B.; Donnadieu, B.; Canac, Y.; Bertrand, G. *Angew. Chem. Int. Ed.* **2007**, *46*, 2899–2902.

[121] Frey, G. D.; Dewhurst, R. D.; Kousar, S.; Donnadieu, B.; Bertrand, G. *J. Organomet. Chem.* **2008**, *693*, 1674–1682.

[122] Zeng, X.; Frey, G. D.; Kinjo, R.; Donnadieu, B.; Bertrand, G. *J. Am. Chem. Soc.* **2009**, *131*, 8690–8696.

[123] Herrmann, W. A. *Angew. Chem. Int. Ed.* **2002**, *41*, 1290–1309.

[124] Crudden, C. M.; Allen, D. P. *Coord. Chem. Rev.* **2004**, *248*, 2247–2273.

[125] Nolan, S. P. *Acc. Chem. Res.* **2011**, *44*, 91–100.

[126] Wang, F.; jun Liu, L.; Wang, W.; Li, S.; Shi, M. *Coord. Chem. Rev.* **2012**, *256*, 804–853.

[127] Crabtree, R. H. *Coord. Chem. Rev.* **2013**, *257*, 755–766.

[128] Back, O.; Donnadieu, B.; Parameswaran, P.; Frenking, G.; Bertrand, G. *Nat. Chem.* **2010**, *2*, 369–373.

[129] Fukuda, Y.; Maeda, Y.; Ishii, S.; Kondo, K.; Aoyama, T. *Synthesis* **2006**, *589*.

[130] Song, J. J.; Gallou, F.; Reeves, J. T.; Tan, Z.; Yee, N. K.; Senanayake, C. H. *J. Org. Chem.* **2006**, *71*, 1273–1276.

[131] Suzuki, Y.; Bakar, A.; M.D.,; Muramatsu, K.; Sato, M. *Tetrahedron* **2006**, *62*, 4227–4231.

[132] Rodriguez, M.; Marrot, S.; Kato, T.; Stérin, S.; Fleury, E.; Baceiredo, A. *J. Organomet. Chem.* **2007**, *692*, 705–708.

[133] Zhang, Y.; Chen, E. Y.-X. *Angew. Chem. Int. Ed.* **2012**, *51*, 2465–2469.

[134] Dove, A. P. *ACS Macro Lett.* **2012**, *1*, 1409–1412.

[135] Fevre, M.; Pinaud, J.; Gnanou, Y.; Vignolle, J.; Taton, D. *Chem. Soc. Rev.* **2013**, *42*, 2142–2172.

[136] Wang, Y.; Xie, Y.; Wei, P.; King, R. B.; Schaefer, H. F., III; Schleyer, P. v. R.; Robinson, G. H. *Science* **2008**, *321*, 1069–1071.

[137] Sidiropoulos, A.; Jones, C.; Stasch, A.; Klein, S.; Frenking, G. *Angew. Chem. Int. Ed.* **2009**, *48*, 9701–9704.

[138] Mondal, K. C.; Roesky, H. W.; Schwarzer, M. C.; Frenking, G.; Niepötter, B.; Wolf, H.; Herbst-Irmer, R.; Stalke, D. *Angew. Chem. Int. Ed.* **2013**, *52*, 2963–2967.

[139] Xiong, Y.; Yao, S.; Tan, G.; Inoue, S.; Driess, M. *J. Am. Chem. Soc.* **2013**, *135*, 5004–5007.

[140] Jones, C.; Sidiropoulos, A.; Holzmann, N.; Frenking, G.; Stasch, A. *Chem. Comm.* **2012**, *48*, 9855–9857.

[141] Braunschweig, H.; Dewhurst, R. D.; Hammond, K.; Mies, J.; Radacki, K.; Vargas, A. *Science* **2012**, *336*, 1420–1422.

[142] Wang, Y.; Quillian, B.; Wei, P.; Xie, Y.; Wannere, C. S.; King, R. B.; Schaefer, H. F., III; Schleyer, P. v. R.; Robinson, G. H. *J. Am. Chem. Soc.* **2008**, *130*, 3298–3299.

[143] Kinjo, R.; Donnadieu, B.; Celik, M. A.; Frenking, G.; Bertrand, G. *Science* **2011**, *333*, 610–613.

[144] Wang, Y.; Xie, Y.; Wei, P.; King, R. B.; Schaefer, H. F., III; Schleyer, P. v. R.; Robinson, G. H. *J. Am. Chem. Soc.* **2008**, *130*, 14970–14971.

[145] Abraham, M. Y.; Wang, Y.; Xie, Y.; Wei, P.; Schaefer, H. F., III; Schleyer, P. v. R.; Robinson, G. H. *Chem. Eur. J.* **2010**, *16*, 432–435.

[146] Ueng, S.-H.; Makhlouf Brahmi, M.; Derat, É.; Fensterbank, L.; Lacôte, E.; Malacria, M.; Curran, D. P. *J. Am. Chem. Soc.* **2008**, *130*, 10082–10083.

[147] Tehfe, M.-A.; Makhlouf Brahmi, M.; Fouassier, J.-P.; Curran, D. P.; Malacria, M.; Fensterbank, L.; Lacôte, E.; Lalevée, J. *Macromolecules* **2010**, *43*, 2261–2267.

[148] Arrowsmith, M.; Hill, M. S.; Kociok-Köhn, G.; MacDougall, D. J.; Mahon, M. F. *Angew. Chem. Int. Ed.* **2012**, *51*, 2098–2100.

[149] Schmidt, D.; Berthel, J. H. J.; Pietsch, S.; Radius, U. *Angew. Chem. Int. Ed.* **2012**, *51*, 8881–8885.

[150] Al-Rafia, S. M. I.; McDonald, R.; Ferguson, M. J.; Rivard, E. *Chem. Eur. J.* **2012**, *18*, 13810–13820.

[151] Kroto, H. W.; Heath, J. R.; ÓBrien, S. C.; Curl, R. F.; Smalley, R. E. *Nature* **1985**, *318*, 162–163.

[152] Georgakilas, V.; Perman, J. A.; Tucek, J.; Zboril, R. *Chem. Rev.* **2015**, *115*, 4744–4822.

[153] Gonzalez Szwacki, N.; Sadrzadeh, A.; Yakobson, B. I. *Phys. Rev. Lett.* **2007**, *98*, 166804.

[154] Gonzalez Szwacki, N.; Sadrzadeh, A.; Yakobson, B. I. *Phys. Rev. Lett.* **2007**, *100*, 159901.

[155] Zhai, H.-J. et al. *Nat. Chem.* **2014**, *6*, 727–731.

[156] Iijima, S. *Nature* **1991**, *354*, 56–58.

[157] Jorio, A.; Dresselhaus, G.; Dresselhaus, M.; Terrones, M.; Filho, A. S.; Rao, A. *Carbon Nanotubes*; Springer Berlin Heidelberg, 2008; Vol. 111; pp 531–566.

[158] Singh, A. K.; Sadrzadeh, A.; Yakobson, B. I. *Nano Lett.* **2008**, *8*, 1314–1317.

[159] Yang, X.; Ding, Y.; Ni, J. *Phys. Rev. B* **2008**, *77*, 041402.

[160] Ciuparu, D.; Klie, R. F.; Zhu, Y.; Pfefferle, L. *J. Phys. Chem. B* **2004**, *108*, 3967–3969.

[161] Dresselhaus, M.; Dresselhaus, G.; Eklund, P. In *Science of Fullerenes and Carbon Nanotubes*; Eklund, M. D. D., Ed.; Academic Press: San Diego, 1996; pp 224–270.

[162] Pierson, H. O. In *Handbook of Carbon, Graphite, Diamonds and Fullerenes*; Pierson, H. O., Ed.; William Andrew Publishing: Oxford, 1993; pp 244–277.

[163] Pierson, H. O. In *Handbook of Carbon, Graphite, Diamonds and Fullerenes*; Pierson, H. O., Ed.; William Andrew Publishing: Oxford, 1993; pp 43–69.

[164] Paine, R. T.; Narula, C. K. *Chem. Rev.* **1990**, *90*, 73–91.

[165] Golberg, D.; Bando, Y.; Tang, C.; Zhi, C. *Adv. Mater.* **2007**, *19*, 2413–2432.

[166] Xu, M.; Liang, T.; Shi, M.; Chen, H. *Chem. Rev.* **2013**, *113*, 3766–3798.

[167] Panchakarla, L. S.; Subrahmanyam, K. S.; Saha, S. K.; Govindaraj, A.; Krishnamurthy, H. R.; Waghmare, U. V.; Rao, C. N. R. *Adv. Mat.* **2009**, *21*, 4726–4730.

[168] Georgakilas, V.; Otyepka, M.; Bourlinos, A. B.; Chandra, V.; Kim, N.; Kemp, K. C.; Hobza, P.; Zboril, R.; Kim, K. S. *Chem. Rev.* **2012**, *112*, 6156–6214.

[169] Mao, H. Y.; Laurent, S.; Chen, W.; Akhavan, O.; Imani, M.; Ashkarran, A. A.; Mahmoudi, M. *Chem. Rev.* **2013**, *113*, 3407–3424.

[170] Watanabe, K.; Taniguchi, T.; Kanda, H. *Nat. Mater.* **2004**, *3*, 404–409.

[171] Geim, A. K.; Grigorieva, I. V. *Nature* **2013**, *499*, 419–425.

[172] Dean, C. R.; Young, A. F.; Meric, I.; Lee, C.; Wang, L.; Sorgenfrei, S.; Watanabe, K.; Taniguchi, T.; Kim, P.; Shepard, K. L.; Hone, J. *Nat. Nanotechnol.* **2010**, *5*, 722–726.

[173] Purkait, T. K.; Swarnakar, A. K.; De Los Reyes, G. B.; Hegmann, F. A.; Rivard, E.; Veinot, J. G. C. *Nanoscale* **2015**, *7*, 2241–2244.

[174] Wang, Y.; Robinson, G. H. *Dalton Trans.* **2012**, *41*, 337–345.

[175] Rivard, E. *Dalton Trans.* **2014**, *43*, 8577–8586.

[176] Mondal, K. C.; Roesky, H. W.; Stückl, A. C.; Ehret, F.; Kaim, W.; Dittrich, B.; Maity, B.; Koley, D. *Angew. Chem. Int. Ed.* **2013**, *52*, 11804–11807.

[177] Vogel, U.; Timoshkin, A. Y.; Scheer, M. *Angew. Chem.* **2001**, *113*, 4541–4544.

[178] Vogel, U.; Hoemensch, P.; Schwan, K.-C.; Timoshkin, A. Y.; Scheer, M. *Chem. Eur. J.* **2003**, *9*, 515–519.

[179] Schwan, K.-C.; Timoskin, A. Y.; Zabel, M.; Scheer, M. *Chem. Eur. J.* **2006**, *12*, 4900–4908.

[180] Marquardt, C.; Adolf, A.; Stauber, A.; Bodensteiner, M.; Virovets, A. V.; Timoshkin, A. Y.; Scheer, M. *Chem. Eur. J.* **2013**, *19*, 11887–11891.

[181] Adolf, A.; Vogel, U.; Zabel, M.; Timoshkin, A. Y.; Scheer, M. *Eur. J. Inorg. Chem.* **2008**, *2008*, 3482–3492.

[182] Vogel, U.; Timoshkin, A. Y.; Schwan, K.-C.; Bodensteiner, M.; Scheer, M. *J. Organomet. Chem.* **2006**, *691*, 4556 – 4564.

[183] Timoshkin, A. Y. *Inorg. Chem.* **2009**, *48*, 8145–8153.

[184] Lisovenko, A. S.; Timoshkin, A. Y. *Inorg. Chem.* **2010**, *49*, 10357–10369.

[185] Thimer, K. C.; Al-Rafia, S. M. I.; Ferguson, M. J.; McDonald, R.; Rivard, E. *Chem. Comm.* **2009**, 7119–7121.

[186] Al-Rafia, S. M. I.; Malcolm, A. C.; Liew, S. K.; Ferguson, M. J.; Rivard, E. *J. Am. Chem. Soc.* **2011**, *133*, 777–779.

[187] Al-Rafia, S. M. I.; Malcolm, A. C.; McDonald, R.; Ferguson, M. J.; Rivard, E. *Angew. Chem. Int. Ed.* **2011**, *50*, 8354–8357.

[188] Al-Rafia, S. M. I.; Malcolm, A. C.; McDonald, R.; Ferguson, M. J.; Rivard, E. *Chem. Comm.* **2012**, *48*, 1308–1310.

[189] Al-Rafia, S. M. I.; Shynkaruk, O.; McDonald, S. M.; Liew, S. K.; Ferguson, M. J.; McDonald, R.; Herber, R. H.; Rivard, E. *Inorg. Chem.* **2013**, *52*, 5581–5589.

[190] Al-Rafia, S. M. I.; Momeni, M. R.; Ferguson, M. J.; McDonald, R.; Brown, A.; Rivard, E. *Organometallics* **2013**, *32*, 6658–6665.

[191] Al-Rafia, S. M. I.; Malcolm, A. C.; Liew, S. K.; Ferguson, M. J.; McDonald, R.; Rivard, E. *Chem. Comm.* **2011**, *47*, 6987–6989.

[192] Swarnakar, A. K.; McDonald, S. M.; Deutsch, K. C.; Choi, P.; Ferguson, M. J.; McDonald, R.; Rivard, E. *Inorg. Chem.* **2014**, *53*, 8662–8671.

[193] Schrödinger, E. *Phys. Rev.* **1926**, *28*, 1049–1070.

[194] Born, M.; Oppenheimer, R. *Ann. Phys.* **1927**, *389*, 457–484.

[195] McQuarrie, D. A. *Quantum Chemistry*; University Science Books, Mill Valey, CA, 1983.

[196] Merzbacher, E. *Quantum Mechanics*; Wiley, New York, 2nd edition, 1970.

[197] Levine, I. N. *Quantum Chemistry*; Prentice Hall, Englewood Cliffs, N J, 4th edition, 1991.

[198] Szabo, A.; Ostlund, N. S. *Modern Quantum Chemistry: Introduction to Advanced Electronic Structure Theory*; McGraw-Hill, New York, 1989.

[199] Slater, J. C. *Phys. Rev. 34*, 1293–1322.

[200] Harrison, R.; Handy, N. *Chem. Phys. Lett.* **1983**, *95*, 386 – 391.

[201] Brillouin, L. *Actual. Sci. Ind.* **1933**, *71*.

[202] Brillouin, L. *Actual. Sci. Ind.* **1934**, *159*.

[203] MacDonald, J. K. L. *Phys. Rev.* **1933**, *43*, 830–833.

[204] Roos, B. O.; Taylor, P. R.; Siegbahn, P. E. *Chem. Phys.* **1980**, *48*, 157–173.

[205] Møller, C.; Plesset, M. S. *Phys. Rev.* **1934**, *46*, 618–622.

[206] Andersson, K.; Malmqvist, P.-A.; Roos, B. O. *J. Chem. Phys.* **1992**, *96*, 1218–1226.

[207] Bartlett, R. J.; Musial, M. *Rev. Mod. Phys.* **2007**, *79*, 291–352.

[208] Dykstra, C. E.; Kirtman, B. *Ann. Rev. Phys. Chem.* **1990**, *41*, 155–174.

[209] Saebø, S.; Pulay, P. *Ann. Rev. Phys. Chem.* **1993**, *44*, 213–236.

[210] Saebø, S.; Pulay, P. *J. Chem. Phys.* **1988**, *88*, 1884–1890.

[211] Kats, D.; Korona, T.; Schütz, M. *J. Chem Phys.* **2006**, *125*, 104106.

[212] Kats, D.; Korona, T.; Schütz, M. *J. Chem Phys.* **2007**, *127*, 064107.

[213] Kats, D.; Schütz, M. *J. Chem. Phys.* **2009**, *131*, 124117.

[214] Kats, D.; Schütz, M. *Z PHYS CHEM* **2001**, *224*, 601–616.

[215] Ledermüller, K.; Kats, D.; Schütz, M. *J. Chem Phys.* **2013**, *139*, 084111.

[216] Koch, H.; Christiansen, O.; J, P.; Sanchez de Merás, A. M.; Helgaker, T. *J. Chem Phys.* **1997**, *106*, 1808–1818.

[217] Noga, J.; Bartlett, R. J. *J. Chem Phys.* **1987**, *86*, 7041–7050.

[218] Scuseria, G. E.; Schaefer, H. F., III *Chem. Phys. Lett.* **1988**, *152*, 382–386.

[219] Raghavachari, K.; Trucks, G. W.; Pople, J. A.; Head-Gordon, M. *Chem. Phys. Lett.* **1988**, *157*, 479–483.

[220] Řezáč, J.; Hobza, P. *J. Chem. Theory Comput.* **2013**, *9*, 2151–2155.

[221] Oliphant, N.; Adamowicz, L. *J. Chem Phys.* **1991**, *94*, 1229–1235.

[222] Oliphant, N.; Adamowicz, L. *J. Chem Phys.* **1992**, *96*, 3739–3744.

[223] Piecuch, P.; Oliphant, N.; Adamowicz, L. *J. Chem Phys.* **1993**, *99*, 1875–1900.

[224] Oliphant, N.; Adamowicz, L. *Int. Rev. Phys. Chem.* **1993**, *12*, 339–362.

[225] Piecuch, P.; Adamowicz, L. *J. Chem Phys.* **1994**, *100*, 5792–5809.

[226] Piecuch, P.; Adamowicz, L. *Chem. Phys. Lett.* **1994**, *221*, 121–128.

[227] Piecuch, P.; Adamowicz, L. *J. Chem. Phys.* **1995**, *102*, 898–904.

[228] Ghose, K. B.; Piecuch, P.; Adamowicz, L. *J. Chem. Phys.* **1995**, *103*, 9331–9346.

[229] Ghose, K. B.; Piecuch, P.; Pal, S.; Adamowicz, L. *J. Chem. Phys.* **1996**, *104*, 6582–6589.

[230] Piecuch, P.; Kucharski, S. A.; Bartlett, R. J. *J. Chem. Phys.* **1999**, *110*, 6103–6122.

[231] Piecuch, P.; Kucharski, S. A.; Špirko, V. *J. Chem. Phys.* **1999**, *111*, 6679–6692.

[232] Kállay, M.; Szalay, P. G.; Surján, P. R. *J. Chem. Phys.* **2002**, *117*, 980–990.

[233] Fan, P.-D.; Hirata, S. *J. Chem. Phys.* **2006**, *124*, 104108.

[234] Becke, A. D. *J. Chem. Phys.* **2014**, *140*, 18A301.

[235] Hohenberg, P.; Kohn, W. *Phys. Rev.* **1964**, *136*, B864–B871.

[236] Becke, A. D. *Phys. Rev. A* **1988**, *38*, 3098–3100.

[237] Lee, C.; Yang, W.; Parr, R. G. *Phys. Rev. B* **1988**, *37*, 785–789.

[238] Miehlich, B.; Savin, A.; Stoll, H.; Preuss, H. *Chem. Phys. Lett.* **1989**, *157*, 200–206.

[239] Vosko, S. H.; Wilk, L.; Nusair, M. *Can. J. Phys.* **1980**, *58*, 1200–1211.

[240] Zhao, Y.; Truhlar, D. G. *J. Chem. Phys.* **2006**, *125*, 194101.

[241] Adamo, C.; Barone, V. *Chem. Phys. Lett.* **1997**, *274*, 242–250.

[242] Becke, A. *J. Chem. Phys.* **1996**, *104*, 1040–1046.

[243] Zhao, Y.; Truhlar, D. *Theor. Chem. Acc.* **2008**, *120*, 215–241.

[244] Perdew, J. P.; Schmidt, K. *AIP Conf. Proc.* **2001**, *577*, 1–20.

[245] Casida, M. E. *Time-dependent density-functional response theory for molecules, in: D.P. Chong (Ed.), Recent Advances in Density Functional Methods, Part 1*; World Scientific, Singapor, 1995; p 155.

[246] Dreuw, A.; Head-Gordon, M. *Chem. Rev.* **2005**, *105*, 4009–4037.

[247] Hirata, S.; Head-Gordon, M.; Bartlett, R. J. *J. Chem. Phys.* **1999**, *111*, 10774–10786.

[248] Grabo, T.; Petersilka, M.; Gross, E. *J. Mol. Struct. THEOCHEM* **2000**, *501–502*, 353–367.

[249] Hirata, S.; Head-Gordon, M. *Chem. Phys. Lett.* **1999**, *314*, 291–299.

[250] Fetter, A. L.; Walecka, J. D. *Quantum Theory of Many-Particle Systems*; McGraw-Hill: New York, 1971.

[251] Hsu, C.-P.; Hirata, S.; Head-Gordon, M. *J. Phys. Chem. A* **2001**, *105*, 451–458.

[252] Casida, M. E. *J. Mol. Struct. THEOCHEM* **2009**, *914*, 3–18.

[253] Moore, B.; Autschbach, J. *J. Chem. Theory Comput.* **2013**, *9*, 4991–5003.

[254] Zhekova, H.; Krykunov, M.; Autschbach, J.; Ziegler, T. *J. Chem. Theory Comput.* **2014**, *10*, 3299–3307.

[255] Dowd, P. *Acc. Chem. Res.* **1972**, *5*, 242–248.

[256] Brooks, B. R.; Schaefer, H. F., III *J. Am. Chem. Soc.* **1979**, *101*, 307–311.

[257] Casida, M. E.; Jamorski, C.; Casida, K. C.; Salahub, D. R. *J. Chem. Phys.* **1998**, *108*, 4439–4449.

[258] Stein, T.; Kronik, L.; Baer, R. *J. Am. Chem. Soc.* **2009**, *131*, 2818–2820.

[259] Gimon, T.; Ipatov, A.; Heßelmann, A.; Görling, A. *J. Chem. Theory Comput.* **2009**, *5*, 781–785.

[260] Savin, A. *in Recent Developments and Applications of Modern Density Functional Theory*; Ed. Seminario J.M. (Elsevier, Amsterdam), p. 327, 1996.

[261] Yanai, T.; Tew, D. P.; Handy, N. C. *Chem. Phys. Lett.* **2004**, *393*, 51–57.

[262] Champagne, B.; Perpète, E. A.; van Gisbergen, S. J. A.; Baerends, E.-J.; Snijders, J. G.; Soubra-Ghaoui, C.; Robins, K. A.; Kirtman, B. *J. Chem. Phys.* **1998**, *109*, 10489–10498.

[263] Champagne, B.; Perpète, E. A.; Jacquemin, D.; van Gisbergen, S. J. A.; Baerends, E.-J.; Soubra-Ghaoui, C.; Robins, K. A.; Kirtman, B. *J. Phys. Chem. A* **2000**, *104*, 4755–4763.

[264] Qian, Z.; Constantinescu, A.; Vignale, G. *Phys. Rev. Lett.* **2003**, *90*, 066402.

[265] Lorenzana, J.; Seibold, G. *Phys. Rev. Lett.* **2003**, *90*, 066404.

[266] Marini, A.; Del Sole, R.; Rubio, A. *Phys. Rev. Lett.* **2003**, *91*, 256402.

[267] Varsano, D.; Marini, A.; Rubio, A. *Phys. Rev. Lett.* **2008**, *101*, 133002.

[268] Van Faassen, M. *Int. J. Mod. Phys. B* **2006**, *20*, 3419–3463.

[269] Mazziotti, D. A. *Acc. Chem. Res.* **2006**, *39*, 207–215.

[270] Löwdin, P.-O. *Phys. Rev.* **1955**, *97*, 1474–1489.

[271] Weinhold, F.; Landis, C. R. *Discovering Chemistry with Natural Bond Orbitals*; John Wiley & Sons, Inc., Hoboken, New Jersey, 2012.

[272] `http://nbo6.chem.wisc.edu/webnbo_css.htm`.

[273] Bader, R. F. W. *Atoms in Molecules: A Quantum Theory*; Oxford University Press: Oxford, 1990.

[274] Bader, R. F. W. *Chem. Rev.* **1991**, *91*, 893–928.

[275] Bader, R. F. W. *Monatsh. Chem.* **2005**, *136*, 819–854.

[276] Cremer, D.; Kraka, E. *Angew. Chem. Int. Ed.* **1984**, *23*, 627–628.

[277] Zhao, W.; Carreira, E. M. *Chem. Eur. J.* **2006**, *12*, 7254–7263.

[278] Uppsten, M.; Durbeej, B. *J. Comput. Chem.* **2012**, *33*, 1892–1901.

[279] Céron-Carrasco, J. P.; Siard, A.; Jacquemin, D. *Dyes Pigments* **2013**, *99*, 972–978.

[280] Boulanger, P.; Chibani, S.; Le Guennic, B.; Duchemin, I.; Blase, X.; Jacquemin, D. *J. Chem. Theory Comput.* **2014**, *10*, 4548–4556.

[281] Chibani, S.; Laurent, A. D.; Le Guennic, B.; Jacquemin, D. *J. Chem. Theory Comput.* **2014**, *10*, 4574–4582.

[282] Charaf-Eddin, A.; Le Guennic, B.; Jacquemin, D. *RSC Adv.* **2014**, *4*, 49449–49456.

[283] Rhee, Y. M.; Head-Gordon, M. *J. Phys. Chem. A* **2007**, *111*, 5314–5326.

[284] Goerigk, L.; Grimme, S. *J. Chem. Phys.* **2010**, *132*, 184103.

[285] Petrushenko, I.; Petrushenko, K. *Spectrochim. Acta A* **2015**, *138*, 623–627.

[286] Perdew, J. P.; Burke, K.; Ernzerhoff, M. *Phys. Rev. Lett.* **1996**, *77*, 3865–3868.

[287] Perdew, J. P.; Burke, K.; Ernzerhoff, M. *Phys. Rev. Lett.* **1996**, *78*, 1396–1396.

[288] Adamo, C.; Barone, V. *J. Chem. Phys.* **1999**, *110*, 6158–6169.

[289] Dunning Jr., T. H. *J. Chem. Phys.* **1990**, *90*, 1007–1023.

[290] Woon, D. E.; Dunning Jr., T. H. *J. Chem. Phys.* **1993**, *98*, 1358–1371.

[291] Jacquemin, D.; Wathelet, V.; Perpète, E. A.; Adamo, C. *J. Chem. Theory Comput.* **2009**, *5*, 2420–2435.

[292] Cances, E.; Mennucci, B.; Tomasi, J. *J. Chem. Phys.* **1997**, *107*, 3032–3041.

[293] Cossi, M.; Scalmani, G.; Rega, N.; Barone, V. *J. Chem. Phys.* **2002**, *117*, 43–54.

[294] Iikura, H.; Tsuneda, T.; Yanai, T.; Hirao, K. *J. Chem. Phys.* **2001**, *115*, 3540–3544.

[295] Song, J.-W.; Hirosawa, T.; Tsuneda, T.; Hirao, K. *J. Chem. Phys.* **2007**, *126*, 154105.

[296] Chai, J.-D.; Head-Gordon, M. *Phys. Chem. Chem. Phys.* **2008**, *10*, 6615–6620.

[297] Vydrov, O. A.; Scuseria, G. E. *J. Chem. Phys.* **2006**, *125*, 234109.

[298] Vydrov, O. A.; Heyd, J.; Krukau, A. V.; Scuseria, G. E. *J. Chem. Phys.* **2006**, *125*, 074106.

[299] Vydrov, O. A.; Scuseria, G. E.; Perdew, J. P. *J. Chem.Phys.* **2007**, *126*, 154109.

[300] Foresman, J. B.; Head-Gordon, M.; Pople, J. A.; Frisch, M. J. *J. Phys. Chem.* **1992**, *96*, 135–149.

[301] Head-Gordon, M.; Rico, R. J.; Oumi, M.; Lee, T. J. *Chem. Phys. Lett.* **1994**, *219*, 21–29.

[302] Koch, H.; Jorgensen, P. *J. Chem. Phys.* **1990**, *93*, 3333–3344.

[303] Stanton, J. F.; Bartlett, R. J. *J. Chem. Phys.* **1993**, *98*, 7029–7039.

[304] Koch, H.; Kobayashi, R.; Sanchez de Merás, A.; Jorgensen, P. *J. Chem. Phys.* **1994**, *100*, 4393–4400.

[305] Kállay, M.; Gauss, J. *J. Chem. Phys.* **2004**, *121*, 9257–9269.

[306] Freundorfer, K.; Kats, D.; Korona, T.; Schütz, M. *J. Chem. Phys.* **2010**, *133*, 244110.

[307] Nakatsuji, H. *Chem. Phys. Lett.* **1979**, *67*, 334–342.

[308] Widmark, P.-O.; Malmqvist, P.-r.; Roos, B. O. *Theor. Chem. Acc.* **1990**, *77*, 291–306.

[309] Celani, P.; Werner, H.-J. *J. Chem. Phys.* **2000**, *112*, 5546–5557.

[310] Forsberg, N.; Åke Malmqvist, P. *Chem. Phys. Lett.* **1997**, *274*, 196–204.

[311] Kendall, R. A.; Dunning Jr., T. H.; Harrison, R. J. *J. Chem. Phys.* **1992**, *96*, 6796–6806.

[312] Le Bahers, T.; Adamo, C.; Ciofini, I. *J. Chem. Theory Comput.* **2011**, *7*, 2498–2506.

[313] Jacquemin, D.; Bahers, T. L.; Adamo, C.; Ciofini, I. *Phys. Chem. Chem. Phys.* **2012**, *14*, 5383–5388.

[314] Cižek, J. In *Advances in Chemical Physics*; Hariharan, P. C., Ed.; Wiley Interscience, 1969; Vol. 14; p 35.

[315] Purvis, G. D.; Bartlett, R. J. *J. Chem. Phys.* **1982**, *76*, 1910–1918.

[316] Scuseria, G. E.; Janssen, C. L.; Schaefer, H. F., III *J. Chem. Phys.* **1988**, *89*, 7382–7387.

[317] Scuseria, G. E.; Schaefer, H. F., III *J. Chem. Phys.* **1989**, *90*, 3700–3703.

[318] Pople, J. A.; HeadGordon, M.; Raghavachari, K. *J. Chem. Phys.* **1987**, *87*, 5968–5975.

[319] Lee, T. J.; Taylor, P. R. *Int. J. Quantum Chem. Symp.* **1989**, *23*, 199–207.

[320] Karton, A.; Rabinovich, E.; Martin, J. M. L.; Ruscic, B. *J. Chem. Phys.* **2006**, *125*, 144108.

[321] Tishchenko, O.; Zheng, J.; Truhlar, D. G. *J. Chem. Theory Comput.* **2008**, *4*, 1208–1219.

[322] Frisch, M. J. et al. Gaussian 09 Revision B.1. Gaussian Inc. Wallingford CT 2009.

[323] Werner, H.-J. et al. MOLPRO, version 2012.1, A package of ab initio programs. 2012; see http://www.molpro.net.

[324] Aidas, K. et al. *WIREs Comput. Mol. Sci.* **2014**, *4*, 269–284.

[325] Dalton, A Molecular Electronic Structure Program, Release DALTON 2015.0. See http://daltonprogram.org/, 2015.

[326] Mao, M.; Xiao, S.; Yi, T.; Zou, K. *J. Fluorine Chem.* **2011**, *132*, 612–616.

[327] Ross, T. W.; Sathyamoorthi, G.; Boyer, J. H. *Het. Chem.* **1993**, *4*, 609–612.

[328] Bañuelos, J.; Arbeloa, F. L.; Martinez, V.; Liras, M.; Costela, A.; Moreno, I. G.; Arbeloa, I. n. L. *Phys. Chem. Chem. Phys.* **2011**, *13*, 3437–3445.

[329] Wu, L.; Burgess, K. *J. Am. Chem. Soc.* **2008**, *130*, 4089–4096.

[330] Baranov, M. S.; Lukyanov, K. A.; Borissova, A. O.; Shamir, J.; Kosenkov, D.; Slipchenko, L. V.; Tolbert, L. M.; Yampolsky, I. V.; Solntsev, K. M. *J. Am. Chem. Soc.* **2012**, *134*, 6025–6032.

[331] Sathyamoorthi, G.; Boyer, J. H.; Allik, T. H.; Chandra, S. *Het. Chem.* **1994**, *5*, 403–407.

[332] Kubota, Y.; Tsuzuki, T.; Funabiki, K.; Ebihara, M.; Matsui, M. *Org. Lett.* **2010**, *12*, 4010–4013.

[333] Ziessel, R.; Goze, C.; Ulrich, G. *SYNTHESIS-STUTTGART* **2007**, 936–949.

[334] Goud, T. V.; Tutar, A.; Biellmann, J.-F. *Tetrahedron* **2006**, *62*, 5084–5091.

[335] Boyer, J. H.; Haag, A. M.; Sathyamoorthi, G.; Soong, M.-L.; Thangaraj, K.; Pavlopoulos, T. G. *Het. Chem.* **1993**, *4*, 39–49.

[336] Walczak, E.; Szefczyk, B.; Andruniów, T. *J. Chem. Theory Comput.* **2013**, *9*, 4915–4927.

[337] Send, R.; Kühn, M.; Furche, F. *J. Chem. Theory Comput.* **2011**, *7*, 2376–2386.

[338] Goerigk, L.; Moellmann, J.; Grimme, S. *Phys. Chem. Chem. Phys.* **2009**, *11*, 4611–4620.

[339] Barone, V.; Bloino, J.; Biczysko, M.; Santoro, F. *J. Chem. Theory Comput.* **2009**, *5*, 540–554.

[340] Gorelsky, S. AOMix: Program for Molecular Orbital Analysis; version 6.X, University of Ottawa, 2013, http://www.sg-chem.net/.

[341] Gorelsky, S.; Lever, A. *J. Organomet. Chem.* **2001**, *635*, 187–196.

[342] Tozer, D. J. *J. Chem. Phys.* **2003**, *119*, 12697–12699.

[343] Dreuw, A.; Head-Gordon, M. *J. Am. Chem. Soc.* **2004**, *126*, 4007–4016.

[344] Grimme, S.; Neese, F. *J. Chem. Phys.* **2007**, *127*, 154116.

[345] Briggs, E. A.; Besley, N. A.; Robinson, D. *J. Phys. Chem. A* **2013**, *117*, 2644–2650.

[346] Buyuktemiz, M.; Duman, S.; Dede, Y. *J. Phys. Chem. A* **2013**, *117*, 1665–1669.

[347] Valiev, R.; Sinelnikov, A.; Aksenova, Y.; Kuznetsova, R.; Berezin, M.; Semeikin, A.; Cherepanov, V. *Spectrochim. Acta Mol. Biomol. Spectrosc.* **2014**, *117*, 323–329.

[348] Jiang, X.-D.; Zhang, H.; Zhang, Y.; Zhao, W. *Tetrahedron* **2012**, *68*, 9795–9801.

[349] Tanaka, K.; Yamane, H.; Yoshii, R.; Chujo, Y. *Bioorg. Med. Chem.* **2013**, *21*, 2715–2719.

[350] Killoran, J.; Allen, L.; Gallagher, J. F.; Gallagher, W. M.; ÓShea, D. F. *Chem. Comm.* **2002**, 1862–1863.

[351] Bellier, Q.; Pégaz, S.; Aronica, C.; Guennic, B. L.; Andraud, C.; Maury, O. *Org. Lett.* **2011**, *13*, 22–25.

[352] Bouit, P.-A.; Kamada, K.; Feneyrou, P.; Berginc, G.; Toupet, L.; Maury, O.; Andraud, C. *Adv. Mat.* **2009**, *21*, 1151–1154.

[353] Jiao, L.; Wu, Y.; Wang, S.; Hu, X.; Zhang, P.; Yu, C.; Cong, K.; Meng, Q.; Hao, E.; Vicente, M. G. H. *J. Org. Chem.* **2014**, *79*, 1830–1835.

[354] Lim, S. H.; Thivierge, C.; Nowak-Sliwinska, P.; Han, J.; van den Bergh, H.; Wagniéres, G.; Burgess, K.; Lee, H. B. *J. Med. Chem.* **2010**, *53*, 2865–2874.

[355] Momeni, M. R.; Brown, A. *J. Chem. Theory Comput.* **2015**, *11*, 2619–2632.

[356] Jacquemin, D.; Duchemin, I.; Blase, X. *J. Chem. Theory Comput.* **2015**, *11*, 3290–3304.

[357] Röhr, H.; Trieflinger, C.; Rurack, K.; Daub, J. *Chem. Eur. J.* **2006**, *12*, 689–700.

[358] Yokoi, H.; Hiroto, S.; Shinokubo, H. *Org. Lett.* **2014**, *16*, 3004–3007.

[359] Misra, R.; Dhokale, B.; Jadhav, T.; Mobin, S. M. *New J. Chem.* **2014**, *38*, 3579–3585.

[360] Grimme, S.; Steinmetz, M. *Phys. Chem. Chem. Phys.* **2013**, *15*, 16031–16042.

[361] Goerigk, L.; Grimme, S. *Phys. Chem. Chem. Phys.* **2011**, *13*, 6670–6688.

[362] Hohenstein, E. G.; Chill, S. T.; Sherrill, C. D. *J. Chem. Theory Comput.* **2008**, *4*, 1996–2000.

[363] Zhang, Y.; Yang, W. *Phys. Rev. Lett.* **1998**, *80*, 890–890.

[364] Becke, A. D. *J. Chem. Phys.* **1993**, *98*, 5648–5652.

[365] Yang, K.; Zheng, J.; Zhao, Y.; Truhlar, D. G. *J. Chem. Phys.* **2010**, *132*, 164117.

[366] Zhao, Y.; Lynch, B. J.; Truhlar, D. G. *J. Phys. Chem. A* **2004**, *108*, 4786–4791.

[367] Grimme, S. *J. Chem. Phys* **2006**, *124*, 034108.

[368] Schwabe, T.; Grimme, S. *Phys. Chem. Chem. Phys.* **2006**, *8*, 4398–4401.

[369] Karton, A.; Tarnopolsky, A.; Lamère, J.-F.; Schatz, G. C.; Martin, J. M. L. *J. Phys. Chem. A* **2008**, *112*, 12868–12886.

[370] Sancho-García, J. C.; Pérez-Jiménez, A. J. *J. Chem. Phys.* **2009**, *131*, 084108.

[371] Kozuch, S.; Martin, J. M. L. *J. Comput. Chem.* **2013**, *34*, 2327–2344.

[372] Chai, J.-D.; Mao, S.-P. *Chem. Phys. Lett.* **2012**, *538*, 121 – 125.

[373] Brémond, E.; Adamo, C. *J. Chem. Phys.* **2011**, *135*, 024106.

[374] Neese, F.; Wennmohs, F.; Hansen, A.; Becker, U. *Chem. Phys.* **2009**, *356*, 98 – 109.

[375] Eichkorn, K.; Weigend, F.; Treutler, O.; Ahlrichs, R. *Theor. Chem. Acc.* **1997**, *97*, 119–124.

[376] Weigend, F. *Phys. Chem. Chem. Phys.* **2006**, *8*, 1057–1065.

[377] Weigend, F.; Köhn, A.; Hättig, C. *J. Chem. Phys.* **2002**, *116*, 3175–3183.

[378] Yu, C.; Jiao, L.; Zhang, P.; Feng, Z.; Cheng, C.; Wei, Y.; Mu, X.; Hao, E. *Org. Lett.* **2014**, *16*, 3048–3051.

[379] Hellweg, A.; Hättig, C.; Höfener, S.; Klopper, W. *Theor. Chem. Acc.* **2007**, *117*, 587–597.

[380] Steinmetz, M.; Grimme, S. *Chem. Open* **2013**, *2*, 115–124.

[381] Goerigk, L.; Grimme, S. *WIREs Comput. Mol. Sci.* **2014**, *4*, 576–600.

[382] Schirmer, J. *Phys. Rev. A* **1982**, *26*, 2395–2416.

[383] Trofimov, A. B.; Schirmer, J. *J. Phys. B: At., Mol. Opt. Phys.* **1995**, *28*, 2299–2324.

[384] Lawetz, V.; Orlandi, G.; Siebrand, W. *J. Chem. Phys.* **1972**, *56*, 4058–4072.

[385] Robinson, G. W.; Frosch, R. P. *J. Chem. Phys.* **1963**, *38*, 1187–1203.

[386] Marian, C. M. *WIREs Comput. Mol. Sci.* **2012**, *2*, 187–203.

[387] Yu-Tzu Li, E.; Jiang, T.-Y.; Chi, Y.; Chou, P.-T. *Phys. Chem. Chem. Phys.* **2014**, *16*, 26184–26192.

[388] Heß, B. A.; Marian, C. M.; Wahlgren, U.; Gropen, O. *Chem. Phys. Lett.* **1996**, *251*, 365–371.

[389] Rinkevicius, Z.; Tunell, I.; Sałek, P.; Vahtras, O.; Å gren, H. *J. Chem. Phys.* **2003**, *119*, 34–46.

[390] Danovich, D.; Marian, C. M.; Neuheuser, T.; Peyerimhoff, S. D.; Shaik, S. *J. Phys. Chem. A* **1998**, *102*, 5923–5936.

[391] Tatchen, J.; Marian, C. M. *Chem. Phys. Lett.* **1999**, *313*, 351 – 357.

[392] Alberto, M. E.; Simone, B. C. D.; Mazzone, G.; Quartarolo, A. D.; Russo, N. *J. Chem. Theory Comput.* **2014**, *10*, 4006–4013.

[393] Werner, H.-J.; Knowles, P. J.; Knizia, G.; Manby, F. R.; Schütz, M. *WIREs Comput. Mol. Sci.* **2012**, *2*, 242–253.

[394] Neese, F. ORCA: *An ab initio, density functional and semiempirical program package*, V. 3.0.2. Max Planck Institute for Bioinorganic Chemistry: Muelheim/Ruhr, Germany, 2012.

[395] Neese, F. *WIREs Comput. Mol. Sci.* **2012**, *2*, 73.

[396] Li, H.-J.; Fu, W.-F.; Li, L.; Gan, X.; Mu, W.-H.; Chen, W.-Q.; Duan, X.-M.; Song, H.-B. *Org. Lett.* **2010**, *12*, 2924–2927.

[397] Poirel, A.; Nicola, A. D.; Retailleau, P.; Ziessel, R. *J. Org. Chem.* **2012**, *77*, 7512–7525.

[398] Pawluć, P.; Franczyk, A.; Walkowiak, J.; Hreczycho, G.; Kubicki, M.; Marciniec, B. *Org. Lett.* **2011**, *13*, 1976–1979.

[399] Hayashi, Y.; Yamaguchi, S.; Cha, W. Y.; Kim, D.; Shinokubo, H. *Org. Lett.* **2011**, *13*, 2992–2995.

[400] Nepomnyashchii, A. B.; Bröring, M.; Ahrens, J.; Bard, A. J. *J. Am. Chem. Soc.* **2011**, *133*, 8633–8645.

[401] Ventura, B.; Marconi, G.; Broring, M.; Kruger, R.; Flamigni, L. *New J. Chem.* **2009**, *33*, 428–438.

[402] Wu, W.; Cui, X.; Zhao, J. *Chem. Comm.* **2013**, *49*, 9009–9011.

[403] Nakamura, M.; Tahara, H.; Takahashi, K.; Nagata, T.; Uoyama, H.; Kuzuhara, D.; Mori, S.; Okujima, T.; Yamada, H.; Uno, H. *Org. Biomol. Chem.* **2012**, *10*, 6840–6849.

[404] Iversen, K. J.; Wilson, D. J. D.; Dutton, J. L. *Dalton Trans.* **2013**, *42*, 11035–11038.

[405] Frey, G. D.; Masuda, J. D.; Donnadieu, B.; Bertrand, G. *Angew. Chem. Int. Ed.* **2010**, *49*, 9444–9447.

[406] Heuclin, H.; Ho, S. Y.-F.; Le Goff, X. F.; So, C.-W.; Mézailles, N. *J. Am. Chem. Soc.* **2013**, *135*, 8774–8777.

[407] Fukui, K. *Acc. Chem. Res.* **1981**, *14*, 363–368.

[408] Hratchian, H. P.; Schlegel, H. B. *J. Chem. Phys.* **2004**, *120*, 9918–9924.

[409] Hratchian, H. P.; Schlegel, H. B. *J. Chem. Theory Comput.* **2005**, *1*, 61–69.

[410] NBO Version 3.1, E. D. Glendening, A. E. Reed, J. E. Carpenter, and F. Weinhold.

[411] Keith, T. A. AIMAll (version 13.01.27); TK Gristmill Software: Overland Park, KS, USA, 2013.

[412] Tonner, R.; Frenking, G. *Chem. Eur. J.* **2008**, *14*, 3273–3289.

[413] Dixon, D. A.; Gutowski, M. *J. Phys. Chem. A* **2005**, *109*, 5129–5135.

[414] Shriver, D. F.; Atkins, P. W. *Inorganic Chemistry*; 4th ed.; p. 288.

[415] Frey, G. D.; Donnadieu, B.; Soleilhavoup, M.; Bertrand, G. *Chem. Asian J.* **2011**, *6*, 402–405.

[416] Singh, A. P.; Samuel, P. P.; Roesky, H. W.; Schwarzer, M. C.; Frenking, G.; Sidhu, N. S.; Dittrich, B. *J. Am. Chem. Soc.* **2013**, *135*, 7324–7329.

[417] Tan, M.; Zhang, Y.; Ying, J. *Adv. Synth. Cat.* **2009**, *351*, 1390–1394.

[418] Jones, C. *Chem. Comm.* **2001**, 2293–2298.

[419] Kuhn, N.; Al-Sheikh, A. *Coord. Chem. Rev.* **2005**, *249*, 829–857.

[420] Prabusankar, G.; Sathyanarayana, A.; Suresh, P.; Babu, C. N.; Srinivas, K.; Metla, B. P. R. *Coord. Chem. Rev.* **2014**, *269*, 96–133.

[421] Kuhn, N.; Bohnen, H.; Kreutzberg, J.; Bläser, D.; Boese, R. *J. Chem. Soc. Chem. Comm.* **1993**, 1136–1137.

[422] Fürstner, A.; Alcarazo, M.; Goddard, R.; Lehmann, C. W. *Angew. Chem. Int. Ed.* **2008**, *47*, 3210–3214.

[423] Dumrath, A.; Wu, X.-F.; Neumann, H.; Spannenberg, A.; Jackstell, R.; Beller, M. *Angew. Chem. Int. Ed.* **2010**, *49*, 8988–8992.

[424] Malcolm, A. C.; Sabourin, K. J.; McDonald, R.; Ferguson, M. J.; Rivard, E. *Inorg. Chem.* **2012**, *51*, 12905–12916.

[425] Al-Rafia, S. M. I.; Momeni, M. R.; McDonald, R.; Ferguson, M. J.; Brown, A.; Rivard, E. *Angew. Chem. Int. Ed.* **2013**, *52*, 6390–6395.

[426] Wang, Y.; Abraham, M. Y.; Gilliard, R. J.; Sexton, D. R.; Wei, P.; Robinson, G. H. *Organometallics* **2013**, *32*, 6639–6642.

[427] Ghadwal, R. S.; Reichmann, S. O.; Engelhardt, F.; Andrada, D. M.; Frenking, G. *Chem. Comm.* **2013**, *49*, 9440–9442.

[428] Berger, C. J.; He, G.; Merten, C.; McDonald, R.; Ferguson, M. J.; Rivard, E. *Inorg. Chem.* **2014**, *53*, 1475–1486.

[429] Bestmann, H. J.; Sühs, K.; Röder, T. *Angew. Chem. Int. Ed.* **1981**, *20*, 1038–1039.

[430] Breitsameter, F.; Schrödel, H.-P.; Schmidpeter, A.; Nöth, H.; Rojas-Lima, S. *Z. Anorg. Allg. Chem.* **1999**, *625*, 1293–1300.

[431] Zhao, Y.; Schultz, N. E.; Truhlar, D. G. *J. Chem. Theory Comput.* **2006**, *2*, 364–382.

[432] Peterson, K. A.; Puzzarini, C. *Theor. Chem. Acc.* **2005**, *114*, 283–296.

[433] Figgen, D.; Peterson, K. A.; Dolg, M.; Stoll, H. *J. Chem. Phys.* **2009**, *130*, 164108.

[434] Feller, D. *J. Comp. Chem.* **1996**, *17*, 1571–1586.

[435] Schuchardt, K. L.; Didier, B. T.; Eslethagen, T.; Sun, L.; Gurumoorthi, V.; Chase, J.; Li, J.; Windus, T. L. *J. Chem. Inf. Model* **2007**, *47*, 1045–1052.

[436] Perdew, J. P. *Phys. Rev. B* **1986**, *33*, 8822–8824.

[437] Dunning, T. H. *J. Chem. Phys.* **1971**, *55*, 716–723.

[438] Morokuma, K. *J. Chem. Phys.* **1971**, *55*, 1236–1244.

[439] Ziegler, T.; Rauk, A. *Theor. Chim. Acta* **1977**, *46*, 1–10.

[440] Bickelhaupt, F. M.; Baerends, E. J. *Rev. Comput. Chem.* **2000**, *15*, 1–86.

[441] Te Velde, G.; Bickelhaupt, E. J., F. M. Baerends; Fonseca Guerra, C.; Van Gisbergen, J. A.; Snijders, J.; Ziegler, T. *J. Comput. Chem.* **2001**, *22*, 931–967.

[442] Frenking, G.; Wichmann, K.; Frohlich, N.; Loschen, C.; Lein, M.; Frunzke, J.; Rayon, V. M. *Coord. Chem. Rev.* **2003**, *238*, 55–82.

[443] Lein, M.; Frenking, G. In *Theory and Applications of Computational Chemistry: The First 40 Years*; Dykstra, C. E., Frenking, G., Kim, K. S., Scuseria, G. E., Eds.; Elsevier, Amsterdam, 2001; pp 367–414.

[444] Mitoraj, M. P.; Michalak, A.; Ziegler, T. *J. Chem. Theory Comput.* **2009**, *5*, 962–975.

[445] Schleyer, P. v. R.; Maerker, C.; Dransfeld, A.; Jiao, H.; Hommes, N. J. R. v. E. *J. Am. Chem. Soc.* **1996**, *118*, 6317–6318.

[446] ADF2013, SCM, Theoretical Chemistry, Vrije Universiteit, Amsterdam, The Netherlands, http://www.scm.com.

[447] Xu, H.; Pittman, C. U. Jr.,; Saebø, S. *Struc. Chem.* **2013**, *24*, 1383–1393.

[448] Cui, W.; Wang, C.; Shao, J.; Zhu, X. *Int. J. Quant. Chem.* **2013**, *113*, 2251–2260.

[449] Sutjianto, A.; Pandey, R.; Manuel Recio, J. *Int. J. Quant. Chem.* **1994**, *52*, 199–210.

[450] Martin, J. M.; El-Yazal, J.; François, J.-P. *Chem. Phys. Lett.* **1996**, *248*, 95 – 101.

[451] Martin, J. M.; El-Yazal, J.; Francois, J.-P.; Gijbels, R. *Chem. Phys. Lett.* **1995**, *232*, 289 – 294.

[452] Martin, J.; Francois, J.; Gijbels, R. *Chem. Phys. Lett.* **1992**, *193*, 243 – 250.

[453] Martin, J. M. *Mol. Phys.* **2014**, *112*, 785–793.

[454] Karton, A.; Martin, J. M. L. *J. Chem. Phys.* **2006**, *125*, –.

[455] Martin, J. M. L.; Lee, T. J.; Scuseria, G. E.; Taylor, P. R. *J. Chem. Phys.* **1992**, *97*, 6549–6556.

[456] Asmis, K. R.; Taylor, T. R.; Neumark, D. M. *Chem. Phys. Lett.* **1998**, *295*, 75 – 81.

[457] Lorenz, M.; Agreiter, J.; Smith, A. M.; Bondybey, V. E. *J. Chem. Phys.* **1996**, *104*, 3143–3146.

[458] Curran, D. P.; Solovyev, A.; Makhlouf Brahmi, M.; Fensterbank, L.; Malacria, M.; Lacôte, E. *Angew. Chem. Int. Ed.* **2011**, *50*, 10294–10317.

[459] Sabourin, K. J.; Malcolm, A. C.; McDonald, R.; Ferguson, M. J.; Rivard, E. *Dalton Trans.* **2013**, *42*, 4625–4632.

[460] Stubbs, N. E.; Jurca, T.; Leitao, E. M.; Woodall, C. H.; Manners, I. *Chem. Comm.* **2013**, *49*, 9098–9100.

[461] Reed, A. E.; Schleyer, P. v. R. *J. Am. Chem. Soc.* **1990**, *112*, 1434–1445.

[462] Paetzold, P.; von Plotho, C.; Schmid, G.; Boese, R.; Schrader, B.; Bougeard, D.; Pfeiffer, U.; Gleiter, R.; Schäfer, W. *Chem. Ber.* **1984**, *117*, 1089.

[463] Rivard, E.; Merrill, W. A.; Fettinger, J. C.; Wolf, R.; Spikes, G. H.; Power, P. P. *Inorg. Chem.* **2007**, *46*, 2971–2978.

[464] Luthin, W.; Elter, G.; Heine, A.; Stalke, D.; Sheldrick, G. M.; Meller, A. *Z. Anorg. Allg. Chem.* **1992**, *608*, 147–152.

[465] Elter, G.; Neuhaus, M.; Meller, A.; Schmidt-Bäse, D. *J. Organomet. Chem.* **1990**, *381*, 299–313.

[466] Bartlett, R. A.; Chen, H.; Dias, H. V. R.; Olmstead, M. M.; Power, P. P. *J. Am. Chem. Soc.* **1988**, *110*, 446–449.

[467] Tai, T. B.; Nguyen, M. T. *Angew. Chem. Int. Ed.* **2013**, *52*, 4554–4557.

[468] Holzmann, N.; Stasch, A.; Jones, C.; Frenking, G. *Chem. Eur. J.* **2011**, *17*, 13517–13525.

[469] Holzmann, N.; Stasch, A.; Jones, C.; Frenking, G. *Chem. Eur. J.* **2013**, *19*, 6467–6479.

[470] Momeni, M. R.; Rivard, E.; Brown, A. *Organometallics* **2013**, *32*, 6201–6208.

[471] Sarmah, S.; Guha, A. K.; Phukan, A. K. *Eur. J. Inorg. Chem.* **2013**, 3233–3239.

[472] Loschen, C.; Voigt, K.; Frunzke, J.; Diefenbach, A.; Diedenhofen, M.; Frenking, G. *Z. Anorg. Allg. Chem.* **2002**, *628*, 1294–1304.

[473] Bessac, F.; Frenking, G. *Inorg. Chem.* **2003**, *42*, 7990–7994.

[474] Bessac, F.; Frenking, G. *Inorg. Chem.* **2006**, *45*, 6956–6964.

[475] Fischer, R. C.; Power, P. P. *Chem. Rev.* **2010**, *110*, 3877–3923.

[476] He, G.; Shynkaruk, O.; Lui, M. W.; Rivard, E. *Chem. Rev.* **2014**, *114*, 7815–7880.

[477] Ogata, S.; Ohba, N.; Kouno, T. *J. Phys. Chem. C* **2013**, *117*, 17960–17968.

[478] Hutter, J.; Curioni, A. *Chem. Phys. Chem.* **2005**, *6*, 1788–1793.

[479] Doltsinis, N. L.; Marx, D. *Phys. Rev. Lett.* **2002**, *88*, 166402.

[480] Craig, C. F.; Duncan, W. R.; Prezhdo, O. V. *Phys. Rev. Lett.* **2005**, *95*, 163001.

[481] Tapavicza, E.; Tavernelli, I.; Rothlisberger, U. *Phys. Rev. Lett.* **2007**, *98*, 023001.

[482] Riplinger, C.; Neese, F. *J. Chem. Phys.* **2013**, *138*, 034106.

[483] Sparta, M.; Riplinger, C.; Neese, F. *J. Chem. Theory Comput.* **2014**, *10*, 1099–1108.

[484] Calbo, J.; Ortí, E.; Sancho-García, J. C.; Aragó, J. *J. Chem. Theory Comput.* **2015**, *11*, 932–939.

[485] Liakos, D. G.; Sparta, M.; Kesharwani, M. K.; Martin, J. M. L.; Neese, F. *J. Chem. Theory Comput.* **2015**, *11*, 1525–1539.

[486] Liakos, D. G.; Neese, F. *J. Chem. Theory Comput.* **2015**, *11*, 2137–2143.

[487] Hyttinen, N.; Kupiainen-Määttä, O.; Rissanen, M. P.; Muuronen, M.; Ehn, M.; Kurtén, T. *J. Phys. Chem. A* **2015**, *119*, 6339–6345.

[488] Elm, J.; Myllys, N.; Hyttinen, N.; Kurtén, T. *J. Phys. Chem. A* **2015**, *119*, 8414–8421.

[489] Liakos, D. G.; Neese, F. *J. Chem. Theory Comput.* **2015**, DOI: 10.1021/acs.jctc.5b00359.

Appendix A

Appendix for Chapter 3.

TABLE A.1: Configuration interaction vectors (CI Vector) for all the structures along with the energy of each state at CASSCF/cc-pVDZ level of theory. Only coefficients > 0.05 (for at least one of the states considered) are listed.

Molecule (**1**)		A_1 state
CI Vector: Ground State		S_0
222000	22200	0.9014105
222200	22000	-0.1252693
2b2a00	22200	-0.0880127
2a2b00	22200	0.0880127
202200	22200	-0.0854636
222000	22020	-0.0539157
TOTAL ENERGY		-677.85840530

Molecule (**1**)		B_2 state	B_2 state
CI Vector: Excited State		S_1	S_2
222b00	22a00	0.5439336	-0.2774005
222a00	22b00	-0.5439336	0.2774005
222a00	2b200	-0.2616851	-0.4980206
222b00	2a200	0.2616851	0.4980206
22a200	22b00	-0.0768692	-0.2628495
22b200	22a00	0.0768692	0.2628495
2a2200	22b00	-0.1163715	0.0452494
2b2200	22a00	0.1163715	-0.0452494
222a00	220b0	-0.0969089	0.0293266
222b00	220a0	0.0969089	-0.0293266
222b00	2aab0	-0.0289545	-0.0603101
222a00	2bba0	-0.0289545	-0.0603101
2220a0	2b200	0.0570766	-0.0010905
2220b0	2a200	-0.0570766	0.0010905
2b2a0b	22a00	-0.0569339	0.0417183
2a2b0a	22b00	-0.0569339	0.0417183
b22a0b	22a00	0.0522480	-0.0206657
a22b0a	22b00	0.0522480	-0.0206657
222b00	2ab0a	0.0520082	0.0320977
222a00	2ba0b	0.0520082	0.0320977
TOTAL ENERGIES		-677.75442260	-677.70769719

Molecule (**2**)		A_1 state
CI Vector: Ground State		S_0
222000	22200	0.8898604
222200	22000	-0.1130943
222200	20200	-0.1119766
22ba00	22200	-0.0909718
22ab00	22200	0.0909718
222200	2ba00	0.0826821
222200	2ab00	-0.0826821
202200	22200	-0.0635908
220200	22200	-0.0625382
2b2a00	2a2b0	0.0503791
2a2b00	2b2a0	0.0503791
TOTAL ENERGY		-693.85649011

Molecule (**2**)		B_2 state
CI Vector: Excited State		S_1
222a00	22b00	-0.6006278
222b00	22a00	0.6006278
22b200	22a00	0.1326160
22a200	22b00	-0.1326160
222b00	2aba0	0.0882914
222a00	2bab0	0.0882914
22aba0	22b00	0.0789554
22bab0	22a00	0.0789554
2b2a0b	22a00	0.0757173
2a2b0a	22b00	0.0757173
222a00	2b200	-0.0554592
222b00	2a200	0.0554592
2220a0	2b200	0.0553116
2220b0	2a200	-0.0553116
22a200	2b200	0.0548761
22b200	2a200	-0.0548761
222a00	220b0	-0.0527308
222b00	220a0	0.0527308
222a00	2abb0	-0.0508749
222b00	2baa0	-0.0508749
TOTAL ENERGY		-693.76223164

Molecule (**3**)	A′ State	A′ State
CI Vector:	S_0	S_1
22222200000	0.9078941	0.0977762
22222ba0000	0.0828312	-0.6099698
22222ab0000	-0.0828312	0.6099698
22220220000	-0.0877350	-0.0419091
2222a20b000	-0.0028466	-0.0797450
2222b20a000	0.0028466	0.0797450
22222002000	-0.0701156	-0.0428281
2222abba000	-0.0043655	0.0630910
2222baab000	-0.0043655	0.0630910
222a220b000	-0.0014483	-0.0581622
222b220a000	0.0014483	0.0581622
22222000200	-0.0579816	-0.0153152
222b2aab000	0.0092554	-0.0555832
222a2bba000	0.0092554	-0.0555832
2222abb000a	0.0077159	-0.0528588
2222baa000b	0.0077159	-0.0528588
22022200020	-0.0514116	0.0000257
22202202000	-0.0509665	0.0068177
TOTAL ENERGIES	-677.88009631	-677.74415715

Molecule (**4**)	A′ State	A′ State
CI Vector:	S_0	S_1
22222200000	0.9097005	-0.0677598
22222ba0000	-0.0618680	-0.6096321
22222ab0000	0.0618680	0.6096321
2222b20a000	0.0075881	-0.0939389
2222a20b000	-0.0075881	0.0939389
22220220000	-0.0912832	0.0421203
222b220a000	-0.0027723	0.0690876
222a220b000	0.0027723	-0.0690876
22222002000	-0.0672951	0.0248862
22222000200	-0.0623473	0.0186747
2222abba000	0.0002181	0.0593394
2222baab000	0.0002181	0.0593394
222a2bba000	0.0035536	0.0567357
222b2aab000	0.0035536	0.0567357
2222abb000a	-0.0042891	-0.0540053
2222baa000b	-0.0042891	-0.0540053
22022200020	-0.0509137	0.0025691
22202202000	-0.0502984	-0.0055310
TOTAL ENERGIES	-693.89497686	-693.75044783

Molecule ($\mathbf{5}_H$)	A′ State	A′ State
CI Vector:	S_0	S_1
2222220000	0.9336532	0.0126697
22222ba000	0.0212084	-0.6310302
22222ab000	-0.0212084	0.6310302
2222a20b00	-0.0368133	-0.0995031
2222b20a00	0.0368133	0.0995031
2222200200	-0.0969010	-0.0816294
2220220020	-0.0932945	0.0053098
2222abba00	0.0107759	0.0832567
2222baab00	0.0107759	0.0832567
2222022000	-0.0792742	0.0211109
2222abab00	0.0276335	-0.0758753
2222baba00	0.0276335	-0.0758753
22202ab020	0.0052671	-0.0680735
22202ba020	-0.0052671	0.0680735
222a22000b	0.0094115	0.0602741
222b22000a	-0.0094115	-0.0602741
222a2b2000	-0.0005245	-0.0564431
222b2a2000	0.0005245	0.0564431
222202a00b	-0.0542376	0.0002286
222202b00a	0.0542376	-0.0002286
2222202000	-0.0531662	0.0352601
222b2a0020	0.0501988	-0.0336386
222a2b0020	-0.0501988	0.0336386
TOTAL ENERGIES	-671.98892209	-671.80764637

Molecule (**5**)	A′ State	A′ State
CI Vector:	S_0	S_1
2222220000	0.9337900	0.0233738
22222ba000	0.0291851	-0.6345658
22222ab000	-0.0291851	0.6345658
2222200200	-0.0966723	-0.0800361
2222b20a00	-0.0353235	-0.0904204
2222a20b00	0.0353235	0.0904204
2220220020	-0.0891458	0.0027862
2222baab00	-0.0089109	-0.0816218
2222abba00	-0.0089109	-0.0816218
2222022000	-0.0795612	0.0095266
2222baba00	-0.0276445	0.0732068
2222abab00	-0.0276445	0.0732068
22202ba020	-0.0058537	0.0652992
22202ab020	0.0058537	-0.0652992
222b2a2000	-0.0023497	0.0550781
222a2b2000	0.0023497	-0.0550781
222b22000a	0.0084523	0.0543114
222a22000b	-0.0084523	-0.0543114
2222202000	-0.0534083	0.0343663
222202a00b	0.0520561	0.0024017
222202b00a	-0.0520561	-0.0024017
TOTAL ENERGIES	-827.96875419	-827.79589147

Molecule (**6**)	A′ State
CI Vector	S_0
222000 222000	0.9078594
22ab00 222000	0.0637026
22ba00 222000	-0.0637026
222000 220020	-0.0624647
220020 222000	-0.0605684
220200 222000	-0.0584790
220000 222020	-0.0541352
TOTAL ENERGY	-770.62770441

Molecule (**6**)	A″ State
CI Vector	S_1
22b000 222a00	-0.6024277
22a000 222b00	0.6024277
222a00 22b000	-0.1096131
222b00 22a000	0.1096131
220b00 222a00	0.0866164
220a00 222b00	-0.0866164
b2a0b0 222a00	0.0674663
a2b0a0 222b00	0.0674663
22b000 22aba0	0.0655509
22a000 22bab0	0.0655509
2bab00 222a00	0.0595048
2aba00 222b00	0.0595048
b2a00b 222a00	-0.0531579
a2b00a 222b00	-0.0531579
2b2000 2220a0	-0.0514718
2a2000 2220b0	0.0514718
2220a0 2b2000	0.0503294
2220b0 2a2000	-0.0503294
TOTAL ENERGY	-770.48424267

Molecule (**7**)	A State	A State
CI Vector	S_0	S_1
2222220000	0.9298003	0.0219354
22222ba000	0.0230406	-0.6349376
22222ab000	-0.0230406	0.6349376
2222202000	-0.0916482	0.0186780
222a2bb00a	-0.0076190	-0.0846017
222b2aa00b	-0.0076190	-0.0846017
2222baab00	-0.0090838	0.0794190
2222abba00	-0.0090838	0.0794190
2222022000	-0.0781245	-0.0311427
2220222000	-0.0774793	0.0195103
2222ba2000	-0.0502142	-0.0762346
2222ab2000	0.0502142	0.0762346
2222200020	-0.0637197	-0.0574860
2222b200a0	0.0112835	0.0608870
2222a200b0	-0.0112835	-0.0608870
222b2a2000	-0.0094286	0.0570768
222a2b2000	0.0094286	-0.0570768
2222b2a000	-0.0517122	0.0165893
2222a2b000	0.0517122	-0.0165893
TOTAL ENERGIES	-924.70337367	-924.57438315

Molecule (**8**)	A′ State	A′ State
CI Vector	S_0	S_1
22222200000	0.9201578	-0.0345942
22222ba0000	-0.0057247	-0.6414704
22222ab0000	0.0057247	0.6414704
22202202000	-0.0979579	-0.0026391
22220220000	-0.0892145	-0.0373950
22222020000	-0.0832187	0.0285581
22202ba2000	0.0041151	0.0684470
22202ab2000	-0.0041151	-0.0684470
2222abb00a0	0.0224236	0.0557459
2222baa00b0	0.0224236	0.0557459
22022200002	-0.0537473	-0.0005375
2222ba20000	-0.0506577	-0.0467230
2222ab20000	0.0506577	0.0467230
TOTAL ENERGIES	-943.36603417	-943.20751595

Molecule (**9**)	A′ State	A′ State
CI Vector	S_0	S_1
22222200000	0.8943672	-0.1448346
22222ab0000	0.1207499	0.6174324
22222ba0000	-0.1207499	-0.6174324
22222020000	-0.1061561	-0.0171421
22220220000	-0.0905191	0.0416709
2222ba20000	0.0747012	-0.0395989
2222ab20000	-0.0747012	0.0395989
22022200002	-0.0727595	0.0149477
2222abba000	-0.0057526	-0.0711843
2222baab000	-0.0057526	-0.0711843
222a2bb00a0	-0.0088899	0.0695954
222b2aa00b0	-0.0088899	0.0695954
22222000200	-0.0641689	0.0621917
22202220000	-0.0613487	-0.0002406
2222baa0b00	-0.0113716	0.0586625
2222abb0a00	-0.0113716	0.0586625
222220ab000	-0.0255818	0.0531017
222220ba000	0.0255818	-0.0531017
2222b20a000	0.0016796	-0.0507370
2222a20b000	-0.0016796	0.0507370
TOTAL ENERGIES	-940.72248931	-940.60206957

Molecule (**10**)	A State	A State
CI Vector	S_0	S_1
2222220000	0.9364653	-0.0784593
22222ba000	-0.0566429	-0.6354895
22222ab000	0.0566429	0.6354895
222a2b2000	0.0017674	0.0778725
222b2a2000	-0.0017674	-0.0778725
2222022000	-0.0656654	-0.0367545
2220222000	-0.0655590	0.0117194
2222b20a00	-0.0124310	0.0648131
2222a20b00	0.0124310	-0.0648131
2222200200	-0.0645767	0.0528515
2222abb0a0	-0.0080318	0.0638276
2222baa0b0	-0.0080318	0.0638276
222a2bb00a	0.0063337	0.0635700
222b2aa00b	0.0063337	0.0635700
2222020020	-0.0579440	0.0076842
222202b0a0	0.0542592	0.0152202
222202a0b0	-0.0542592	-0.0152202
222a2200b0	-0.0035106	0.0538874
222b2200a0	0.0035106	-0.0538874
TOTAL ENERGIES	-771.70965662	-771.57634813

Molecule (**11**)	A State
CI Vector	S_0
222000 22200	0.9227842
220000 22220	-0.1447939
222000 22ab0	0.0921460
222000 22ba0	-0.0921460
222000 22020	-0.0787311
2ab000 22220	-0.0745039
2ba000 22220	0.0745039
202000 22220	-0.0687181
202200 22200	-0.0534343
220200 22200	-0.0527928
TOTAL ENERGY	-1003.61867068

Molecule (**11**)	B State
CI Vector	S_1
22b000 222a0	-0.6386956
22a000 222b0	0.6386956
22a000 22b20	0.1339633
22b000 22a20	-0.1339633
22b000 22aba	0.0791060
22a000 22bab	0.0791060
220b00 222a0	-0.0646749
220a00 222b0	0.0646749
2b2000 22a20	0.0569283
2a2000 22b20	-0.0569283
2b2000 222a0	-0.0533557
2a2000 222b0	0.0533557
TOTAL ENERGY	-1003.50849006

Molecule (**12**)	A′ State
CI Vector	S_0
2222000 2200	0.9251844
222ba00 2200	-0.0706602
222ab00 2200	0.0706602
2222000 0220	-0.0628180
2222000 2002	-0.0610122
2202020 2200	-0.0573049
2220200 2200	-0.0544369
TOTAL ENERGY	-846.33882780

Molecule (**12**)	A″ State
CI Vector	S_1
222a000 22b0	-0.6231520
222b000 22a0	0.6231520
2220a00 22b0	0.1057308
2220b00 22a0	-0.1057308
222a000 2bab	-0.0801306
222b000 2aba	-0.0801306
22ba0b0 22a0	-0.0642660
22ab0a0 22b0	-0.0642660
2222b00 a200	0.0616741
2222a00 b200	-0.0616741
2222b00 2a00	-0.0588635
2222a00 2b00	0.0588635
a22b00a 22b0	-0.0548503
b22a00b 22a0	-0.0548503
b22ab00 22a0	-0.0509502
a22ba00 22b0	-0.0509502
TOTAL ENERGIES	-846.21075889

Molecule (**13**)	A′ State
CI Vector	S_0
220 220	0.9637074
222 200	-0.1095098
2ba 220	-0.0999619
2ab 220	0.0999619
202 220	-0.0712245
022 220	-0.0605623
222 020	-0.0579285
220 022	-0.0514325
TOTAL ENERGY	-982.45356829

Molecule (**13**)	A″ State
CI Vector	S_1
22b 2a0	-0.6766167
22a 2b0	0.6766167
2b2 2a0	-0.1290295
2a2 2b0	0.1290295
22b aba	-0.0947492
22a bab	-0.0947492
2b0 22a	-0.0537814
2a0 22b	0.0537814
22a abb	0.0512710
22b baa	0.0512710
TOTAL ENERGIES	-982.31955683

Molecule (**14**)	A State	A State
CI Vector	S_0	S_1
2222200000	0.9084913	0.1453701
2222ba0000	0.0924114	-0.6134651
2222ab0000	-0.0924114	0.6134651
22b2a20000	0.0218157	0.0995944
22a2b20000	-0.0218157	-0.0995944
2220220000	-0.0938996	0.0186258
2202220000	-0.0692874	-0.0426819
22b2aa0b00	-0.0069088	0.0685983
22a2bb0a00	-0.0069088	0.0685983
22b22a0000	0.0672022	-0.0028302
22a22b0000	-0.0672022	0.0028302
2b22aa00b0	0.0086926	-0.0668476
2a22bb00a0	0.0086926	-0.0668476
2222020000	-0.0658926	-0.0103868
222baab000	0.0127724	0.0652072
222abba000	0.0127724	0.0652072
222ab20000	0.0381658	-0.0621383
222ba20000	-0.0381658	0.0621383
TOTAL ENERGIES	-1114.20749643	-1114.10002857

Molecule (**15**)	A State	A State
CI Vector	S_0	S_1
2222200000	0.9149257	0.1010782
2222ba0000	0.0597394	-0.6187419
2222ab0000	-0.0597394	0.6187419
2220220000	-0.0898286	0.0225066
222ba20000	0.0291092	-0.0880469
222ab20000	-0.0291092	0.0880469
22b2a20000	-0.0373374	-0.0757728
22a2b20000	0.0373374	0.0757728
2222020000	-0.0750791	-0.0145961
2202220000	-0.0738524	-0.0371871
2a22bb00a0	0.0055153	-0.0693959
2b22aa00b0	0.0055153	-0.0693959
22a2bb0a00	-0.0061711	0.0640157
22b2aa0b00	-0.0061711	0.0640157
22b2aab000	-0.0191312	0.0595321
22a2bba000	-0.0191312	0.0595321
222a2b0000	0.0572509	0.0173043
222b2a0000	-0.0572509	-0.0173043
22b22a0000	-0.0524702	0.0161591
22a22b0000	0.0524702	-0.0161591
222abba000	-0.0235502	-0.0523390
222baab000	-0.0235502	-0.0523390
TOTAL ENERGIES	-1026.66350113	-1026.55739974

Molecule (**16**)	A′ State
CI Vector	S_0
2200 2200	0.9331462
2220 2000	-0.1143162
2ba0 2200	0.0826905
2ab0 2200	-0.0826905
2220 0200	-0.0743617
0220 2200	-0.0730967
2200 2002	-0.0572373
2200 0220	-0.0561528
2220 ba00	0.0508749
2220 ab00	-0.0508749
TOTAL ENERGY	-1026.66233488

Molecule (**16**)	A″ State
CI Vector	S_1
22b0 2a00	-0.6426759
22a0 2b00	0.6426759
2b20 2a00	0.1262531
2a20 2b00	-0.1262531
22b0 aba0	-0.1013537
22a0 bab0	-0.1013537
22b0 baa0	0.0578477
22a0 abb0	0.0578477
220b a200	-0.0549028
220a b200	0.0549028
2bab 2a00	-0.0548479
2aba 2b00	-0.0548479
2a00 220b	-0.0525734
2b00 220a	0.0525734
220b 200a	-0.0508572
220a 200b	0.0508572
TOTAL ENERGY	-1026.53527348

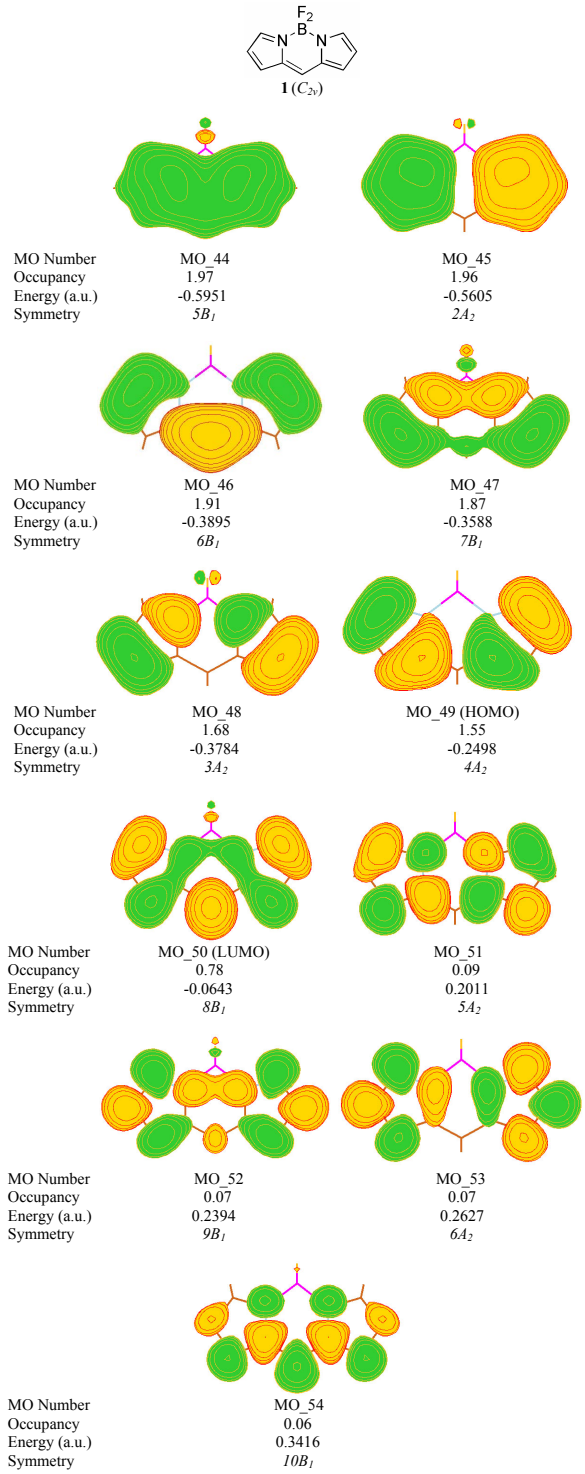

FIGURE A.1: All the selected occupied (MOs 44-49) and unoccupied (MOs 50-54) optimized molecular orbitals (after rotation and with isovalue of 0.02 a.u.) considered for the active space of (**1**) (12 electrons in 11 orbitals) along with their occupancies, energies, and symmetries computed at the CASSCF/cc-pVDZ//PBE0/cc-pVTZ level of theory.

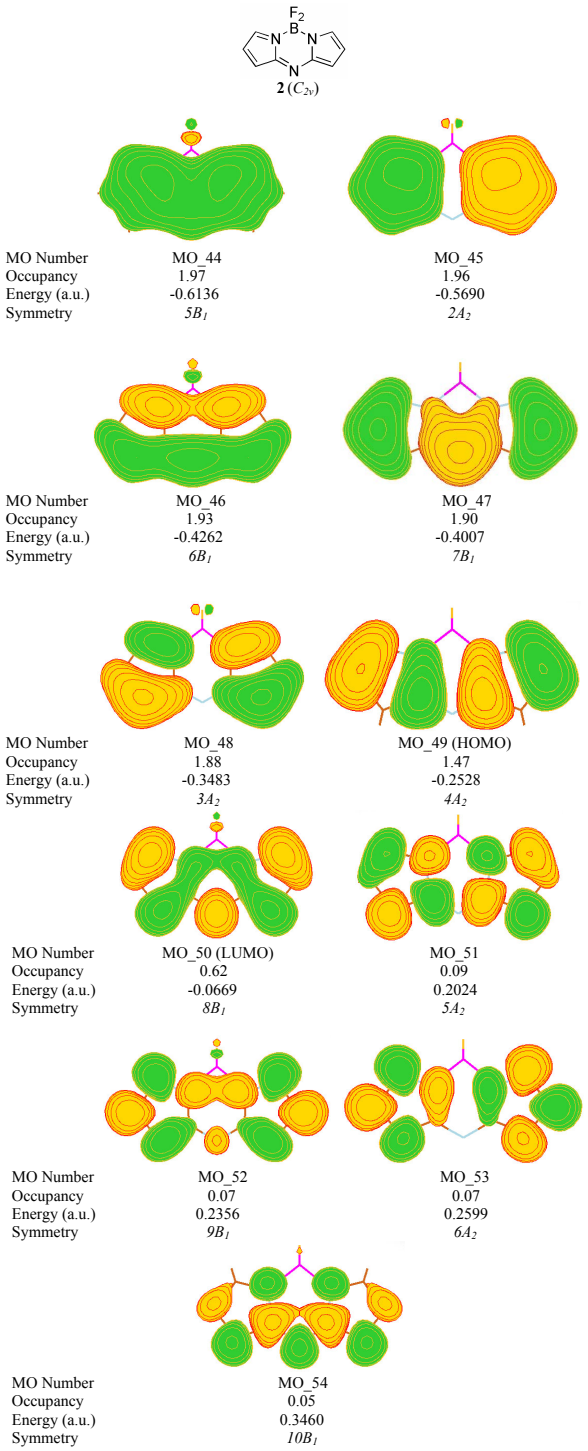

FIGURE A.2: All the selected occupied (MOs 44-49) and unoccupied (MOs 50-54) optimized molecular orbitals (after rotation and with isovalue of 0.02 a.u.) considered for the active space of (**2**) (12 electrons in 11 orbitals) along with their occupancies, energies, and symmetries computed at the CASSCF/cc-pVDZ//PBE0/cc-pVTZ level of theory.

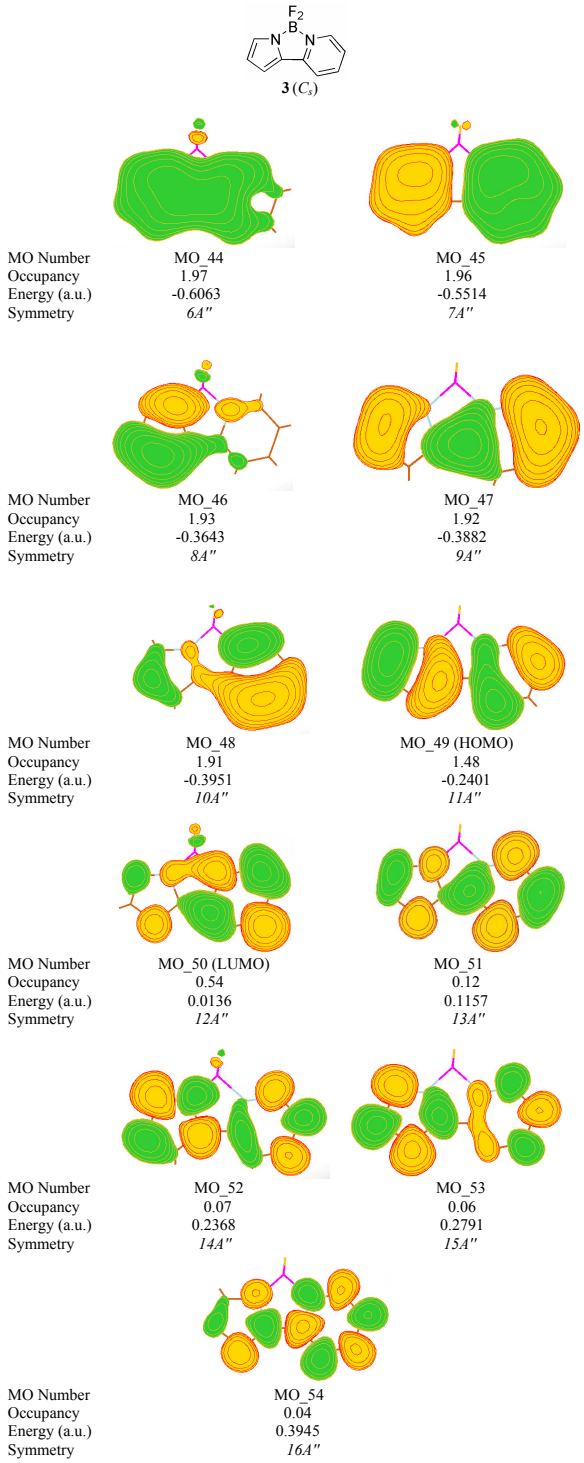

FIGURE A.3: All the selected occupied (MOs 44-49) and unoccupied (MOs 50-54) optimized molecular orbitals (after rotation and with isovalue of 0.02 a.u.) considered for the active space of (**3**) (12 electrons in 11 orbitals) along with their occupancies, energies, and symmetries computed at the CASSCF/cc-pVDZ//PBE0/cc-pVTZ level of theory.

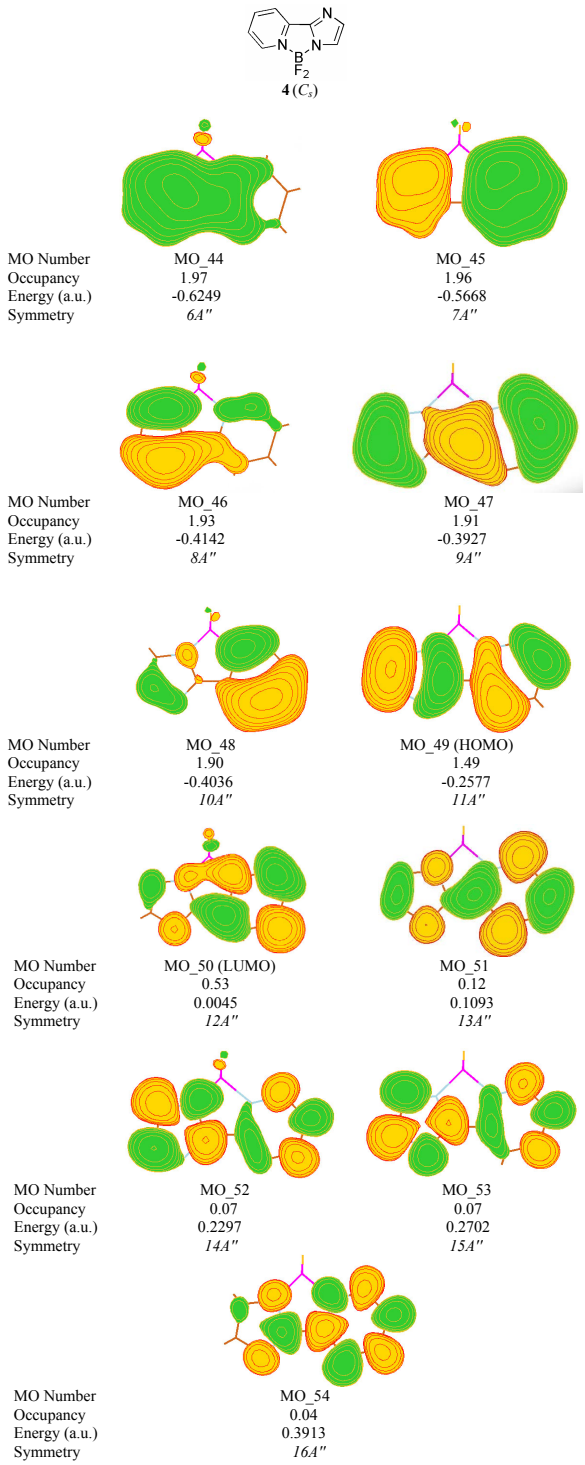

FIGURE A.4: All the selected occupied (MOs 44-49) and unoccupied (MOs 50-54) optimized molecular orbitals (after rotation and with isovalue of 0.02 a.u.) considered for the active space of (**4**) (12 electrons in 11 orbitals) along with their occupancies, energies, and symmetries computed at the CASSCF/cc-pVDZ//PBE0/cc-pVTZ level of theory.

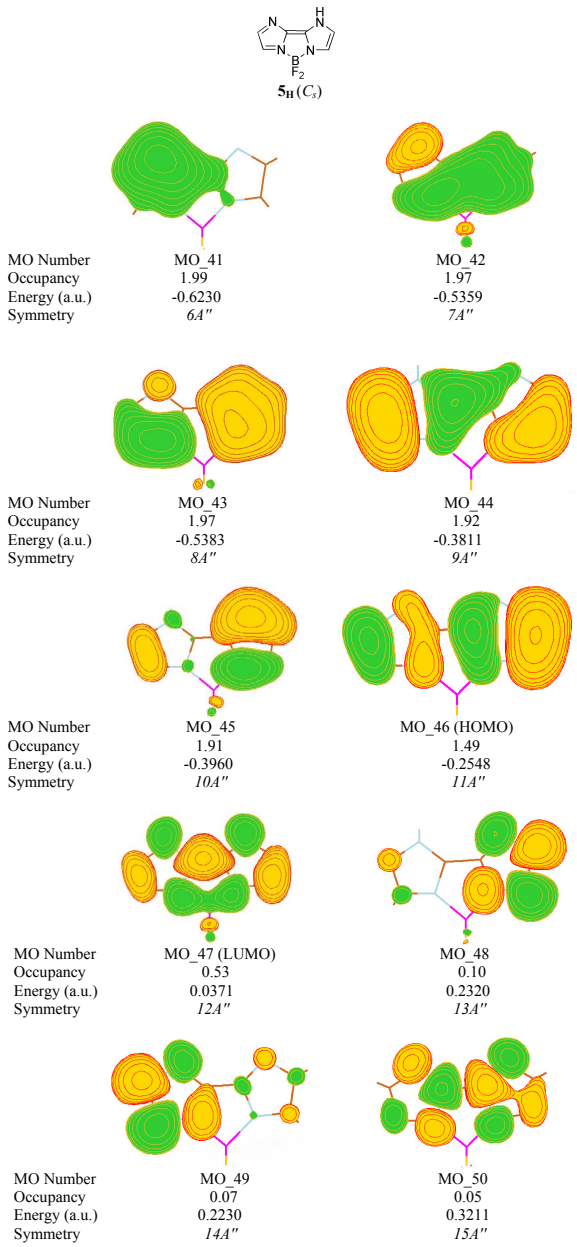

FIGURE A.5: All the selected occupied (MOs 41-46) and unoccupied (MOs 47-50) optimized molecular orbitals (after rotation and with isovalue of 0.02 a.u.) considered for the active space of ($\mathbf{5}_H$) (12 electrons in 10 orbitals) along with their occupancies, energies, and symmetries computed at the CASSCF/cc-pVDZ//PBE0/cc-pVTZ level of theory.

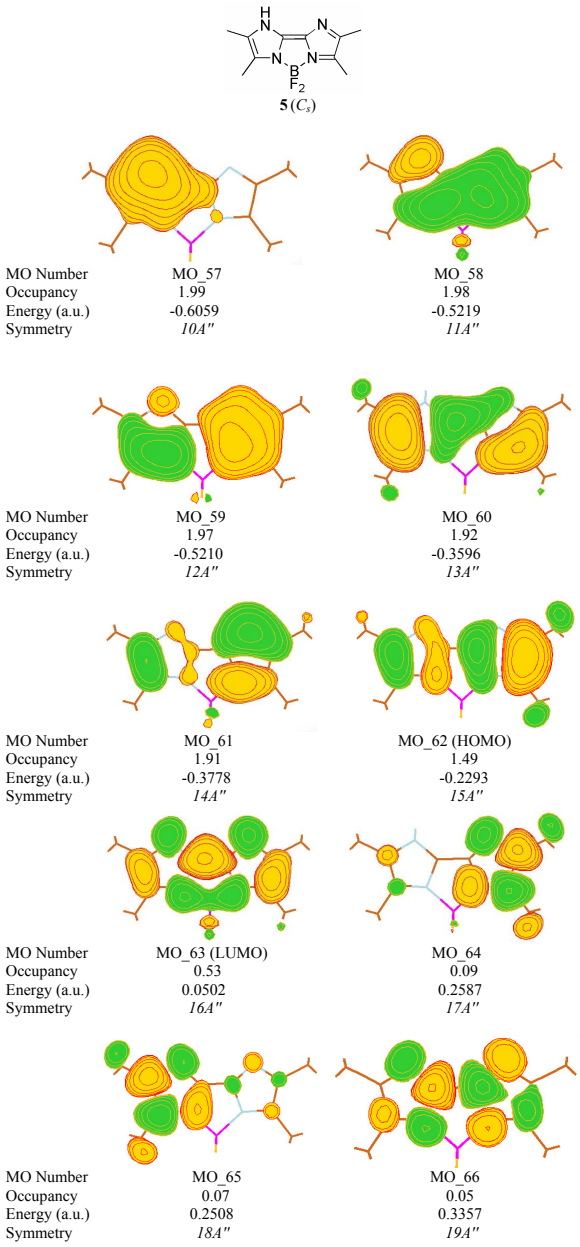

FIGURE A.6: All the selected occupied (MOs 57-62) and unoccupied (MOs 63-66) optimized molecular orbitals (after rotation and with isovalue of 0.02 a.u.) considered for the active space of (**5**) (12 electrons in 10 orbitals) along with their occupancies, energies, and symmetries computed at the CASSCF/cc-pVDZ//PBE0/cc-pVTZ level of theory.

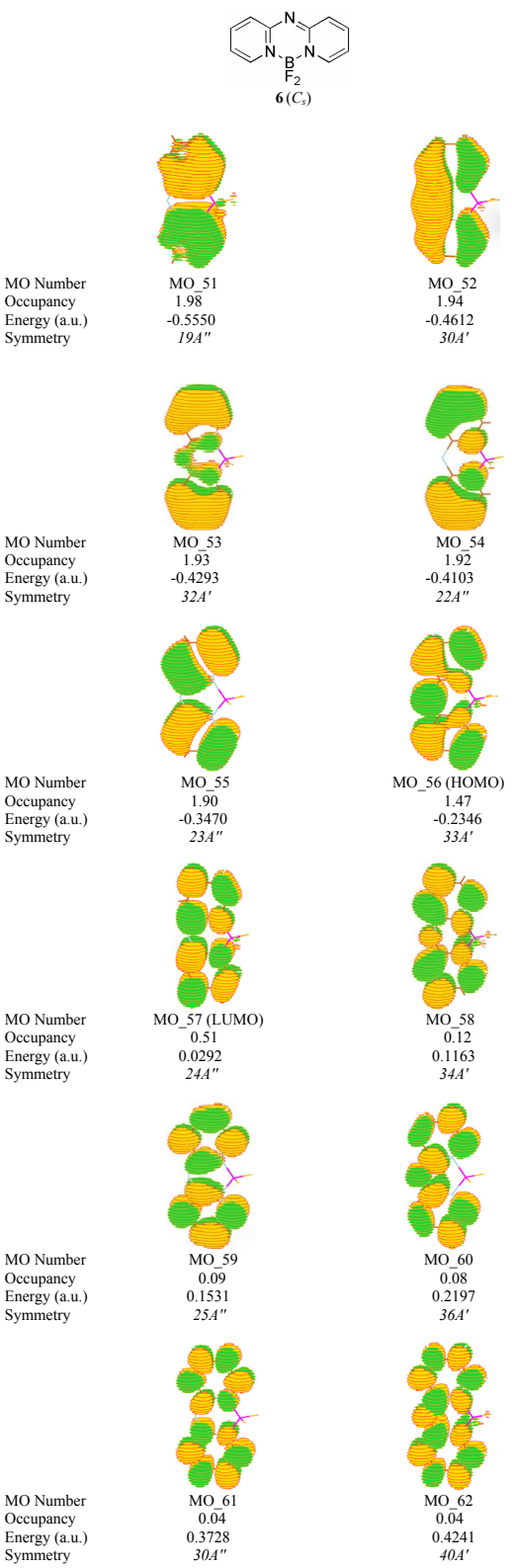

FIGURE A.7: All the selected occupied (MOs 51-56) and unoccupied (MOs 57-62) optimized molecular orbitals (after rotation and with isovalue of 0.02 a.u.) considered for the active space of (**6**) (12 electrons in 12 orbitals) along with their occupancies, energies, and symmetries computed at the CASSCF/cc-pVDZ//PBE0/cc-pVTZ level of theory.

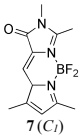

7 (C_1)

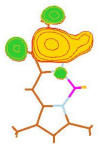


MO Number	MO_64	MO_65
Occupancy	2.00	1.97
Energy (a.u.)	-0.4988	-0.5684
Symmetry	*64A*	*65A*

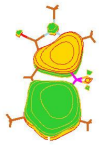
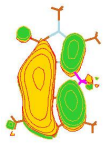

MO Number	MO_66	MO_67
Occupancy	1.97	1.93
Energy (a.u.)	-0.5406	+0.3801
Symmetry	*66A*	*67A*

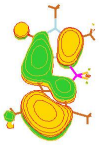
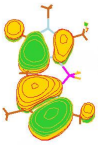

MO Number	MO_68	MO_69 (HOMO)
Occupancy	1.91	1.47
Energy (a.u.)	-0.3459	-0.2263
Symmetry	*68A*	*69A*

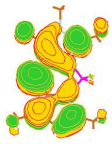
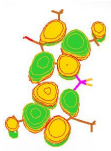

MO Number	MO_70 (LUMO)	MO_71
Occupancy	0.56	0.07
Energy (a.u.)	+0.0003	+0.2328
Symmetry	*70A*	*71A*

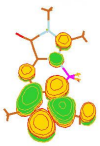
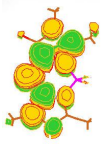

MO Number	MO_72	MO_73
Occupancy	0.07	0.05
Energy (a.u.)	-0.2503	+0.3154
Symmetry	*72A*	*73A*

FIGURE A.8: All the selected occupied (MOs 64-69) and unoccupied (MOs 70-73) optimized molecular orbitals (after rotation and with isovalue of 0.02 a.u.) considered for the active space of (**7**) (12 electrons in 10 orbitals) along with their occupancies, energies, and symmetries computed at the CASSCF/cc-pVDZ//PBE0/cc-pVTZ level of theory.

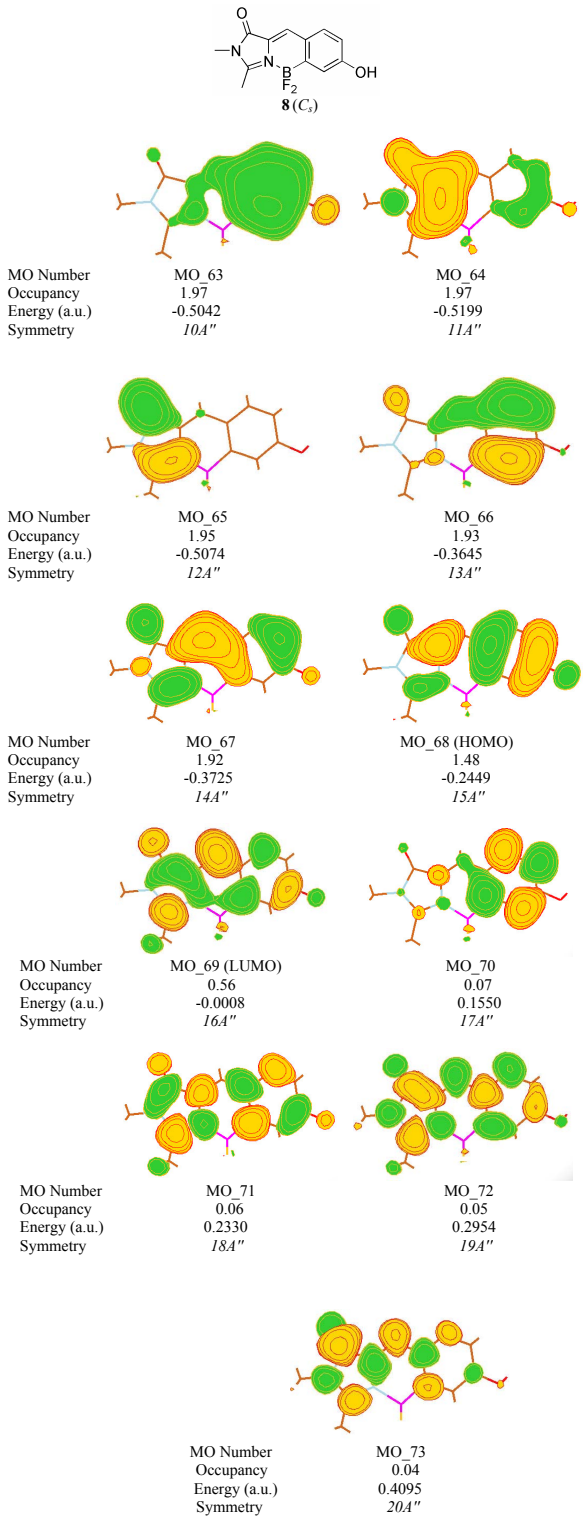

FIGURE A.9: All the selected occupied (MOs 63-68) and unoccupied (MOs 69-73) optimized molecular orbitals (after rotation and with isovalue of 0.02 a.u.) considered for the active space of (**8**) (12 electrons in 11 orbitals) along with their occupancies, energies, and symmetries computed at the CASSCF/cc-pVDZ//PBE0/cc-pVTZ level of theory.

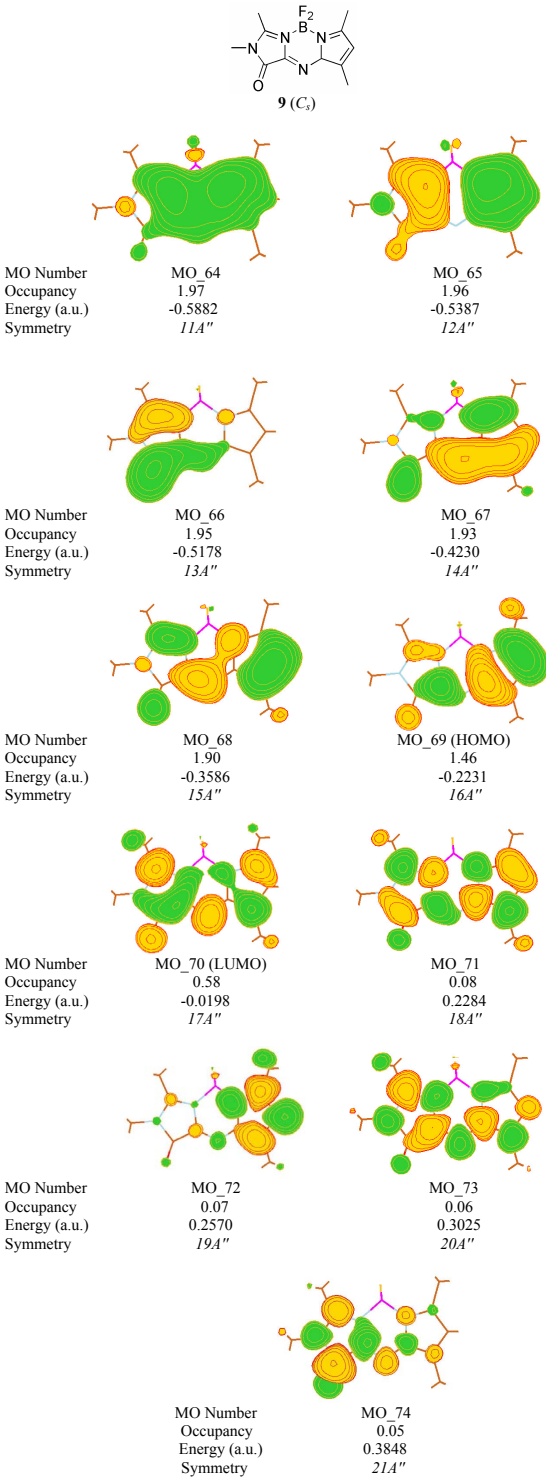

FIGURE A.10: All the selected occupied (MOs 64-69) and unoccupied (MOs 70-74) optimized molecular orbitals (after rotation and with isovalue of 0.02 a.u.) considered for the active space of (**9**) (12 electrons in 11 orbitals) along with their occupancies, energies, and symmetries computed at the CASSCF/cc-pVDZ//PBE0/cc-pVTZ level of theory.

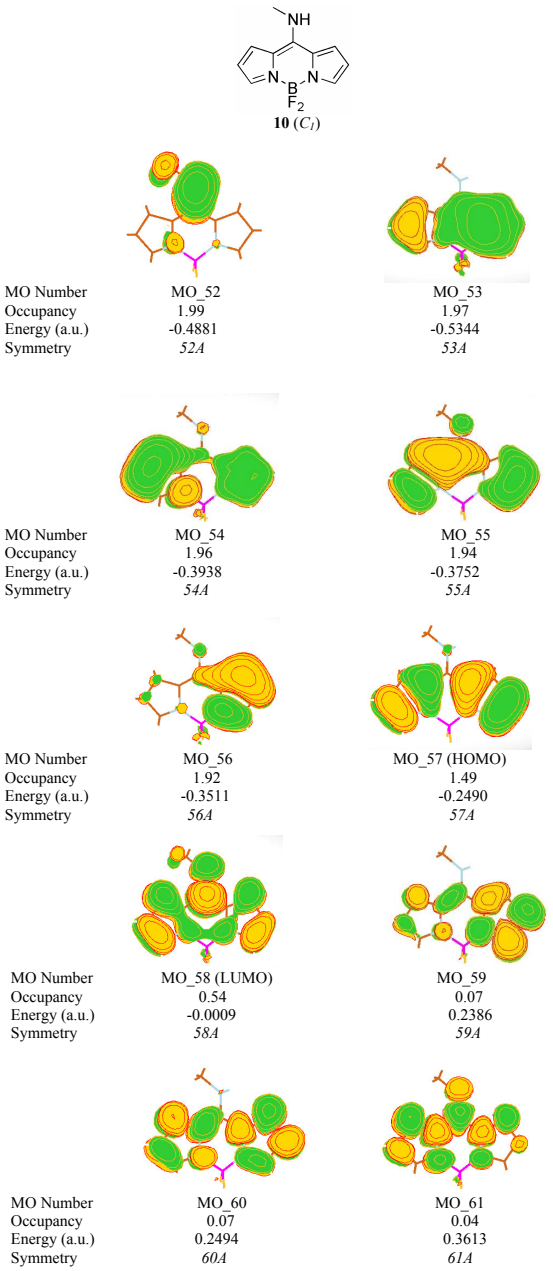

FIGURE A.11: All the selected occupied (MOs 52-57) and unoccupied (MOs 58-61) optimized molecular orbitals (after rotation and with isovalue of 0.02 a.u.) considered for the active space of (**10**) (12 electrons in 10 orbitals) along with their occupancies, energies, and symmetries computed at the CASSCF/cc-pVDZ//PBE0/cc-pVTZ level of theory.

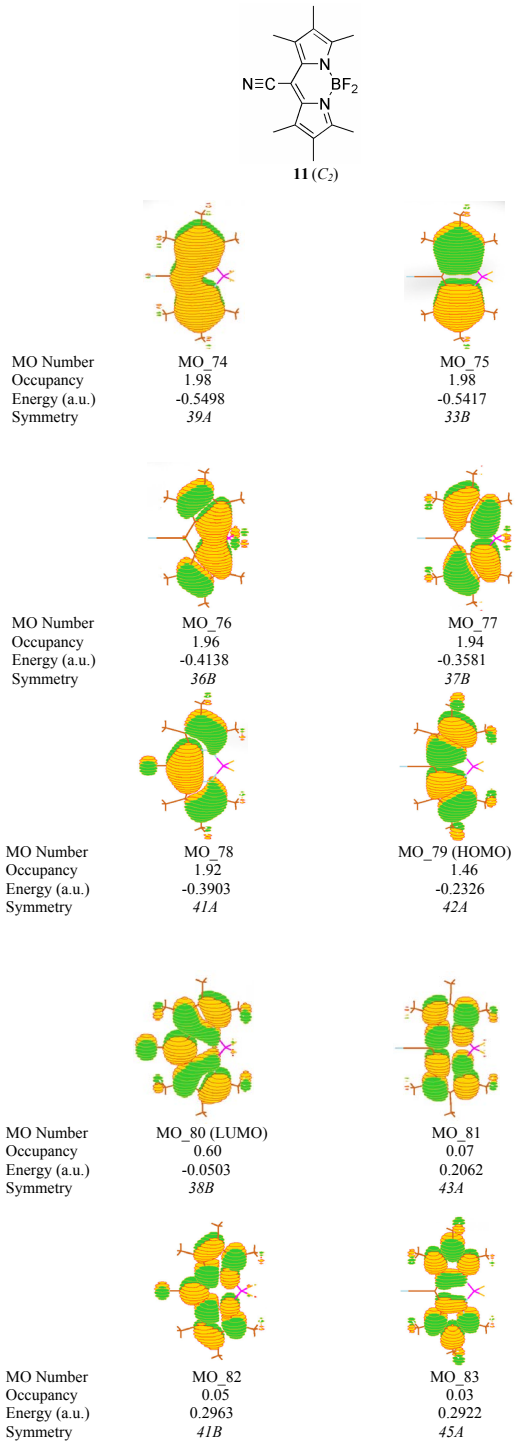

FIGURE A.12: All the selected occupied (MOs 74-79) and unoccupied (MOs 80-83) optimized molecular orbitals (after rotation and with isovalue of 0.02 a.u.) considered for the active space of (**11**) (12 electrons in 10 orbitals) along with their occupancies, energies, and symmetries computed at the CASSCF/cc-pVDZ//PBE0/cc-pVTZ level of theory.

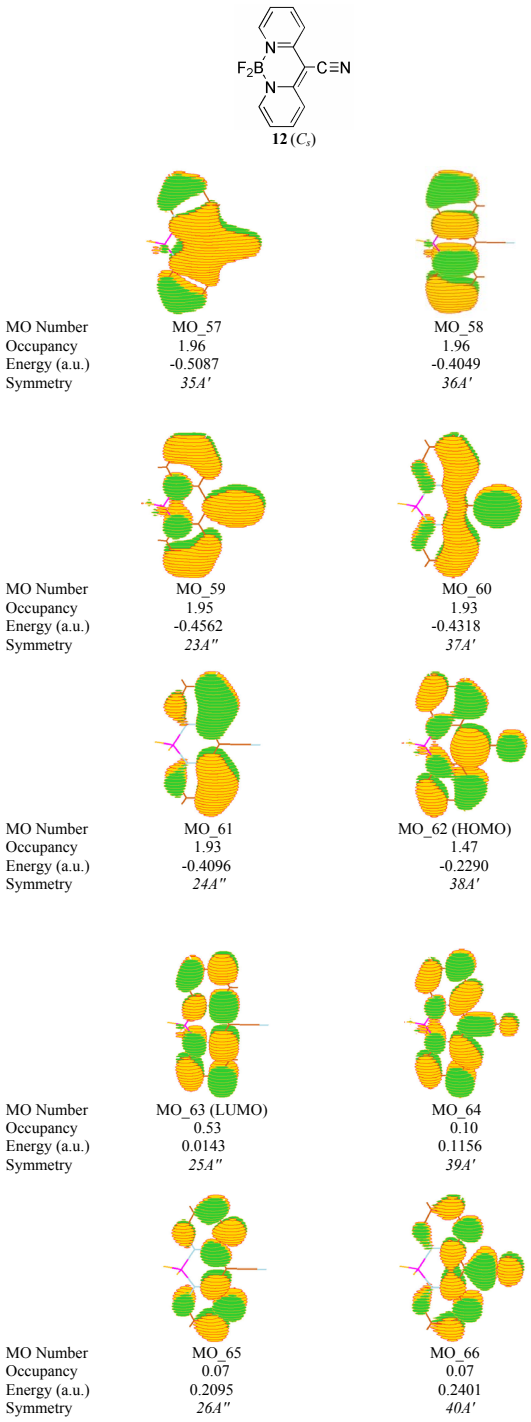

FIGURE A.13: All the selected occupied (MOs 57-62) and unoccupied (MOs 63-66) optimized molecular orbitals (after rotation and with isovalue of 0.02 a.u.) considered for the active space of (**12**) (12 electrons in 10 orbitals) along with their occupancies, energies, and symmetries computed at the CASSCF/cc-pVDZ//PBE0/cc-pVTZ level of theory.

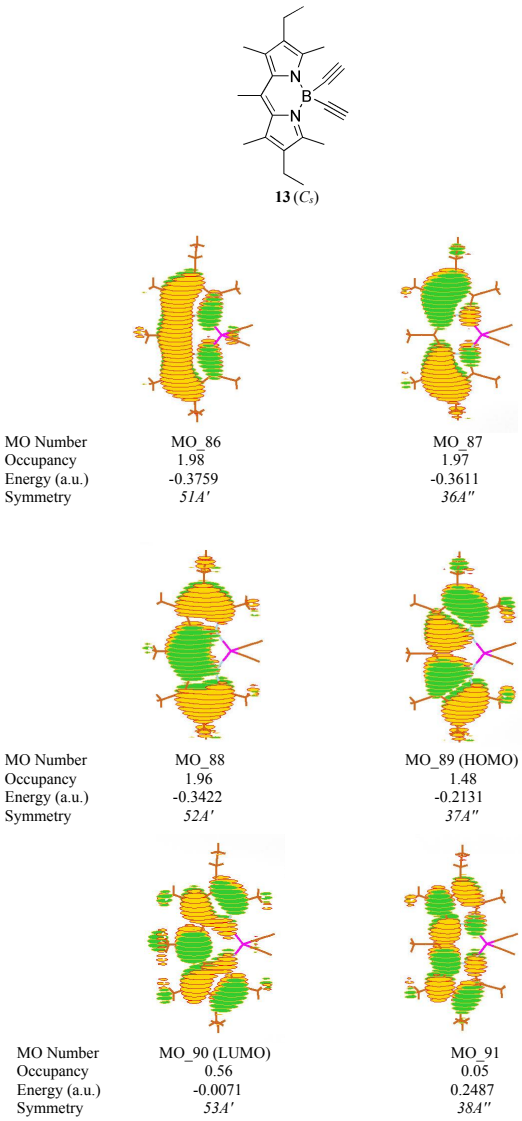

FIGURE A.14: All the selected occupied (MOs 86-89) and unoccupied (MOs 90-91) optimized molecular orbitals (after rotation and with isovalue of 0.02 a.u.) considered for the active space of (**13**) (8 electrons in 6 orbitals) along with their occupancies, energies, and symmetries computed at the CASSCF/cc-pVDZ//PBE0/cc-pVTZ level of theory.

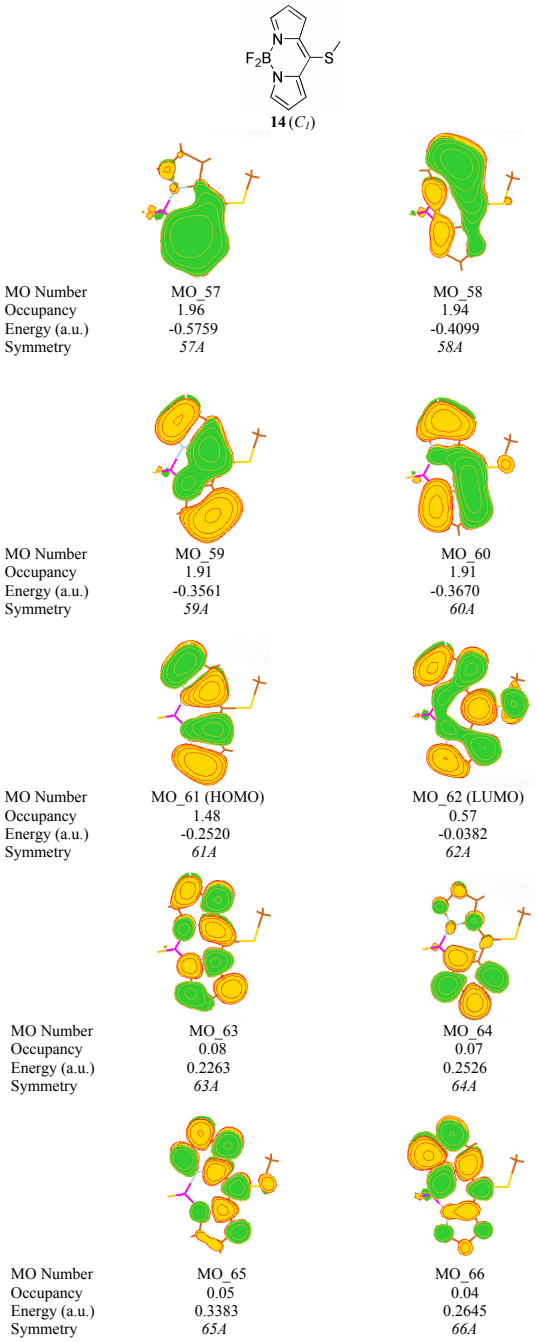

FIGURE A.15: All the selected occupied (MOs 57-61) and unoccupied (MOs 62-66) optimized molecular orbitals (after rotation and with isovalue of 0.02 a.u.) considered for the active space of (**14**) (10 electrons in 10 orbitals) along with their occupancies, energies, and symmetries computed at the CASSCF/cc-pVDZ//PBE0/cc-pVTZ level of theory.

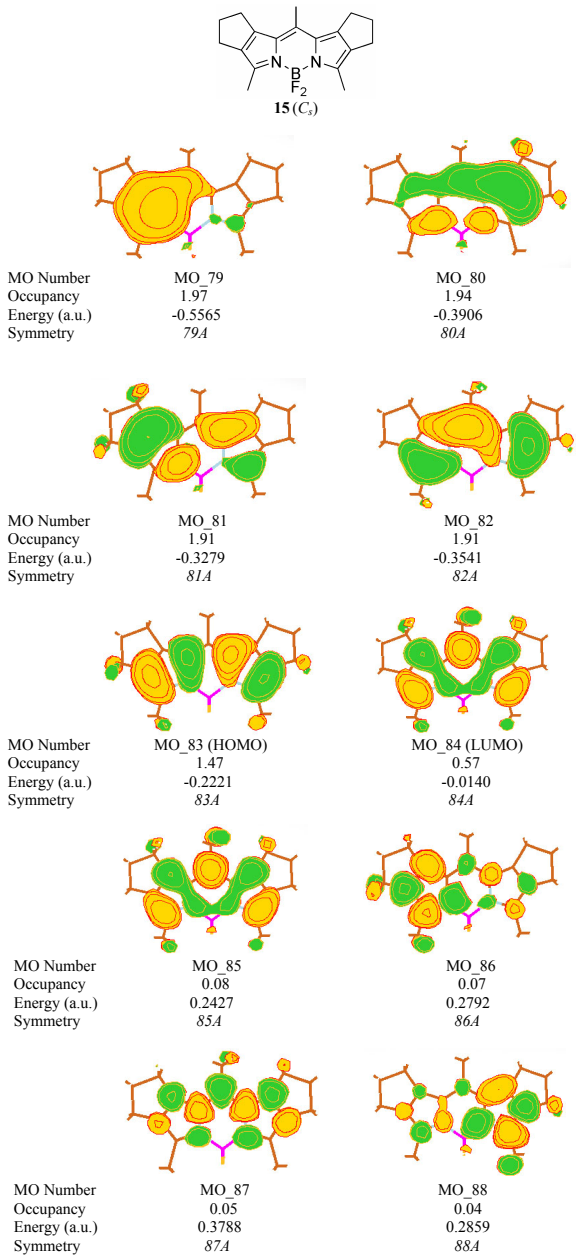

FIGURE A.16: All the selected occupied (MOs 79-83) and unoccupied (MOs 84-88) optimized molecular orbitals (after rotation and with isovalue of 0.02 a.u.) considered for the active space of (**15**) (10 electrons in 10 orbitals) along with their occupancies, energies, and symmetries computed at the CASSCF/cc-pVDZ//PBE0/cc-pVTZ level of theory.

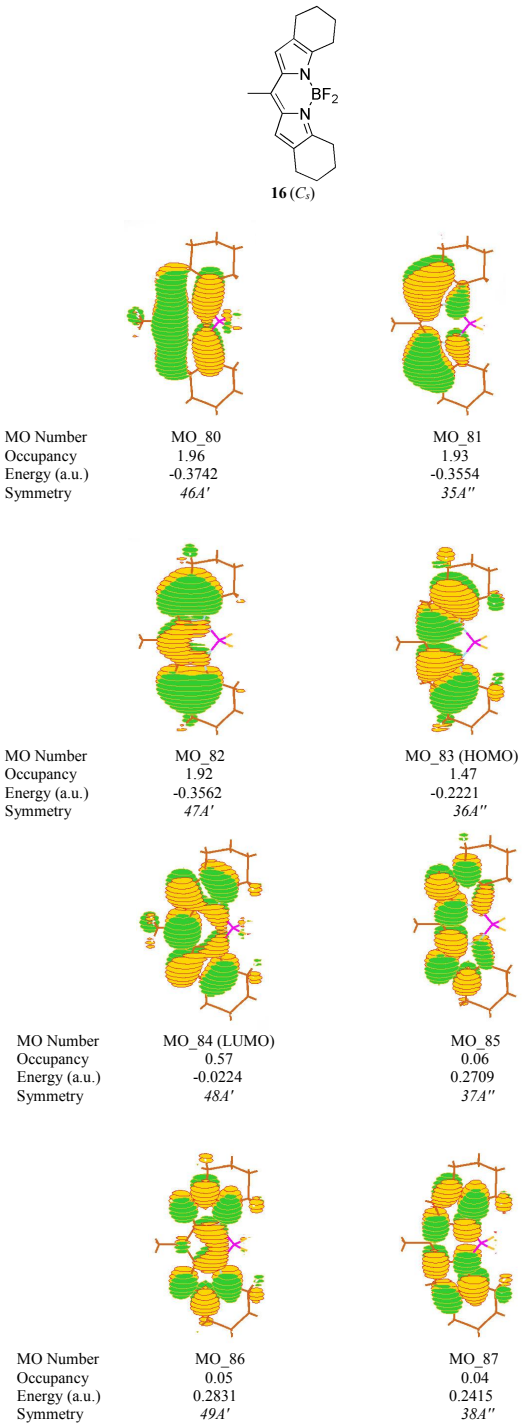

FIGURE A.17: All the selected occupied (MOs 80-83) and unoccupied (MOs 84-87) optimized molecular orbitals (after rotation and with isovalue of 0.02 a.u.) considered for the active space of (**16**) (8 electrons in 8 orbitals) along with their occupancies, energies, and symmetries computed at the CASSCF/cc-pVDZ//PBE0/cc-pVTZ level of theory.

Appendix B

Appendix for Chapter 4.

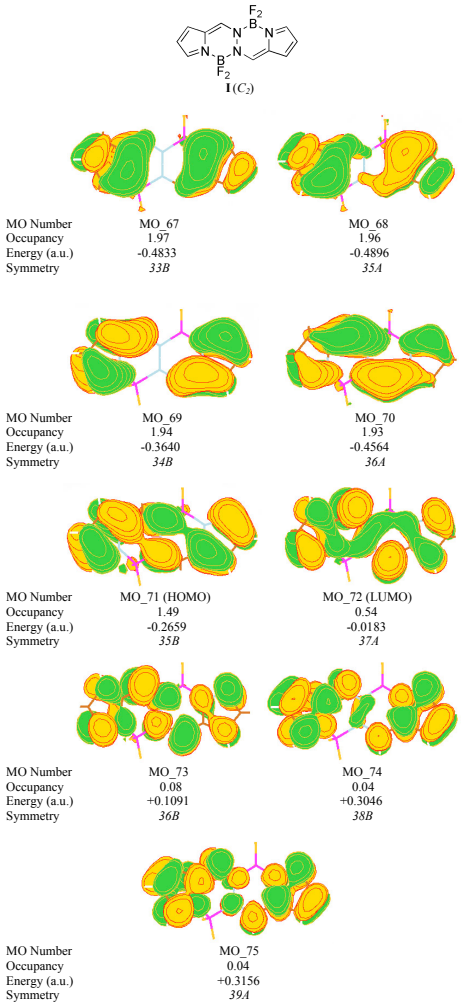

FIGURE B.1: All the selected occupied (MOs 67-71) and unoccupied (MOs 72-75) optimized molecular orbitals (after rotation and with isovalue of 0.02 a.u.) considered for the active space of (**I**) (10 electrons in 9 orbitals) along with their occupancies, energies, and symmetries computed at the CASSCF/cc-pVDZ//M06-2X/cc-pVDZ level of theory.

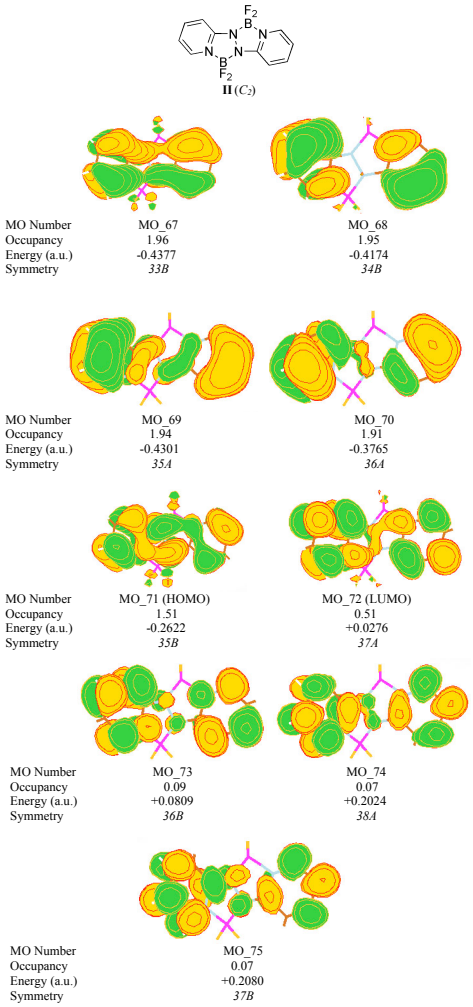

FIGURE B.2: All the selected occupied (MOs 67-71) and unoccupied (MOs 72-75) optimized molecular orbitals (with isovalue of 0.02 a.u.) considered for the active space of (**II**) (10 electrons in 9 orbitals) along with their occupancies, energies, and symmetries computed at the CASSCF/cc-pVDZ//M06-2X/cc-pVDZ level of theory.

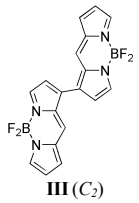

III (C_2)

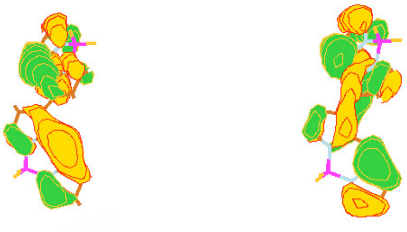

MO Number	MO_93	MO_94
Occupancy	1.99	1.96
Energy (a.u.)	-0.4127	-0.3217
Symmetry	*46B*	*48A*

MO Number	MO_95	MO_96
Occupancy	1.95	1.95
Energy (a.u.)	-0.3897	-0.3921
Symmetry	*47B*	*49A*

MO Number	MO_97 (HOMO)	MO_98 (LUMO)
Occupancy	1.51	0.52
Energy (a.u.)	-0.2480	-0.0520
Symmetry	*48B*	*50A*

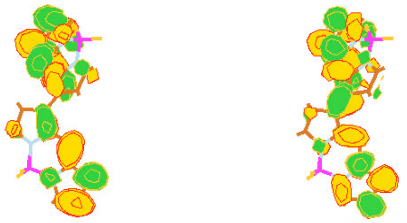

MO Number	MO_99	MO_100
Occupancy	0.08	0.04
Energy (a.u.)	+0.1029	+0.2533
Symmetry	*49B*	*51A*

FIGURE B.3: All the selected occupied (MOs 93-97) and unoccupied (MOs 98-100) optimized molecular orbitals (with isovalue of 0.02 a.u.) considered for the active space of (**III**) (10 electrons in 8 orbitals) along with their occupancies, energies, and symmetries computed at the CASSCF/cc-pVDZ//M06-2X/cc-pVDZ level of theory.

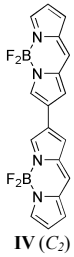

IV (C_2)

MO Number	MO_93	MO_94
Occupancy	1.98	1.95
Energy (a.u.)	-0.3977	-0.4245
Symmetry	*47A*	*47B*

MO Number	MO_95	MO_96
Occupancy	1.93	1.92
Energy (a.u.)	-0.3833	-0.2926
Symmetry	*48A*	*48B*

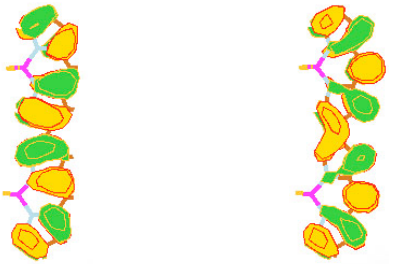

MO Number	MO_97 (HOMO)	MO_98 (LUMO)
Occupancy	1.53	0.51
Energy (a.u.)	-0.2295	-0.0365
Symmetry	*49A*	*49B*

MO Number	MO_99	MO_100
Occupancy	0.14	0.03
Energy (a.u.)	+0.0281	+0.2633
Symmetry	*50A*	*50B*

FIGURE B.4: All the selected occupied (MOs 93-97) and unoccupied (MOs 98-100) optimized molecular orbitals (with isovalue of 0.02 a.u.) considered for the active space of (**IV**) (10 electrons in 8 orbitals) along with their occupancies, energies, and symmetries computed at the CASSCF/cc-pVDZ//M06-2X/cc-pVDZ level of theory.

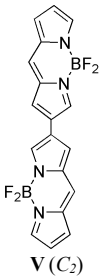

V (C_2)

MO Number	MO_93	MO_94
Occupancy	1.98	1.95
Energy (a.u.)	-0.3977	-0.4245
Symmetry	*46B*	*48A*

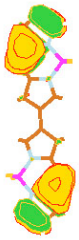

MO Number	MO_95	MO_96
Occupancy	1.93	1.92
Energy (a.u.)	-0.3833	-0.2926
Symmetry	*47B*	*49A*

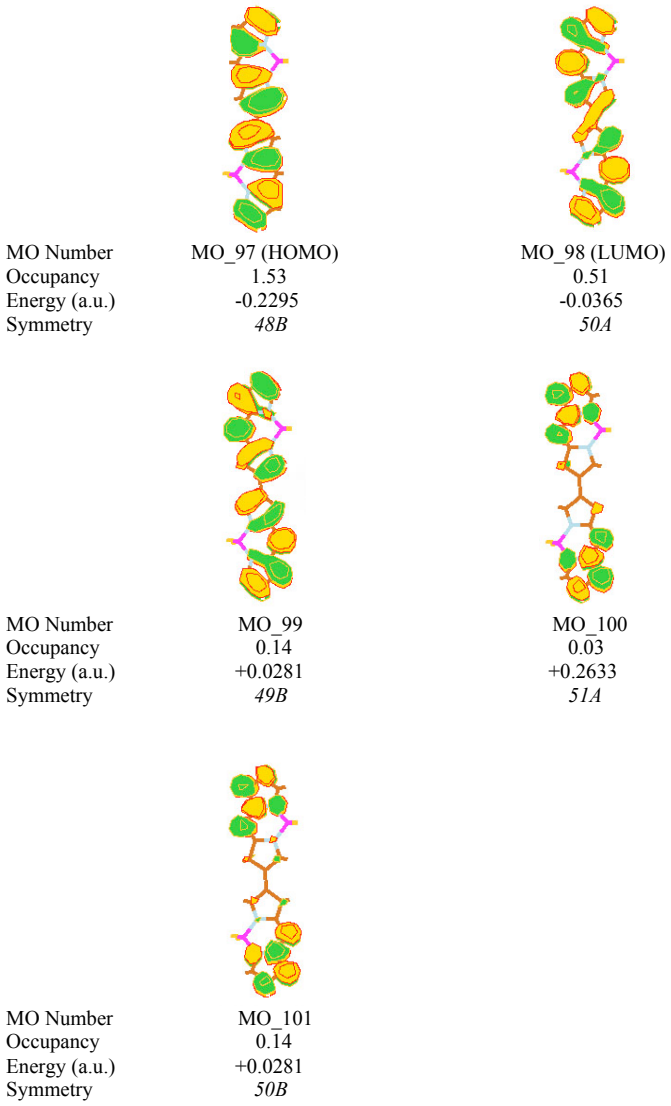

FIGURE B.5: All the selected occupied (MOs 93-97) and unoccupied (MOs 98-101) optimized molecular orbitals (with isovalue of 0.02 a.u.) considered for the active space of (**V**) (10 electrons in 9 orbitals) along with their occupancies, energies, and symmetries computed at the CASSCF/cc-pVDZ//M06-2X/cc-pVDZ level of theory.

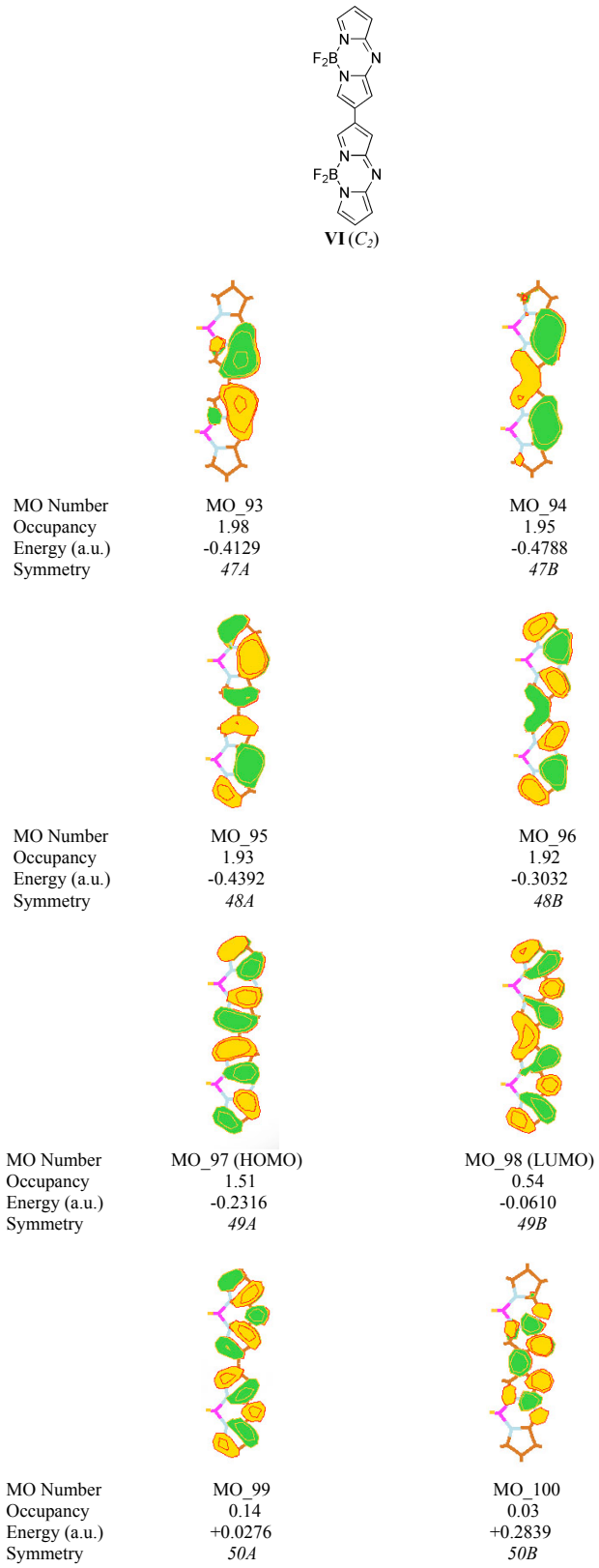

FIGURE B.6: All the selected occupied (MOs 93-97) and unoccupied (MOs 98-100) optimized molecular orbitals (with isovalue of 0.02 a.u.) considered for the active space of (**VI**) (10 electrons in 8 orbitals) along with their occupancies, energies, and symmetries computed at the CASSCF/cc-pVDZ//M06-2X/cc-pVDZ level of theory.

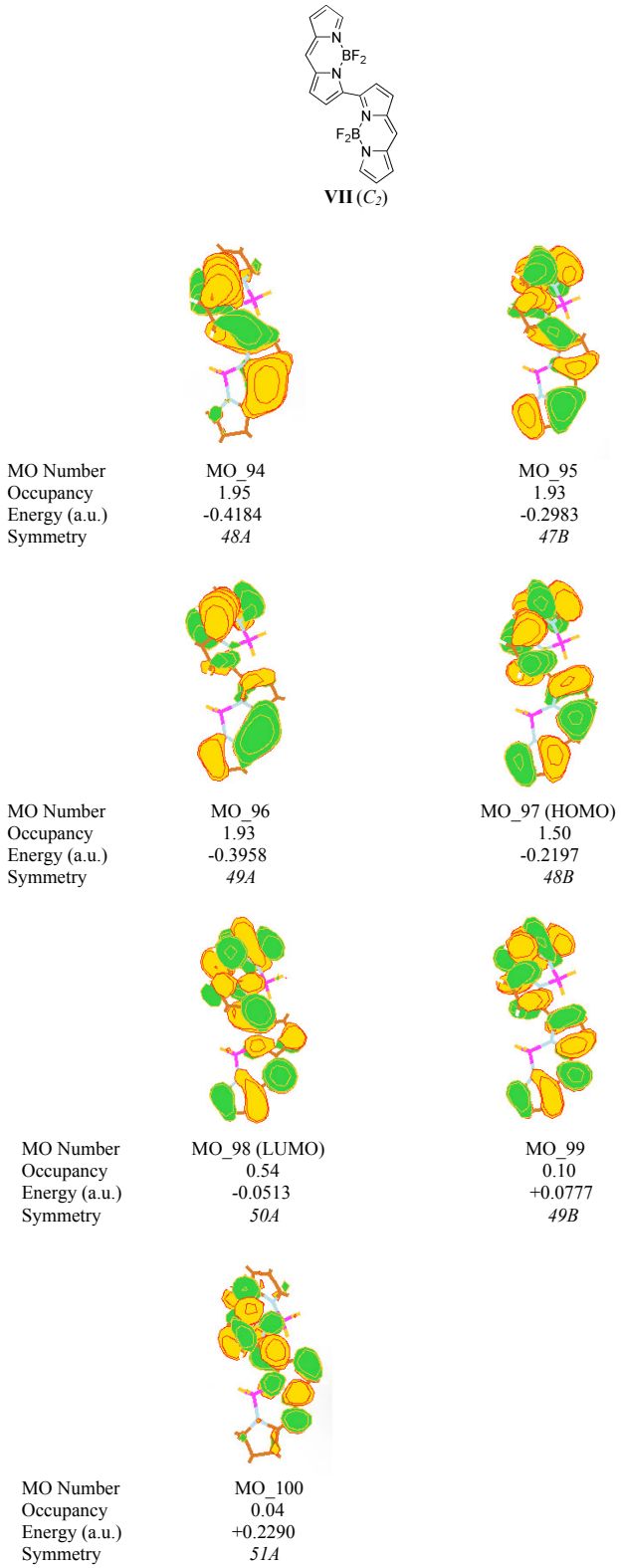

FIGURE B.7: All the selected occupied (MOs 94-97) and unoccupied (MOs 98-100) optimized molecular orbitals (with isovalue of 0.02 a.u.) considered for the active space of (**VII**) (8 electrons in 7 orbitals) along with their occupancies, energies, and symmetries computed at the CASSCF/cc-pVDZ//M06-2X/cc-pVDZ level of theory.

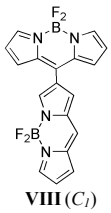

VIII (C_1)


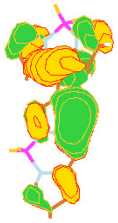

MO Number	MO_94	MO_95
Occupancy	1.96	1.94
Energy (a.u.)	-0.4184	-0.2983
Symmetry	*94A*	*95A*


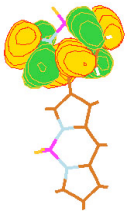

MO Number	MO_96	MO_97 (HOMO)
Occupancy	1.89	1.48
Energy (a.u.)	-0.3958	-0.2197
Symmetry	*96A*	*97A*


MO Number	MO_98 (LUMO)	MO_99
Occupancy	0.58	0.10
Energy (a.u.)	-0.0513	+0.0777
Symmetry	*98A*	*99A*

MO Number	MO_100
Occupancy	0.04
Energy (a.u.)	+0.2290
Symmetry	*100A*

FIGURE B.8: All the selected occupied (MOs 94-97) and unoccupied (MOs 98-100) optimized molecular orbitals (with isovalue of 0.02 a.u.) considered for the active space of (**VIII**) (8 electrons in 7 orbitals) along with their occupancies, energies, and symmetries computed at the CASSCF/cc-pVDZ//M06-2X/cc-pVDZ level of theory.

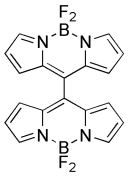

IX (C_2)

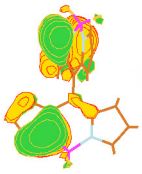
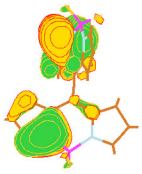

MO Number	MO_94	MO_95
Occupancy	1.96	1.96
Energy (a.u.)	-0.4811	-0.4789
Symmetry	*48A*	*47B*

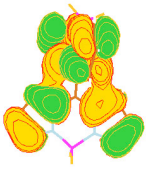
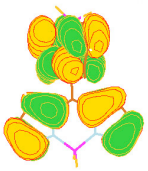

MO Number	MO_96	MO_97 (HOMO)
Occupancy	1.51	1.38
Energy (a.u.)	-0.2486	-0.2247
Symmetry	*49A*	*48B*

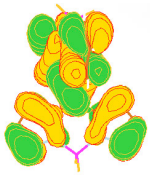
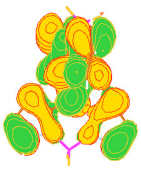

MO Number	MO_98 (LUMO)	MO_99
Occupancy	0.65	0.47
Energy (a.u.)	-0.0654	-0.0337
Symmetry	*50A*	*49B*

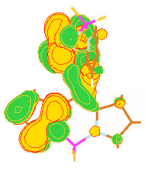
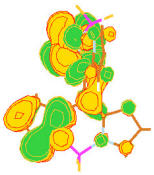

MO Number	MO_100	MO_101
Occupancy	0.04	0.04
Energy (a.u.)	+0.3333	+0.3337
Symmetry	*51A*	*51A*

FIGURE B.9: All the selected occupied (MOs 94-97) and unoccupied (MOs 98-101) optimized molecular orbitals (with isovalue of 0.02 a.u.) considered for the active space of (**IX**) (8 electrons in 8 orbitals) along with their occupancies, energies, and symmetries computed at the CASSCF/cc-pVDZ//M06-2X/cc-pVDZ level of theory.

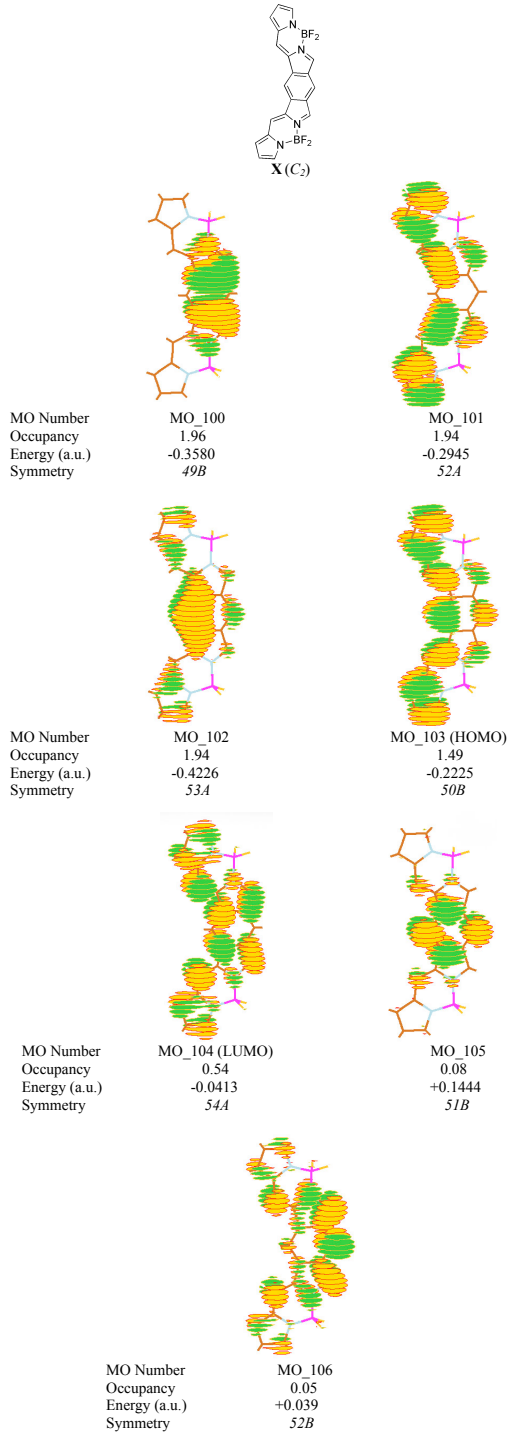

FIGURE B.10: All the selected occupied (MOs 100-103) and unoccupied (MOs 104-106) optimized molecular orbitals (with isovalue of 0.02 a.u.) considered for the active space of (**X**) (8 electrons in 7 orbitals) along with their occupancies, energies, and symmetries computed at the CASSCF/cc-pVDZ//M06-2X/cc-pVDZ level of theory.

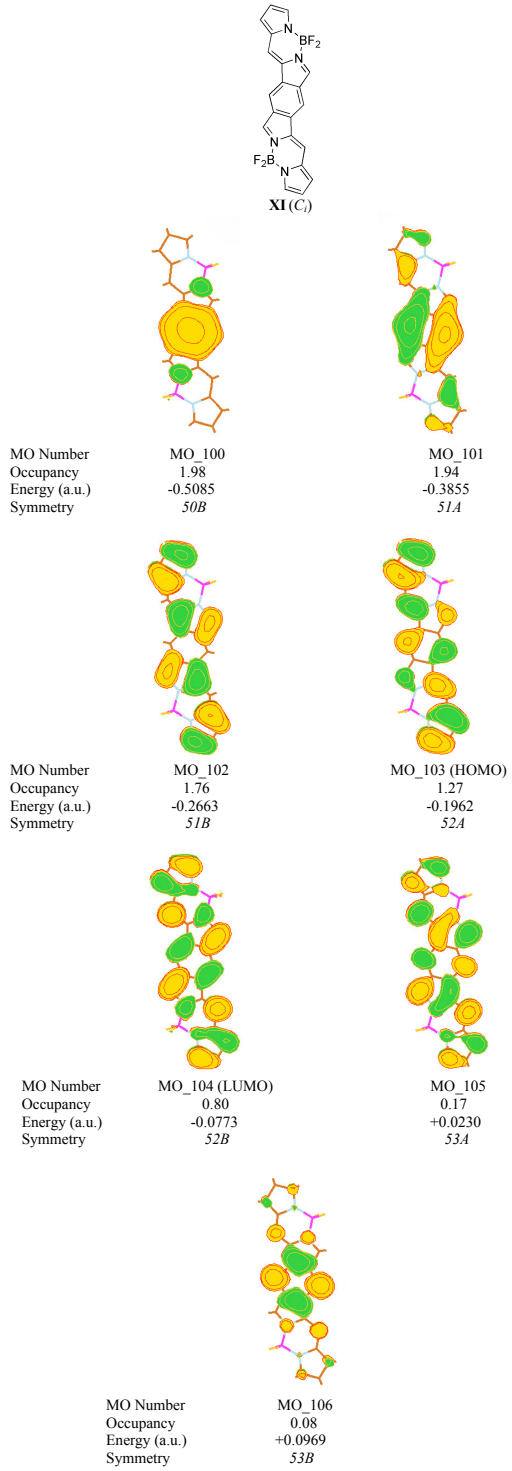

FIGURE B.11: All the selected occupied (MOs 100-103) and unoccupied (MOs 104-106) optimized molecular orbitals (with isovalue of 0.02 a.u.) considered for the active space of (**XI**) (8 electrons in 7 orbitals) along with their occupancies, energies, and symmetries computed at the CASSCF/cc-pVDZ//M06-2X/cc-pVDZ level of theory.

Appendix C

Appendix for Chapter 5.

TABLE C.1: Results of the NBO analyses for $ImMe_2$ and ^{Me}CAAC along with their BH_3 substituted complexes computed at the M06-2X/cc-pVDZ level of theory in the gas-phase (see Figure 5.2 for the atom numberings).

Species	NBO Charge	Bond A-B	Occ	(A) %	Hyb (A)	(B) %	Hyb (B)	WBI
$ImMe_2$	N_2 -0.499	N_2-C_3 (σ)	1.978	68.7	$sp^{1.81}$	31.3	$sp^{3.02}$	1.232
	C_3 +0.143	C_3-N_4 (σ)	1.978	31.3	$sp^{3.02}$	68.7	$sp^{1.81}$	1.233
		C_3-N_4 (π)	1.868	20.2	p	79.8	p	
		N_2 (LP)	1.562	-	p	-	-	-
		C_3 (LP)	1.923	-	$sp^{0.95}$	-	-	-
^{Me}CAAC	N_2 -0.488	N_2-C_3 (σ)	1.985	68.59	$sp^{1.48}$	31.4	$sp^{2.80}$	1.508
	C_3 +0.105	N_2-C_3 (π)	1.948	78.40	p	21.6	p	
	C_4 +0.156	C_3-C_4 (σ)	1.951	44.6	$sp^{2.42}$	55.4	$sp^{3.15}$	0.985
		C_3 (LP)	1.903	-	$sp^{1.22}$	-	-	-
BH_3	B +0.337	B-H (σ)	1.998	44.4	$sp^{2.00}$	55.6	s	0.982
	H -0.112							
$ImMe_2$-BH_3	N_2 -0.441	N_2-C_3 (σ)	1.979	65.5	$sp^{1.81}$	34.5	$sp^{2.96}$	1.236
	C_3 +0.377	C_3-N_4 (σ)	1.981	34.6	$sp^{2.85}$	65.40	$sp^{1.76}$	1.246
	B -0.423	C_3-N_4 (π)	1.879	24.2	p	75.8	p	
	H_1 -0.013	C_3-B (σ)	1.968	69.90	$sp^{1.04}$	30.1	$sp^{3.63}$	0.902
	H_2 -0.015	B-H_1 (σ)	1.946	48.1	$sp^{2.96}$	51.9	s	0.941
	H_3 -0.034	B-H_2 (σ)	1.952	48.1	$sp^{2.91}$	51.9	s	0.947
		B-H_3 (σ)	1.973	47.7	$sp^{2.62}$	52.3	s	0.968
		N_2 (LP)	1.536	-	p	-	-	-
^{Me}CAAC-BH_3	N_2 -0.429	N_2-C_3 (σ)	1.986	65.59	$sp^{1.47}$	34.4	$sp^{2.96}$	1.474
	C_3 +0.282	N_2-C_3 (π)	1.951	75.2	p	24.8	p	
	C_4 -0.109	C_3-C_4 (σ)	1.956	49.1	$sp^{2.42}$	50.9	$sp^{3.11}$	0.9719
	B -0.415	C_3-B (σ)	1.964	70	$sp^{1.21}$	30	$sp^{3.51}$	0.932
	H_1 -0.012	B-H_1 (σ)	1.952	48.3	$sp^{2.81}$	51.7	s	0.948
	H_2 +0.024	B-H_2 (σ)	1.895	48.6	$sp^{3.29}$	51.4	s	0.896
	H_3 -0.031	B-H_3 (σ)	1.972	47.8	$sp^{2.54}$	52.2	s	0.967
BH_2NHMe	B +0.454	B-H_1 (σ)	1.986	44.7	$sp^{1.82}$	55.3	s	0.972
	H_1 -0.100	B-H_2 (σ)	1.986	45	$sp^{1.83}$	55	s	0.974
	H_2 -0.094	B-N (σ)	1.99	22.1	$sp^{2.41}$	77.90	$sp^{1.20}$	1.203
	N -0.890	B-N (π)	1.972	15.5	p	84.5	p	

TABLE C.2: Results of the NBO analyses for the $ImMe_2$ complexes with BH_2NHMe, SiH_4, and SiH_3Ph along with the ^{Me}CAAC complex with BH_2NHMe computed at the M06-2X/cc-pVDZ level of theory in the gas-phase (see Figure 5.2 for the atom numberings).

Species	NBO Charge	Bond (A-B)	Occ	(A) %	Hyb (A)	(B) %	Hyb (B)	WBI
$ImMe_2$-BH_2NHMe	N_2 -0.439	N_2-C_3 (σ)	1.98	65.5	$sp^{1.80}$	34.5	$sp^{2.89}$	1.243
	C_3 +0.352	C_3-N_4 (σ)	1.981	34.79	$sp^{2.83}$	65.2	$sp^{1.77}$	1.262
	N_4 -0.435	C_3-N_4 (π)	1.879	24.8	p	75.2	p	
	B +0.082	C_3-B (σ)	1.963	71.09	$sp^{1.06}$	28.9	$sp^{3.58}$	0.84
	N_9 -0.968	B-N_9 (σ)	1.979	24.6	$sp^{3.07}$	75.40	$sp^{1.53}$	0.786
	H_1 -0.033	B-H_1 (σ)	1.943	47.1	$sp^{2.82}$	52.9	s	0.933
	H_2 -0.074	B-H_2 (σ)	1.958	45.8	$sp^{2.64}$	54.2	s	0.931
		N_2 (LP)	1.536	-	p	-	-	-
		N_9 (LP)	1.895	-	$sp^{6.94}$	-	-	-
^{Me}CAAC-BH_2NHMe	N_2 -0.425	N_2-C_3 (σ)	1.986	65.7	$sp^{1.48}$	34.29	$sp^{2.88}$	1.492
	C_3 +0.271	N_2-C_3 (π)	1.951	75.09	p	24.9	p	
	C_4 -0.110	C_3-C_4 (σ)	1.957	49.3	$sp^{2.34}$	50.7	$sp^{3.11}$	0.977
	B +0.079	C_3-B (σ)	1.96	71.3	$sp^{1.25}$	28.7	$sp^{3.46}$	0.855
	N_9 -0.967	B-N_9 (σ)	1.98	25	$sp^{2.97}$	75	$sp^{1.51}$	0.797
	H_1 -0.053	B-H_1 (σ)	1.947	46.5	$sp^{2.60}$	53.5	s	0.925
	H_2 -0.015	B-H_2 (σ)	1.913	47.1	$sp^{3.05}$	52.9	s	0.906
		N_9 (LP)	1.903	-	$sp^{7.15}$	-	-	-
SiH_4	Si +0.597	Si-H (σ)	1.991	42.5	$sp^{2.97}$	57.5	s	0.961
	H -0.149							
SiH_3Ph	Si +0.903	Si-H_1 (σ)	1.985	42	$sp^{3.01}$	58	s	0.95
	H_1 -0.157	Si-H_2 (σ)	1.983	42.1	$sp^{2.99}$	57.9	s	0.942
	H_2 -0.156	Si-H_3 (σ)	1.986	41.9	$sp^{3.02}$	58.1	s	0.952
	H_3 -0.158	Si-C_{Ph} (σ)	1.965	28	$sp^{2.85}$	72	$sp^{2.32}$	0.795
$ImMe_2$-SiH_4	N_2 -0.488	N_2-C_3 (σ)	1.979	68.3	$sp^{1.79}$	31.7	$sp^{2.92}$	1.242
	C_3 +0.131	N_2-C_3 (π)	1.87	79.09	p	20.9	p	
	N_4 -0.489	C_3-N_4 (σ)	1.979	31.7	$sp^{2.93}$	68.3	$sp^{1.80}$	1.241
	Si +0.610	Si-H_1 (σ)	1.99	42.1	$sp^{2.83}$	57.9	s	0.956
	H_1 -0.157	Si-H_2 (σ)	1.99	42.6	$sp^{2.86}$	57.4	s	0.96
	H_2 -0.148	Si-H_3 (σ)	1.99	42.3	$sp^{2.87}$	57.7	s	0.957
	H_3 -0.153	Si-H_4 (σ)	1.989	41.3	$sp^{3.34}$	58.7	s	0.926
	H_4 -0.183	C_3 (LP)	1.893	-	$sp^{0.99}$	-	-	-
		N_4 (LP)	1.556	-	p	-	-	-
$ImMe_2$-SiH_3Ph	N_2 -0.487	N_2-C_3 (σ)	1.979	68.2	$sp^{1.79}$	31.8	$sp^{2.91}$	1.243
	C_3 +0.136	C_3-N_4 (σ)	1.979	31.7	$sp^{2.92}$	68.3	$sp^{1.79}$	1.242
	N_4 -0.487	Si-H_1 (σ)	1.981	41.7	$sp^{2.85}$	58.3	s	0.940
	Si +0.910	Si-H_2 (σ)	1.983	41.9	$sp^{2.88}$	58.1	s	0.95
	H_1 -0.164	Si-H_3 (σ)	1.981	42.1	$sp^{2.88}$	57.9	s	0.943
	H_2 -0.157	Si-C_{Ph} (σ)	1.96	26.4	$sp^{3.27}$	73.59	$sp^{2.19}$	0.733
	H_3 -0.155	N_2 (LP)	1.556	-	p	-	-	-
		C_3 (LP)	1.883	-	sp	-	-	-
		N_4 (LP)	1.556	-	p	-	-	-

TABLE C.3: Results of the NBO analyses for the diphenyl and triphenyl silane complexes with $ImMe_2$ along with the diphenylsilane complex with ^{Me}CAAC computed at the M06-2X/cc-pVDZ level of theory in the gas-phase (see Figure 5.2 for the atom numberings).

Species	NBO Charge	Bond A-B	Occ	(A) %	Hyb (A)	(B) %	Hyb (B)	WBI
SiH_2Ph_2	Si +1.207	Si-H (σ)	1.977	41.6	$sp^{3.02}$	58.4	s	0.935
	H -0.163	Si-C_{Ph} (σ)	1.96	27.3	$sp^{2.91}$	72.7	$sp^{2.77}$	0.777
$SiHPh_3$	Si +1.515	Si-H (σ)	1.97	41.4	$sp^{3.02}$	58.6	s	0.925
	H -0.164	Si-C_{Ph} (σ)	1.954	26.6	$sp^{2.95}$	73.40	$sp^{2.20}$	0.755
$ImMe_2$-SiH_2Ph_2	N_2 -0.427	N_2-C_3 (σ)	1.98	65.40	$sp^{1.82}$	34.6	$sp^{2.66}$	1.272
	C_3 +0.178	N_2-C_3 (π)	1.88	74	p	26	p	
	N_4 -0.427	C_3-N_4 (σ)	1.98	34.6	$sp^{2.66}$	65.40	$sp^{1.82}$	1.272
	Si +1.259	C_3-Si (σ)	1.927	79.7	$sp^{1.19}$	20.3	$sp^{4.47}$	0.606
	H_1 -0.321	Si-H_1 (σ)	1.778	28.1	$sp^{2.94}$	71.90	s	0.691
	H_2 -0.321	Si-H_2 (σ)	1.778	28.1	$sp^{2.94}$	71.90	s	0.691
		Si-C_{Ph} (σ)	1.907	24.2	$sp^{2.42}$	75.8	$sp^{2.16}$	0.683
		Si-C_{Ph} (σ)	1.907	24.2	$sp^{2.42}$	75.8	$sp^{2.16}$	0.683
		N_4 (LP)	1.512	-	p	-	-	-
^{Me}CAAC-SiH_2Ph_2	N_2 -0.412	N_2-C_3 (σ)	1.986	65.7	$sp^{1.47}$	34.29	$sp^{2.72}$	1.552
	C_3 +0.107	N_2-C_3 (π)	1.958	73.7	p	26.3	p	
	C_4 -0.116	C_3-C_4 (σ)	1.959	49.4	$sp^{2.03}$	50.6	$sp^{3.19}$	0.988
	Si +1.270	C_3-Si (σ)	1.911	81.09	$sp^{1.49}$	18.89	$sp^{3.99}$	0.583
	H_1 -0.311	Si-H_1 (σ)	1.782	28.7	$sp^{2.73}$	71.3	s	0.707
	H_2 -0.305	Si-H_2 (σ)	1.752	27.8	$sp^{2.99}$	72.2	s	0.665
		Si-C_{Ph} (σ)	1.92	24.9	$sp^{2.55}$	75.09	$sp^{2.12}$	0.701

$ImMe_2$

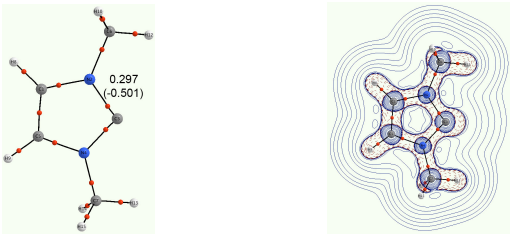

$ImMe_2\_BH_3$

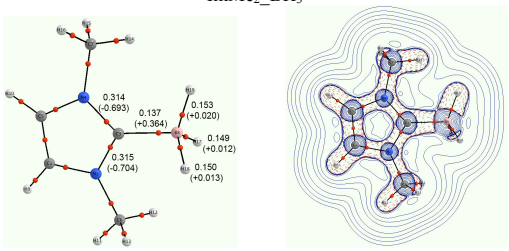

$ImMe_2\_BH_2NHMe$

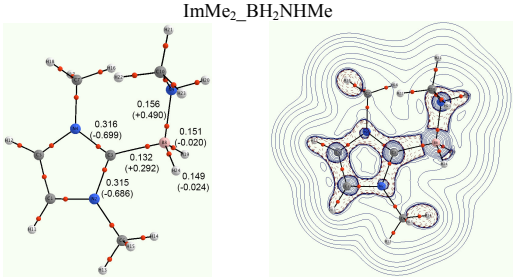

$ImMe_2\_SiH_4$

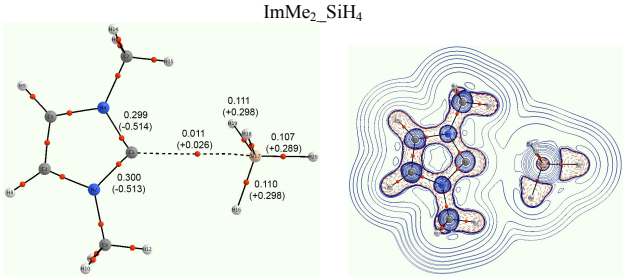

$ImMe_2\_SiH_3Ph$

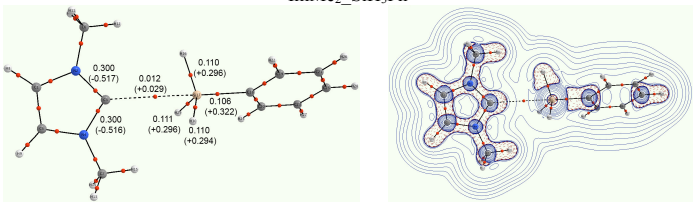

$ImMe_2\ SiH_2Ph_2$

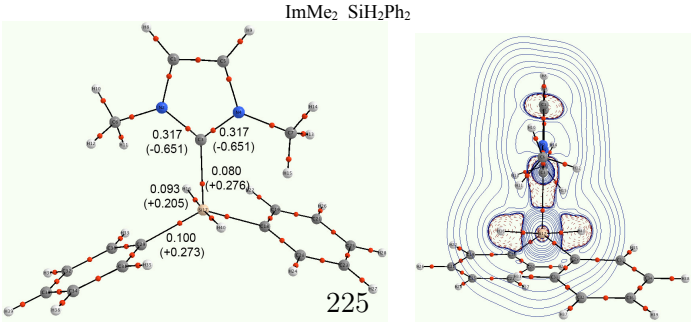

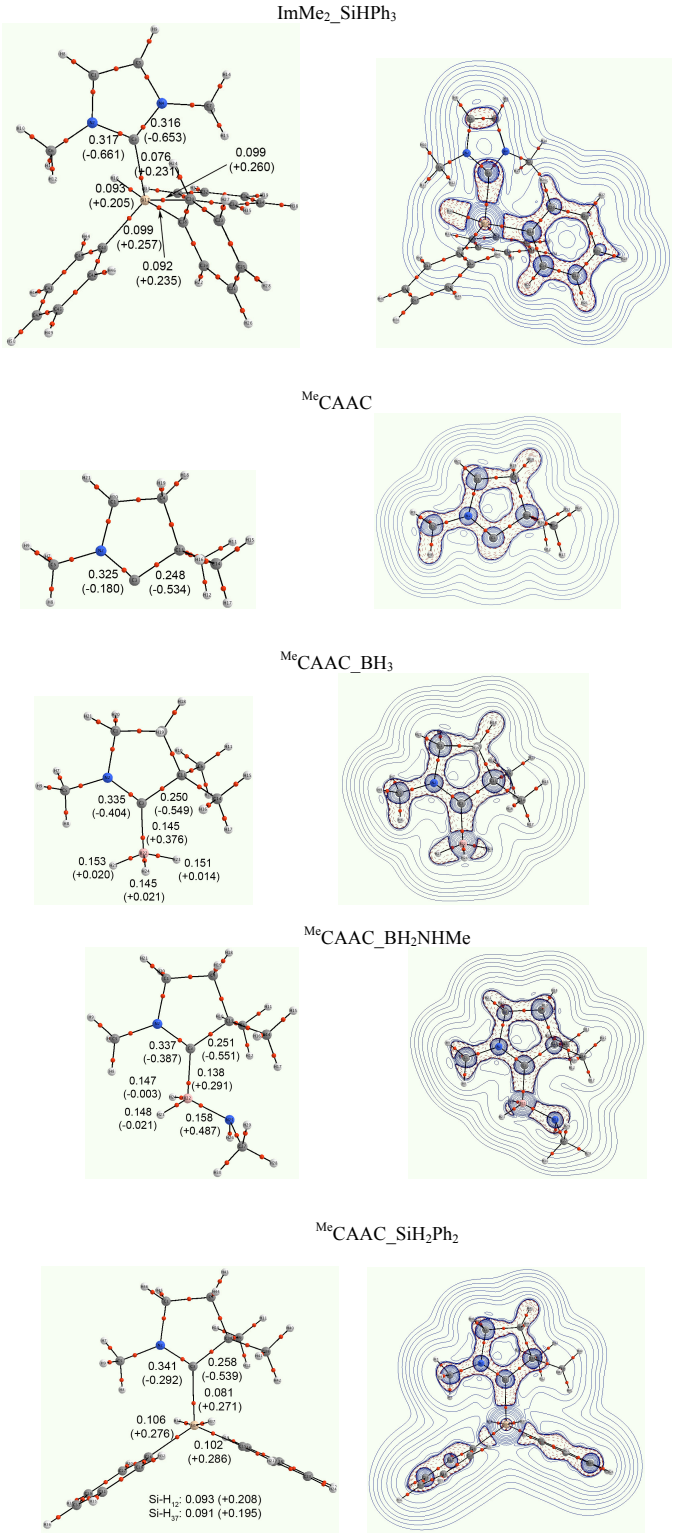

FIGURE C.1: AIM parameters including ρ(r) and $\nabla^2\rho$ (in parenthesis) using the gas-phase M06-2X/cc-pVDZ density for the structures: $ImMe_2$, $ImMe_2$-BH_3, $ImMe_2$-BH_2NHMe, $ImMe_2$-$SiHPh_3$, $ImMe_2$-SiH_4, $ImMe_2$-SiH_3Ph, $ImMe_2$-SiH_2Ph_2, $ImMe_2$-$SiHPh_3$, ^{Me}CAAC, ^{Me}CAAC-BH_3, ^{Me}CAAC-BH_2NHMe, and ^{Me}CAAC-SiH_2Ph_2. Contour plots of $\nabla^2\rho$ (r) in the N-C-B or N-C-Si planes are also displayed for each structure (dark gray corresponds to the local charge concentrations while light gray shows charge depletions).

Appendix D

Appendix for Chapter 6.

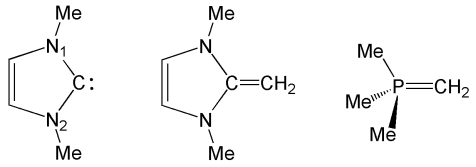

TABLE D.1: NBO analysis for the ligands at the M05-2X/cc-pVTZ level of theory.

Species	NBO Charge	Bond A-B	Occ	(A) %	Hyb (A)	(B) %	Hyb (B)	WBI
$ImMe_2$								
C_{2v}	C 0.070	C-N_1 (σ)	1.979	33.6	$sp^{2.70}$	66.4	$sp^{1.82}$	1.258
	N_1 -0.393	C-N_1 (π)	1.865	19.5	$p^{1.00}$	80.5	$p^{1.00}$	
	N_2 -0.393	C (LP)	1.921	-	$sp^{1.11}$	-	-	-
		N_2 (LP)	1.571	-	$p^{1.00}$	-	-	-
$ImMe_2CH_2$								
C_{2v}	C 0.366	C-N (σ)	1.979	38.6	$sp^{2.51}$	61.4	$sp^{2.00}$	1.091
	$C(H_2)$ -0.722	C-$C(H_2)$ (σ)	1.982	53.1	$sp^{1.32}$	46.9	$sp^{1.71}$	1.613
	N -0.384	C-$C(H_2)$ (π)	1.988	37.3	$p^{1.00}$	62.7	$p^{1.00}$	
		N (LP)	1.662	-	$p^{1.00}$	-	-	-
Me_3PCH_2								
C_s	P 1.567	P-$C(H_2)$ (σ)	1.987	43.7	$sp^{1.97}$	56.3	$sp^{2.02}$	1.328
	$C(H_2)$ -1.268	$C(H_2)$ (LP)	1.700	-	$sp^{19.69}$	-	-	-

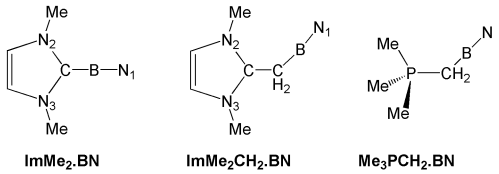

TABLE D.2: NBO analysis for the BN systems at the M05-2X/cc-pVTZ level of theory. With the exception of the cyclic C=C bonds in the $ImMe_2$ and $ImMe_2CH_2$ containing complexes, all other double bonds have been omitted for simplicity from the above and following figures.

Species	NBO Charge	Bond A-B	Occ	(A) %	Hyb (A)	(B) %	Hyb (B)	WBI
BN (singlet)								
$C_{\infty v}$	B 0.861	B-N (σ)	1.985	15.2	$sp^{6.70}$	84.8	$sp^{0.01}$	3.012
	N -0.861	B-N (π_1)	2.000	28.8	$p^{1.00}$	71.2	$p^{1.00}$	
		B-N (π_2)	2.000	28.8	$p^{1.00}$	71.2	$p^{1.00}$	
		B-N(π_3)	1.975	33.0	$sp^{0.18}$	67.0	$sp^{99.99}$	
BN (triplet)								
$C_{\infty v}$	B 0.677	B-N(α)(σ)	1.000	23.9	$sp^{2.18}$	76.1	$sp^{1.34}$	0.546
	N -0.677	B-N(α) (π_1)	1.000	25.6	$p^{1.00}$	74.4	$p^{1.00}$	
		B-N (α) (π_2)	1.000	21.1	$p^{1.00}$	78.9	$p^{1.00}$	
		B (α) (LP)	0.997	-	$sp^{0.42}$	-	-	-
		N (α) (LP)	0.996	-	$sp^{0.73}$	-	-	-
		B-N (β)(σ)	1.000	23.6	$p^{1.00}$	76.4	$p^{1.00}$	0.449
		B-N (β)(π)	1.000	32.9	$sp^{0.17}$	67.1	$sp^{3.63}$	
		N (β) (LP)	0.950	-	$sp^{0.27}$	-		-
$ImMe_2$· BN								
C_{2v}	B 0.230	B-N_1 (σ)	1.994	30.0	$sp^{1.05}$	70.0	$sp^{0.69}$	2.622
	N_1 -0.753	B-N_1 (π_1)	1.963	37.6	$p^{1.00}$	62.4	$p^{1.00}$	
	C 0.203	B-N_1 (π_2)	1.892	39.1	$p^{1.00}$	60.9	$p^{1.00}$	
	N_2 -0.297	B-C (σ)	1.969	32.2	$sp^{0.95}$	67.8	$sp^{1.39}$	0.944
	N_3 -0.297	C-N_2 (σ)	1.981	38.2	$sp^{2.42}$	61.8	$sp^{1.90}$	1.266
		C-N_2 (π)	1.875	26.1	$p^{1.00}$	73.9	$p^{1.00}$	
		C-N_3 (σ)	1.981	38.2	$sp^{2.42}$	61.8	$sp^{1.90}$	1.266
		N_1 (LP)	1.966	-	$sp^{1.43}$	-	-	-
		N_3 (LP)	1.525	-	$p^{1.00}$	-	-	-

Species	NBO Charge	Bond A-B	Occ	(A) %	Hyb (A)	(B) %	Hyb (B)	WBI
$ImMe_2CH_2$· BN								
C_1	B 0.367	B-N_1 (σ)	1.988	34.1	$sp^{0.91}$	65.9	$sp^{2.84}$	2.656
	N_1 -0.887	B-N_1 (π_1)	1.974	33.6	$sp^{99.99}$	66.4	$sp^{99.99}$	
	N_2 -0.320	B-N_1 (π_2)	1.959	33.6	$sp^{99.99}$	66.4	$p^{1.00}$	
	N_3 -0.336	B-C(H_2)(σ)	1.914	29.0	$sp^{1.14}$	71.0	$sp^{3.06}$	0.772
	C(H_2) -0.821	C-N_2(σ)	1.982	39.4	$sp^{2.37}$	60.6	$sp^{1.76}$	1.288
	C 0.523	C-N_2 (π)	1.897	24.4	$p^{1.00}$	75.6	$p^{1.00}$	
		C-N_3 (σ)	1.982	39.1	$sp^{2.38}$	60.9	$sp^{1.74}$	1.271
		N_1 (LP)	1.951	-	$sp^{0.36}$	-	-	-
		N_3 (LP)	1.575	-	$p^{1.00}$	-	-	-
Me_3PCH_2 · BN								
C_s	B 0.382	B-N (σ)	1.995	29.2	$sp^{1.16}$	70.8	$sp^{0.65}$	2.604
	N -0.945	B-N (π_1)	1.973	34.4	$p^{1.00}$	65.6	$p^{1.00}$	
	P 1.630	B-N (π_2)	1.955	35.3	$sp^{99.99}$	64.7	$sp^{99.99}$	
	C(H_2) -1.046	B-C(H_2)(σ)	1.964	30.4	$sp^{0.88}$	69.6	$sp^{2.36}$	0.872
		P-C(H_2)(σ)	1.961	41.6	$sp^{2.66}$	58.4	$sp^{3.34}$	0.955
		N(LP)	1.959	-	$sp^{1.55}$	-	-	-

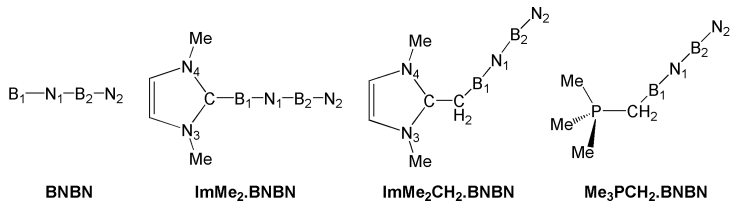

TABLE D.3: NBO analysis for the BNBN systems at the M05-2X/cc-pVTZ level of theory.

Species	NBO Charge	Bond A-B	Occ	(A) %	Hyb (A)	(B) %	Hyb (B)	WBI
BNBN (singlet)								
C_s	B_1 0.703	B_1-N_1 (σ)	1.951	20.2	$sp^{1.19}$	79.8	$sp^{1.28}$	1.230
	B_2 0.879	B_1-N_1 (π)	1.873	11.3	$p^{1.00}$	88.7	$p^{1.00}$	
	N_1 -1.214	B_2-N_1 (σ)	1.986	25.4	$sp^{1.07}$	74.6	$sp^{1.06}$	1.340
	N_2 -0.368	B_2-N_1 (π)	1.774	17.6	$sp^{99.99}$	82.4	$sp^{12.42}$	
		B_2-N_2 (σ)	1.994	31.7	$sp^{0.95}$	68.3	$sp^{1.58}$	1.604
		B_2-N_2 (π)	1.992	20.4	$p^{1.00}$	79.6	$p^{1.00}$	
		N_2 (LP)	1.977	-	$sp^{0.63}$	-	-	-

Species	NBO Charge	Bond A-B	Occ	(A) %	Hyb (A)	(B) %	Hyb (B)	WBI
BNBN (triplet)								
C_s	B_1 0.945	B_1-N_1 (α) (σ)	0.994	19.3	$sp^{1.85}$	80.7	$sp^{0.87}$	0.443
	B_2 0.925	B_1-N_1 (α) (π_1)	0.967	19.5	$p^{1.00}$	80.5	$p^{1.00}$	
	N_1 -1.286	B_1-N_1 (α)(π_2)	0.962	18.7	$p^{1.00}$	81.3	$p^{1.00}$	
	N_2 -0.584	B_2-N_1 (α) (σ)	0.994	24.4	$sp^{1.11}$	75.6	$sp^{1.15}$	0.234
		B_2-N_2(α) (σ)	0.999	30.8	$sp^{0.90}$	69.2	$sp^{1.44}$	0.553
		B_2-N_2 (α)(π_1)	0.993	21.5	$p^{1.00}$	78.5	$p^{1.00}$	
		B_2-N_2 (α) (π_2)	0.989	25.8	$p^{1.00}$	74.2	$p^{1.00}$	
		B_1(α) (LP)	0.989	-	$sp^{0.53}$	-	-	-
		N_2(α) (LP)	0.987	-	$sp^{0.69}$	-	-	-
		B_1-N_1 (β) (σ)	0.994	20.3	$sp^{0.61}$	79.7	$sp^{0.95}$	0.370
		B_1-N_1 (β) (π_1)	0.964	15.4	$sp^{99.99}$	84.6	$sp^{99.99}$	
		B_1-N_1 (β)(π_2)	0.905	12.4	$p^{1.00}$	87.6	$p^{1.00}$	
		B_2-N_1 (β) (σ)	0.992	24.2	$sp^{1.14}$	75.8	$sp^{1.05}$	0.276
		B_2-N_2(β) (σ)	0.998	31.8	$sp^{0.91}$	68.2	$sp^{1.39}$	0.416
		B_2-N_2 (β)(π)	0.982	29.5	$sp^{99.99}$	70.5	$sp^{99.99}$	
		N_2(β) (LP)	0.985	-	$sp^{0.73}$	-	-	-
$ImMe_2$· BNBN								
C_{2v}	B_1 0.608	B_1-N_1 (σ)	1.982	25.7	$sp^{1.12}$	74.3	$sp^{0.88}$	2.062
	B_2 0.519	B_1-N_1 (π_1)	1.941	26.9	$p^{1.00}$	73.1	$p^{1.00}$	
	N_1 -0.851	B_1-N_1 (π_2)	1.903	27.5	$p^{1.00}$	72.5	$p^{1.00}$	
	N_2 -0.829	B_2-N_1 (σ)	1.980	23.8	$sp^{1.17}$	76.2	$sp^{1.14}$	0.915
	N_3 -0.281	B_2-N_2 (σ)	1.990	30.3	$sp^{0.86}$	69.7	$sp^{0.84}$	2.431
	N_4 -0.281	B_2-N_2 (π_1)	1.926	33.7	$p^{1.00}$	66.3	$p^{1.00}$	
	C 0.140	B_2-N_2 (π_2)	1.827	35.8	$p^{1.00}$	64.2	$p^{1.00}$	
		B_1-C (σ)	1.969	33.3	$sp^{0.90}$	66.7	$sp^{1.48}$	0.966
		C-N_3 (σ)	1.982	38.7	$sp^{2.33}$	61.3	$sp^{1.93}$	1.262
		C-N_4 (σ)	1.982	38.7	$sp^{2.33}$	61.3	$sp^{1.93}$	1.262
		C-N_4(π)	1.875	28.1	$p^{1.00}$	71.9	$p^{1.00}$	
		N_2 (LP)	1.965	-	$sp^{1.17}$	-	-	-
		N_3 (LP)	1.513	-	$p^{1.00}$	-	-	-
$ImMe_2CH_2$· BNBN								
C_1	B_1 0.838	B_1-N_1 (σ)	1.986	25.1	$sp^{1.20}$	74.9	$sp^{0.86}$	2.018
	B_2 0.602	B_1-N_1 (π_1)	1.935	21.7	$sp^{99.99}$	78.3	$sp^{1.00}$	
	N_1 -1.006	B_1-N_1 (π_2)	1.936	24.9	$sp^{99.99}$	75.1	$p^{1.00}$	
	N_2 -1.062	B_2-N_1 (σ)	1.977	23.6	$sp^{1.13}$	76.4	$sp^{1.16}$	0.866
	N_3 -0.275	B_2-N_2 (σ)	1.992	29.4	$sp^{0.90}$	70.6	$sp^{0.78}$	2.449
	N_4 -0.311	B_2-N_2 (π_1)	1.957	31.1	$sp^{99.99}$	68.9	$sp^{99.99}$	
	$C(H_2)$ -0.794	B_2-N_2 (π_2)	1.941	31.7	$sp^{99.99}$	68.3	$sp^{99.99}$	
	C 0.479	B_1-$C(H_2)$ (σ)	1.954	33.1	$sp^{0.85}$	66.9	$sp^{2.83}$	0.898
		C-$C(H_2)$ (σ)	1.965	50.7	$sp^{1.65}$	49.3	$sp^{2.86}$	1.026
		C-N_3 (σ)	1.982	38.8	$sp^{2.17}$	61.2	$sp^{1.88}$	1.315
		C-N_3 (π)	1.886	29.7	$sp^{99.99}$	70.3	$p^{1.00}$	
		C-N_4 (σ)	1.981	38.3	$sp^{2.26}$	61.7	$sp^{1.88}$	1.269
		N_2 (LP)	1.951	-	$sp^{1.32}$	-	-	-
		N_4 (LP)	1.536	-	$p^{1.00}$	-	-	-

Species	NBO Charge	Bond A-B	Occ	(A) %	Hyb (A)	(B) %	Hyb (B)	WBI
$Me_3PCH_2 \cdot BNBN$								
C_s	B_1 0.858	B_1-N_1 (σ)	1.986	25.2	$sp^{1.23}$	74.8	$sp^{0.86}$	1.997
	B_2 0.625	B_1-N_1 (π_1)	1.936	25.1	$p^{1.00}$	74.9	$p^{1.00}$	
	N_1 -1.013	B_1-N_1 (π_2)	1.930	20.7	$sp^{99.99}$	79.3	$sp^{99.99}$	
	N_2 -1.072	B_2-N_1 (σ)	1.976	23.7	$sp^{1.12}$	76.3	$sp^{1.16}$	0.875
	$C(H_2)$ -1.075	B_2-N_2 (σ)	1.992	29.5	$sp^{0.90}$	70.5	$sp^{0.80}$	2.406
	P 1.617	B_2-N_2 (π_1)	1.943	29.9	$sp^{99.99}$	70.1	$sp^{65.94}$	
		B_2-N_2 (π_2)	1.932	31.6	$p^{1.00}$	68.4	$p^{1.00}$	
		B_1-$C(H_2)$ (σ)	1.975	32.5	$sp^{0.83}$	67.5	$sp^{2.54}$	0.931
		P-$C(H_2)$ (σ)	1.952	39.1	$sp^{3.15}$	60.9	$sp^{3.21}$	0.906
		N_2 (LP)	1.952	-	$sp^{1.31}$	-	-	-

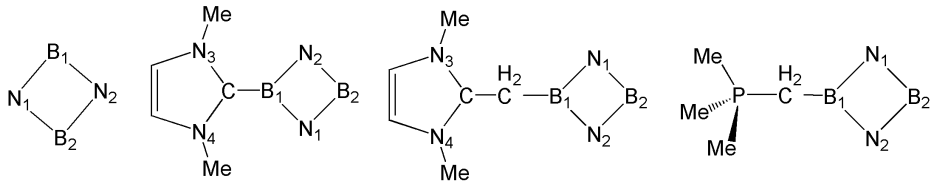

TABLE D.4: NBO analysis for B_2N_2 and its mono-substituted complexes at the M05-2X/cc-pVTZ level of theory.

Species	NBO Charge	Bond A-B	Occ	(A) %	Hyb (A)	(B) %	Hyb (B)	WBI
B_2N_2 (singlet)								
D_{2h}	B_1 1.069	B_1-N_1 (σ)	1.853	29.3	$sp^{1.02}$	70.7	$sp^{2.81}$	1.221
	B_2 1.069	B_1-N_2 (σ)	1.853	29.3	$sp^{1.02}$	70.7	$sp^{2.81}$	1.221
	N_1 -1.069	B_1-N_2 (π)	1.745	12.7	$p^{1.00}$	87.3	$p^{1.00}$	
	N_2 -1.069	B_2-N_1 (σ)	1.853	29.3	$sp^{1.02}$	70.7	$sp^{2.81}$	1.221
		B_2-N_1 (π)	1.745	12.7	$p^{1.00}$	87.3	$p^{1.00}$	
		B_2-N_2 (σ)	1.853	29.3	$sp^{1.02}$	70.7	$sp^{2.81}$	1.221
		N_1 (LP)	1.884	-	$sp^{1.08}$	-	-	-
		N_2 (LP)	1.884	-	$sp^{1.08}$	-	-	-

Species	NBO Charge	Bond A-B	Occ	(A) %	Hyb (A)	(B) %	Hyb (B)	WBI
$ImMe_2CH_2 \cdot B_2N_2$								
C_s	B_1 0.783	B_1-N_1 (σ)	1.784	29.3	$sp^{2.12}$	70.7	$sp^{2.35}$	0.969
	B_2 0.853	B_1-N_2 (σ)	1.784	29.3	$sp^{2.16}$	70.7	$sp^{2.38}$	0.969
	N_1 -1.129	B_1-N_2 (π)	1.739	11.6	$sp^{99.99}$	88.4	$sp^{99.99}$	
	N_2 -1.129	B_2-N_1 (σ)	1.956	31.1	$sp^{1.21}$	68.9	$sp^{2.64}$	1.344
	N_3 -0.301	B_2-N_1 (π)	1.761	12.8	$sp^{99.99}$	87.2	$sp^{99.99}$	
	N_4 -0.301	B_2-N_2 (σ)	1.956	31.1	$sp^{1.20}$	68.9	$sp^{2.62}$	1.344
	$C(H_2)$ -0.738	B_1-$C(H_2)$ (σ)	1.910	32.6	$sp^{1.76}$	67.4	$sp^{2.69}$	0.801
	C 0.509	C-$C(H_2)$ (σ)	1.966	51.9	$sp^{1.55}$	48.1	$sp^{2.96}$	1.059
		C-N_3 (σ)	1.981	38.4	$sp^{2.29}$	61.6	$sp^{1.89}$	1.284
		C-N_3 (π)	1.880	26.6	$p^{1.00}$	73.4	$sp^{99.99}$	
		C-N_4 (σ)	1.981	38.4	$sp^{2.29}$	61.6	$sp^{1.89}$	1.284
		N_1 (LP)	1.928	-	$sp^{1.33}$	-	-	-
		N_2 (LP)	1.928	-	$sp^{1.33}$	-	-	-
		N_4 (LP)	1.517	-	$p^{1.00}$	-	-	-
$Me_3PCH_2 \cdot B_2N_2$								
C_s	B_1 0.769	B_1-N_1 (σ)	1.806	30.1	$sp^{1.87}$	69.9	$sp^{2.07}$	1.096
	B_2 0.860	B_1-N_2 (σ)	1.757	29.1	$sp^{2.48}$	70.9	$sp^{2.90}$	0.846
	N_1 -1.051	B_1-N_2 (π)	1.743	8.3	$p^{1.00}$	91.7	$p^{1.00}$	
	N_2 -1.202	B_2-N_1 (σ)	1.948	31.8	$sp^{1.17}$	68.2	$sp^{2.91}$	1.316
	P 1.637	B_2-N_1 (π)	1.708	13.5	$p^{1.00}$	86.5	$p^{1.00}$	
	$C(H_2)$ -1.037	B_2-N_2 (σ)	1.966	30.1	$sp^{1.21}$	69.9	$sp^{2.24}$	1.372
		B_1-$C(H_2)$ (σ)	1.956	32.1	$sp^{1.74}$	67.9	$sp^{2.36}$	0.840
		P-$C(H_2)$ (σ)	1.975	41.4	$sp^{2.69}$	58.6	$sp^{3.06}$	0.964
		N_1 (LP)	1.928	-	$sp^{1.35}$	-	-	-
		N_2 (LP)	1.932	-	$sp^{1.28}$	-	-	-

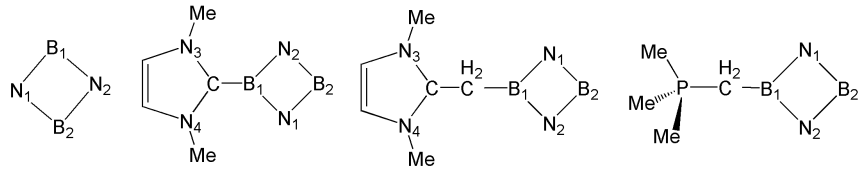

TABLE D.5: NBO analysis for the di-substituted B_2N_2 complexes at the M05-2X/cc-pVTZ level of theory.

Species	NBO Charge	Bond A-B	Occ	(A) %	Hyb (A)	(B) %	Hyb (B)	WBI
$(ImMe_2)_2 \cdot B_2N_2$								
C_{2v}	B_1 0.676	B_1-N_1 (σ)	1.880	25.6	$sp^{1.61}$	74.4	$sp^{2.44}$	1.068
	B_2 0.676	B_1-N_1 (π)	1.643	8.8	$sp^{24.07}$	91.2	$sp^{46.22}$	
	N_1 -1.233	B_2-N_1 (σ)	1.926	28.5	$sp^{2.14}$	71.5	$sp^{2.20}$	1.068
	N_2 -1.233	B_1-C (σ)	1.962	32.0	$sp^{3.05}$	68.0	$sp^{1.38}$	0.817
	N_3 -0.291	B_2-C (σ)	1.966	32.0	$sp^{2.69}$	68.0	$sp^{1.38}$	0.817
	C 0.268	C-N_2 (σ)	1.982	37.4	$sp^{2.43}$	62.6	$sp^{1.86}$	1.300
		C-N_2 (π)	1.870	26.1	$p^{1.00}$	73.9	$p^{1.00}$	
		C-N_3 (σ)	1.982	37.4	$sp^{2.43}$	62.6	$sp^{1.86}$	1.300
		N_1 (LP)	1.917	-	$sp^{1.64}$	-	-	-
		N_3 (LP)	1.504	-	$p^{1.00}$	-	-	-

Species	NBO Charge	Bond A-B	Occ	(A) %	Hyb (A)	(B) %	Hyb (B)	WBI
$(ImMe_2CH_2)_2 \cdot B_2N_2$								
C_2	B 0.826	B-N_1 (σ)	1.927	26.7	$sp^{1.85}$	73.3	$sp^{2.06}$	1.079
	N_1 -1.300	B-N_1 (π)	1.744	13.2	$sp^{40.36}$	86.8	$sp^{67.34}$	
	N_2 -1.300	B-N_2 (σ)	1.914	26.8	$sp^{1.64}$	73.2	$sp^{2.20}$	1.028
	N_3 -0.326	B-C(H_2) (σ)	1.865	29.0	$sp^{3.05}$	71.0	$sp^{2.90}$	0.685
	N_4 -0.320	C-N_3 (σ)	1.980	38.0	$sp^{2.38}$	62.0	$sp^{1.89}$	1.246
	C(H_2) -0.756	C-N_4 (σ)	1.980	38.2	$sp^{2.34}$	61.8	$sp^{1.89}$	1.254
	C 0.527	C-N_4 (π)	1.874	24.6	$sp^{99.99}$	75.4	$sp^{99.99}$	
		C-C(H_2) (σ)	1.971	52.4	$sp^{1.46}$	47.6	$sp^{2.80}$	1.126
		N_1 (LP)	1.914	-	$sp^{1.84}$	-	-	-
		N_2 (LP)	1.914	-	$sp^{1.84}$	-	-	-
		N_3 (LP)	1.548	-	$p^{1.00}$	-	-	-
$(Me_3PCH_2)_2 \cdot B_2N_2$								
C_2	B 0.820	B-N_1 (σ)	1.932	27.0	$sp^{1.58}$	73.0	$sp^{1.88}$	1.062
	N_1 -1.328	B-N_2 (σ)	1.925	26.6	$sp^{2.02}$	73.4	$sp^{2.34}$	1.031
	N_2 -1.328	B-N_2 (π)	1.745	12.2	$sp^{46.16}$	87.8	$sp^{99.99}$	
	C(H_2) -1.058	B-C(H_2) (σ)	1.956	29.0	$sp^{2.86}$	71.0	$sp^{2.27}$	0.763
	P 1.647	P-C(H_2) (σ)	1.977	42.4	$sp^{2.51}$	57.6	$sp^{3.18}$	0.988
		N_1 (LP)	1.918	-	$sp^{1.85}$	-	-	-
		N_2 (LP)	1.918	-	$sp^{1.85}$	-	-	-

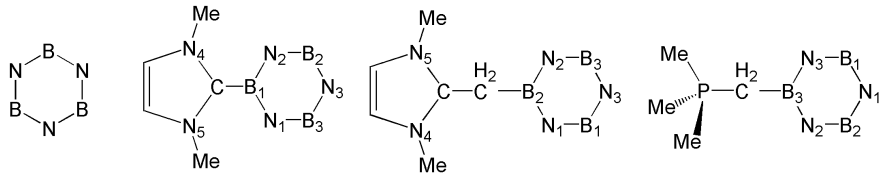

TABLE D.6: NBO analysis for B_3N_3 and its mono-substituted complexes at the M05-2X/cc-pVTZ level of theory.

Species	NBO Charge	Bond A-B	Occ	(A) %	Hyb (A)	(B) %	Hyb (B)	WBI
B_3N_3								
D_{3h}	B 1.058	B-N (σ)	1.919	27.6	$sp^{1.01}$	72.4	$sp^{2.08}$	1.326
	N -1.508	B-N (π)	1.761	17.6	$p^{1.00}$	82.4	$p^{1.00}$	
		N (LP)	1.773	-	$sp^{1.79}$	-	-	-
$ImMe_2{\cdot}B_3N_3$								
C_1	B_1 1.041	B_1-N_1 (σ)	1.981	27.6	$sp^{1.00}$	72.4	$sp^{1.51}$	1.405
	B_2 0.749	B_1-N_3 (σ)	1.917	27.4	$sp^{1.05}$	72.6	$sp^{2.04}$	1.314
	B_3 1.046	B_1-N_3 (π)	1.758	17.4	$p^{1.00}$	82.6	$p^{1.00}$	
	C 0.251	B_2-N_1 (σ)	1.902	27.3	$sp^{1.82}$	72.7	$sp^{1.91}$	1.082
	N_1 -1.171	B_2-N_1 (π)	1.738	16.2	$p^{1.00}$	83.8	$sp^{99.99}$	
	N_2 -1.178	B_2-N_2 (σ)	1.905	27.2	$sp^{1.79}$	72.8	$sp^{1.89}$	1.082
	N_3 -1.081	B_3-N_2 (σ)	1.981	27.5	$sp^{1.00}$	72.5	$sp^{1.49}$	1.398
	N_4 -0.288	B_3-N_2 (π)	1.782	18.1	$p^{1.00}$	81.9	$p^{1.00}$	
	N_5-0.289	B_3-N_3 (σ)	1.918	27.4	$sp^{1.05}$	72.6	$sp^{2.03}$	1.316
		B_2-C (σ)	1.962	31.8	$sp^{2.47}$	68.2	$sp^{1.39}$	0.837
		C-N_4 (σ)	1.982	37.5	$sp^{2.42}$	62.5	$sp^{1.85}$	1.298
		C-N_4 (π)	1.872	26.7	$p^{1.00}$	73.3	$p^{1.00}$	
		C-N_5 (σ)	1.982	37.5	$sp^{2.42}$	62.5	$sp^{1.85}$	1.297
		N_1 (LP)	1.842	-	$sp^{2.82}$	-	-	-
		N_2 (LP)	1.840	-	$sp^{2.89}$	-	-	-
		N_3 (LP)	1.789	-	$sp^{1.88}$	-	-	-
		N_5 (LP)	1.503	-	$p^{1.00}$	-	-	-
$ImMe_2CH_2 \cdot B_3N_3$								
C_1	B_1 1.031	B_1-N_1 (σ)	1.979	27.5	$sp^{1.01}$	72.5	$sp^{1.45}$	1.415
	B_2 0.863	B_1-N_1 (π)	1.806	18.0	$p^{1.00}$	82.0	$sp^{99.99}$	
	B_3 1.023	B_1-N_3 (σ)	1.919	27.4	$sp^{1.06}$	72.6	$sp^{1.99}$	1.315
	C 0.551	B_2-N_1 (σ)	1.894	25.6	$sp^{1.93}$	74.4	$sp^{1.93}$	1.022
	$C(H_2)$ -0.763	B_2-N_2(σ)	1.899	26.3	$sp^{1.77}$	73.7	$sp^{1.83}$	1.096
	N_1 -1.232	B_2-N_2 (π)	1.735	16.3	$sp^{99.99}$	83.7	$p^{1.00}$	
	N_2 -1.157	B_3-N_2 (σ)	1.977	28.0	$sp^{0.99}$	72.0	$sp^{1.56}$	1.436
	N_3 -1.097	B_3-N_3 (σ)	1.917	27.4	$sp^{1.07}$	72.6	$sp^{2.03}$	1.295
	N_4 -0.310	B_3-N_3 (π)	1.763	16.9	$p^{1.00}$	83.1	$p^{1.00}$	
	N_5 -0.318	B_2-$C(H_2)$ (σ)	1.901	29.8	$sp^{2.38}$	70.2	$sp^{2.65}$	0.749
		C-$C(H_2)$(σ)	1.975	52.2	$sp^{1.49}$	47.8	$sp^{2.78}$	1.088
		C-N_4 (σ)	1.981	37.9	$sp^{2.30}$	62.1	$sp^{1.85}$	1.275
		C-N_4 (π)	1.881	25.2	$p^{1.00}$	74.8	$sp^{99.99}$	
		C-N_5 (σ)	1.980	37.8	$sp^{2.38}$	62.2	$sp^{1.86}$	1.263
		N_1 (LP)	1.846	-	$sp^{2.91}$	-	-	-
		N_2 (LP)	1.830	-	$sp^{2.82}$	-	-	-
		N_3 (LP)	1.790	-	$sp^{1.92}$	-	-	-
		N_5 (LP)	1.539	-	$p^{1.00}$	-	-	-

Species	NBO Charge	Bond A-B	Occ	(A) %	Hyb (A)	(B) %	Hyb (B)	WBI
$Me_3PCH_2 \cdot B_3N_3$								
C_1	B_1 1.007	B_1-N_1 (σ)	1.922	27.6	$sp^{1.11}$	72.4	$sp^{1.98}$	1.302
	B_2 1.007	B_1-N_1 (π)	1.770	17.1	$p^{1.00}$	82.9	$p^{1.00}$	
	B_3 0.690	B_1-N_3 (σ)	1.966	28.9	$sp^{1.00}$	71.1	$sp^{2.28}$	1.378
	$C(H_2)$ -1.062	B_2-N_1 (σ)	1.922	27.6	$sp^{1.11}$	72.4	$sp^{1.98}$	1.301
	P 1.658	B_2-N_2 (σ)	1.965	28.9	$sp^{1.00}$	71.1	$sp^{2.29}$	1.379
	N_1 -1.097	B_2-N_2 (π)	1.746	18.1	$p^{1.00}$	81.9	$p^{1.00}$	
	N_2 -1.076	B_3-N_2 (σ)	1.866	28.0	$sp^{1.47}$	72.0	$sp^{1.68}$	1.145
	N_3 -1.080	B_3-N_3 (σ)	1.865	28.0	$sp^{1.48}$	72.0	$sp^{1.68}$	1.143
		B_3-N_3 (π)	1.751	18.7	$sp^{99.99}$	81.3	$p^{1.00}$	
		B_3-$C(H_2)$ (σ)	1.903	28.8	$sp^{4.22}$	71.2	$sp^{2.38}$	0.689
		P-$C(H_2)$ (σ)	1.980	41.3	$sp^{2.03}$	58.7	$sp^{2.72}$	1.046
		N_1 (LP)	1.789	-	$sp^{1.99}$	-	-	-
		N_2 (LP)	1.841	-	$sp^{2.03}$	-	-	-
		N_3 (LP)	1.842	-	$sp^{2.05}$	-	-	-

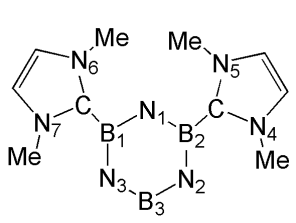

$(ImMe_2)_2.B_3N_3$

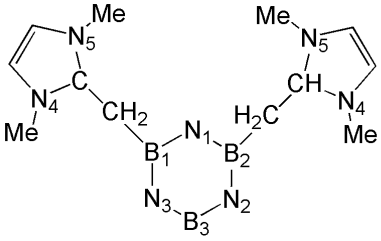

$(ImMe_2CH_2)_2.B_3N_3$

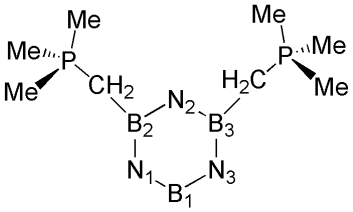

$(Me_3PCH_2)_2.B_3N_3$

Di-substituted B_3N_3 Complexes

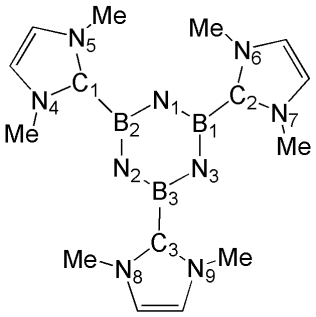

$(ImMe_2)_3.B_3N_3$

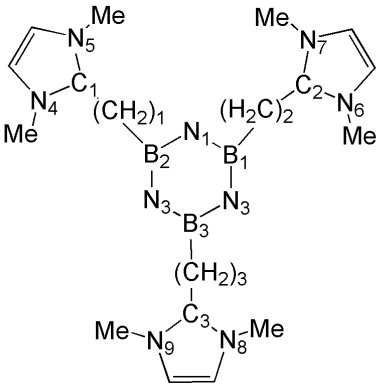

$(ImMe_2CH_2)_3.B_3N_3$

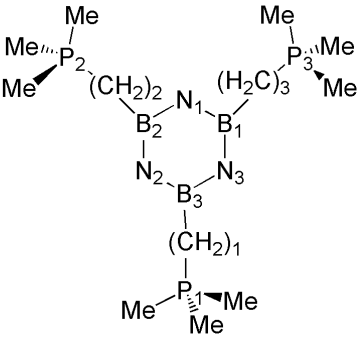

$(Me_3PCH_2)_3.B_3N_3$

Tri-substituted B_3N_3 Complexes

TABLE D.7: NBO analysis for the di-substituted B_3N_3 complexes at the M05-2X/cc-pVTZ level of theory.

Species	NBO Charge	Bond A-B	Occ	(A) %	Hyb (A)	(B) %	Hyb (B)	WBI
$(ImMe_2)_2 \cdot B_3N_3$								
C_2	B_1 0.720	B_1-N_1 (σ)	1.975	27.4	$sp^{1.65}$	72.6	$sp^{1.44}$	1.163
	B_2 0.720	B_1-N_3 (σ)	1.904	27.2	$sp^{1.83}$	72.8	$sp^{1.90}$	1.088
	B_3 1.058	B_1-N_3 (π)	1.731	17.2	$p^{1.00}$	82.8	$sp^{99.99}$	
	C 0.279	B_2-N_1 (σ)	1.975	27.4	$sp^{1.65}$	72.6	$sp^{1.44}$	1.163
	N_1 -1.237	B_2-N_1 (π)	1.745	17.4	$p^{1.00}$	82.6	$p^{1.00}$	
	N_2 -1.175	B_2-N_2 (σ)	1.904	27.2	$sp^{1.83}$	72.8	$sp^{1.89}$	1.088
	N_3 -1.175	B_3-N_2 (σ)	1.978	27.0	$sp^{1.07}$	73.0	$sp^{1.46}$	1.375
	N_4 -0.301	B_3-N_2 (π)	1.753	18.1	$p^{1.00}$	81.9	$p^{1.00}$	
	N_5 -0.300	B_3-N_3 (σ)	1.978	27.0	$sp^{1.07}$	73.0	$sp^{1.46}$	1.375
	N_6 -0.300	B_1-C (σ)	1.962	30.9	$sp^{2.73}$	69.1	$sp^{1.34}$	0.823
	N_7 -0.301	C-N_4 (σ)	1.982	37.1	$sp^{2.48}$	62.9	$sp^{1.84}$	1.290
		C-N_4 (π)	1.869	25.4	$p^{1.00}$	74.6	$p^{1.00}$	
		C-N_5 (σ)	1.982	37.1	$sp^{2.46}$	62.9	$sp^{1.83}$	1.293
		C-N_6 (σ)	1.982	37.1	$sp^{2.46}$	62.9	$sp^{1.83}$	1.293
		C-N_6 (π)	1.872	25.4	$p^{1.00}$	74.6	$p^{1.00}$	
		C-N_7 (σ)	1.982	37.1	$sp^{2.48}$	62.9	$sp^{1.84}$	1.290
		N_1 (LP)	1.867	-	$sp^{4.44}$	-	-	-
		N_2 (LP)	1.852	-	$sp^{2.97}$	-	-	-
		N_3 (LP)	1.852	-	$sp^{2.97}$	-	-	-
		N_5 (LP)	1.515	-	$p^{1.00}$	-	-	-
		N_7 (LP)	1.513	-	$p^{1.00}$	-	-	-

Species	NBO Charge	Bond (A-B)	Occ	(A) %	Hyb (A)	B (%)	Hyb (B)	WBI
$(ImMe_2CH_2)_2 \cdot B_3N_3$								
C_2	B_1 0.861	B_1-N_1 (σ)	1.971	26.2	$sp^{1.65}$	73.8	$sp^{1.41}$	1.153
	B_2 0.861	B_1-N_1 (π)	1.762	16.2	$sp^{99.99}$	83.8	$p^{1.00}$	
	B_3 1.058	B_1-N_3 (σ)	1.902	25.7	$sp^{1.83}$	74.3	$sp^{1.86}$	1.053
	$C(H_2)$ -0.749	B_2-N_1 (σ)	1.971	26.2	$sp^{1.65}$	73.8	$sp^{1.41}$	1.153
	C 0.525	B_2-N_2 (σ)	1.902	25.7	$sp^{1.83}$	74.3	$sp^{1.86}$	1.053
	N_1 -1.308	B_2-N_2 (π)	1.745	15.4	$sp^{99.99}$	84.6	$p^{1.00}$	
	N_2 -1.235	B_3-N_2 (σ)	1.974	27.0	$sp^{1.09}$	73.0	$sp^{1.45}$	1.373
	N_3 -1.235	B_3-N_3 (σ)	1.974	27.0	$sp^{1.09}$	73.0	$sp^{1.45}$	1.373
	N_4 -0.318	B_3-N_3 (π)	1.784	17.4	$p^{1.00}$	82.6	$p^{1.00}$	
	N_5 -0.320	B_1-$C(H_2)$ (σ)	1.875	28.4	$sp^{2.73}$	71.6	$sp^{2.70}$	0.702
		C-$C(H_2)$ (σ)	1.972	52.6	$sp^{1.46}$	47.4	$sp^{2.89}$	1.111
		C-N_4 (σ)	1.981	38.1	$sp^{2.35}$	61.9	$sp^{1.88}$	1.259
		C-N_4 (π)	1.877	24.8	$sp^{99.99}$	75.2	$p^{1.00}$	
		C-N_5 (σ)	1.981	38.1	$sp^{2.37}$	61.9	$sp^{1.88}$	1.256
		N_1 (LP)	1.867	-	$sp^{4.74}$	-	-	-
		N_2 (LP)	1.848	-	$sp^{3.05}$	-	-	-
		N_3 (LP)	1.848	-	$sp^{3.05}$	-	-	-
		N_5 (LP)	1.544	-	$sp^{1.00}$	-	-	-
$(Me_3PCH_2)_2 \cdot B_3N_3$								
C_1	B_1 1.055	B_1-N_1 (σ)	1.976	27.5	$sp^{1.07}$	72.5	$sp^{1.30}$	1.443
	B_2 0.839	B_1-N_1 (π)	1.781	18.9	$p^{1.00}$	81.1	$p^{1.00}$	
	B_3 0.849	B_1-N_3 (σ)	1.976	26.5	$sp^{1.10}$	73.5	$sp^{1.42}$	1.309
	$C(H_2)_1$ -1.051	B_2-N_1 (σ)	1.895	26.6	$sp^{1.79}$	73.4	$sp^{1.89}$	1.075
	$C(H_2)_2$ -1.053	B_2-N_2 (σ)	1.973	26.4	$sp^{1.74}$	73.6	$sp^{1.51}$	1.126
	P_1 1.644	B_2-N_2 (π)	1.764	15.5	$p^{1.00}$	84.4	$p^{1.00}$	
	P_2 1.646	B_3-N_2 (σ)	1.974	26.5	$sp^{1.62}$	73.5	$sp^{1.31}$	1.173
	N_1 -1.165	B_3-N_3 (σ)	1.908	25.6	$sp^{1.90}$	74.4	$sp^{1.87}$	1.035
	N_2 -1.318	B_3-N_3 (π)	1.772	14.6	$p^{1.00}$	85.4	$p^{1.00}$	
	N_3 -1.298	B_2-$C(H_2)_1$ (σ)	1.951	28.1	$sp^{2.62}$	71.9	$sp^{2.18}$	0.763
		B_3-$C(H_2)_2$ (σ)	1.953	27.9	$sp^{2.67}$	72.1	$sp^{2.13}$	0.762
		P_1-$C(H_2)_1$ (σ)	1.979	42.7	$sp^{2.43}$	57.3	$sp^{3.19}$	0.995
		P_2-$C(H_2)_2$ (σ)	1.980	38.4	$sp^{3.68}$	61.6	$sp^{2.59}$	1.000
		N_1 (LP)	1.839	-	$sp^{2.96}$	-	-	-
		N_2 (LP)	1.870	-	$sp^{4.87}$	-	-	-
		N_3 (LP)	1.858	-	$sp^{3.12}$	-	-	-

TABLE D.8: NBO analysis for the tri-substituted B_3N_3 complexes at the M05-2X/cc-pVTZ level of theory.

Species	NBO Charge	Bond (A-B)	Occ	(A) %	Hyb (A)	B (%)	Hyb (B)	WBI
$(ImMe_2)_3 \cdot B_3N_3$								
C_2	B_1 0.757	B_1-N_1 (σ)	1.972	26.7	$sp^{1.64}$	73.3	$sp^{1.43}$	1.141
	B_2 0.757	B_1-N_3 (σ)	1.971	26.9	$sp^{1.63}$	73.1	$sp^{1.46}$	1.144
	B_3 0.748	B_1-N_3 (π)	1.722	17.7	$p^{1.00}$	82.3	$sp^{99.99}$	
	C_1 0.292	B_2-N_1 (σ)	1.972	26.7	$sp^{1.64}$	73.3	$sp^{1.43}$	1.141
	C_2 0.292	B_2-N_1 (π)	1.731	17.5	$sp^{99.99}$	82.5	$p^{1.00}$	
	C_3 0.311	B_2-N_2 (σ)	1.971	26.8	$sp^{1.63}$	73.2	$sp^{1.46}$	1.144
	N_1 -1.248	B_3-N_2 (σ)	1.970	26.7	$sp^{1.62}$	73.3	$sp^{1.42}$	1.148
	N_2 -1.238	B_3-N_2 (π)	1.729	18.1	$sp^{99.99}$	81.9	$sp^{99.99}$	
	N_3 -1.238	B_3-N_3 (σ)	1.970	26.7	$sp^{1.62}$	73.3	$sp^{1.42}$	1.148
	N_4 -0.310	B_1-C_2 (σ)	1.958	29.4	$sp^{3.15}$	70.6	$sp^{1.30}$	0.797
	N_5 -0.310	B_2-C_1 (σ)	1.959	29.4	$sp^{3.14}$	70.6	$sp^{1.30}$	0.797
	N_6 -0.310	B_3-C_3 (σ)	1.957	29.5	$sp^{3.20}$	70.5	$sp^{1.30}$	0.792
	N_7 -0.310	C_1-N_4 (σ)	1.981	36.8	$sp^{2.51}$	63.2	$sp^{1.81}$	1.286
	N_8 -0.316	C_1-N_5 (σ)	1.982	36.8	$sp^{2.52}$	63.2	$sp^{1.80}$	1.286
	N_9 -0.316	C_1-N_5 (π)	1.870	24.5	$p^{1.00}$	75.5	$p^{1.00}$	
		C_2-N_6 (σ)	1.982	36.8	$sp^{2.52}$	63.2	$sp^{1.80}$	1.286
		C_2-N_6 (π)	1.870	24.5	$p^{1.00}$	75.5	$p^{1.00}$	
		C_2-N_7 (σ)	1.981	36.8	$sp^{2.51}$	63.2	$sp^{1.81}$	1.286
		C_3-N_8 (σ)	1.981	36.7	$sp^{2.51}$	63.3	$sp^{1.81}$	1.286
		C_3-N_8 (π)	1.871	23.9	$p^{1.00}$	76.1	$p^{1.00}$	
		C_3-N_9 (σ)	1.982	36.7	$sp^{2.51}$	63.3	$sp^{1.81}$	1.286
		N_1 (LP)	1.867	-	$sp^{4.56}$	-	-	-
		N_2 (LP)	1.873	-	$sp^{4.48}$	-	-	-
		N_3 (LP)	1.873	-	$sp^{4.48}$	-	-	-
		N_4 (LP)	1.523	-	$p^{1.00}$	-	-	-
		N_7 (LP)	1.523	-	$p^{1.00}$	-	-	-
		N_9 (LP)	1.529	-	$p^{1.00}$	-	-	-

Species	NBO Charge	Bond (A-B)	Occ	(A) %	Hyb (A)	B (%)	Hyb (B)	WBI
$(ImMe_2CH_2)_3 \cdot B_3N_3$								
C_1	B_1 0.904	B_1-N_1 (σ)	1.967	25.3	$sp^{1.60}$	74.7	$sp^{1.38}$	1.135
	B_2 0.909	B_1-N_1 (π)	1.761	16.4	$sp^{99.99}$	83.6	$sp^{99.99}$	
	B_3 0.909	B_1-N_3 (σ)	1.964	25.5	$sp^{1.60}$	74.5	$sp^{1.43}$	1.121
	$C(H_2)_1$ -0.750	B_2-N_1 (σ)	1.966	25.4	$sp^{1.59}$	74.6	$sp^{1.41}$	1.124
	$C(H_2)_2$ -0.750	B_2-N_2 (σ)	1.966	25.3	$sp^{1.58}$	74.7	$sp^{1.38}$	1.137
	$C(H_2)_3$ -0.751	B_2-N_2 (π)	1.758	16.4	$sp^{99.99}$	83.6	$sp^{99.99}$	
	C_1 0.525	B_3-N_2 (σ)	1.966	25.3	$sp^{1.57}$	74.7	$sp^{1.41}$	1.126
	C_2 0.524	B_3-N_3 (σ)	1.966	25.3	$sp^{1.57}$	74.7	$sp^{1.37}$	1.145
	C_3 0.527	B_3-N_3 (π)	1.760	16.7	$sp^{99.99}$	83.3	$sp^{99.99}$	
	N_1 -1.332	B_1-$C(H_2)_2$ (σ)	1.842	26.4	$sp^{3.36}$	73.6	$sp^{2.89}$	0.642
	N_2 -1.331	B_2-$C(H_2)_1$ (σ)	1.835	26.2	$sp^{3.44}$	73.8	$sp^{2.96}$	0.633
	N_3 -1.326	B_3-$C(H_2)_3$ (σ)	1.824	25.9	$sp^{3.54}$	74.1	$sp^{3.06}$	0.620
	N_4 -0.331	C_1-$C(H_2)_1$ (σ)	1.973	52.8	$sp^{1.42}$	47.2	$sp^{2.78}$	1.154
	N_5 -0.327	C_2-$C(H_2)_2$ (σ)	1.973	52.8	$sp^{1.43}$	47.2	$sp^{2.81}$	1.145
	N_6 -0.325	C_3-$C(H_2)_3$ (σ)	1.974	52.8	$sp^{1.41}$	47.2	$sp^{2.72}$	1.167
	N_7 -0.328	C_1-N_4 (σ)	1.980	38.0	$sp^{2.42}$	62.0	$sp^{1.88}$	1.232
	N_8 -0.334	C_1-N_5 (σ)	1.980	38.1	$sp^{2.39}$	61.9	$sp^{1.88}$	1.238
	N_9 -0.333	C_1-N_5 (π)	1.873	23.8	$sp^{99.99}$	76.2	$sp^{99.99}$	
		C_2-N_6 (σ)	1.980	38.1	$sp^{2.39}$	61.9	$sp^{1.88}$	1.242
		C_2-N_6 (π)	1.874	24.0	$sp^{99.99}$	76.0	$sp^{99.99}$	
		C_2-N_7 (σ)	1.980	38.1	$sp^{2.40}$	61.9	$sp^{1.88}$	1.238
		C_3-N_8 (σ)	1.980	38.0	$sp^{2.41}$	62.0	$sp^{1.88}$	1.230
		C_3-N_8 (π)	1.873	23.3	$sp^{99.99}$	76.7	$sp^{99.99}$	
		C_3-N_9 (σ)	1.980	38.0	$sp^{2.42}$	62.0	$sp^{1.88}$	1.230
		N_1 (LP)	1.866	-	$sp^{4.96}$	-	-	-
		N_2 (LP)	1.867	-	$sp^{4.97}$	-	-	-
		N_3 (LP)	1.869	-	$sp^{4.91}$	-	-	-
		N_4 (LP)	1.561	-	$p^{1.00}$	-	-	-
		N_7 (LP)	1.556	-	$p^{1.00}$	-	-	-
		N_9 (LP)	1.561	-	$p^{1.00}$	-	-	-

Species	NBO Charge	Bond A-B	Occ	(A) %	Hyb (A)	(B) %	Hyb (B)	WBI
$(Me_3PCH_2)_3 \cdot B_3N_3$								
C_1	B_1 0.871	B_1-N_1 (σ)	1.968	25.3	$sp^{1.61}$	74.7	$sp^{1.32}$	1.149
	B_2 0.854	B_1-N_3 (σ)	1.969	24.8	$sp^{1.66}$	75.2	$sp^{1.29}$	1.118
	B_3 0.869	B_1-N_3 (π)	1.781	16.3	$sp^{99.99}$	83.7	$sp^{99.99}$	
	$C(H_2)_1$ -1.070	B_2-N_1 (σ)	1.966	25.2	$sp^{1.69}$	74.8	$sp^{1.43}$	1.099
	$C(H_2)_2$ -1.051	B_2-N_1 (π)	1.745	16.0	$sp^{99.99}$	84.0	$sp^{99.99}$	
	$C(H_2)_3$ -1.052	B_2-N_2 (σ)	1.966	25.7	$sp^{1.62}$	74.3	$sp^{1.38}$	1.164
	P_1 1.645	B_3-N_2 (σ)	1.966	26.0	$sp^{1.57}$	74.0	$sp^{1.36}$	1.201
	P_2 1.645	B_3-N_2 (π)	1.740	18.7	$sp^{99.99}$	81.3	$sp^{99.99}$	
	P_3 1.643	B_3-N_3 (σ)	1.967	25.0	$sp^{1.66}$	75.0	$sp^{1.47}$	1.072
	N_1 -1.341	B_1-$C(H_2)_3$ (σ)	1.924	26.0	$sp^{3.21}$	74.0	$sp^{2.22}$	0.704
	N_2 -1.260	B_2-$C(H_2)_2$ (σ)	1.928	26.4	$sp^{3.12}$	73.6	$sp^{2.21}$	0.713
	N_3 -1.381	B_3-$C(H_2)_1$ (σ)	1.931	25.7	$sp^{3.29}$	74.3	$sp^{2.22}$	0.700
		P_1-$C(H_2)_1$ (σ)	1.978	43.5	$sp^{2.32}$	56.5	$sp^{3.24}$	1.024
		P_2-$C(H_2)_2$ (σ)	1.971	43.1	$sp^{2.37}$	56.9	$sp^{3.51}$	1.014
		P_3-$C(H_2)_3$ (σ)	1.972	43.3	$sp^{2.34}$	56.7	$sp^{3.54}$	1.019
		N_1 (LP)	1.872	-	$sp^{5.24}$	-	-	-
		N_2 (LP)	1.871	-	$sp^{5.22}$	-	-	-
		N_3 (LP)	1.870	-	$sp^{5.17}$	-	-	-

B_3N_3 (s)

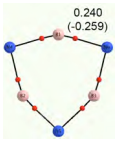

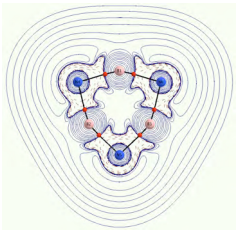

****

C_6H_6

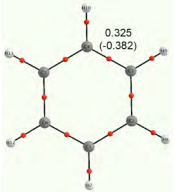

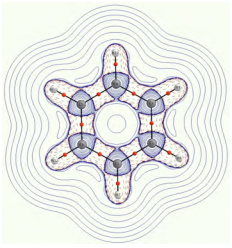

****

$ImMe_2$

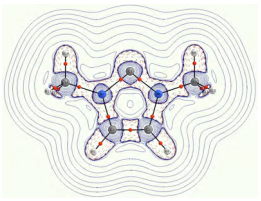

****

$ImMe_2CH_2$

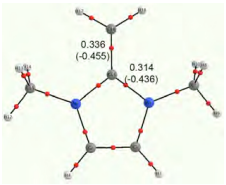

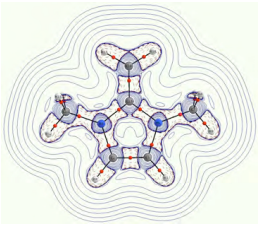

****

Me_3PCH_2

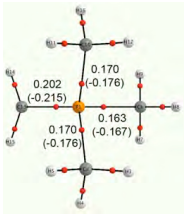

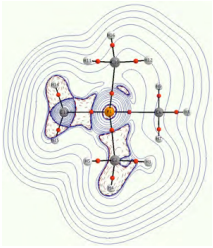

****

$ImMe_2$·BN

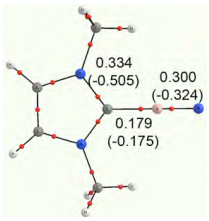

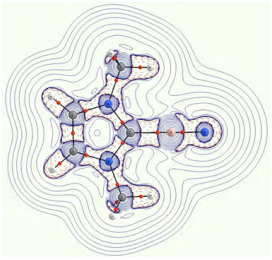

****

$ImMe_2CH_2$·BN

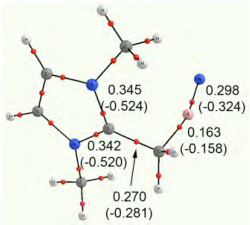

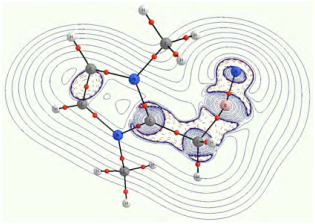

****

Me_3PCH_2·BN

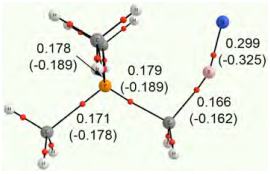

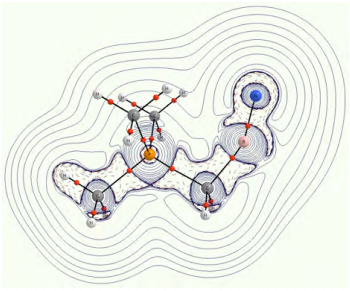

****

$ImMe_2$·BNBN

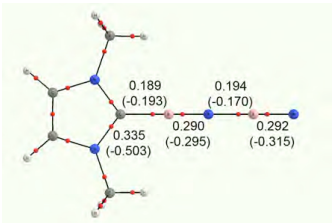

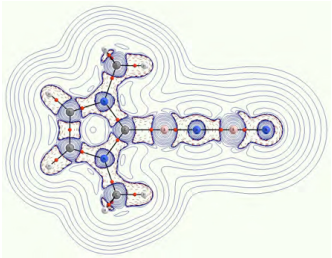

****

$ImMe_2CH_2$·BNBN

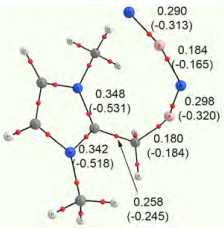

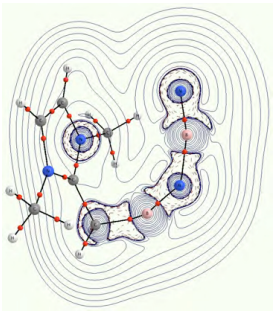

****

Me_3PCH_2·BNBN

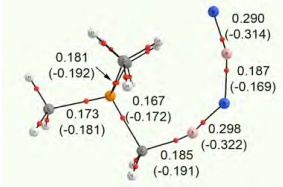

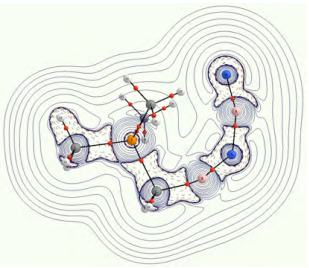

****

$ImMe_2{\cdot}B_2N_2$

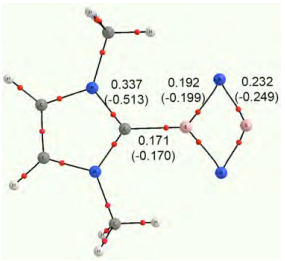

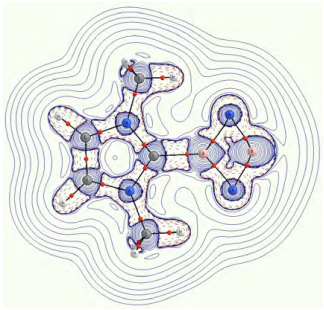

****

$ImMe_2CH_2{\cdot}B_2N_2$

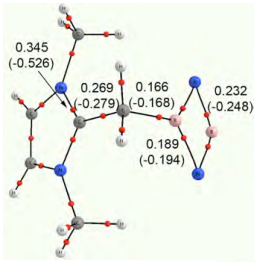

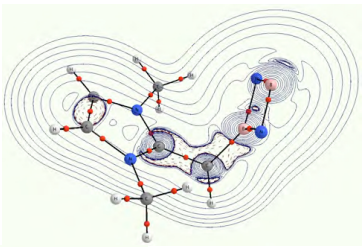

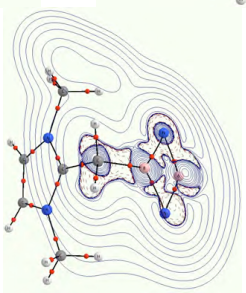

****

$Me_3PCH_2{\cdot}B_2N_2$

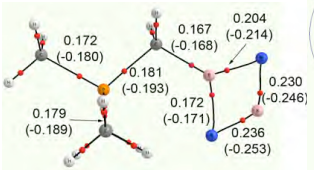

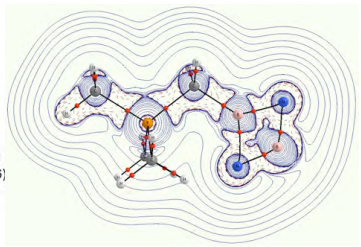

****

$(ImMe_2)_2{\cdot}B_2N_2$

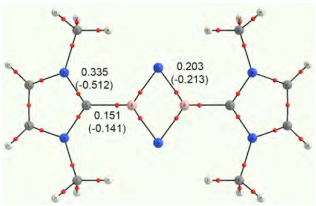

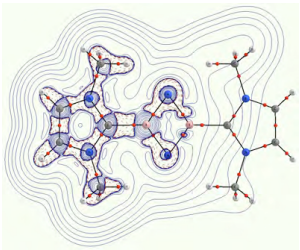

****

$(ImMe_2CH_2)_2{\cdot}B_2N_2$

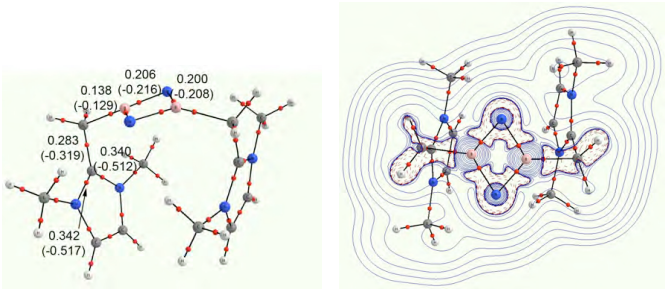

****

$(Me_3PCH_2)_2{\cdot}B_2N_2$

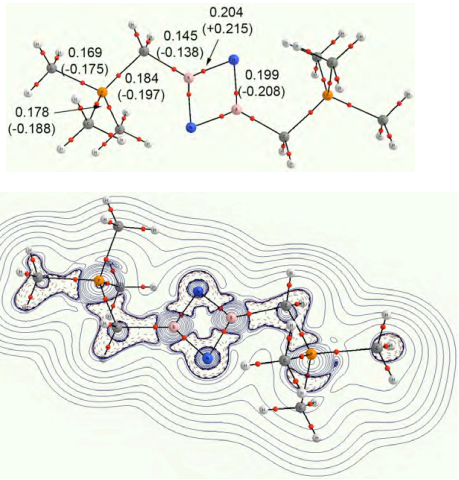

****

$ImMe_2{\cdot}B_3N_3$

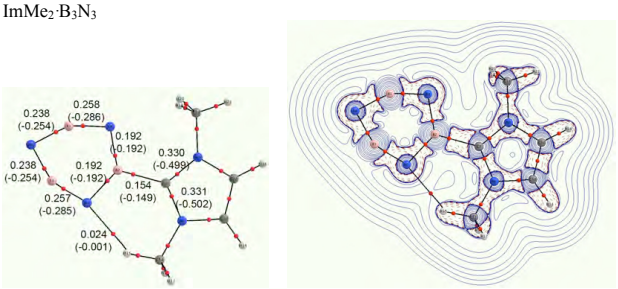

****

$ImMe_2CH_2{\cdot}B_3N_3$

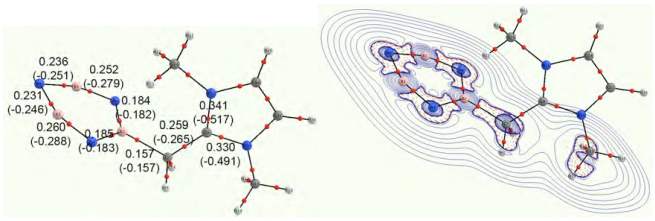

****

$Me_3PCH_2{\cdot}B_3N_3$

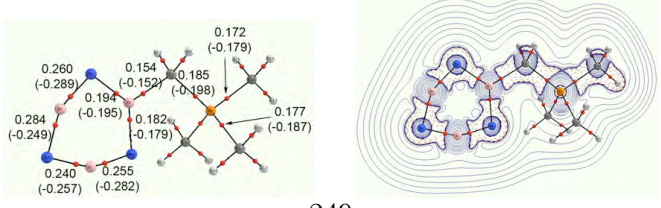

****

$(ImMe_2)_2{\cdot}B_3N_3$

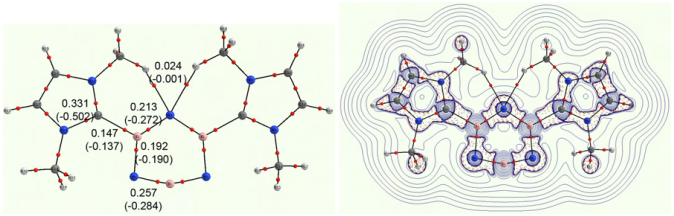

****

$(ImMe_2CH_2)_2{\cdot}B_3N_3$

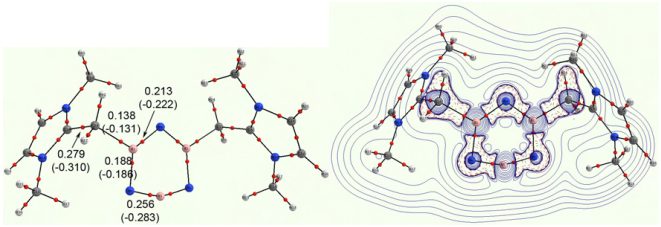

****

$(Me_3PCH_2)_2{\cdot}B_3N_3$

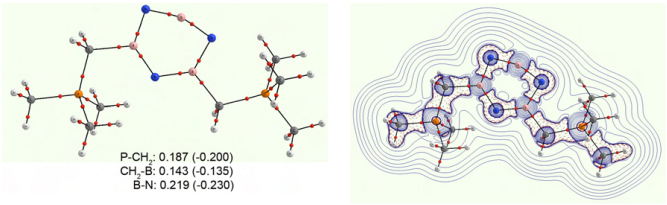

****

$(ImMe_2)_3{\cdot}B_3N_3$

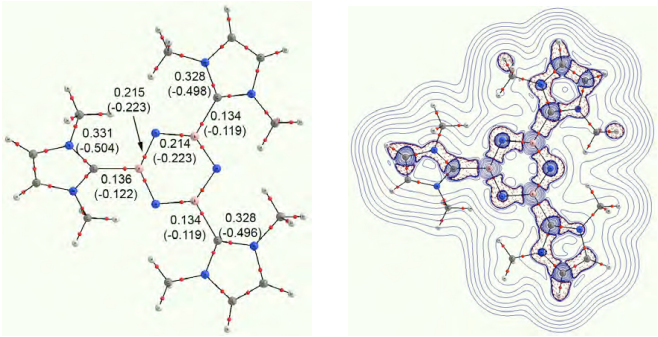

****

$(ImMe_2CH_2)_3$-B_3N_3

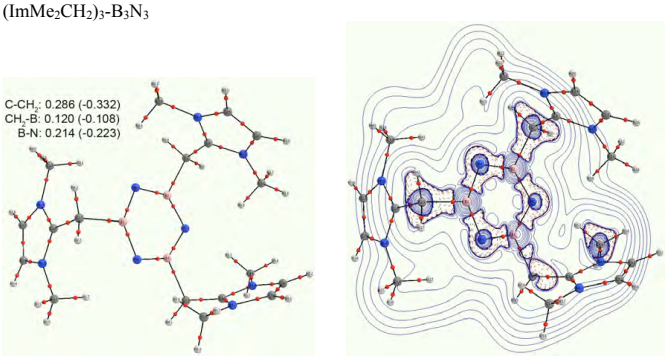

****

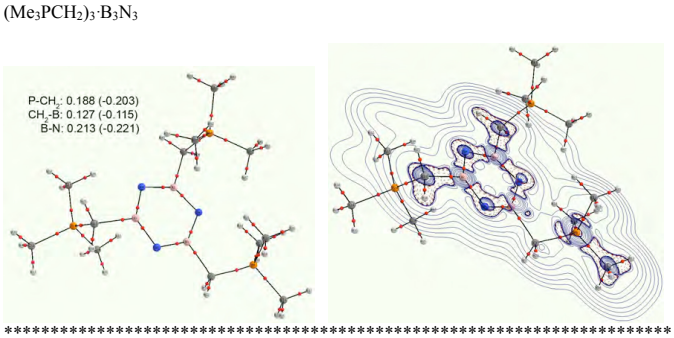

FIGURE D.1: M05-2X/cc-pVTZ calculated AIM results, i.e., ρ (r) and H(r) (in parenthesis), for all the structures in this study. Average values of the ρ (r) and H(r) are provided for some of the two and three Lewis base substituted complexes.